# UNIVERSITÉ DE STRASBOURG

*ÉCOLE DOCTORALE DES SCIENCES CHIMIQUES*

**Institut de Science et d'Ingénierie Supramoléculaires (I.S.I.S.)**

**UMR 7006 Laboratoire de Nanochimie**

# THÈSE présentée par :


## Maria Girolama DEL ROSSO


soutenue le : **06 Juillet 2015**

pour obtenir le grade de : **Docteur de l'université de Strasbourg**

Discipline/ Spécialité : Chimie-Physique

# EXPLORING SUPRAMOLECULAR INTERACTIONS IN HYBRID MATERIALS

**THÈSE dirigée par :**

| | |
|---|---|
| **SAMORÌ Paolo** | Professeur, Université de Strasbourg |

**RAPPORTEURS :**

| | |
|---|---|
| **PATRONIAK Violetta** | Professeur, Université Adam Mickiewicz, Poznań |
| **STEFANKIEWICZ Artur R.** | Docteur, Wielkopolska Center for Advanced Technologies (WCAT), Poznań |

---

**AUTRES MEMBRES DU JURY :**

| | |
|---|---|
| **MAURO Matteo** | Docteur, Université de Strasbourg |

# Résumé

Le domaine de la *chimie supramoléculaire* a été défini pour la première fois en 1978 par J.-M. Lehn comme étant la «chimie de l'assemblage moléculaire et de lien intermoléculaire". [1] C'est une branche de la chimie qui étudie les assemblages d'éléments constitutifs moléculaires interagissant par des forces non covalentes, telles que des interactions électrostatiques, des liaisons hydrogène, des interactions π-π, des forces de van der Waals, etc.

Une entité supramoléculaire simple est habituellement produite à partir d'un processus de reconnaissance entre les deux blocs de constructions moléculaires appelés *récepteur* et *substrat*.

Depuis les premières études dans ce domaine, par Cram, Pedersen et Lehn pour lesquelles les trois scientifiques ont été récompensés par le prix Nobel en 1987, le monde de la chimie supramoléculaire est devenu de plus en plus large, donnant naissance à d'autres branches de la chimie, comme la *nanochimie*.[2]

Grâce à l'auto-assemblage de molécules de structure approprié, comportant des fonctions *ad hoc*, il est possible de concevoir des nanostructures hautement ordonnées 1D, 2D et 3D possédant des propriétés chimiques et physiques spécifiques. Dans cette thèse, nous nous sommes concentrés sur l'étude des différentes interactions supramoléculaires à partir d'interactions chimiques *hôte-invité* simples, en employant des interactions supramoléculaires afin de produire un matériau désiré et finalement, utiliser ces interactions

supramoléculaires dans des dispositifs électroniques. Les principaux thèmes étudiés sont donc:

- Etude de la complexation réversible du cryptand [2.2.2] avec l'ion potassium par titration calorimétrique isotherme (ITC);

- Exploitation des interactions supramoléculaires pour la production de graphène préparé par exfoliation en phase liquide (LPE graphène);

- Réalisation d'électrodes asymétriques qui peuvent répondre de façon indépendante à une excitation lumineuse, grâce à la fonctionnalisation sélective de chaque électrode à travers la chimisorption de monocouches auto-assemblées de deux molécules photochromiques différentes.

La titration calorimétrique isotherme (ITC) est un outil performant, principalement utilisé en biologie pour explorer des interactions non covalentes complexes. Très récemment, cette technique a commencé à être utilisée en chimie supramoléculaire, dans le but d'étudier les interactions des liaisons *hôte- invité*.[3] L'ITC permet de déterminer simultanément, et avec une grande précision, les paramètres thermodynamiques et la stœchiométrie d'une interaction ligand-récepteur en une seule expérience, en mesurant les incréments de chaleur survenant au cours des expériences de titrage. Étonnamment, dans la littérature, seuls de rares exemples peuvent être trouvés sur l'application de l'ITC sur une simple chimie *hôte-invité* en solution aqueuse.

Afin de mieux comprendre le mode de fonctionnement de l'ITC, ses avantages, ses inconvénients et ses possibles applications futures, une étude détaillée a été effectuée sur un système modèle basé sur la thermodynamique de la complexation des ions potassium par

1,10-diaza-4, 7,13,16,21,24-hexaoxabicyclo [8.8.8] hexacosane (cryptand [2.2.2]) en solution aqueuse. Le cryptand [2.2.2] a été l'un des premiers cryptands à avoir été synthétisé par Lehn et ses collègues, et ses propriétés thermodynamiques ont déjà été étudiées en détails par spectroscopie RMN.

Une solution aqueuse de cryptand [2.2.2] est alcaline, et la réaction d'hydrolyse résultante conduit à une solution aqueuse de cryptand [2.2.2] diluée contenant une fraction importante du ligand dans sa forme monoprotonée. La protonation est un moyen d'inhibition de la liaison des cations métalliques par le cryptand. Par conséquent, dans ce travail, nous avons étudié les conditions optimales pour la détermination de la constante de complexation d'un ligand, qui peut subir une hydrolyse importante dans l'eau. De plus en modifiant le pH de la solution, il a été possible d'induire de manière réversible la complexation / de-complexation du cryptand dans des expériences subséquentes *in situ* (fig.1).

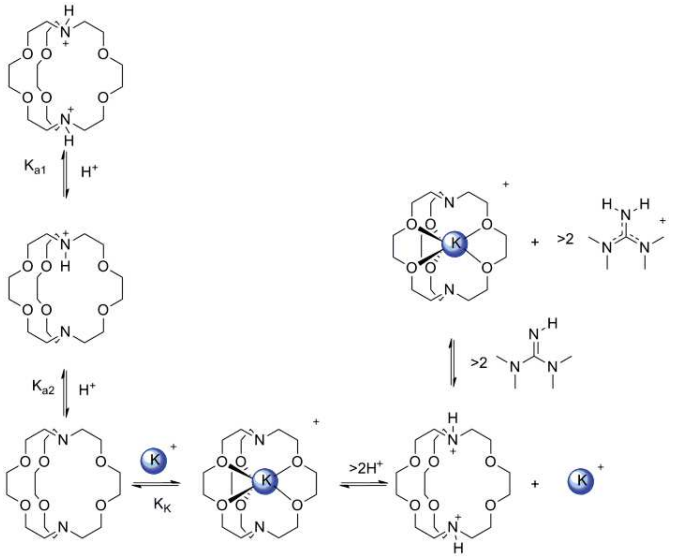


**Figure 1** : schématisation du processus de complexation réversible *in situ* du cryptand [2.2.2]

Les interactions supramoléculaires entre des blocs de construction bien définis déterminent les caractéristiques particulières d'un ensemble ou d'un système. Le graphène est un matériau unique, présentant des propriétés optiques, électriques et mécaniques exceptionnelles, le rendant ainsi attrayant pour de nombreuses applications technologiques. Le graphène a été pour la première fois isolé par exfoliation mécanique du graphite. Le graphite, du grec γράφειν - écrire, est l'un des exemples des plus célèbres matériaux supramoléculaires présents dans la nature. Il est composé de monocouches d'atomes de carbone hybridés sp2, maintenues ensemble par des interactions π-π.

Deux approches sont possibles pour la production de graphène: une approche *bottom-up,* à partir de petits blocs de construction, ou une approche *top-down,* qui utilise le graphite comme matériel de départ. Parmi les approches top-down, une méthode facilement applicable à grande échelle est l'exfoliation du graphite dans des milieux liquides en utilisant l'ultrasonication.

La méthode d'exfoliation en phase liquide (LPE) présente un intérêt grandissant du fait de son extrême polyvalence: elle peut être utilisée pour déposer du graphène dans une variété d'environnements et sur différents substrats, non accessibles en utilisant le clivage mécanique ou des méthodes de croissance. La procédure LPE consiste en trois étapes: (i) dispersion du graphite dans le solvant choisi, (ii) sonication, et (iii) purification par centrifugation.[4] L'exfoliation du graphite se produit grâce à des forces de cisaillement et à la cavitation, agissant sur le matériau pendant l'ultrasonication. Le choix du solvant est crucial car, après l'exfoliation, l'interaction solvant-graphène doit contrebalancer les forces attractives entre les feuilles de graphène.

Il a été largement étudié et prouvé que les milieux liquides ayant une tension de surface d'environ 40 mJ $m^{-2}$, comme la N-méthyl-2-pyrrolidone (NMP) ou l'orto-dichlorobenzène (*o*-DCB), sont les meilleurs choix pour la technique d'exfoliation, car ils minimisent l'énergie interfaciale entre le solvant et le graphène et permettent ainsi de surpasser les forces de van der Waals entre les couches de graphène adjacentes.

Récemment, il a été montré que l'addition de petites molécules organiques et / ou polymères, présentant une forte affinité pour la surface de graphène, au cours de LPE du graphite, permet de maitriser le rendement de l'exfoliation ainsi que la qualité du graphène et, dans certains cas, peut conférer des propriétés supplémentaires au matériau exfolié.

Dans ce travail, nous montrons que la qualité et la quantité des dispersions de graphène sans défauts, composé de quelques couches d'épaisseur, dans des solvants tels que l'orto-dichlorobenzène, peuvent être améliorées. Cela est réalisé en ajoutant des molécules organiques simples, en tirant parti ainsi de leurs interactions supramoléculaires avec le graphite pendant l'exfoliation, ainsi qu'après l'exfoliation, avec le graphène.

Nous avons utilisé, en particulier, les hydrocarbures aromatiques polycycliques (HAP) qui interagissent avec le graphène grâce à des interactions π-π. De plus, nous avons étudié comment la fonctionnalisation de ces molécules, avec des atomes tels que le chlore, pourraient affecter le processus d'exfoliation améliorant les interactions avec les feuillets du graphène. Cet effet particulier peut être attribué à la polarizabilité des molécules chlorées, qui permettent une meilleure interaction de la molecule avec le graphène, comme l'a été démontré par des calculs théoriques effectués par nos collaborateurs.

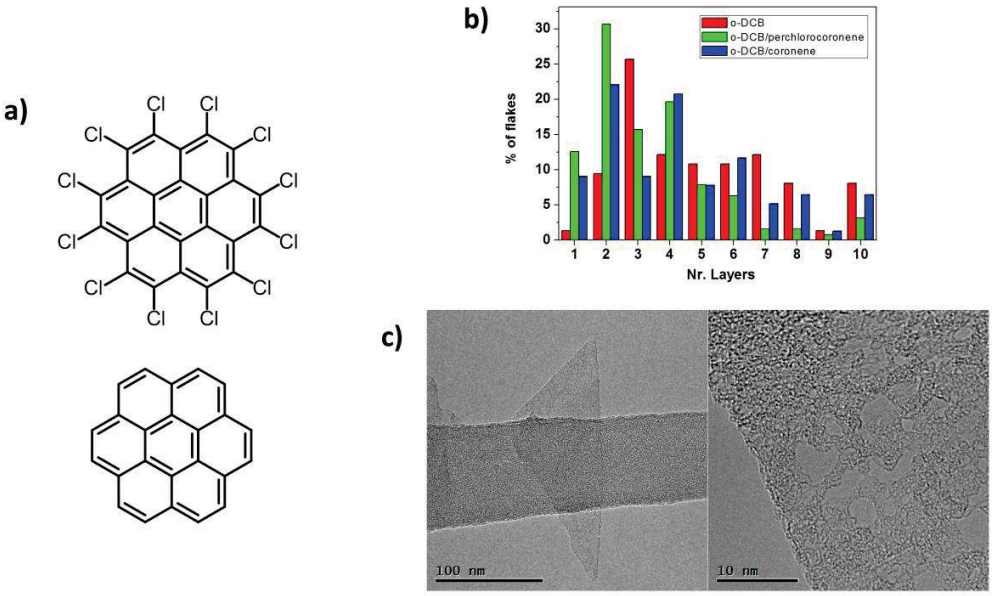


**Figure 2 :** a) molécules utilisées pour l'exfoliation ; b) pourcentage des monocouches de graphène obtenu par analyse TEM ; c) images TEM et HRTEM des monocouches de graphène

Dans la dernière partie de la thèse, nous avons exploité les interactions supramoléculaires pour la fabrication de dispositifs multifonctionnels en modifiant des électrodes en or par l'utilisation de monocouches chimisorbées et auto-assemblées (SAM) de molécules thiolées. Les SAM sont parmi les plus fascinants structures dans le domaine de la nanochimie.[5] La formation de SAM la plus populaire est induite par la création spontanée d'une liaison chimique entre les groupes fonctionnels spécifiques et la surface de l'or. L'interaction intermoléculaire est nécessaire pour stabiliser les SAM. Les SAM les plus connues et les plus robustes sont celles possédant une fonction thiol, réagissant sur l'or.

En modulant la structure moléculaire, et par le choix approprié du groupement terminal, les propriétés physiques et chimiques de la surface peuvent être contrôlées avec une grande précision Le but de ce travail était d'étudier la possibilité de recouvrement d'électrodes d'or adjacentes de façon asymétrique, par chimisorption de SAM de molécules photochromiques sur leurs surfaces. De telles SAM pourraient donc être commutées indépendamment lors de l'application de différents stimuli lumineux. L'incorporation de SAM photochromique à une interface métal-semi-conducteur a été conçue en vue de pouvoir fournir un caractère photosensible à l'injection et l'extraction de charges en, changeant la barrière tunnel ou le travail de sortie de l'électrode, lors de l'éclairage.

La fabrication d'électrodes asymétriques a été réalisée grâce à un processus en trois étapes qui comprend l'adsorption de la molécule avec la formation de la SAM la plus stable sur les électrodes d'or, la désorption électrochimique de la SAM de l'une des deux électrodes, et l'adsorption successive de la seconde SAM sur l'électrode précédemment désorbée .

Pour ce faire, deux molécules différentes ont été conçues et synthétisées par nos collaborateurs: un thioacétate de byphenylazobenzene (AZO) et un diaryléthène thioacétate fonctionnalisé avec des groupes tert-butyle (t-DAE).

Les azobenzènes sont des systèmes photochromiques bien connus, qui peuvent subir une isomérisation photochimique entre un état thermiquement stable *trans* (E) et un état métastable *cis* (Z), par irradiation avec la lumière UV. L'isomérisation inverse peut être déclenchée par irradiation avec de la lumière visible, ou par relaxation thermique. Dans le cas de la molécule AZO nous avons utilisé respectivement des longueurs d'onde d'irradiation de 365 et 455 nm.

D'autre part, les diaryléthènes (DAE) sont une classe de molécules qui subissent une isomérisation entre deux isomères thermodynamiquement stables, à savoir la forme ouverte et fermée. Le t-DAE a une forme ouverte se caractérisant par la présence d'un épaulement de pic à 310 nm. L'irradiation à cette longueur d'onde cause la conversion de la forme ouverte vers la forme fermée, qui est alors entièrement conjuguée. Cette forme est caractérisée par un pic dans la région visible à. 540 nm et un double pic dans la région des UV, à environ 365 nm.

Tout d'abord, à l'aide d'expériences d'absorption UV-Vis effectuée sur des mélanges des deux molécules photochromiques en solution, nous avons démontré la possibilité de commuter un type de molécule sans affecter l'autre. Ensuite, après l'optimisation précise des paramètres d'absorption/désorption, nous avons pu fonctionnaliser entièrement deux électrodes interdigitées avec les deux différentes SAM respectivement sur chaque électrode, dont le procédé est fondamental afin de les tester dans des transistors à effet de champs organiques.

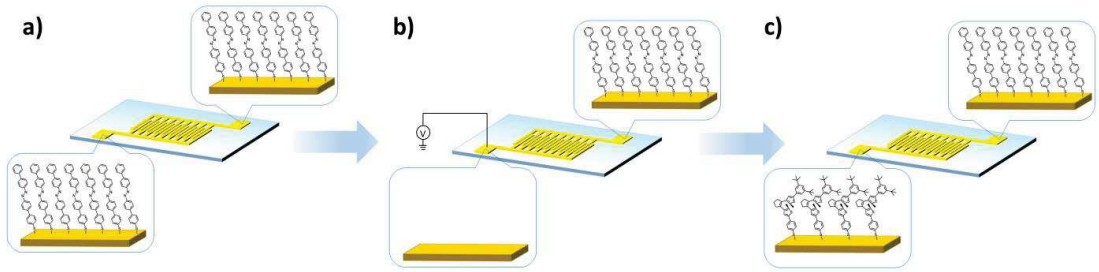


**Figure 3 :** représentation schématique de la préparation des électrodes asymétriques. a) première étape : formation de la SAM AZO ; b) deuxième étape : désorption de la SAM AZO de l'une des

électrodes ; c) troisième étape : immersion de l'échantillon dans une solution de t-DAE SAM pour former une SAM DAE sur l'électrode précédemment desorbée par voie électrochimique

En conclusion, ce travail de thèse vise à explorer les interactions supramoléculaires et à les utiliser afin de moduler les propriétés physico-chimiques de systèmes et de matériaux complexes. D'abord, une interaction classique hôte-invité a été étudiée, au moyen d'une technique innovante telle que l'ITC, puis nous avons exploité les interactions supramoléculaires afin de maitriser la production de graphène exfolié en phase liquide, en mettant un accent particulier sur l'amélioration de la qualité et la quantité du matériau produit. Enfin, nous avons étendu l'utilisation de la chimie supramoléculaire à un dispositif réel par la fonctionnalisation des électrodes d'or avec des molécules photochromiques, ouvrant alors la voie à des dispositifs organiques multifonctionnels, pouvant être contrôlés par la lumière.

1. J. M. Lehn, *Pure Appl Chem*, 1978, 50, 871-892.

2. G. A. Ozin and A. Arsenault, eds., *Nanochemistry – a chemical approach to nanomaterials*, The Royal Society of Chemistry, 2005.

3. F. P. Schmidtchen, in *Analytical Methods in Supramolecular Chemistry* ed. C. A. Schalley, Wiley-VCH, Weinheim, 2007, pp. 55-78.

4. A. Ciesielski and P. Samori, *Chem Soc Rev*, 2014, 43, 381-398.

5. A. Ulman, *Chem Rev*, 1996, 96, 1533-1554.

# Abstract

The field of S*upramolecular Chemistry* was defined for the first time in 1978 by J.-M. Lehn as the "chemistry of molecular assembly and of intermolecular bond".[1] It is the branch of chemistry which deals with studies of the assembly of molecular building blocks interacting through non–covalent forces, such as electrostatic interactions, hydrogen bonding, π-π interactions, van der Waals forces, etc.

A simple supermolecular entity is usually generated from a *recognition process* between the two molecular building blocks called *receptor* and *substrate*.

Since the first studies in this field by D. J. Cram, C. J. Pedersen and J.-M. Lehn for which the three scientists were awarded with the Nobel Prize in 1987, the world of supramolecular chemistry has become broader and broader giving birth to other branches of chemistry, such as *nanochemistry*.[2]

Through self-assembly of suitably designed molecules incorporating *ad-hoc* functionalities it is possible to generate highly ordered one- (1D), two- (2D) and three-dimensional (3D) nanostructures possessing specific chemical and physical properties.

In this thesis we focused on the investigation of different supramolecular interactions starting from a simple host-guest system, going through the employment of supramolecular interactions in order to produce a desired material and finally applying the principles of supramolecular chemistry in electronic devices.

The principal topics investigated thus are:

- Study of the reversible complexation of cryptand [2.2.2] with potassium ion by Isothermal Titration Calorimetry (ITC);
- Exploitation of supramolecular interactions for the production of graphene via liquid phase exfoliation (LPE);
- Realization of asymmetric electrodes that can independently respond to a light stimulus, *via* the selective functionalization of each electrode through the chemisorption of self-assembled monolayers of two different photochromic molecules.

***Abstract***

Isothermal Titration Calorimetry (ITC) is a powerful tool that is primarily used in biology to explore complex non-covalent interactions. Just recently it started being used also in supramolecular chemistry to investigate host-guest binding interactions.[3] ITC makes it possible to determine simultaneously and with a high degree of precision the thermodynamic parameters and stoichiometry of a ligand–receptor interaction in a single experiment by measuring the increments of heat occurring during stepwise titration experiments. Surprisingly only few examples can be found in literature on the application of ITC on simple host- guest chemistry in aqueous solution.

In order to better understand the working principles of ITC, its advantages, its drawbacks and its possible future applications a detailed study has been performed on a model system based on the thermodynamics of the complexation of potassium ions by 1,10-diaza-4,7,13,16,21,24-hexaoxabicyclo[8.8.8] hexacosane (cryptand [2.2.2]) in aqueous solution. Cryptand [2.2.2] was one of the first cryptands to be synthetized by Lehn and co-workers and its thermodynamic properties have been previously studied in depth by $^{1}$H NMR spectroscopy.

A solution of cryptand [2.2.2] in water is alkaline, and the resulting hydrolysis reaction results in a dilute aqueous solution of cryptand [2.2.2] containing a significant fraction of the ligand in its monoprotonated form. Protonation is one means of inhibiting metal-cation binding by the cryptand. Thus, in this work, we have investigated the optimum conditions for determination of the complexation constant for a ligand that may undergo significant hydrolysis in water. Moreover, by changing the pH of the solution, it was possible to trigger the reversible complexation/de-complexation of the cryptand in subsequent *in situ* experiments.

Supramolecular interactions between well-defined building blocks determine peculiar characteristic of an ensemble or system. Graphene is a unique material exhibiting exceptional optical, electrical and mechanical properties rendering it appealing for numerous technological applications. Graphene was for the first time isolated by mechanical exfoliation of graphite. Graphite, from the old Greek γράφειν – to write, is one of the well-known examples of supramolecular materials present in nature. It is made by single layers of carbon atoms in $sp^2$ hybridization which are held together by face-to-face π-π interactions.

Two approaches are possible for the production of graphene: a *bottom-up* approach starting from smaller building blocks or a *top-down* approach which exploits graphite as starting material. Among the *top-down* approaches, an easily up-scalable one consists of the exfoliation of graphite in liquid media by making use of ultrasonication. The liquid-phase exfoliation (LPE) method is becoming

more and more interesting because it is extremely versatile: it can be used to deposit graphene in a variety of environments and on different substrates not accessible using mechanical cleavage or growth methods. The LPE process consists of three stages: (i) dispersion of graphite in the chosen solvent, (ii) sonication, and (iii) purification through centrifugation.[4]

Exfoliation of graphite occurs thanks to shear forces and cavitation, acting on the bulk material during ultrasonication. The choice of the solvent is crucial since, after exfoliation, the solvent–graphene interaction needs to balance the attractive forces between graphene sheets.

It has been widely studied and proved that liquid media having surface tension around 40 mJ $m^{-2}$, like N-Methyl-2-pyrrolidone (NMP) or *orto*-dichlorobenzene (*o*-DCB), are the best choice for exfoliation technique, since they minimize the interfacial energy between the solvent and graphene and thus allowing for the overcoming of the van der Waals forces between adjacent graphene layers. Recently, it has been shown that the addition of small organic molecules and/or polymers, featuring a high affinity for the surface of graphene, during LPE of graphite can harness both the yield of exfoliation and quality of graphene and, in particular cases, can confer additional properties to the exfoliated material. In this work we show that the quality and quantity of defect-free, few layer thick graphene dispersions in solvents such as *orto*-dichlorobenzene, can be increased by addition of simple organic molecules taking advantage of their supramolecular interaction with graphite before exfoliation and graphene after. We have employed in particular polycyclic aromatic hydrocarbons which interact with graphene thanks to π-π interactions. We have moreover investigated how the functionalization of these molecules with atoms such as chlorine could affect the exfoliation process, improving the interactions with graphene sheets. This peculiarity effect can be ascribed to the higher polarizability of the chlorine atoms respect to carbon which improves the dispersion interactions with graphene, as revealed by theoretical calculations performed by our collaborators.

In the last part of the thesis we exploited supramolecular interactions for the fabrication of multifunctional devices by engineering gold electrodes using chemisorbed self-assembled monolayers (SAMs) of thiolated molecules. SAMs are one among the most fascinating scaffolds in *nanochemistry*.[5] On gold surfaces SAM formation is most commonly driven by the spontaneous chemical bond formation of specific functional groups with the gold surface. The interactions between adjacent molecules are necessary to stabilize the SAMs. The most robust and well-known SAMs are those comprising thiolated moieties on gold. By design of the molecular backbone and

proper choice of terminal group, the physical and chemical properties of the exposed surface can be controlled with a great precision. The aim of the work was to explore the possibility of coating adjacent gold electrodes in an asymmetric fashion by chemisorbing on their surfaces different SAMs of photochromic molecules. Such SAMs could therefore be switched independently upon application of different light stimuli. The incorporation of photochromic SAMs at the metal-semiconductor interface was conceived in view of the possibility to provide a photoresponsive nature to the charge injection and extraction by changing the tunneling barrier or the electrode work function upon illumination.

The fabrication of asymmetric electrodes has been achieved through a three steps process which involves the adsorption of the most stable SAM forming molecule on the gold electrodes, the electrochemical desorption of the SAM from one of the two electrodes, and the successive adsorption of the second SAM on the gold electrode left exposed by desorption.

For this purpose two different molecules have been designed and synthetized by our collaborators: a byphenylazobenzene thioacetate (AZO) and a thioacetate diarylethene functionalized with *tert*-butyl groups (t-DAE).

Azobenzenes are well-known photochromic systems which can undergo photochemical isomerization between a thermally stable *trans* state (E) and a meta-stable *cis* state (Z) by irradiation with UV light. Inverse isomerization can be triggered by irradiation with visible light or thermal relaxation. In the case of molecule AZO we used respectively 365 and 455 nm irradiation wavelengths.

On the other hand diarylethenes (DAE) are a class of molecules, that undergoes isomerization between two thermodynamically stable isomers, i.e. the open and closed form. The t-DAE in the open form is characterized by the presence of a shoulder peak at 310 nm. Irradiating at this wavelength it is possible to convert the open form to the fully conjugated closed form which shows a peak in the visible region at ca. 540 nm and a double peak in the UV region at ca. 365 nm.

First, through UV-Vis absorption experiments of mixtures of the two photochromic molecules in solution we demonstrated the possibility of switching one type of molecule without affecting the other

Finally, after careful tune of absorption/desorption parameters we were able to functionalize two fully interdigitated electrodes with the two different SAMs, a fundamental process in order to test them in organic field effect transistors.

In conclusion this thesis is aimed at exploring supramolecular interactions and using them in order to modulate physico-chemical properties of complex systems and materials. First, a classical host-guest interaction was studied by means of the ITC technique, then we exploited supramolecular interactions in order to harness the production of liquid-phase exfoliated graphene, with a particular focus on improving the quality and quantity of material produced. Finally, we extended the use of supramolecular chemistry to a real device by functionalization of gold electrodes with photochromic molecules, hence paving the way towards multifunctional organic devices and in prospective to graphene based light-controlled multifunctional devices.

1. J. M. Lehn, *Pure Appl Chem*, 1978, **50**, 871-892.
2. G. A. Ozin and A. Arsenault, eds., *Nanochemistry – a chemical approach to nanomaterials*, The Royal Society of Chemistry, 2005.
3. F. P. Schmidtchen, in *Analytical Methods in Supramolecular Chemistry* ed. C. A. Schalley, Wiley-VCH, Weinheim, 2007, pp. 55-78.
4. A. Ciesielski and P. Samorì, *Chem Soc Rev*, 2014, **43**, 381-398.
5. A. Ulman, *Chem Rev*, 1996, **96**, 1533-1554.

# Table of Contents

# 1. Introduction

## 1.1. From Supramolecular Chemistry to Nanotechnology

The concept of Supramolecular *chemistry* was defined for the first time in 1979 by Jean-Marie Lehn as "the chemistry of molecular assemblies and of the intermolecular bond"[1], even though the term *supramolecule* appeared for the first time already in 1903 in Webster's dictionary[2] and examples of supramolecular chemistry date back to the early days of modern chemistry (with the discovery of chlorine hydrate by Sir Humphrey Davy in 1810 for example). The recognition of supramolecular chemistry as a specific research field in fact started in 1960s with the studies on the selective binding of alkali metal cations by natural[3] as well as synthetic macrocyclic and macropolycyclic ligands, the crown ethers[4] and cryptands.[1, 5] Because of this reason, at the beginning, supramolecular chemistry was associated with the chemistry of the *host-guest* interactions.

After the establishment of this field, based on synthetic receptors which were designed with a particular geometry or rigidity in order to fit their potential guest in a selective way, supramolecular chemistry research horizons were expanded to "self-organization processes". In these processes a *reversible* and *spontaneous* organization of single entities takes place thanks to non-covalent interactions forming ordered structures. This is the branch of *self-assembly*.[6]

With time, the objective of the study of researchers in the supramolecular field, changed from *molecular recognition per-se* to *molecular recognition as a tool*, taking advantage of the increasing knowledge on non-covalent interactions, towards the development of functional supramolecular architectures of nanometric size.[7] This led to the engineering of advanced *supramolecular materials*, such as supramolecular polymers and liquid crystals paving the way towards a new field: *nanochemistry*.[8] *Nanochemistry* is concerned with the synthesis and study of assemblies of atoms or molecules in highly ordered two-and three dimensional nanostructures, which have spatial dimensions ranging between 2–200 nm. *Nanochemistry* is now a *per-se* discipline but much of its success comes from the ability acquired by supramolecular chemists in manipulating non-covalent

forces and exploiting them in the engineering of well order structures in the nanometric scale with specific properties encoded in the molecular building blocks. Supramolecular chemistry is therefore one of the fundamental *tools* employed to design new *nanomaterials* in the more general field of *nanotechnology* in order to produce nanotechnological devices starting from a bottom-up approach (nanochemistry) (**Figure 1.1**).[9] Nanomaterials can be defined as materials with at least one dimension inferior to 100nm whose properties scale and emerge according to the length scale of the system. One of the major examples of this concept is given by carbon allotropes. Carbon can arrange in 3D (diamond), quasi-2D (graphite), 2D (graphene), 1D (carbon nanotubes), or 0D (Fullerene) structures. Nanoforms of carbon based materials, such as fullerenes, carbon nanotubes and graphene have outstanding electrical and mechanical properties that emerge from their dimensionality.


**Figure 4.1:** Schematic representation of the broad field of nanotechnology. Reproduced from reference 9

This thesis is aimed at exploring supramolecular interactions and using them in order to modulate physico-chemical properties of complex systems and materials from different perspectives covering the fields of host-guest chemistry, nanomaterials and in general nanotechnology. In the following paragraphs the principal non-covalent interactions that are at the basis of supramolecular chemistry and the two main branches of supramolecular chemistry, i.e. host-guest chemistry and self-assemby will be described, considering a particular evolution of self-assembly in nanochemistry, that is chemisorbed self-assembled monolayers (SAMs) and their application in organic field effect transistors (OFETs). In chapter 2 a brief summary of the properties and fabrication methods of

graphene, the new "wonder material" of nanochemistry will be given. The principal experimental techniques employed in the experimental work of this thesis will be briefly summarized in chapter 3. Then in chapter 4 it will be shown how one of the first example of supramolecular host-guest chemistry, the complexation of potassium ion by cryptand [2.2.2] can be studied by isothermal titration calorimetry (ITC) revealing the advantages and drawbacks of this technique. Chapter 5 illustrates how supramolecular interactions can be exploited in order to produce graphene through a liquid-phase exfoliation process, with a particular focus on improving the quality and quantity of material produced. In chapter 6 the use SAMs will be extended to organic electronic devices, showing how SAMs can be implemented on gold electrodes paving the way toward multiresponsive devices. Conclusions and perspectives will be outlined in chapter 7.

## 1.2. Non-covalent interactions: the toolbox of supramolecular chemistry

Supramolecular entities are held together through non-covalent forces that are generally weaker than covalent bonds and their energetic range goes from 2 kJ $mol^{-1}$ for dispersion forces to 300 kJ $mol^{-1}$ for ion-ion interactions. In **Table 1.1** a summary of the non-covalent forces is reported.[2]

| **Supramolecular interactions** | **Bond energy (kJ $mol^{-1}$)** |
|---|---|
| Ion-Ion | 200-300 |
| Ion-dipole | 50-200 |
| Dipole-dipole | 5-50 |
| Hydrogen bonding | 4-120 |
| Cation-π | 5-80 |
| π-π | 0-50 |
| Van der Waals | <5 kJ $mol^{-1}$ but variable according to the surface area |
| Hydrophobic | Related to solvent- solvent interaction energy |

**Table 1.1:** Summary of non-covalent forces and their strength range

*Ionic and dipolar interactions* can be divided in three categories: *(i)* ion-ion, *(ii)* ion-dipole, and *(iii)* dipole-dipole interactions. The strongest of these interactions is the ion-ion interaction, given that its energy range is of the same order of covalent interactions. Moreover ion-ion interaction are

non-directional forces because they can occur at any particular orientation of the two interacting species, while ion-dipole and dipole-dipole interactions are orientation dependent and they are useful in order to bring species into alignment.

*Hydrogen bond* is the "master-key" non-covalent interaction in supramolecular chemistry, due to its high directionality and strength.[10] It is a special kind of dipole-dipole interaction between a proton donor (D) and a proton acceptor (A). The hydrogen donors are groups with hydrogen attached to an electronegative atom, giving rise to a dipole with a partial positive charge carried by the hydrogen. The proton acceptors are electron-withdrawing atoms, which interact with the hydrogen dipole (**Figure 1.2**).

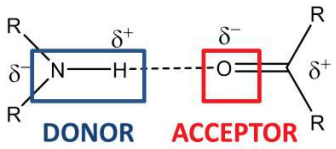


**Figure 1.2:** Example of hydrogen bond, a carbonyl accepting a hydrogen bond from a secondary amine donor.

*Van der Waals interactions*, the weakest among non-covalent interactions, consist of an attractive (dispersion) component, named *London dispersion* and a short-range repulsive component often called '*exchange repulsion'*.

*London dispersion* forces are non-covalent forces which are originated by the attraction between induced polarized electron clouds. This force is present in a small part in all intermolecular interactions. The strength of this interaction depends from the *polarizability* of the molecules (i.e. how easily the electron cloud of the molecule can be distorted) and from the surface area of the molecule. The greater the surface of the molecule is, the more the area of the electron cloud which can interact with another molecule, the stronger the force. Exchange repulsion interactions include nuclear-nuclear repulsion and electron-electron repulsion, as well as changes in electronic kinetic energy.

*π interactions* can be divided in two main class: *π-cation* interaction and *π-π interactions.* Cation- π interactions involve binding of a cation to π-electrons, while π- π interactions occur between two aromatic systems. π-π interactions can be in general of two types: *face to face,* when the aromatic moieties interacting are parallel to each other (**Figure 1.3a** and **1.3b**) and *face to edge* interactions when the hydrogen atom of one ring interacts with a perpendicular orientation respect to the other ring (**Figure 1.3c**). Hunter has demonstrated that π-π interactions can be viewed more like σ-π

attraction of the negatively charged π cloud of one of the two conjugated systems involved, and the positively σ system of the second aromatic molecule.[11] Therefore face to face interactions in which the centres of the molecules are along the same axe are in general unfavourable (repulsive) while parallel displaced interaction are favored as well as face to edge interactions. In **Figure 1.3d** a scheme of the different geometries of benzene-benzene interactions and a general scheme of how the interaction varies from repulsive to attractive varying the geometry of interaction of the molecules are reported.[12]

π interaction are given by the complex interplay of other non-covalent forces. In fact, from theoretical calculations, it has been derived that the electrostatic energy is responsible for the geometry of the dimer, whereas the stabilization of the dimer is due to van der Waals interactions (and solvophobic effects).[11]

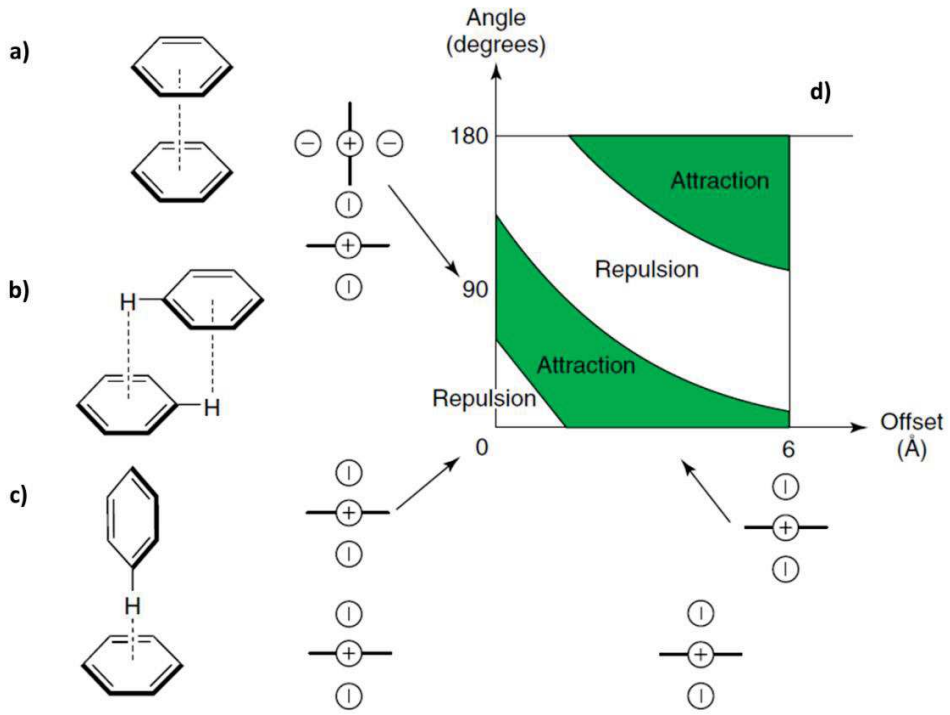


**Figure 1.3:** a) face to face parallel interaction; b) face to face parallel displaced interaction; c) edge to face interaction for two benzene molecules; d) diagram showing how the π-π interaction can change from repulsive to attractive according to the orientation of one molecule compared to the other one. Taken from ref. 12.

Heteroatoms such as fluorine decorating one of the two aromatic molecules can change the electrostatic potential of the surface of the halogenated aromatic molecule and therefore the

molecules can interact in a parallel fashion to the other aromatic molecule, as depicted in **Figure 1.4**.[13]

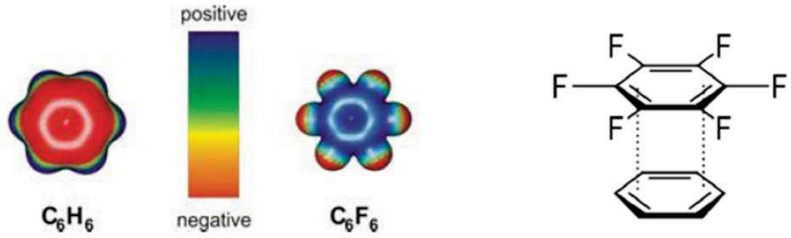


**Figure 1.4:** Surface electrostatic potential of benzene and fluorine showing that they are respectively negative and positive and parallel face to face interaction.

A well-known example in nature of π-π interaction is graphite, which is constituted by sheets of $sp^2$ carbons atoms held together by weak face to face π- π interactions.

From graphite through exfoliation processes it is possible to isolate the single carbon sheets in order to obtain graphene, the "material of the future", which possesses extraordinary properties. In chapter 2 we will introduce this material, which is part of the nanochemistry world, and the fabrication processes employed for its production. In chapter 5 we will show that through exfoliation of graphite in a liquid medium it is possible to obtain dispersion of graphene sheets and the quality of the dispersions can be improved by addition of molecules which can interact with graphene sheets through non covalent interactions such as π-π stacking or van der Waals forces.

## 1.3. Host-guest chemistry

Host-guest chemistry studies the interaction between a molecule (host) which is capable of enclosing another small molecule/ion (guest) through non-covalent interactions. It is worth to point out that a stable host guest system is given by the *multiple* and *simultaneous* effect of non-covalent interactions. In a host-guest system the stabilization obtained by a host with two or more binding sites covalently linked between each other in binding the guest is higher than a system in which the binding sites are acting separately from each other. This phenomenon is called *cooperativity*. The *cooperativity* between sites is also a generalization of the *chelate* effect **(Figure 1.5).**

Above the chelate effect, an ulterior factor, which helps in increasing the organization order, is the design of the host in a way that no significant conformational change is needed to interact with the

guest. This feature is achieved when the host is formed by one or more rings (*corands*) which form a cavity of a correct size to accept the potential guest species. The increased stability obtained thanks to this effect compared to the acyclic corresponding molecules (*podands*) is called *macrocyclic effect*. Pedersen in 1962[4a, 14] isolated as a side product an unusual material that had unexpected solubilizing effects on alkali metal cations; a microcycle of the family of *crown-ethers*, the first example of macrocyclic effect in supramolecular chemistry (an example of crown ether [18]crown-6 is shown in **Figure 1.6b**). If the number of rings increases, making the cavity more rigid, the level of *pre-organisation* increases (see **Figure 1.5**). Lehn and coworkers were the first to synthetize bicyclic ligands, named cryptands from the greek cryptos= cave,[15] cryptand[2.2.2.][16] (**Figure 1.6c**) being one of the most known in the family.

Another factor beside pre-organization that influences the stabilization of the host-guest system is the *complementarity* between host and guest. Therefore, ions have to match the size of the cavity of the host, the electronic interactions between host and guest should be attractive and so on. As Cram said: "*To complex, hosts must have binding sites which can simultaneously contact and attract binding sites of guests without generating internal strains or strong nonbonded repulsions*".[17] Cram is the father of another class of macrocycles in which the oxygen atoms form a small cavity with octahedral geometry, named *spherands*[18] (in **Figure 1.6d** spherand-6 selective for Litihium is reported).

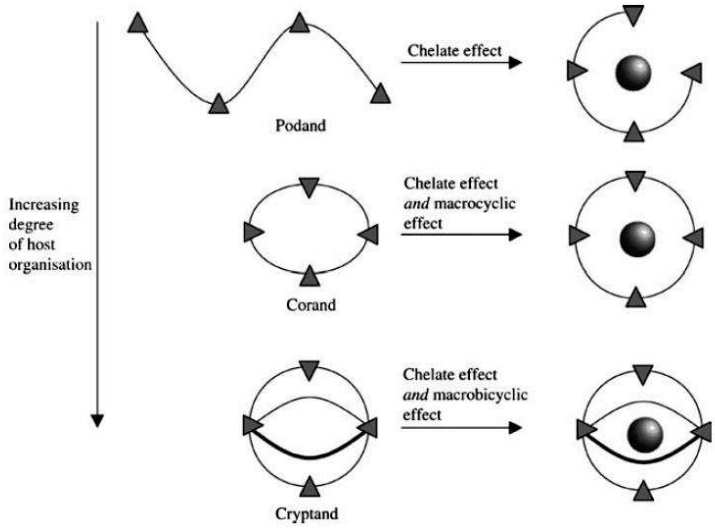


**Figure 1.5:** Increasing of the pre-organization in host systems from chelate effect to macrobicyclic effect. Image reproduced from reference 19.

With the pioneer work of Pedersen, Lehn and Cram an official new branch of chemistry, supramolecular chemistry, was born and the three scientists were awarded in 1987 with the Nobel Prize.

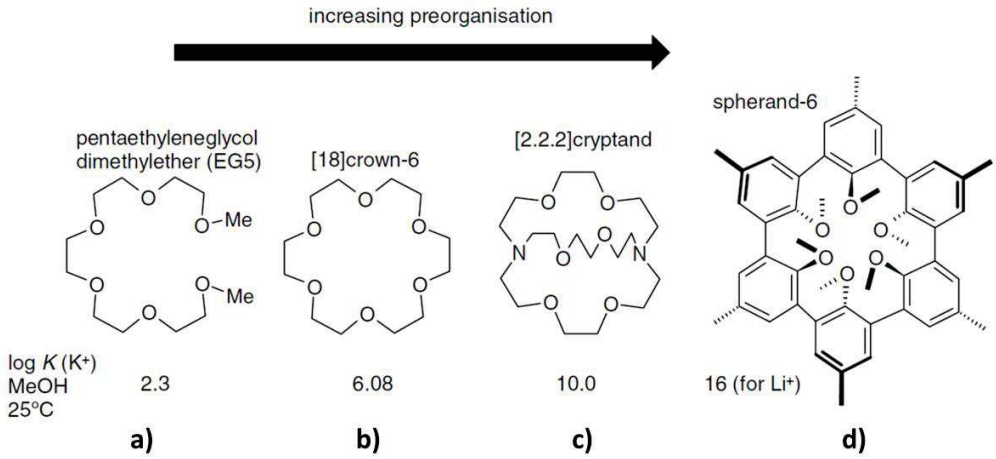


**Figure 1.6**: Increasing of preorganisation and complementarity going from a) EG5; b) 18crown-6; c) cryptand [2.2.2]; d) spherand-6. Reproduced from reference 19.

However the fundamental concepts of supramolecular chemistry date much time before with the idea of coordination chemistry by Werner(1893),[20] *the lock and key* principle developed by Emil Fisher in 1894[21] in order to describe the complementarity in shape between the enzyme and the substrate and the concept of *receptors* developed by Paul Ehrlich in 1903 *("Corpora non agunt nisi fixata")*.[22] Such a temporal gap in the starting of a proper field of supramolecular chemistry arises from two main factors.[23] First, time had to pass before scientist could accept that the properties of a molecule were influenced also by the interaction with the surroundings and were not properties of the molecule *per-se*; second, the absence of good analytical methods to study such weak forces. Usually in the study of a host-guest system it is of fundamental importance to unveil the thermodynamics of the system. The first methods to be developed were based on UV-Vis spectroscopy and NMR, which were able to determine the association constant $K_a$ and through van 't Hoff analysis the enthalpy of the process. More recently in the 80's with the advent of modern calorimetry, biological recognition processes began to be studied deeply by means of this technique. In the last decades isothermal titration calorimetry (ITC) has been employed also in supramolecular chemistry. The main advantage of this technique is that performing a single experiment it is possible to extract all the fundamental thermodynamic parameters, such as the association constant, enthalpy,

entropy and Gibbs energy. ITC measures directly the enthalpy of a binding event thus avoiding errors generated by improper use of van 't Hoff analysis.[24] Most of the studies of host-guest binding systems have been performed in organic solvents, in particular aprotic and nonpolar solvents that maximize electrostatic interactions between molecules. However, in the natural world, supramolecular interactions occur in water and the role of the solvent is crucial. Therefore, in chapter 4 we focus our attention on the study of a model host-guest system such as the complexation of the potassium ion by cryptand [2.2.2] in water, by means of ITC revealing the weak and the strong points of ITC technique and all the precautions that have to be taken in order to perform a correct experiment.

## 1.4. From self-assembly to self-assembled monolayers

Self-assembly is a process in which large ordered structures are formed spontaneously by single components initially in disorder, through non-covalent interactions, thanks to the intrinsic *information* embedded in the single components.[6] The self-assembly process on solid surfaces (2-D self-assembly) is the result of a delicate interplay between three main interactions: molecule-molecule, molecule-substrate and eventually molecule-solvent interaction if the deposition of the molecules takes place from solution.[25]

In nanochemistry self-assembly can be used to form ordered self-assembled monolayers (SAMs) chemisorbed on a surface. SAMs are obtained via chemisorption of molecules on a substrate thanks to a reactive head group followed by a slow reorganization of the tail group. In fact the backbone of the molecule is designed in such a way that dispersive forces stabilize the supramolecular assembly creating a long range order which can extend from few to several nanometers. The terminal group of the molecule or the backbone itself can provide a chemical functionality to the SAM (**Figure 1.7**).

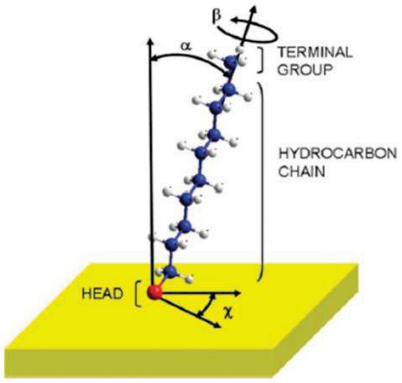


**Figure 1.7:** Schematic representation of a decanethiol molecule adsorbed on Au(111) in a standing up configuration. In red the sulphur atom, in blue the carbon backbone and in white the hydrogens. Reproduced from reference 26.

SAMs applications in nanotechnology are numerous and involve different fields (**Figure 1.8**).[27] In micro and nanofabrication SAMs are employed as resist in soft-lithography and as inks in microcontact printing for creating well defined pattern of molecules and biomolecules on gold; in molecular electronics they are employed as active or passive elements in OFETs (see section 1.4.1); in biology they are used in order to immobilize biomolecules on surfaces for sensing or to create biocompatible coatings for application in implants. Thanks to SAMs it is possible to tune the wettability of a substrate and it has been possible thanks to surface initiated polymerization reactions to create polymer brushes.

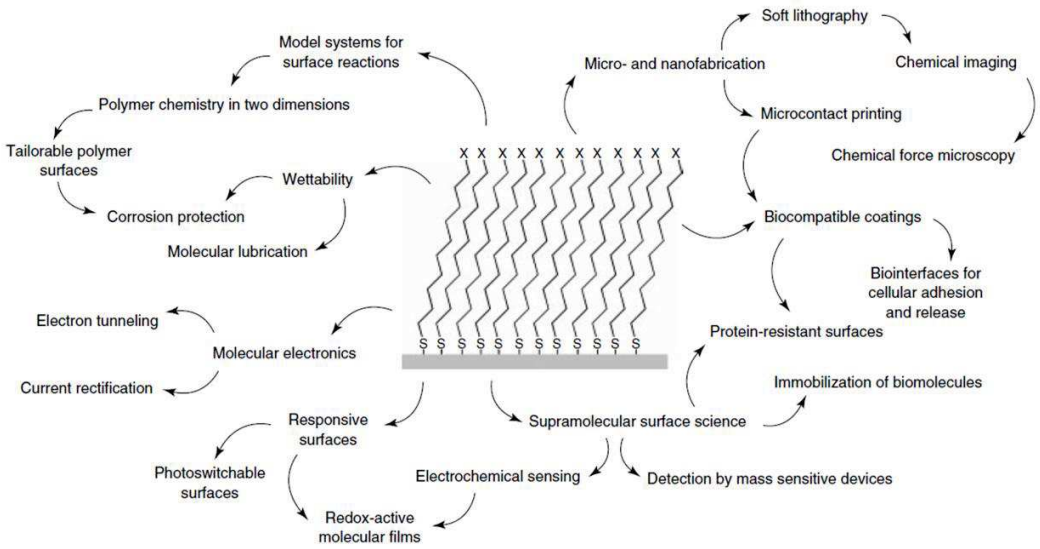


**Figure 1.8:** Possible applications of self-assembled monolayers. Reproduced from reference 28:

In general SAM formation can occur from liquid phase or from gas phase. It involves first a physisorption step (**Figure 1.9a**), followed by a phase in which the molecules lye with their axis parallel to the substrate (striped phase, **Figure 1.9b**); then a nucleation of standing-up phase domains starts (**Figure1.9c**) thanks to van der Waals forces and non-covalent forces and it increases in size and packing density giving rise finally to an ordered SAM (**Figure 1.9d**).[26]

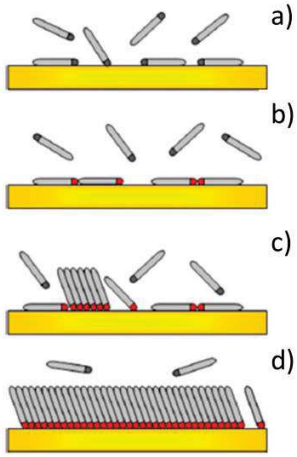


**Figure 1.9:** Different steps taking place during the self-assembly of thiols on Au (reproduced from Ref. 26): a) physisorption; b) molecules lying with their axis parallel to the substrate; c) nucleation of the standing up phase; d) completion of the SAM.

This is a very general picture of what can really happen during the formation of a SAM, since there are many other factors influencing the assembly such as the concentration of the molecules, the interaction of the molecules with the solvent, the temperature at which the formation of the SAM occurs.[27]

The most robust and well-known SAMs are those comprising thiolated moieties on gold. The reaction that leads to chemisorption of the SAM takes some minutes and involves the loss of the mercaptan H, forming finally the thiolate Therefore the process can be described by the following equation:

$$R - SH + Au \rightarrow (R - SH)_{phys}Au \rightarrow RS - Au + {}^{1}/_{2}\, H_2$$

The mechanism which has been proposed for this reaction is an oxidative adsorption of the alkanethiol RS–H bond to the metallic gold substrate,[29] but the nature of the species involved in the process (ion, radical…) is unknown. XPS studies have confirmed the covalent nature of the S-Au bond which has a homolytic bond strength of ~44 kcal/mol,[30] even though the fate of the hydrogen bond is not clear. If the formation of the SAM occurs from the gas phase the most accredited

hypothesis is the formation of $H_2$.[31] In solution, beside formation of $H_2$, the H can react with oxygen present in solution leading to the formation of water. Some studies instead propose that the adsorption occurs without the loss of the hydrogen.[32]

### 1.4.1.Use of self-assembled monolayers in organic electronics.

SAMs play an important role in improving the organic device performance. They can be employed at different interfaces of the device. In particular, in organic field-effect transistors (OFETs), SAMs can be exploited in the modification of source and drain electrodes and in the modification of the dielectric interface.

Growth of SAMs on source and drain electrodes can improve the charge injection of the carriers in the organic semiconductor. In fact molecules possessing a dipole moment perpendicular to the surface can shift the work function ϕ of the substrate material of a value Δϕ given by the Helmholtz equation:[33]

$$\Delta\phi = \frac{q\ N\ \mu_{\perp}}{\varepsilon_0\ \varepsilon_{SAM}}$$

where q is the elementary charge, N the surface dipole density, $\mu_{\perp}$ the dipole moment perpendicular to the surface, $\varepsilon_0$ the vacuum permittivity, and $\varepsilon_{SAM}$ the relative dielectric constant.

Dielectric surface treatment with SAMs produces benefits in the charge carrier transport, since the charges implied in OFET transport are usually confined in the first 5 nm of organic semiconductor from the semiconductor/dielectric interface.[34] Functionalizing for example the $SiO_2$ surface with an octadecyl trichlorosilane (OTS) SAM the charge trapping caused by Si-OH groups on the dielectric surface can be easily prevented.[35]

Tunneling is the most common transport mechanism in SAMs and is defined by the Arrhenius equation:

$$R_t = R_0 e^{\beta L}$$

where $R_t$ is tunneling resistance, $R_0$ is the effective contact resistance, $\beta$ is the exponential prefactor that depends on the nature of bonding in the molecular back-bone and L is the SAM thickness.[36]

Recently SAMs, have been implemented in OFETs in order to confer new functionalities to the device, opening new scenarios in the world of multiresponsive organic electronic devices.

Among molecules which are intrinsically functional, the class of photochromic molecules is one of the most exploited in organic electronics. Photochromic molecules are molecules which upon a light

stimulus undergo an isomerization which causes a variation in their absorption spectrum (i.e. their color). Photochromic molecules belong to the more generic class of *molecular switches*,[37] which are molecule able to undergo isomerization between two states upon a proper stimulus. In **Figure 1.10** a diagram of the potential energy surfaces of a switchable molecule is reported. In photochromic systems light excitation can cause the conversion from a more stable isomer (state A) to an isomer (state B) with a higher free energy. State B can reconvert to state A overcoming a more or less high energetic barrier ($\Delta E_{act}$). Sometimes the photogenerated isomer B is kinetically inert and the back reaction to A can occur only upon a second light stimulus, as in the case of diarylethenes. If instead the activation barrier is not very high, like in the case of azobenzene (($\Delta E_{act} \sim 1eV$)[38] the conversion can occur also thermally.[39]

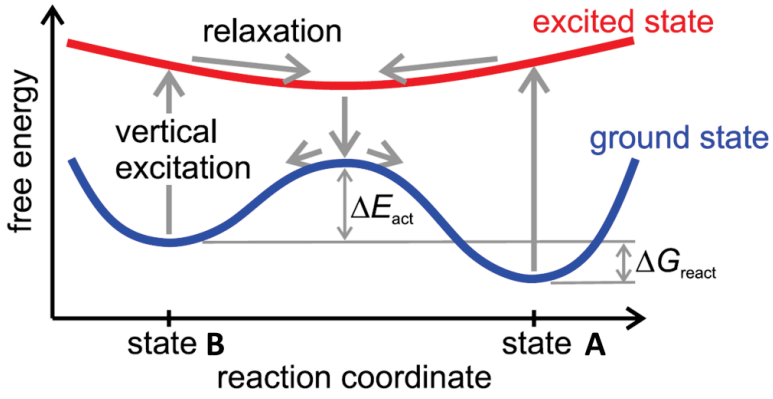


**Figure 1.10:** Energy profile of a molecular switch. Adapted from reference 37a.

The most important families of photochromics are reported in **Figure 1.11**. There are three main photochromic classes which have been employed in multifunctional OFETs: azobenzenes, diarylethenes and spiropyrans. Azobenzene (**Figure 1.11d**) can undergo a *stereoisomerization* between the thermally stable *trans* form and the *cis* form upon illumination with a specific wavelength The *cis* to *trans* back reaction can occur again by light stimulus at a different wavelength or thermally, because the activation barrier $\Delta E_{act}$ is small. Spiropyrans (**Figure 1.11c**) can switch between a neutral, colorless form to a zwitterionic, colored form and also in this case the zwitterionic form can go back thermally or by light stimulus to the colourless form. Diarylethenes are instead a particular class of stilbenes which can undergo isomerization from an open to a closed formed upon light illumination, and with repect to azobenzene and spiropyrans they are thermally stable.[40] The particular class depicted in **Figure 1.11a** is that of bisthienylethenes. The most striking

feature of this class of compounds is their resistance to fatigue: the switching cycle can be repeated more than $10^4$ times still keeping the photochromic performance.[41]

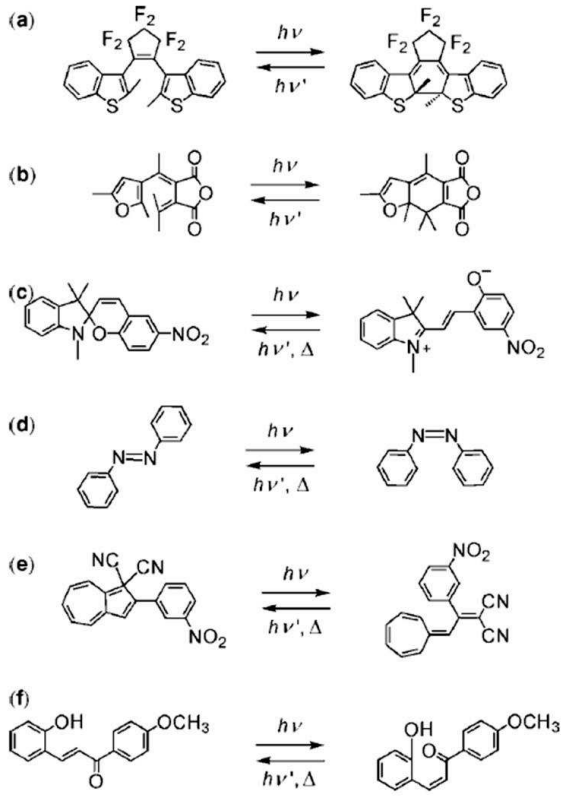


**Figure 1.11:** Major families of photochromic compounds: a) diarylethenes; b) fulgides; c) spiropyrans; d) azobenzenes; e) dihydroazulenes; f) flavylium compounds. Figure reproduced from reference [39]

Even though the properties of these molecules were known since long time it is only in the past 15 years that the first experiment aimed to connect such molecules to metals have been performed. Experiments have shown that a molecule that switches in solution, once it is immobilized on the surface, may or may not lose its functionalities.[42] The loss of the switching properties can be due to: *(i) steric hindrance*, since the molecule when bounded can lose freedom in the movement if it is constrained by neighboring molecules or by the surface; *(ii) electronic coupling* between the molecule and the electrodes: when the molecule is strongly coupled with the electrode, the first atoms on the electrode surface and the molecules itself can be considered as a whole unit and the isomerization can be in some cases blocked; *(iii) quenching due to electromagnetic dipole coupling*: to the exciton (electron-hole pair) formed upon irradiation in the molecular switch, a mirror dipole in the electrodes corresponds, causing energy transfer from the molecule to the metal, which may

lead to loss of the light-induced switching properties. Non-conjugated spacers can be inserted to avoid *(i)* and *(ii)* but this may lead to a decrease of the conductance.[42]

The incorporation of photochromic molecules at interfaces allows the tuning of properties such as charge injection in two and three terminal devices.

Different interfaces/surfaces of the OFETs have been engineered employing photochromic moieties. To the best of our knowledge, only two examples of photochromic SAMs applied to OFET can be found in literature. Our group was the first to exploit a photochromic SAM in OFETs on source and drain electrodes (**Figure 1.12a**).[43] A biphenyl-azobenzene was employed as photochromic molecule, since it had been shown in previous studies that this molecule is able to form highly ordered and tightly packed SAMs thanks to strong π-π interactions.[44] Moreover this molecule has good switching properties once immobilized on the surface showing an isomerization yield exceeding 96%.[44] The injection in the organic semiconductor is modulated through a variation of the tunneling barrier when passing form *trans* to *cis* and *vice versa,* caused by a variation of the tunneling length of the molecule, which implies changes in the current and threshold voltage (**Figure 1.12b**)

The second example of photochromic SAMs applied in OFETs is the one by Zhang and coworkers, in which a spiropyran SAM was introduced at the gate dielectric / semiconductor interface.[45] By photoinduced change of its dipole moment the spiropyran SAM is able to induce a change in the carrier injection.

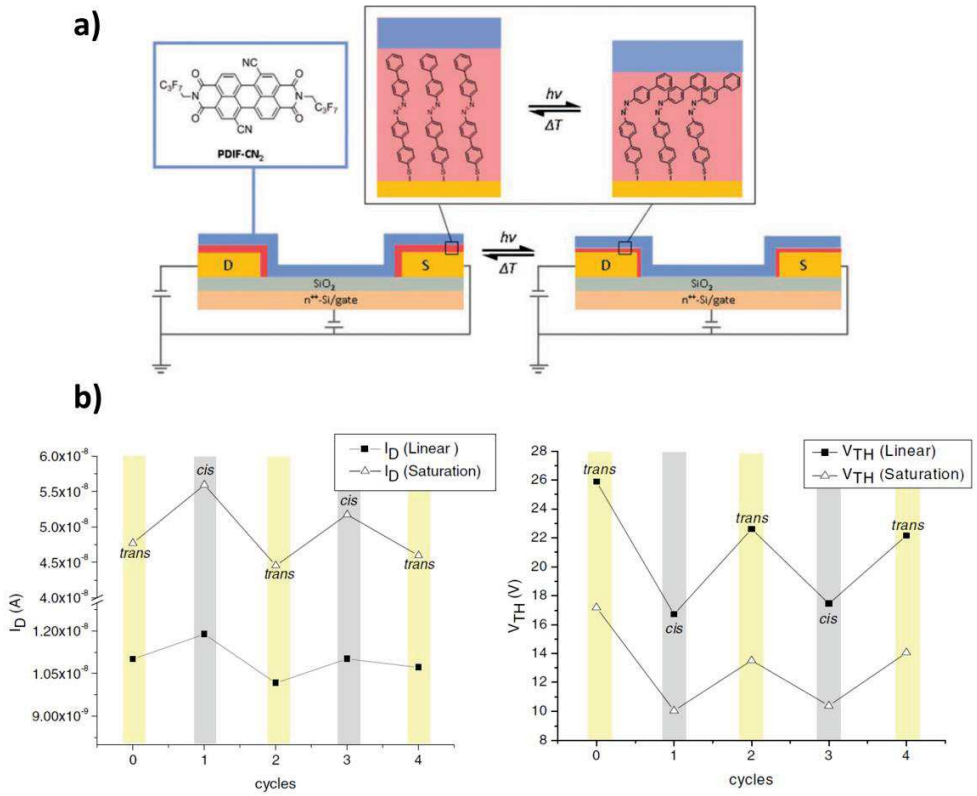


**Figure 1.12**: a) schematic representation of a OFET bearing an azobenzene SAM on the electrodes and the change in isomerization upon switching; b) variation of the current ($I_D$)and of the threshold voltage ($V_{TH}$) in linear and saturation regime upon isomerization of the azobenzene SAM for consecutive switching cycles

Chapter 6 of this thesis is part of this framework and aims at implementing multiple functionalities in an OFET. In order to do so we have tried to implement two SAMs belonging to different photochromic class, i.e. diarylethene and azobenzene in the same device. In the specific, we have tried to build asymmetric electrodes with an azobenzene SAM on one electrode and a diarylethene SAM on the second electrode. Preliminary tests have been done in order to show the independent switching of the two SAMs upon illumination in the device.

## 1.5. References


1. Lehn, J. M., Cryptates - Inclusion Complexes of Macropolycyclic Receptor Molecules. *Pure Appl Chem* **1978,** *50* (9-10), 871-892.
2. Steed, J. W.; Turner, D. R.; Wallace, K., *Core concepts in supramolecular chemistry and nanochemistry*. John Wiley & Sons: 2007.
3. Ovchinnikov, Y. A., Second FEBS-Ferdinand Springer lecture: Membrane active complexones. Chemistry and biological function. *FEBS letters* **1974,** *44* (1), 1-21.
4. (a) Pedersen, C. J., Cyclic polyethers and their complexes with metal salts. *J. Am. Chem. Soc.* **1967,** *89* (26), 7017-7036; (b) Cram, D. J., Von molekularen Wirten und Gästen sowie ihren Komplexen (Nobel-Vortrag). *Angew. Chem.* **1988,** *100* (8), 1041-1052; (c) Pedersen, C. J., The Discovery of Crown Ethers (Noble Lecture). *Angew. Chem., Int. Ed. Engl.* **1988,** *27* (8), 1021-1027.
5. (a) Lehn, J. M., Cryptates: the chemistry of macropolycyclic inclusion complexes. *Acc. Chem. Res.* **1978,** *11* (2), 49-57; (b) Lehn, J.-M., Supramolecular Chemistry—Scope and Perspectives Molecules, Supermolecules, and Molecular Devices (Nobel Lecture). *Angew. Chem., Int. Ed. Engl.* **1988,** *27* (1), 89-112.
6. Whitesides, G. M.; Grzybowski, B., Self-Assembly at All Scales. *Science* **2002,** *295* (5564), 2418-2421.
7. Reinhoudt, D. N., *Supramolecular Materials and Technologies*. John Wiley & Sons Ltd: 1999.
8. Ozin, G. A.; Arsenault, A. C.; Cademartiri, L.; Chemistry, R. S. o., *Nanochemistry: A Chemical Approach to Nanomaterials*. Royal Society of Chemistry: 2009.
9. Iqbal, P.; Preece, J. A.; Mendes, P. M., Nanotechnology: The "Top-Down" and "Bottom-Up" Approaches. In *Supramol. Chem.*, John Wiley & Sons, Ltd: 2012.
10. Jeffrey, G. A., *An Introduction to Hydrogen Bonding*. Oxford University Press: 1997.
11. Hunter, C. A.; Sanders, J. K. M., The nature of .pi.-.pi. interactions. *J. Am. Chem. Soc.* **1990,** *112* (14), 5525-5534.
12. Varshey, D. B.; Sander, J. R. G.; Friščić, T.; MacGillivray, L. R., Supramolecular Interactions. In *Supramol. Chem.*, John Wiley & Sons, Ltd: 2012.
13. Meyer, E. A.; Castellano, R. K.; Diederich, F., Interactions with Aromatic Rings in Chemical and Biological Recognition. *Angew. Chem. Int. Ed.* **2003,** *42* (11), 1210-1250.
14. Pedersen, C. J., The Discovery of Crown Ethers (Noble Lecture). *Angewandte Chemie International Edition in English* **1988,** *27* (8), 1021-1027.
15. Lehn, J.-M., Supramolecular Chemistry—Scope and Perspectives Molecules, Supermolecules, and Molecular Devices (Nobel Lecture). *Angew. Chem., Int. Ed. Engl.* **1988,** *Physical Review B: Condensed Matter and Materials Physics* (1), 89-112.
16. Lehn, J. M.; Sauvage, J. P., Cryptates. XVI. [2]-Cryptates. Stability and selectivity of alkali and alkaline-earth macrobicyclic complexes. *J. Am. Chem. Soc.* **1975,** *97* (23), 6700-6707.
17. Cram, D. J.; Cram, J. M., *Container Molecules and their Guests*. The Royal Society of Chemistry, Cambridge: 1994.
18. (a) Cram, D. J., The Design of Molecular Hosts, Guests, and Their Complexes (Nobel Lecture). *Angewandte Chemie International Edition in English* **1988,** *27* (8), 1009-1020; (b) Cram, D. J.; Kaneda, T.; Helgeson, R. C.; Brown, S. B.; Knobler, C. B.; Maverick, E.; Trueblood, K. N., Host-guest complexation. 35. Spherands, the first completely preorganized ligand systems. *J. Am. Chem. Soc.* **1985,** *107* (12), 3645-3657.
19. Steed, J. W.; Atwood, J. L., *Supramolecular Chemistry*. 2nd Edition ed.; Wiley: 2009.
20. Werner, A., Beitrag zur Konstitution anorganischer Verbindungen. *Zeitschrift für anorganische Chemie* **1893,** *3* (1), 267-330.
21. Fischer, E., Einfluss der Configuration auf die Wirkung der Enzyme. *Berichte der deutschen chemischen Gesellschaft* **1894,** *27* (3), 2985-2993.
22. Ehrlich, P., Chemotherapeutics: scientific principles, methods and results *Lancet* **1913,** *2*, 445-451.
23. Schalley, C. A., *Analytical Methods in Supramolecular Chemistry*. Wiley: 2007.
24. (a) Naghibi, H.; Tamura, A.; Sturtevant, J. M., Significant discrepancies between van't Hoff and calorimetric enthalpies. *Proc. Natl. Acad. Sci.* **1995,** *92* (12), 5597-5599; (b) Liu, Y.; Sturtevant, J. M., Significant discrepancies between van't Hoff and calorimetric enthalpies. III. *Biophys. Chem.* **1997,** *64* (1–3), 121-126; (c) Mizoue, L. S.; Tellinghuisen, J., Calorimetric vs. van't Hoff binding enthalpies from isothermal titration calorimetry: Ba2+-crown ether complexation. *Biophys. Chem.* **2004,** *110* (1–2), 15-24.
25. Palermo, V.; Samorì, P., Molecular Self-Assembly across Multiple Length Scales. *Angew. Chem. Int. Ed.* **2007,** *46* (24), 4428-4432.

26. Vericat, C.; Vela, M. E.; Benitez, G.; Carro, P.; Salvarezza, R. C., Self-assembled monolayers of thiols and dithiols on gold: new challenges for a well-known system. *Chem. Soc. Rev.* **2010,** *39* (5), 1805-1834.
27. Love, J. C.; Estroff, L. A.; Kriebel, J. K.; Nuzzo, R. G.; Whitesides, G. M., Self-Assembled Monolayers of Thiolates on Metals as a Form of Nanotechnology. *Chem. Rev.* **2005,** *105* (4), 1103-1170.
28. Azzaroni, O.; Salvarezza, R. C., Chemisorbed Self-Assembled Monolayers. In *Supramol. Chem.*, John Wiley & Sons, Ltd: 2012.
29. Ulman, A., Formation and structure of self-assembled monolayers. *Chem. Rev.* **1996,** *96* (4), 1533-1554.
30. Dubois, L. H.; Nuzzo, R. G., Synthesis, Structure, and Properties of Model Organic Surfaces. *Annu. Rev. Phys. Chem.* **1992,** *43* (1), 437-463.
31. Kankate, L.; Turchanin, A.; Gölzhäuser, A., On the Release of Hydrogen from the S−H groups in the Formation of Self-Assembled Monolayers of Thiols. *Langmuir* **2009,** *25* (18), 10435-10438.
32. Hasan, M.; Bethell, D.; Brust, M., The Fate of Sulfur-Bound Hydrogen on Formation of Self-Assembled Thiol Monolayers on Gold: 1H NMR Spectroscopic Evidence from Solutions of Gold Clusters. *J. Am. Chem. Soc.* **2002,** *124* (7), 1132-1133.
33. Koch, N., Organic Electronic Devices and Their Functional Interfaces. *ChemPhysChem* **2007,** *8* (10), 1438-1455.
34. Demeyu, L.; Stafström, S.; Bekele, M., Monte Carlo simulations of charge carrier mobility in semiconducting polymer field-effect transistors. *Phys. Rev. B* **2007,** *76* (15), 155202.
35. Salleo, A.; Chabinyc, M. L.; Yang, M. S.; Street, R. A., Polymer thin-film transistors with chemically modified dielectric interfaces. *Appl. Phys. Lett.* **2002,** *81* (23), 4383-4385.
36. Ho Choi, S.; Kim, B.; Frisbie, C. D., Electrical Resistance of Long Conjugated Molecular Wires. *Science* **2008,** *320* (5882), 1482-1486.
37. (a) van der Molen, S. J.; Liljeroth, P., Charge transport through molecular switches. *J. Phys.: Condens. Matter* **2010,** *22* (13), 133001; (b) Weibel, N.; Grunder, S.; Mayor, M., Functional molecules in electronic circuits. *Org. Biomol. Chem.* **2007,** *5* (15), 2343-2353.
38. Rau, H., Azo compounds. *Photochromism: Molecules and Systems* **2003**, 165-+.
39. Balzani, V.; Credi, A.; Venturi, M., *Molecular Devices and Machines: Concepts and Perspectives for the Nanoworld*. Second Edition ed.; Wiley-VCH Verlag GmbH & Co. KGaA: 2008.
40. Irie, M.; Mohri, M., Thermally irreversible photochromic systems. Reversible photocyclization of diarylethene derivatives. *J. Org. Chem* **1988,** *53* (4), 803-808.
41. Irie, M., Diarylethenes for Memories and Switches. *Chem. Rev.* **2000,** *100* (5), 1685-1716.
42. van der Molen, S. J.; Liljeroth, P., Conductance Properties of Switchable Molecules. In *Molecular Switches*, Wiley-VCH Verlag GmbH & Co. KGaA: 2011; pp 719-777.
43. Crivillers, N.; Orgiu, E.; Reinders, F.; Mayor, M.; Samorì, P., Optical Modulation of the Charge Injection in an Organic Field-Effect Transistor Based on Photochromic Self-Assembled-Monolayer-Functionalized Electrodes. *Adv. Mater.* **2011,** *23* (12), 1447-1452.
44. Pace, G.; Ferri, V.; Grave, C.; Elbing, M.; von Hänisch, C.; Zharnikov, M.; Mayor, M.; Rampi, M. A.; Samorì, P., Cooperative light-induced molecular movements of highly ordered azobenzene self-assembled monolayers. *Proc. Natl. Acad. Sci.* **2007,** *104* (24), 9937-9942.
45. Zhang, H.; Guo, X.; Hui, J.; Hu, S.; Xu, W.; Zhu, D., Interface Engineering of Semiconductor/Dielectric Heterojunctions toward Functional Organic Thin-Film Transistors. *Nano Lett.* **2011,** *11* (11), 4939-4946.

# 2. Graphene

## 2.1. Introduction

Graphene is a unique material exhibiting exceptional optical, electrical and mechanical properties rendering it appealing for numerous technological applications. Some of these properties, e.g. high conductivity, had already been predicted theoretically in 1947.[1] Graphene had been already synthetized on Platinum[2] and from SiC[3] in the 1970s, however it was only in 2004, when it was isolated by micromechanical exfoliation by the group of Geim and Novoselov[4], that its properties started to be deeply studied. Such a seminal groundbreaking work has catalysed attention and a notably high research activity on this type of material. Since then, new fascinating properties have been revealed and different synthetic processing approaches have been exploited in order to produce this material in large quantities paving the way towards industrial applications.[5]

In this chapter we will review the fundamental properties of graphene, synthetic routes for its production and the techniques employed for its characterization. Moreover, we will focus our attention on the liquid-phase exfoliation (LPE) of graphite approach since it is the one employed in our experimental work and on the use of surfactants to improve the quantity and quality of the dispersions produced.

## 2.2. Properties

### 2.2.1. Electronic properties

Graphene is a two-dimensional sheet of $sp^2$-hybridized carbon atoms arranged in a honeycomb lattice. The unit cell contains two inequivalent atoms A and B whose distance is 0.142 nm (**Figure 2.1a**).[6] The Brillouin zone of the reciprocal lattice of graphene is a hexagon with two classes of inequivalent points at the corners named *K* and K' (**Figure 2.1b**). In graphene each carbon atom is linked to three neighbour atoms by strong $\sigma$ bonds. The $\sigma$ bond derives from the hybridization of the *2s*, $2p_x$ and $2p_y$ orbitals of the carbon valence electrons. The fourth electron in the half-filled $2p_z$ orbital, which is perpendicular to the graphitic plane, is responsible for the weaker

$\pi$ bond with the adjacent $2p_z$ orbitals. The $\pi$ electrons determine the electronic properties of graphene. The energy dispersion of $\pi$ electrons was derived by Wallace[1] within the tight binding approximation and it is represented in **Figure 2.1c** as a function of the wave vector $\vec{k}$ . The upper band is called $\pi^*$ or anti-bonding band while the lower band is the bonding $\pi$ band. The two bands degenerate in the *K* and *K'* points and the Fermi Energy level is constituted by the plane connecting these points. In fact the $\pi$ band is completely filled by electrons whereas the $\pi^*$ band is empty.

Since around the *K* and *K'* points the dispersion can be approximated to cones (i.e. is linear) electrons and holes at low energy levels behave like relativistic particles described by the Dirac equation for spin-half particles. Therefore, the electrons and holes are called *Dirac fermions*, and the six corners K and K' of the Brillouin zone are called the *Dirac points*.[7] The equation describing the electronic dispersion relation around the Fermi energy is $E = \hbar v_F |\boldsymbol{k}|$ where the Fermi velocity $v_F$ is approximately 1/300 smaller than the speed of light, therefore $v_F \sim 10^6$ m/s.

The Dirac Fermions in graphene in contrast to other Dirac fermions (e.g. neutrinos), bearing a charge, can be manipulated through an electromagnetic field. This can lead to the observation of many interesting effects such as the quantum Hall effect at room temperature[8] and Berry's phase in graphene.[9]

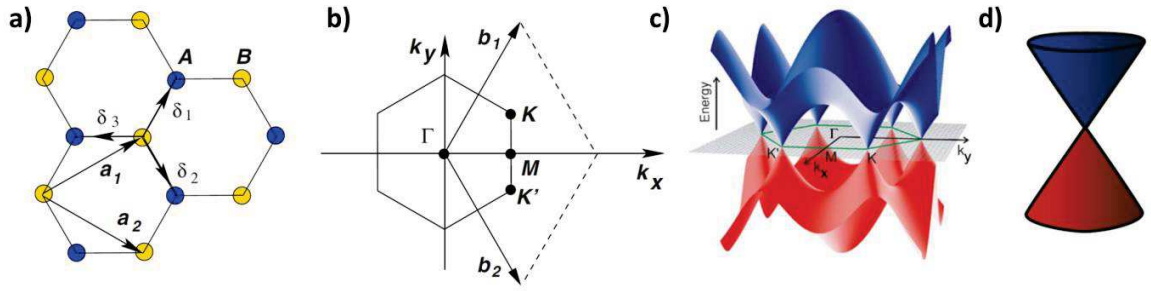


**Figure 2.1:** a) Graphene lattice with unit cell containing two inequivalent carbon atoms A and B; b) Brillouin zone; c) Representation of the energy dispersion of $\pi$ electrons; d) Magnification of the energy dispersion at one of the Dirac points. Figures a) and b) are taken from ref. 6, c) and d) from ref. **7.**

## 2.2.2.Optical properties

Despite being only one atom layer thick, graphene is able to absorb a significant fraction of light such that it can be possible to observe it by naked eye (**Figure 2.2a**).[10] The opacity of graphene surprisingly is not varying with material properties but is depending only from the fine structure constant $\alpha = \frac{e^2}{\hbar c}$ where *e* is the electron charge, $\hbar$ is the reduced Planck constant and *c* is the speed of

light. In fact, calculating the absorption of light by 2-D Dirac fermions with Fermi's golden rule, it leads to an opacity value of $1 - T = \pi\alpha = 2.3\%$, where T is the transmittance. Therefore the origin of the optical properties of graphene derives from its two dimensional nature and its gapless electronic spectrum.

Graphene reflects less than 0.1% of light in the visible region and therefore the absorption can be considered a linear function of the number of layers. *N* layers of graphene will have absorption equal to $N\pi\alpha$ (Fig. 2.2b, inset).[11] The absorption spectrum of single layer graphene is quite flat with a peak around 270 nm (~ 4.6 eV) arising from Van Hove singularity of the band structure (Fig. 2.1c).[12]

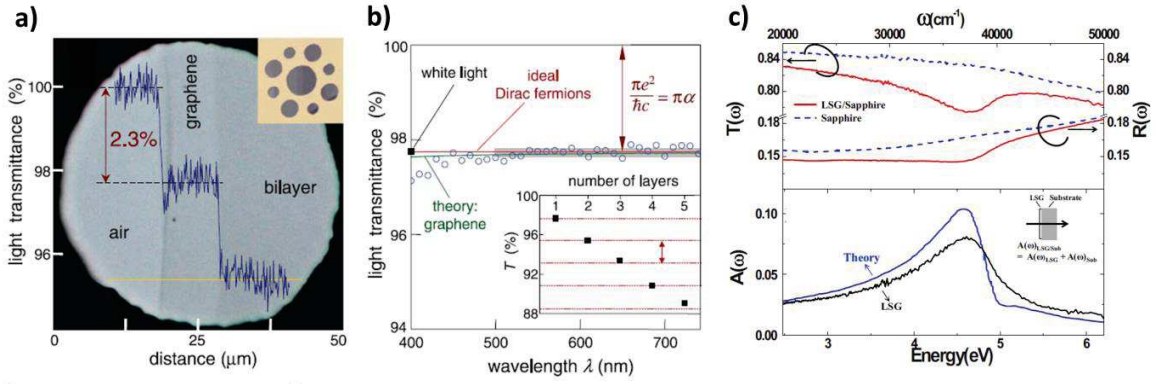


**Figure 2.2**: a) On the right corner: sample prepared using a metal plate with holes of 20, 30 and 50 μm and graphene crystallites placed on them; main figure: photograph of a 50 μm aperture covered by a graphene monolayer and bilayer and transmittance profile along the yellow line. b) Open circle: transmittance of a single layer graphene; red line calculated transmittance for 2-D Dirac fermions and in green the corrected spectrum taking into account a nonlinearity and triangular warping of graphene's electronic spectrum; in the inset: transmittance of the white light as function of the number of layers. The step at each layer (red arrow) corresponds to πα. c) On the top: transmission and reflection of a large scale graphene on a sapphire substrate (red curve) and of the bare sapphire (dashed curve) in the UV-region; on the bottom: experimental (black curve) and theoretical (blue curve) absorbance of the single layer graphene Image reproduce from ref. 12b.

## 2.2.3.Other properties

Graphene is a very elastic material with a Young modulus around 1 TPa. Nevertheless it is a very strong material with a breaking strength of 42 N/m.[13] Moreover, it is impermeable to gases and it has a high thermal conductivity. All the extraordinary properties of this material make it suitable for different applications. In **Table 2.1** a summary of all the principal properties and the related possible applications is reported.

| Property | Value | Ref. | Possible applications |
|---|---|---|---|
| Surface to volume ratio | One atomic layer thickness | 6, 14 | Supercapacitors, |
| Breaking strength | 42 $Nm^{-1}$ | 13 | Composites materials |
| Impermeability | Impermeable to gas molecules | 15 | membrane gas barriers |
| Carrier mobility at room temperature | 200,000 $cm^2V^{-1}s^{-1}$ | 16 | Transistors, photodetectors |
| Maximum current density | $>10^8$ $Acm^{-1}$ | 17 | |
| Thermal conductivity | ~5000 $Wm^{-1}K^{-1}$ | 18 | Heat dissipation |
| Optical absorption coefficient | 2.3% | 10 | Flexible optoelectronics, solar cells, transparent conductive electrodes |
| Young modulus | 1 TPa | 13 | |

**Table 2.1:** Principal properties of graphene and possible applications deriving from them.

## 2.3. Graphene fabrication

Two distinct strategies have been undertaken for graphene production, i.e. the bottom-up and the top-down approach. The former relies on the generation of graphene from suitably designed molecular building blocks undergoing chemical reaction to form covalently linked 2D networks. The latter occurs via exfoliation of graphite into graphene. In **Figure 2.3** a summary of the principal fabrication methods is reported.

Within the *bottom-up* approaches, the more common are the chemical vapour deposition (CVD) technique, the epitaxial growth and the chemical synthesis.

CVD technique consists in growing graphene from volatile precursors which can react or decompose on the chosen substrate. Two main CVD process have been employed in the production of graphene, thermal CVD and plasma enhanced CVD (PECVD). The first thermal CVD growth of a large single layer graphene of the order of $cm^2$ was achieved in 2009 exploiting as substrate copper.[19] Graphene is grown on a copper substrate at T=1000°C using as precursors a mixture of methane and hydrogen gases. Other metallic substrates such as nickel and cobalt have been employed, but they absorb carbon more efficiently than copper and for this reason few layer graphene and chunk of graphite rather than monolayer graphene are more probable to form on their surface. To avoid this, thin films of these metals are evaporated on $Si/SiO_2$ or other substrates rather than use foils.[20] PECVD of graphene arose from the necessity of using lower growth temperature, in

view of industrial automated fabrication processes. Using PECVD it is possible to produce single layer graphene (SLG) sheets at temperature below 500°C[21] even though the quality of the sheets is inferior to those produced by thermal CVD.

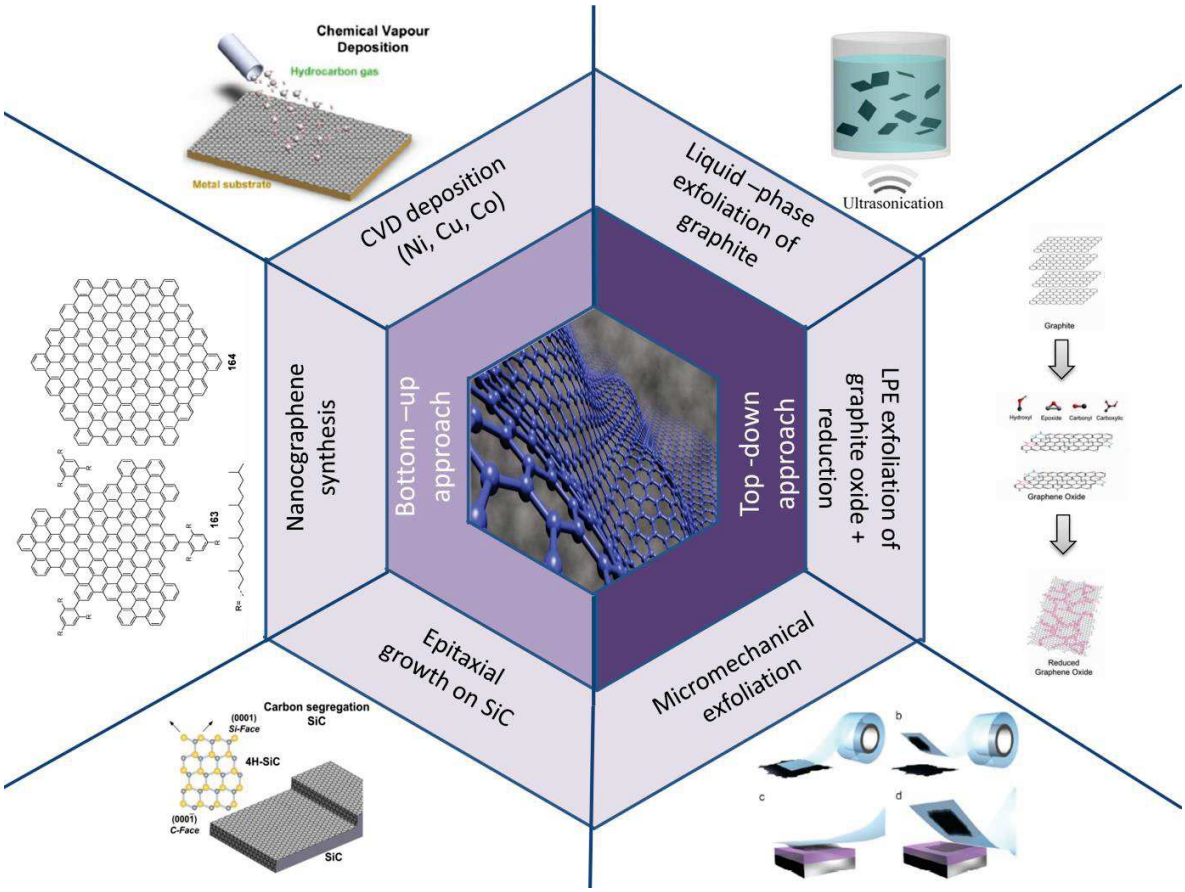


**Figure 2.3:** Different approaches to obtain graphene. The figures are taken from ref. 22, 23, 24**.**

Epitaxial growth on silicon carbide (SiC) of graphene occurs by thermal decomposition of SiC at high temperatures (>1000°C) with evaporation of Si atoms.[25] The term 'epitaxial', even though largely diffuse, is improper in this case since between the SiC and the graphene lattice there is a significant mismatch. It would be desirable to grow graphene on substrates with small lattice mismatch in order to minimize in plane defects.

Through chemical synthesis it is possible to produce nanographenes[23] starting from dendritic precursor transformed by cyclodehydrogenation and planarization or starting from polycyclic

aromatic hydrocarbons (PAHs) by pyrolysis.[26] In a similar way it is possible to produce also graphene nanoribbons (GNRs)[27] and graphene quantum dots (GDs).[28]

Micromechanical exfoliation is the *top-down* approach employed by Geim and Novoselov to produce graphene and study its basic properties.[4] This technique consists of the peeling of graphite by means of scotch tape.[24] Afterwards the scotch tape is attached to the substrate and together with scotch residues and big pieces of graphite, 50 μm wide monolayer thick architectures are left on the substrate and it is possible to visualize them with an optical microscope. However, this technique can be employed only for fundamental research due to the low yield of graphene sheets produced.

Alternative top-down approaches leading to large quantities of produced graphene are solution-based processes such as liquid phase exfoliation (LPE) and reduction of graphene oxide.

The oxidation of graphite was a process developed in 1859 by Brodie[29] using potassium chlorate ($KClO_3$) and fuming nitric acid and then ameliorated until arriving to the well-known Hammer's method[30] which employs a mixture of sulphuric acid, sodium nitrate and potassium permanganate. Once oxidized, graphitic planes present many defects like epoxide, hydroxyl and carboxylic groups that allow obtaining graphene oxide dispersed sheets in different solvents by sonication, stirring or thermal expansion of graphite oxide. Then it is possible to reduce, i.e. decrease the oxidation state of the oxygen-containing groups, in the graphene oxide, chemically by alkaline substances,[31] electrochemically,[32] thermally[33] or by means of UV irradiation,[34] plasma treatment[35] and so on. The reduced graphene oxide (RGO), does not reach the electrical and optical properties of graphene, because the $sp^2$-conjugated network is never completely restored and many defects are present.

More recently, it has been shown that graphite can be directly exfoliated into graphene in liquid media, without needing an oxidation step, by subsequent sonication and centrifugation cycles. Stable dispersions of liquid-phase exfoliated graphene (LPE-G) can be obtained if solvents having a surface tension close to that of graphene are employed.[36]

Another modern approach, which allows a mass production of high quality graphene in liquids, is the electrochemical exfoliation of graphite (EEG) in organic[37] and aqueous solutions.[38] In this process natural graphite or high oriented pyrolytic graphite (HOPG) is employed as electrode and source of graphene in an electrochemical cell.

It has to be pointed out that every technique has its *pros* and *cons*. CVD and epitaxial growth techniques have the advantage of producing high quality big graphene sheets, yet they are difficult to be implemented for large-scale production and are expensive processes. LPE of graphite and reduction of graphene oxide instead are highly upscalable methods but they produce graphene with

small sheet size (~ 1 $\mu m^2$) and of medium quality, which causes still problems when exploiting this material in electronics.

## 2.4. Liquid-phase exfoliated graphene

The LPE process consists of three stages: *(i)* dispersion of graphite in the chosen solvent, *(ii)* sonication, and *(iii)* purification through centrifugation.[39]

Exfoliation of graphite occurs thanks to *shear forces* and *cavitation*, acting on the bulk material during ultrasonication. Acoustic waves, in fact, consist of alternate regions of compression and rarefaction transmitted in a medium along the wave propagation direction. When a negative pressure is exerted on a liquid the Wan der Waals forces between the molecules are overcome and small bubbles (of micrometer range) of gas or cavities grow, nucleate and then collapse.[40] This phenomenon is known as *cavitation.* If the microbubble collapse against graphite this causes a shockwave which will produce compressive stress waves propagating through the graphite; if the collapse happens in the liquid close to the solid a jet of liquid will hit the graphite. For the theory of stress waves,[41] once a compressive wave enters in contact with the plane of graphite a tensile stress on the graphite has to be reflected back causing the exfoliation (**Figure 2.4** left). A second phenomenon, which causes the exfoliation, is the unbalanced lateral compressive stress, which will cause a shear effect causing delamination and dispersion of the flakes. In addition, the jet of liquid can penetrate in between two layers causing the separation of the sheets (**Figure 2.4** right).[42]

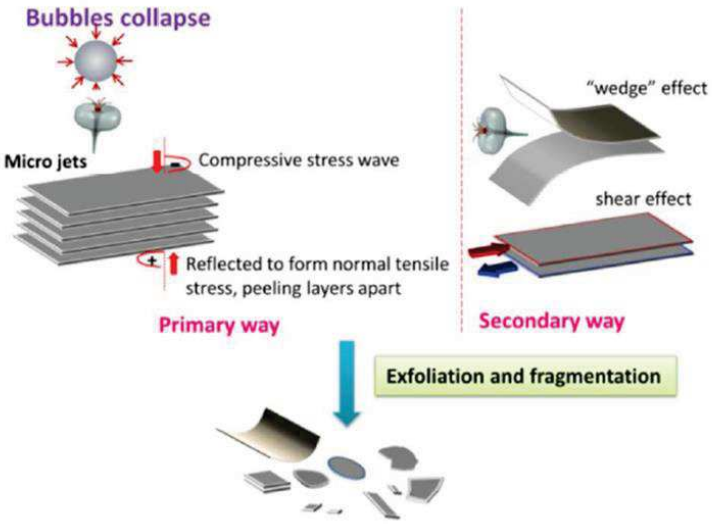


**Figure 2.4:** Scheme of the exfoliation during ultrasonication in a liquid media. Image taken from ref. 42a.

The choice of the solvent is crucial since, after exfoliation, the solvent‑graphene interaction needs to balance the attractive forces between graphene sheets. It has been widely studied and proved that liquid media having surface tension around 40 mJ $m^{-2}$, are the best choice for exfoliation technique, since they minimize the interfacial energy between the solvent and graphene and thus allowing for the overcoming of the van der Waals forces between adjacent graphene layers. Among the most suitable solvents we can include N-Methyl-2-pyrrolidone (NMP - 40 mJ $m^{-2}$),[36] *orto*-dichlorobenzene (*o*-DCB –37 mJ $m^{-2}$)[43], dimethylformamide (DMF – 37.1 mJ $m^{-2}$).[44] However, these solvents have high boiling points and therefore are difficult to remove in view of the further processing of graphene. Other strategies have been employed, like sonication in a mixture of low boiling point solvents such as ethanol/water showing that Young's equation can be used to predict the optimal solvent ratio for the effective exfoliation of graphite.[45] Solvent exchange, starting from a dispersion in NMP is another alternative, which consists of multiple cycles of filtration of the original dispersion and re-dispersion in ethanol until obtaining a final dispersion in ethanol containing less than 0.3% of NMP.[46]

An alternative approach is the use of *stabilizing agents* that, having high adsorption energy on graphene, can promote the exfoliation by supramolecular interactions.[39] At the same time these molecules allow the exfoliation of graphite and stabilization of graphene in less toxic and low boiling point such as water. Moreover, new chemical and physical properties can be conferred to the

material. Some examples and some considerations on the LPE of graphite in presence of stabilizing agents are reported in section 2.4.1.

The last step of liquid phase exfoliation, consisting in the centrifugation of the dispersions immediately after sonication, is crucial since graphite sheets which do not exfoliate properly have to be removed.

### 2.4.1. Use of surfactants in LPE

The use of surfactants in the production of LPE-G is becoming more and more popular in view of the benefits brought, that can vary from the increase of exfoliation yields $Y_M$ and $Y_W$ to the stabilization against reaggregation of the graphene sheets and increase in concentration.

The surfactants employed up to know can be divided in two main categories i.e. small surfactants and polymers. Both categories are then sub-divided into ionic and non-ionic surfactants.

In general the interplays between surfactant, graphene and solvent are very complex but two are the fulfillments to be accomplished in order to promote the exfoliation*: i)* the stabilizing agent needs to have higher adsorption energy on graphene compared to the one of solvent molecules; *ii)* the surfactant needs to be largely soluble in the liquid media.

The use of surfactant in the process of LPE was firstly thought in order to avoid the use of high boiling point and toxic solvents such as NMP. The first surfactants to be employed were ionic surfactants, the same used to stabilize carbon nanotubes, like sodium dodecylbenzene sulfonate (SDBS)[47] or bile salts like sodium cholate (SC) using water as solvent[48]

The mechanism of stabilization for ionic surfactants takes advantage of the adsorption of the core of the molecule by non-covalent interactions (van der Waals, π-π stacking…) on the graphitic plane and at the same time in polar media, the head groups tend to disassociate, imparting an effective charge on the flake. The dispersed flakes are therefore stabilized by columbic repulsion between surfactant-coated flakes. The key parameter for the stabilization issue is the *zeta potential* ζ that is the electric potential at the edge of the layer of bound ions. A study by Lotoya et al revealed that the concentration of the dispersions exfoliated in presence of ionic surfactants increases with the increasing of the zeta potential.[49]

Indeed the interactions leading to the stabilization are more complex. Lin et al.[48] through joint experimental and theoretical calculations demonstrated that SC assembles forming a compact monolayer on graphene and being surrounded by screening sodium counterions and ordered water

molecules. The stabilization was caused only partially by electrostatic interactions and mainly due to steric hindrance induced by the last layer of cholate ions and sodium counterions confined between the two graphene sheets.

Molecules possessing a polycyclic aromatic hydrocarbon core such as pyrene, coronene, perylene, antracene functionalized with hydrophilic groups (such as OH) and ionic groups ( sulphonate groups) have also been employed to tailor the solubility and the electronic properties of LPE.[50] Palermo and coworkers have performed a comparative study on the efficiency in exfoliation of graphite in water by functionalized pyrenes with an increasing number of sulphonate groups, i.e. 1-pyrenesulfonic acid sodium salt (PS1), 6,8 dihydroxy-1,3-pyrenedisulfonic acid disodium salt (PS2), 8-hydroxypyrene-1,3,6-trisulfonic acid trisodium salt (PS3) and pyrene-1,3,6,8-tetrasulfonic acid tetrasodium salt (PS4).[51] Molecular Dynamics simulations were performed in order to understand the process of adsorption of the pyrene derivative molecules on the surface of graphene in a water medium. Also in this case the stabilization process of graphene in water arises from complex interplays and is a too simplistic view that of assigning to the aromatic core the role of interaction with graphene through π-π stacking, and to the eventual functionalization group the role of interacting with the solvent and prevent the aggregation. PS2, having the highest moment dipole and the highest adsorption energy is the most effective in the exfoliation of material. However, the molecular dipole is not important *per se*, but because it promotes the adsorption on graphene by displacing the water molecule layer collocated between the aromatic cores of the dye and the graphene sheet (**Figure 2.5**).

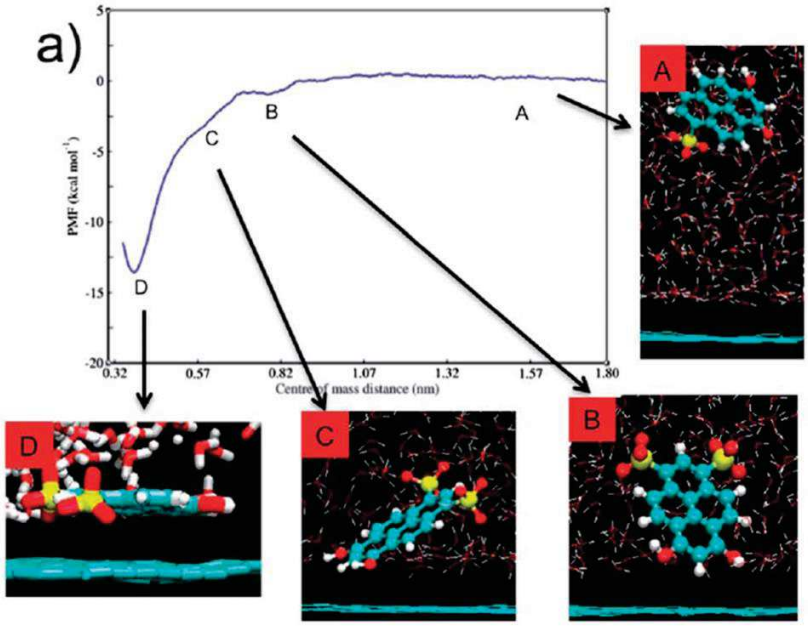


**Figure 2.5:** Potential of mean force (PMF) calculations for the adsorption of molecule PS2 on graphene with the different snapshots of the molecule at different distances from graphene showing how the orientation of the molecule is irrelevant at the beginning (A), then the molecules approaches the surfaces pointing the sulphonate group towards the solvent far for graphene (B) and then, when approaching closer graphene, the molecules tilts (C) and slides between the graphene and water molecule due to the π-π stacking (D). Reproduced from ref. 51.

The use of water as an exfoliation medium is unfortunately not recommended for the fabrication of graphene to be employed in electronic devices because water residues at the interface with dielectrics can enhance charge trapping phenomena.[52] Therefore, the branch of exfoliation in organic solvent has been pursued trying to increase also in this case the quality and quantity of graphene produced upon addition of molecules. This has been done also in our group, by mastering a supramolecular approach, aiming at exploiting the produced graphene for applications in organic electronics.

Samorì and coworkers have demonstrated firstly that by mastering the supramolecular approach it is possible to promote the exfoliation of graphene by use of a simple non-ionic surfactant molecules such 1-phenyloctane and arachidic acid.[53] Moreover, they have found out that there is a linear dependence of the exfoliation yield from the length of the alkyl chains, when comparing the dispersion obtained by sonication of graphite in organic solvents in presence of fatty acids with an increasing number of carbon atoms (**Figure 2.6**).[54] These results have been interpreted by a simple thermodynamic model based on the molecular self-assembly of these molecules on graphene,

showing that the shorter molecules have to pay a higher entropic cost to self-assemble on graphene. These results show the efficacy of this theoretical model as a guide for design of new surfactants.

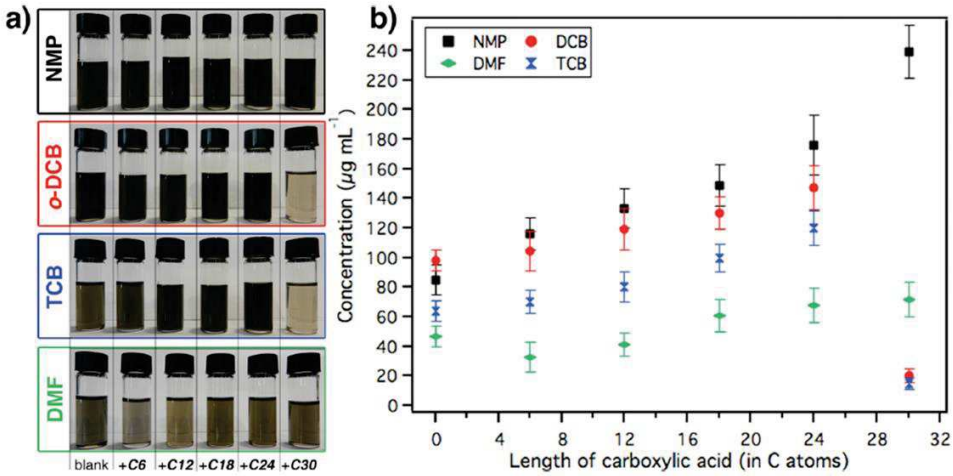


**Figure 2.6:** a) Photograph of graphene dispersions prepared by exfoliation of graphite in different solvents and in the presence /absence of carboxylic molecules. b) Average concentration of the graphene dispersions after the filtration process as function of the carboxylic acid length Reproduced from ref.54.

It is been recently shown that graphite can be successfully exfoliated both in water and in organic solvents using polymers as stabilizing agents.

Polymers, such as Pluronic® [55] and hyper branched polyethylene[56] as surfactants promote higher concentrated dispersions compared to small molecules surfactants, however there is a main drawback constituted by the impossibility of separating the LPE graphene from the polymer, cause to the high adsorption energy, for further processing.

## 2.4.2.Figures of merit in liquid-phase exfoliation

LPE graphene can be characterized using the following figures of merit:

- *Concentration* of the dispersed graphene in solution: the concentration *c* of the dispersion can be determined filtering a known volume of the dispersion onto a filter of known mass and measuring the final mass with a microbalance. An alternative and faster way is to use the absorption coefficient α. Measuring the absorption of a known concentration dispersion and diluting the sample it is possible to obtain α from the Lambert-Beer law: A= αcl where l is the path length. In this way, for all the other samples produced, it is possible to calculate *c* from the Lambert-Beer law. α~2460 $mLmg^{-1}m^{-1}$ has been determined in ref 36 for a variety

of solvents, while other studies report a value of 3620 mL $mg^{-1}$ $m^{-1}$ for dispersions in NMP[47] and a value of~6600 mL $mg^{-1}$ $m^{-1}$ in water.[57] This discrepancy is a sign that this method has to be improved since α should be independent from the concentration.

- *Exfoliation yield*: The exfoliation yield can be defined in terms of weight $Y_w$ or of number of monolayers $Y_M$. $Y_w$ is the ratio between the weight of the dispersed graphene and the weight of the initial graphitic material while $Y_M$ is defined as the number of graphene monolayers divided by the total number of graphitic flakes in solution. $Y_w$ does not give any information about the quality of the dispersion as opposed to $Y_M$. $Y_M$ can be calculated from TEM studies counting the number of layers $N$ on the edges or by diffraction pattern or from Raman spectroscopy analysing carefully the spectrum as explained in section 2.5.2.

## 2.5. Characterization

### 2.5.1. Imaging graphene

Optical microscopy was the first technique used in order to visualize the graphene sheets deposited on a $Si/SiO_2$ substrate and to discriminate the number of layers. In **Figure 2.7** an optical image of graphene sheets is reported. It was found that the contrast in the image depends on the thickness of $SiO_2$,[58] the wavelength of light used and the angle of illumination.[59] If the flakes are sufficiently thin and transparent they add a further optical path, which changes their interference color with respect to an empty wafer. Later on other techniques such as ellipsometry,[60] phase-shifting interferometric imaging,[61] surface plasmon resonance reflectance[62] and Rayleigh[63] and Raman imaging microscopy[64] have been applied to identify graphene layers deposited on different types of substrates.

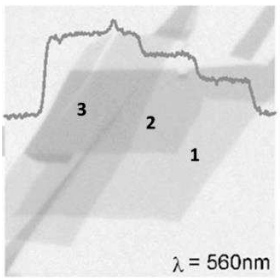


**Figure 2.7:** Optical image of graphene sheets. It is possible to see steplike changes in the contrast for 1, 2, and 3 layers graphene. Image taken from ref. [58].

## 2.5.2.Raman spectroscopy

Raman spectroscopy is an ideal tool for graphene characterization since it is a fast and non-destructive technique, it offers a high resolution, gives structural and electronic information and can be applicable at both laboratory and mass-production scales. Unlike Rayleigh scattering, when using optical microscope, it allows to extract information from any kind of graphene sample. A typical spectrum of LPE graphene, taken at 2.4 eV (514 nm) is reported in **Figure 2.8a** compared with the spectrum of graphite. We show the spectrum of this particular class of graphene since it will be the one treated in this thesis work. The spectrum is composed by two main peaks, the G and the 2D peak at around 1587 $cm^{-1}$ and 2680 $cm^{-1}$ respectively and a D peak at around 1350 $cm^{-1}$.present only when the graphene has defects in it. The G peak is an in plane vibrational mode. The G band position shifts towards lower frequencies, with increasing the number of layers following a 1/n dependence (**Figure 2.8b**).[65] The 2D band is the result of a two phonon lattice vibrational process and is an overtone (second order) of the D band. Unlike the D band, it does not need to be activated by proximity to a defect. For this reason the 2D band is always a strong band in the graphene spectrum, even if the D band is not present and it does not depend from the presence of defects. Also the 2D band is used in order to determine the graphene layer thickness. With increasing the number of layer not only the band position but also the band shape will change as reported in **Figure 2.8c**. When performing this characterization it is important to use always the same laser excitation energy $E_{laser}$ for making comparisons because while for monolayer graphene, the lineshape is simply a single Lorentzian line with a linear dependence of $\omega_{2D}$ on $E_{laser}$ for bilayer graphene, each of the four peaks, depends differently on $E_{laser}$.

The D peak is a breathing mode from $sp^2$ carbon rings, which is activated only when the ring is adjacent to a graphene edge or to a defect. If the D band is very intense, a high number of defects are present in the graphene sample. Because absolute intensity measurement is trivial in Raman spectroscopy, the normalized intensity $I_D/I_G$ ratio is employed to measure the amount of disorder.[67]

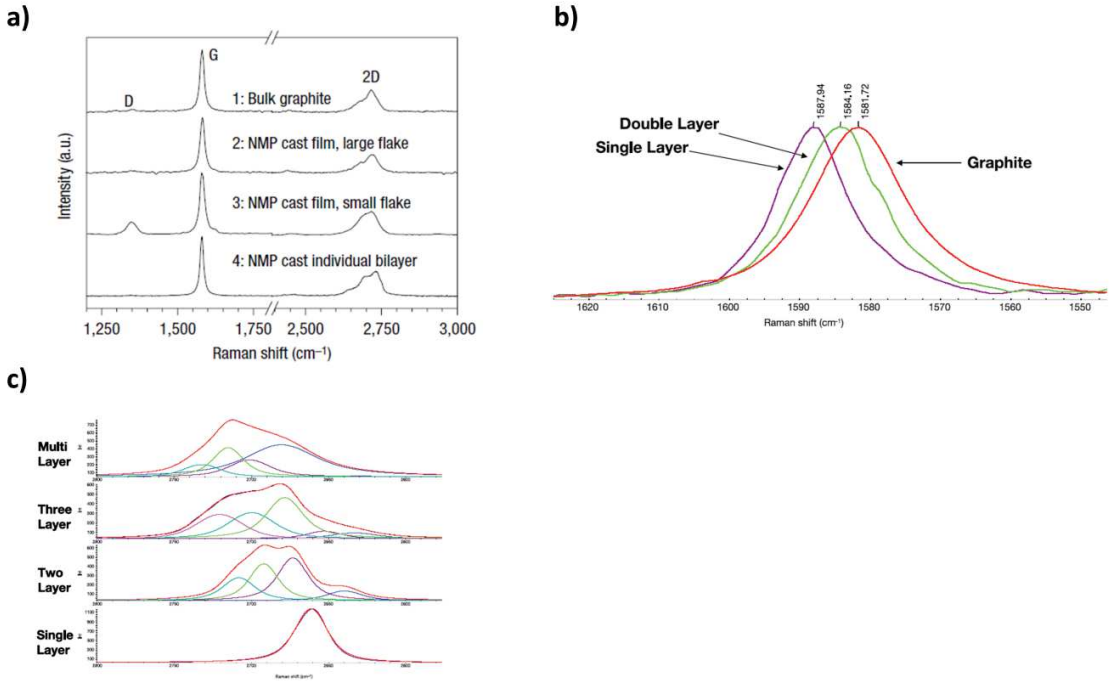


**Figure 2.8:** a) Raman spectrum of liquid phase exfoliated graphene samples compared to the graphite one; b) shift of the G peak with increasing of the number of layers; c) change in the 2D band according to the number of layers. Image a) is taken from ref [36], image b) and c) from ref [66].

## 2.5.3.Transmission electron microscopy

Transmission electron microscopy (TEM) and High Resolution- Transmission microscopy are used to study the quality of graphene sheets suspended on a grid (**Figure 2.9**).[68] The number of layers in a graphene sheet, in fact, can be determined in TEM analysing the edges or through the electron diffraction patterns. Moreover, it is possible to study the presence of inplane defects.

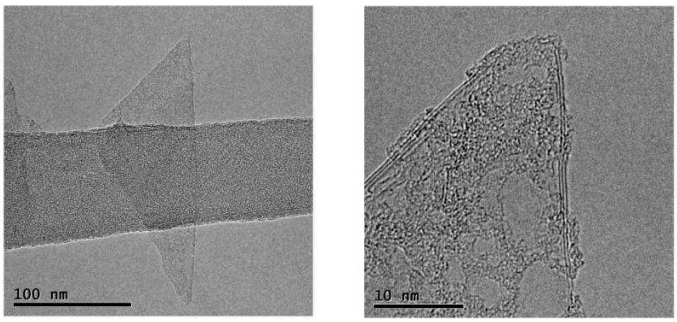


**Figure 2.9:** TEM images of graphene sheets.

## 2.5.4.Atomic force microscopy

Atomic force microscopy (AFM) is employed for analysis of the average size of flakes in some samples and for counting the number of layers in a graphene sheet measuring the step height of the flake deposited on a substrate (**Figure 2.10**).[69] However, the height of the sheets depends from the substrate and from the environmental conditions (humidity, temperature…), leading to different results according to where the measurements are performed and how the sample is prepared. Moreover, AFM is a very time consuming technique.

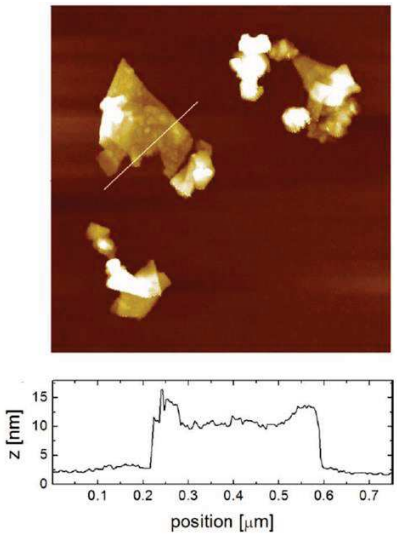


**Figure 2.10:** AFM image of graphene flakes and height profile taken lalong the white line marked in the image. Reproduced from reference 51.

## 2.5.5. X-Ray Photoelectron spectroscopy

X-Ray Photoelectron Spectroscopy gives information about the chemical composition, i.e. on the quantity of hydroxyl, epoxy and carboxylic groups present in the graphene samples. The C1s spectrum of graphene is characterized by a peak at 284.8 eV corresponding to the C-C bond, with an asymmetric tail. Peaks at 284 and 289 eV corresponding respectively to C=O and C-O bonds, are useful in order to estimate the presence of carboxylic and epoxy/hydroxyl group in the graphene sheet. Moreover, it is possible to know if impurities are present.

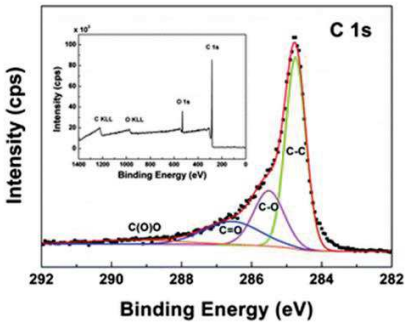


**Figure 2.11:** C1s spectrum and fitting of a graphene sample. In the inset a wide range spectrum.Taken from reference [70]

## 2.6. References


1. Wallace, P. R., The Band Theory of Graphite. *Physical Review* **1947,** *71* (9), 622-634.
2. May, J. W., Platinum surface LEED rings. *Surf. Sci.* **1969,** *17* (1), 267-270.
3. Van Bommel, A. J.; Crombeen, J. E.; Van Tooren, A., LEED and Auger electron observations of the SiC(0001) surface. *Surf. Sci.* **1975,** *48* (2), 463-472.
4. Novoselov, K. S.; Geim, A. K.; Morozov, S. V.; Jiang, D.; Zhang, Y.; Dubonos, S. V.; Grigorieva, I. V.; Firsov, A. A., Electric Field Effect in Atomically Thin Carbon Films. *Science* **2004,** *306* (5696), 666-669.
5. Ferrari, A. C.; Bonaccorso, F.; Fal'ko, V.; Novoselov, K. S.; Roche, S.; Boggild, P.; Borini, S.; Koppens, F. H. L.; Palermo, V.; Pugno, N.; Garrido, J. A.; Sordan, R.; Bianco, A.; Ballerini, L.; Prato, M.; Lidorikis, E.; Kivioja, J.; Marinelli, C.; Ryhanen, T.; Morpurgo, A.; Coleman, J. N.; Nicolosi, V.; Colombo, L.; Fert, A.; Garcia-Hernandez, M.; Bachtold, A.; Schneider, G. F.; Guinea, F.; Dekker, C.; Barbone, M.; Sun, Z.; Galiotis, C.; Grigorenko, A. N.; Konstantatos, G.; Kis, A.; Katsnelson, M.; Vandersypen, L.; Loiseau, A.; Morandi, V.; Neumaier, D.; Treossi, E.; Pellegrini, V.; Polini, M.; Tredicucci, A.; Williams, G. M.; Hee Hong, B.; Ahn, J.-H.; Min Kim, J.; Zirath, H.; van Wees, B. J.; van der Zant, H.; Occhipinti, L.; Di Matteo, A.; Kinloch, I. A.; Seyller, T.; Quesnel, E.; Feng, X.; Teo, K.; Rupesinghe, N.; Hakonen, P.; Neil, S. R. T.; Tannock, Q.; Lofwander, T.; Kinaret, J., Science and technology roadmap for graphene, related two-dimensional crystals, and hybrid systems. *Nanoscale* **2015,** *7* (11), 4598-4810.
6. Castro Neto, A. H.; Guinea, F.; Peres, N. M. R.; Novoselov, K. S.; Geim, A. K., The electronic properties of graphene. *Rev. Mod. Phys.* **2009,** *81* (1), 109-162.
7. Yanqing, W.; Farmer, D. B.; Fengnian, X.; Avouris, P., Graphene Electronics: Materials, Devices, and Circuits. *Proceedings of the IEEE* **2013,** *101* (7), 1620-1637.
8. Novoselov, K. S.; Jiang, Z.; Zhang, Y.; Morozov, S. V.; Stormer, H. L.; Zeitler, U.; Maan, J. C.; Boebinger, G. S.; Kim, P.; Geim, A. K., Room-Temperature Quantum Hall Effect in Graphene. *Science* **2007,** *315* (5817), 1379.
9. Zhang, Y.; Tan, Y.-W.; Stormer, H. L.; Kim, P., Experimental observation of the quantum Hall effect and Berry's phase in graphene. *Nature* **2005,** *438* (7065), 201-204.
10. Nair, R. R.; Blake, P.; Grigorenko, A. N.; Novoselov, K. S.; Booth, T. J.; Stauber, T.; Peres, N. M. R.; Geim, A. K., Fine Structure Constant Defines Visual Transparency of Graphene. *Science* **2008,** *320* (5881), 1308.
11. Bonaccorso, F.; Sun, Z.; Hasan, T.; Ferrari, A. C., Graphene photonics and optoelectronics. *Nat Photon* **2010,** *4* (9), 611-622.
12. (a) Yang, L.; Deslippe, J.; Park, C.-H.; Cohen, M. L.; Louie, S. G., Excitonic Effects on the Optical Response of Graphene and Bilayer Graphene. *Phys. Rev. Lett.* **2009,** *103* (18), 186802; (b) Lee, C.; Kim, J. Y.; Bae, S.; Kim, K. S.; Hong, B. H.; Choi, E. J., Optical response of large scale single layer graphene. *Appl. Phys. Lett.* **2011,** *98* (7), 071905.
13. Lee, C.; Wei, X.; Kysar, J. W.; Hone, J., Measurement of the Elastic Properties and Intrinsic Strength of Monolayer Graphene. *Science* **2008,** *321* (5887), 385-388.
14. El-Kady, M. F.; Kaner, R. B., Scalable fabrication of high-power graphene micro-supercapacitors for flexible and on-chip energy storage. *Nat Commun* **2013,** *4*, 1475.

15. Nair, R. R.; Wu, H. A.; Jayaram, P. N.; Grigorieva, I. V.; Geim, A. K., Unimpeded Permeation of Water Through Helium-Leak-Tight Graphene-Based Membranes. *Science* **2012,** *335* (6067), 442-444.
16. Chen, J.-H.; Jang, C.; Xiao, S.; Ishigami, M.; Fuhrer, M. S., Intrinsic and extrinsic performance limits of graphene devices on SiO2. *Nat Nano* **2008,** *3* (4), 206-209.
17. Murali, R.; Yang, Y.; Brenner, K.; Beck, T.; Meindl, J. D., Breakdown current density of graphene nanoribbons. *Appl. Phys. Lett.* **2009,** *94* (24), 243114.
18. Balandin, A. A.; Ghosh, S.; Bao, W.; Calizo, I.; Teweldebrhan, D.; Miao, F.; Lau, C. N., Superior Thermal Conductivity of Single-Layer Graphene. *Nano Lett.* **2008,** *8* (3), 902-907.
19. Li, X.; Cai, W.; An, J.; Kim, S.; Nah, J.; Yang, D.; Piner, R.; Velamakanni, A.; Jung, I.; Tutuc, E.; Banerjee, S. K.; Colombo, L.; Ruoff, R. S., Large-Area Synthesis of High-Quality and Uniform Graphene Films on Copper Foils. *Science* **2009,** *324* (5932), 1312-1314.
20. Kim, K. S.; Zhao, Y.; Jang, H.; Lee, S. Y.; Kim, J. M.; Kim, K. S.; Ahn, J.-H.; Kim, P.; Choi, J.-Y.; Hong, B. H., Large-scale pattern growth of graphene films for stretchable transparent electrodes. *Nature* **2009,** *457* (7230), 706-710.
21. Kim, J.; Ishihara, M.; Koga, Y.; Tsugawa, K.; Hasegawa, M.; Iijima, S., Low-temperature synthesis of large-area graphene-based transparent conductive films using surface wave plasma chemical vapor deposition. *Appl. Phys. Lett.* **2011,** *98* (9), 091502.
22. Bonaccorso, F.; Lombardo, A.; Hasan, T.; Sun, Z.; Colombo, L.; Ferrari, A. C., Production and processing of graphene and 2d crystals. *Mater. Today* **2012,** *15* (12), 564-589.
23. Sun, Z.; Ye, Q.; Chi, C.; Wu, J., Low band gap polycyclic hydrocarbons: from closed-shell near infrared dyes and semiconductors to open-shell radicals. *Chem. Soc. Rev.* **2012,** *41* (23), 7857-7889.
24. Novoselov, K. S.; Neto, A. H. C., Two-dimensional crystals-based heterostructures: materials with tailored properties. *Phys. Scr.* **2012,** *2012* (T146), 014006.
25. First, P. N.; de Heer, W. A.; Seyller, T.; Berger, C.; Stroscio, J. A.; Moon, J.-S., Epitaxial Graphenes on Silicon Carbide. *MRS Bulletin* **2010,** *35* (04), 296-305.
26. Zhi, L.; Müllen, K., A bottom-up approach from molecular nanographenes to unconventional carbon materials. *J. Mater. Chem.* **2008,** *18* (13), 1472-1484.
27. (a) Cai, J.; Ruffieux, P.; Jaafar, R.; Bieri, M.; Braun, T.; Blankenburg, S.; Muoth, M.; Seitsonen, A. P.; Saleh, M.; Feng, X.; Müllen, K.; Fasel, R., Atomically precise bottom-up fabrication of graphene nanoribbons. *Nature* **2010,** *466* (7305), 470-473; (b) Dössel, L.; Gherghel, L.; Feng, X.; Müllen, K., Graphene Nanoribbons by Chemists: Nanometer-Sized, Soluble, and Defect-Free. *Angew. Chem. Int. Ed.* **2011,** *50* (11), 2540-2543.
28. Yan, X.; Cui, X.; Li, B.; Li, L.-s., Large, Solution-Processable Graphene Quantum Dots as Light Absorbers for Photovoltaics. *Nano Lett.* **2010,** *10* (5), 1869-1873.
29. Brodie, B. C., *Ann. Chim. Phys* **1860,** *59*, 466.
30. Hummers, W. S.; Offeman, R. E., Preparation of Graphitic Oxide. *J. Am. Chem. Soc.* **1958,** *80* (6), 1339-1339.
31. Fan, X.; Peng, W.; Li, Y.; Li, X.; Wang, S.; Zhang, G.; Zhang, F., Deoxygenation of Exfoliated Graphite Oxide under Alkaline Conditions: A Green Route to Graphene Preparation. *Adv. Mater.* **2008,** *20* (23), 4490-4493.
32. Guo, H.-L.; Wang, X.-F.; Qian, Q.-Y.; Wang, F.-B.; Xia, X.-H., A Green Approach to the Synthesis of Graphene Nanosheets. *ACS Nano* **2009,** *3* (9), 2653-2659.
33. Mattevi, C.; Eda, G.; Agnoli, S.; Miller, S.; Mkhoyan, K. A.; Celik, O.; Mastrogiovanni, D.; Granozzi, G.; Garfunkel, E.; Chhowalla, M., Evolution of Electrical, Chemical, and Structural Properties of Transparent and Conducting Chemically Derived Graphene Thin Films. *Adv. Funct. Mater.* **2009,** *19* (16), 2577-2583.
34. (a) Williams, G.; Seger, B.; Kamat, P. V., TiO2-Graphene Nanocomposites. UV-Assisted Photocatalytic Reduction of Graphene Oxide. *ACS Nano* **2008,** *2* (7), 1487-1491; (b) Matsumoto, Y.; Koinuma, M.; Ida, S.; Hayami, S.; Taniguchi, T.; Hatakeyama, K.; Tateishi, H.; Watanabe, Y.; Amano, S., Photoreaction of Graphene Oxide Nanosheets in Water. *J. Phys. Chem. C* **2011,** *115* (39), 19280-19286.
35. Gómez-Navarro, C.; Weitz, R. T.; Bittner, A. M.; Scolari, M.; Mews, A.; Burghard, M.; Kern, K., Electronic Transport Properties of Individual Chemically Reduced Graphene Oxide Sheets. *Nano Lett.* **2007,** *7* (11), 3499-3503.
36. Hernandez, Y.; Nicolosi, V.; Lotya, M.; Blighe, F. M.; Sun, Z.; De, S.; McGovern, I. T.; Holland, B.; Byrne, M.; Gun'Ko, Y. K.; Boland, J. J.; Niraj, P.; Duesberg, G.; Krishnamurthy, S.; Goodhue, R.; Hutchison, J.; Scardaci, V.; Ferrari, A. C.; Coleman, J. N., High-yield production of graphene by liquid-phase exfoliation of graphite. *Nat Nano* **2008,** *3* (9), 563-568.
37. Wang, J.; Manga, K. K.; Bao, Q.; Loh, K. P., High-Yield Synthesis of Few-Layer Graphene Flakes through Electrochemical Expansion of Graphite in Propylene Carbonate Electrolyte. *J. Am. Chem. Soc.* **2011,** *133* (23), 8888-8891.
38. (a) Parvez, K.; Li, R.; Puniredd, S. R.; Hernandez, Y.; Hinkel, F.; Wang, S.; Feng, X.; Müllen, K., Electrochemically Exfoliated Graphene as Solution-Processable, Highly Conductive Electrodes for Organic Electronics.

*ACS Nano* **2013,** *7* (4), 3598-3606; (b) Parvez, K.; Wu, Z.-S.; Li, R.; Liu, X.; Graf, R.; Feng, X.; Müllen, K., Exfoliation of Graphite into Graphene in Aqueous Solutions of Inorganic Salts. *J. Am. Chem. Soc.* **2014,** *136* (16), 6083-6091; (c) Su, C.-Y.; Lu, A.-Y.; Xu, Y.; Chen, F.-R.; Khlobystov, A. N.; Li, L.-J., High-quality thin graphene films from fast electrochemical exfoliation. *ACS Nano* **2011,** *5* (3), 2332-2339.

39. Ciesielski, A.; Samori, P., Graphene via sonication assisted liquid-phase exfoliation. *Chem. Soc. Rev.* **2014,** *43* (1), 381-98.

40. Cravotto, G.; Cintas, P., Power ultrasound in organic synthesis: moving cavitational chemistry from academia to innovative and large-scale applications. *Chem. Soc. Rev.* **2006,** *35* (2), 180-196.

41. Kolsky, H., *Stress Waves in Solids*. Dover Publications, Inc.: 1963.

42. (a) Yi, M.; Shen, Z., A review on mechanical exfoliation for the scalable production of graphene. *J. Mater. Chem. A* **2015**; (b) Cravotto, G.; Cintas, P., Sonication-Assisted Fabrication and Post-Synthetic Modifications of Graphene-Like Materials. *Chem.–Eur. J.* **2010,** *16* (18), 5246-5259.

43. Hamilton, C. E.; Lomeda, J. R.; Sun, Z.; Tour, J. M.; Barron, A. R., High-Yield Organic Dispersions of Unfunctionalized Graphene. *Nano Lett.* **2009,** *9* (10), 3460-3462.

44. Li, X.; Zhang, G.; Bai, X.; Sun, X.; Wang, X.; Wang, E.; Dai, H., Highly conducting graphene sheets and Langmuir-Blodgett films. *Nat Nano* **2008,** *3* (9), 538-542.

45. Halim, U.; Zheng, C. R.; Chen, Y.; Lin, Z.; Jiang, S.; Cheng, R.; Huang, Y.; Duan, X., A rational design of cosolvent exfoliation of layered materials by directly probing liquid–solid interaction. *Nat Commun* **2013,** *4*.

46. Zhang, X.; Coleman, A. C.; Katsonis, N.; Browne, W. R.; van Wees, B. J.; Feringa, B. L., Dispersion of graphene in ethanol using a simple solvent exchange method. *Chem. Commun.* **2010,** *46* (40), 7539-7541.

47. Lotya, M.; Hernandez, Y.; King, P. J.; Smith, R. J.; Nicolosi, V.; Karlsson, L. S.; Blighe, F. M.; De, S.; Wang, Z.; McGovern, I. T.; Duesberg, G. S.; Coleman, J. N., Liquid Phase Production of Graphene by Exfoliation of Graphite in Surfactant/Water Solutions. *J. Am. Chem. Soc.* **2009,** *131* (10), 3611-3620.

48. Lin, S.; Shih, C.-J.; Strano, M. S.; Blankschtein, D., Molecular Insights into the Surface Morphology, Layering Structure, and Aggregation Kinetics of Surfactant-Stabilized Graphene Dispersions. *J. Am. Chem. Soc.* **2011,** *133* (32), 12810-12823.

49. Smith, R. J.; Lotya, M.; Coleman, J. N., The importance of repulsive potential barriers for the dispersion of graphene using surfactants. *New J. Phys.* **2010,** *12* (12), 125008.

50. Schlierf, A.; Samorì, P.; Palermo, V., Graphene-organic composites for electronics: optical and electronic interactions in vacuum, liquids and thin solid films. *J. Mater. Chem. C* **2014,** *2* (17), 3129-3143.

51. Schlierf, A.; Yang, H.; Gebremedhn, E.; Treossi, E.; Ortolani, L.; Chen, L.; Minoia, A.; Morandi, V.; Samorì, P.; Casiraghi, C.; Beljonne, D.; Palermo, V., Nanoscale insight into the exfoliation mechanism of graphene with organic dyes: effect of charge, dipole and molecular structure. *Nanoscale* **2013,** *5* (10), 4205-4216.

52. Chua, L. L.; Zaumseil, J.; Chang, J. F.; Ou, E. C.; Ho, P. K.; Sirringhaus, H.; Friend, R. H., General observation of n-type field-effect behaviour in organic semiconductors. *Nature* **2005,** *434* (7030), 194-9.

53. Ciesielski, A.; Haar, S.; El Gemayel, M.; Yang, H.; Clough, J.; Melinte, G.; Gobbi, M.; Orgiu, E.; Nardi, M. V.; Ligorio, G.; Palermo, V.; Koch, N.; Ersen, O.; Casiraghi, C.; Samorì, P., Harnessing the Liquid-Phase Exfoliation of Graphene Using Aliphatic Compounds: A Supramolecular Approach. *Angew. Chem. Int. Ed.* **2014,** *53* (39), 10355-10361.

54. Haar, S.; Ciesielski, A.; Clough, J.; Yang, H.; Mazzaro, R.; Richard, F.; Conti, S.; Merstorf, N.; Cecchini, M.; Morandi, V.; Casiraghi, C.; Samorì, P., A Supramolecular Strategy to Leverage the Liquid-Phase Exfoliation of Graphene in the Presence of Surfactants: Unraveling the Role of the Length of Fatty Acids. *Small* **2015,** *11* (14), 1691-1702.

55. Guardia, L.; Fernández-Merino, M. J.; Paredes, J. I.; Solís-Fernández, P.; Villar-Rodil, S.; Martínez-Alonso, A.; Tascón, J. M. D., High-throughput production of pristine graphene in an aqueous dispersion assisted by non-ionic surfactants. *Carbon* **2011,** *49* (5), 1653-1662.

56. Xu, L.; McGraw, J.-W.; Gao, F.; Grundy, M.; Ye, Z.; Gu, Z.; Shepherd, J. L., Production of High-Concentration Graphene Dispersions in Low-Boiling-Point Organic Solvents by Liquid-Phase Noncovalent Exfoliation of Graphite with a Hyperbranched Polyethylene and Formation of Graphene/Ethylene Copolymer Composites. *J. Phys. Chem. C* **2013,** *117* (20), 10730-10742.

57. Lotya, M.; King, P. J.; Khan, U.; De, S.; Coleman, J. N., High-Concentration, Surfactant-Stabilized Graphene Dispersions. *ACS Nano* **2010,** *4* (6), 3155-3162.

58. Blake, P.; Hill, E. W.; Castro Neto, A. H.; Novoselov, K. S.; Jiang, D.; Yang, R.; Booth, T. J.; Geim, A. K., Making graphene visible. *Appl. Phys. Lett.* **2007,** *91* (6), 063124.

59. Yu, V.; Hilke, M., Large contrast enhancement of graphene monolayers by angle detection. *Appl. Phys. Lett.* **2009,** *95* (15), 151904.

60. Wurstbauer, U.; Röling, C.; Wurstbauer, U.; Wegscheider, W.; Vaupel, M.; Thiesen, P. H.; Weiss, D., Imaging ellipsometry of graphene. *Appl. Phys. Lett.* **2010,** *97* (23), 231901.
61. Venkatachalam, D. K.; Parkinson, P.; Ruffell, S.; Elliman, R. G., Rapid, substrate-independent thickness determination of large area graphene layers. *Appl. Phys. Lett.* **2011,** *99* (23), 234106.
62. Cheon, S.; Kihm, K. D.; Park, J. S.; Lee, J. S.; Lee, B. J.; Kim, H.; Hong, B. H., How to optically count graphene layers. *Opt. Lett.* **2012,** *37* (18), 3765-3767.
63. Casiraghi, C.; Hartschuh, A.; Lidorikis, E.; Qian, H.; Harutyunyan, H.; Gokus, T.; Novoselov, K. S.; Ferrari, A. C., Rayleigh Imaging of Graphene and Graphene Layers. *Nano Lett.* **2007,** *7* (9), 2711-2717.
64. Havener, R. W.; Ju, S.-Y.; Brown, L.; Wang, Z.; Wojcik, M.; Ruiz-Vargas, C. S.; Park, J., High-Throughput Graphene Imaging on Arbitrary Substrates with Widefield Raman Spectroscopy. *ACS Nano* **2012,** *6* (1), 373-380.
65. (a) Ferrari, A. C.; Meyer, J. C.; Scardaci, V.; Casiraghi, C.; Lazzeri, M.; Mauri, F.; Piscanec, S.; Jiang, D.; Novoselov, K. S.; Roth, S.; Geim, A. K., Raman Spectrum of Graphene and Graphene Layers. *Phys. Rev. Lett.* **2006,** *97* (18), 187401; (b) Dresselhaus, M. S.; Dresselhaus, G.; Hofmann, M., Raman spectroscopy as a probe of graphene and carbon nanotubes. *Phil. Trans. R. Soc. A* **2008,** *366* (1863), 231-236.
66. Wall, M., The Raman Spectroscopy of Graphene and the Determination of Layer Thickness. ThermoScientific: 2011; Vol. Application Note: 52252.
67. Lucchese, M. M.; Stavale, F.; Ferreira, E. H. M.; Vilani, C.; Moutinho, M. V. O.; Capaz, R. B.; Achete, C. A.; Jorio, A., Quantifying ion-induced defects and Raman relaxation length in graphene. *Carbon* **2010,** *48* (5), 1592-1597.
68. Meyer, J. C.; Geim, A. K.; Katsnelson, M. I.; Novoselov, K. S.; Booth, T. J.; Roth, S., The structure of suspended graphene sheets. *Nature* **2007,** *446* (7131), 60-63.
69. Kouroupis-Agalou, K.; Liscio, A.; Treossi, E.; Ortolani, L.; Morandi, V.; Pugno, N. M.; Palermo, V., Fragmentation and exfoliation of 2-dimensional materials: a statistical approach. *Nanoscale* **2014,** *6* (11), 5926-5933.
70. Huang, H.; Xia, Y.; Tao, X.; Du, J.; Fang, J.; Gan, Y.; Zhang, W., Highly efficient electrolytic exfoliation of graphite into graphene sheets based on Li ions intercalation-expansion-microexplosion mechanism. *J. Mater. Chem.* **2012,** *22* (21), 10452-10456.

# 3. Experimental techniques

In this chapter we will describe briefly the working principle of the principal techniques employed in the experimental work.

## 3.1. Isothermal titration calorimetry

### 3.1.1. Working principle

Isothermal titration calorimetry (ITC) is nowadays one of the most widely used instruments used to study the thermodynamics of chemical interactions in solution. A scheme of a power compensation ITC is reported in **Figure 3.1**.[1]

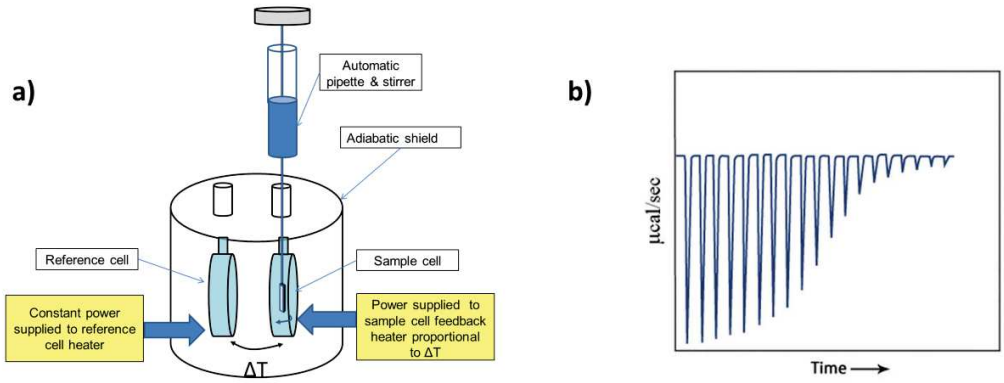


**Figure 3.1 :** a) Representative diagram of a power compensation ITC (reproduced from ref. 2); b) output of an ITC experiment: transfer of heat over time. Each peak corresponds to one injection.

ITC is constituted by two coin shaped cells enclosed in an adiabatic shield, a measurement (sample) cell filled with the solution of one of the reagents (*titrand*) and a reference cell containing the solvent. From a syringe, coaxially inserted in the sample cell, small aliquots of the solution of the second reagent (*titrant*), usually prepared with a concentration 10-20 times higher than the titrand

one, are injected into the sample cell. While the titration experiment occurs, the syringe, which has a paddle shaped end, rotates stirring the cell content.

During the experiment a constant power is always supplied to the reference cell in order to maintain its temperature 0.01°C above the temperature of the insulating jacket. The temperature of the sample cell is instead regulated by a feedback system which modulates the applied thermal power in order to keep the temperature difference between both cells ΔT as low as possible. At any injection of the titrant into the titrand the reaction occurring, causes a release or absorption of heat with a consequent change of temperature which triggers the feedback system to adjust the electrical power in order to maintain the temperature identical in both cells.

The transfer of power per injection is converted into a transfer of heat integrating the transfer of power over time (**Figure 3.1b**). As the reactions approaches completion the transfer of heat diminish reaching a minimum constant value (dilution heat).

The dilution heat of both reagents has to be subtracted from the experiment performing aside dilution experiments. The transfer heat can be converted into a binding isotherm plotting the transfer of heat per amount of titrant injected versus either the volume of titrant injected or the molar ratio titrant/titrand.

From the fitting of the isotherm binding curve with an appropriate model it is possible to extrapolate the binding constant $K_a$, the stoichiometry *n* of the binding process and the standard enthalpy $\Delta H$ per amount of titrant. Moreover using the fundamental equations of thermodynamics:

$$\Delta G = -RT \ln K_a$$

$$\Delta S = \frac{\Delta H}{T} - \frac{\Delta G}{T}$$

where T is the temperature and R is the gas constant, it is possible to calculate the Gibbs energy $\Delta G$ and the entropy $\Delta S$ of the reaction under study.

## 3.1.2. Experimental planning

The main advantage of ITC compared to other analytical techniques such as for example NMR, is to obtain in single experiment accurate values for $K_a$, $\Delta H$, $n$, $\Delta G$ and $\Delta S$, but this is possible only under *optimum conditions*.[2]

In order to extrapolate all this parameters, it is necessary to obtain a correct curvature of the binding isotherm. The curvature in a binding isotherm is defined both from the concentration of the titrate

compound in the cell [M] and the equilibrium constant $K_a$. A key parameter therefore to be estimated, before performing an ITC experiment, is the *Brandt's c parameter*[3] which for a receptor with several non-interacting binding sites corresponds to $c = n\,K[M]$.Usually a *c* value in the range 10-500 allows to obtain an optimal curve, but a careful design of the experiment allows to obtain accurate values of K also for very low values of *c* (*c*<10).[4] In fact *c*>500 results in isotherms which are too steep to determine with accuracy the binding constant $K_a$ (but very good accuracy for $\Delta H$ and *n*), while for *c*<10 shallow titration curves are obtained and it is not possible to determine none of the three parameters (**Figure 3.2**).

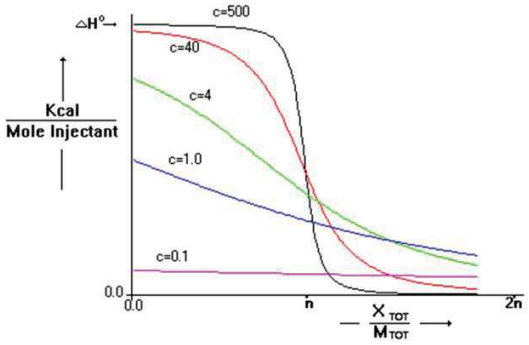


**Figure 3.2 :** Variation of the shape of the isotherm curve with *c.* Reprinted from ref 3b**.**

Once the desired concentrations of the two regents have been determined, care must be taken in solutions preparation.[5] The concentration of the solutions should be as accurate as possible and therefore it is better to prepare ITC solutions by volumetric dilution of stock solution prepared by weight. Moreover, the buffer of the two reagents should be the same to avoid other contributions to the heat measured beside the one of the binding event. It is very important to degas all the solutions before use since air bubbles in the syringe can cause variations in the volume injected or spurious heat signals in the output raw ITC data. In order to eliminate the dilution heats of both titrand $Q_{dil,titrand}$ and titrant $Q_{dil,titrant}$ from the heat measured $Q_{meas}$ in the experiment it is necessary to perform blank experiments. $Q_{dil,titrant}$ is calculated injecting the titrant solution in the sample cell filled with buffer solution, while $Q_{dil,titrand}$ is obtained performing a titration in which the buffer is injected in the sample cell containing the titrand solution. Thus the corrected heat $Q_{corr}$ is:

$$Q_{corr} = Q_{meas} - Q_{dil,titrand} - Q_{dil,titrant}$$

### 3.1.3.Analysing thermodynamic data

In order to fit an ITC isotherm curve first a binding model has to be assumed. The mathematical model is constituted by the equilibrium constant and the conservation of mass, i.e. from the law of mass action.

For example for the simple case of a 1:1 ligand –receptor $X - M$ binding:[6]

$$X + M \Leftrightarrow MX$$

The binding constant is:

$$K = \frac{[MX]}{[M][X]}$$

Knowing that $M_T$ is the total macromolecule bound and unbound:

$$[M_T] = [M] + [MX]$$

and $[X_T]$ the total ligand

$$[X_T] = [X] + [MX]$$

and knowing that the heating released during the experiment $Q$ is correlated to [MX] by:

$$Q = [MX]\Delta HV$$

where $\Delta H$ is the molar enthalpy of binding and $V$ is the volume of the experimental system it is possible to solve for $[MX]$ and to obtain the *Wiseman isotherm:*[7]

$$\frac{dQ}{d[X_T]} = \Delta HV\left(\frac{1}{2} + \frac{1 - X_R - r}{2\sqrt{(1 + X_R + r)^2 - 4X_R}}\right)$$

Where $X_R = [X_T]/[M_T]$ and $r$ is the reciprocal of the $c$ parameter $\frac{1}{r} = c = K[M_T]$. Through an iterative fitting it is possible to estimate *K*, $\Delta H$ and *n.*

In this case the association constant is given by the slope of the sigmoidal curve at the equivalent point, the stoichiometry by the inflection point and the enthalpy of the reaction form the step height of the curve (**Figure 3.3**).

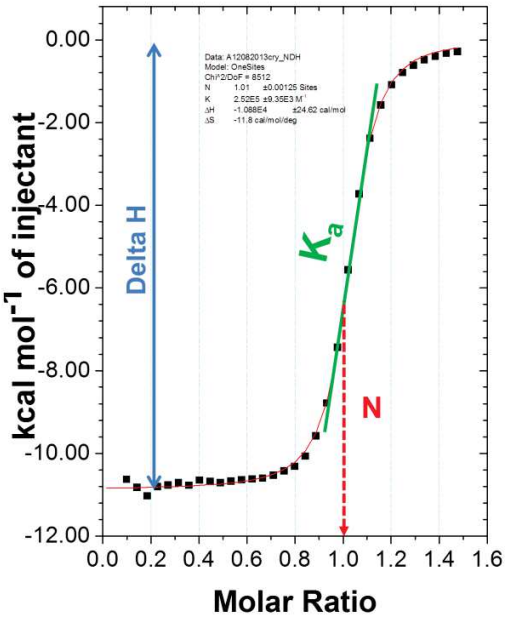


**Figure 3.3 :** Isotherm binding curve for a1:1 binding event

Using the same procedure, it is possible to calculate equations for multiple binding mechanisms, such as multiple sets of independent sites, multiple sets of interacting sites, but at the condition that binding mechanism is known or suspected in advance.

For more complex systems, besides the Wiseman isotherm binding fitting, other methods are possible. One of them consists for example in the use of a binding polynomial. This method represents a model-independent analysis of a binding experiment. In fact it is possible to apply this methodology with systems with one of more binding sites without the need of deciding on any particular binding mechanism in advance.[8] Multiple binding parameters can be determined using software such as HypDeltaH.[9]

In general when multiple binding sites parameters are present it is better to determine some of the parameters by means other techniques (UV-Vis spectroscopy, NMR) and to integrate them in the fitting process.

In chapter 4 we employed a VP-ITC by Microcal® instrument and for the analysis of the data the program built in Origin associated with the instrument and HypDeltaH.[9]

## 3.2. X-Ray Photoelectron Spectroscopy

X-Ray photoelectron spectroscopy (XPS) also known as Electron Spectroscopy for Chemical Analysis (ESCA) is a very powerful technique which gives information about the atomic composition and speciation (i.e. the chemical environment of each atom) of the outer 1-10 nm of any solid substrate. Thus XPS is a *surface* analysis technique that is key for research in fields such as nanomaterials and electronics where the role of the surfaces, interfaces and thin films is crucial.[10]

In XPS experiments the sample is irradiated with a monochromatic X-Ray source and the photons interact with the electrons of the atoms of the sample transferring their energy. If this energy is sufficient the electron will be excited from the core levels of the atom to the vacuum level and will be expelled out of the surface. The kinetic energy of the ejected electrons is then measured (**Figure 3.4**). The Kinetic Energy (K.E.) depends on the irradiating X-Ray energy, while the Binding energy (B.E.) is specific of the chemical element.

K.E. and B.E. are related by the following equation:

$$K.E. = h\nu - \phi - B.E.$$

where *hv* is the photon energy while $\phi$ is the work function of the instrument, a correction factor which takes into account the electrostatic environment in which the electron is generated and measured.

The exact binding energy of an electron depends beside from the level from which the photo emission occurs also from the state of oxidation of the atom and from the local chemical and physical environment.

This will result in in a *chemical shift in the* XPS peak position, whose interpretation can give information about the chemical environment of the atom to which the electron belongs. For example in the case of Silicon (Si), in pure Si wafer, the binding energy of Si2p level amounts to 99 eV, whereas the binding energy of Si2p of Si in $SiO_2$ is 102.3 eV. Usually an increase in oxidation state causes an increase in B.E. due to a decrease in the screening of the bound electron from the ion core.

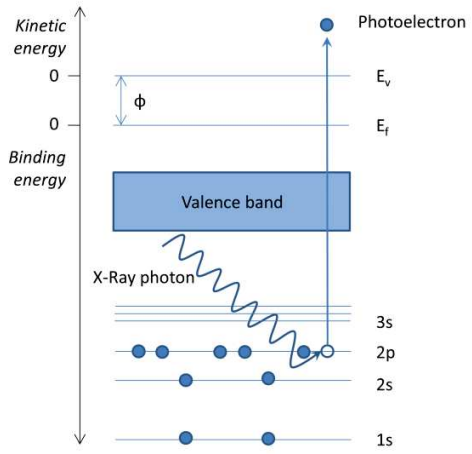


**Figure 3.4:** Schematic diagram of the XPS process, showing the photoionization of an atom by the ejection of a 2p electron

An XPS instrument is generally constituted by an X-Ray Source, an analyser which has the same function of a monochromator and a detection system (**Figure 3.5**). In order to not modify the sample during measurements and to allow the electrode ejected from the surface to reach the detector, the system is under ultrahigh vacuum.

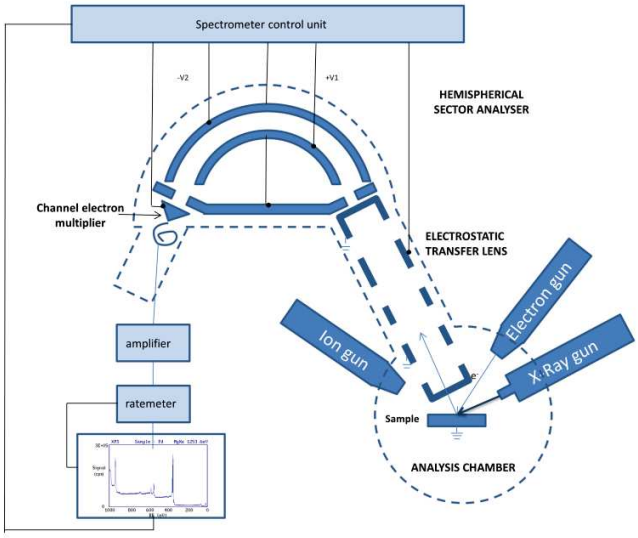


**Figure 3.5**: Schematic representation of an XPS instrument

For all the XPS experiments reported in this thesis a Thermo Scientific K-Alpha X-ray photoelectron spectrometer with a basic chamber pressure of ~$10^{-8}$ mbar and an Al anode as the X-ray source (x-ray radiation of 1486 eV) was used. Spot sizes between 30 µm and 400 µm were employed. Survey spectra are an average of 10 scans with a pass energy of 200.00 eV and a step size of 1 eV. High-resolution spectra are an average of 10 scans (or even 50 or 100 when needed) with a

pass energy of 50.00 eV and a step size of 0.10 or 0.05 eV. The XPS spectra were recorded by Dr. Fanny Richard.

## 3.3. Single point Kelvin Probe

The single point Kelvin probe is an instrument used to measure the workfunction difference, or for nonmetals, the surface potential between a conductive sample and a vibrating tip. The working principle is schematized in **Figure 3.6**.[11] When a contact is made between the tip ad the conducting specimen, the Fermi level of the two will equalize and the consequent flow of electrons from the electrode with lower workfunction to the one with higher workfunction will produce a capacitor with a *contact potential difference* $V_{CPD}$ between the plates. If the tip vibrates a current flowing back and forth between the two electrodes is produced and a variable capacitance is present. Upon application of a *backing potential* $V_b=-V_{CPD}$ the electric field between the two electrodes is nullified. As a result the workfunction difference between the electrodes $\Delta\Phi$ is equivalent to $\Delta\Phi=-eV_{CPD}$.
KP measurement does not give an absolute value of workfunction but always a relative value, therefore a calibration with a sample of known workfunction is necessary.
For our measurements we used a Ambient Single Point Kelvin Probe from KP Technology Ltd. The measurements were performed in collaboration with Thomas Mosciatti.

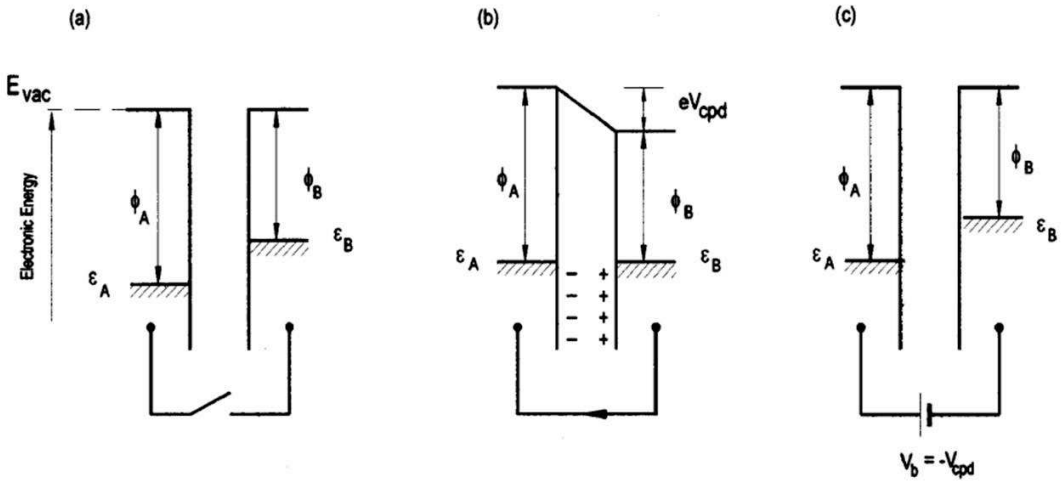


**Figure 3.6:** Working principle of a kelvin probe instrument showing two electrodes A and B a) not in electrical contact, b) in electrical contact, c) with application of a backing potential $V_b$. $\varepsilon_A$ and $\varepsilon_B$ are the Fermi level of the two electrodes, $\Phi_A$ and $\Phi_B$ are the work functions. The other symbol are specified in the text. Image reproduced from ref 11.

## 3.4. Photoelectron yield spectrometer in air (PYSA)

Photoelectron yield spectrometer in air (PYSA) allows the determination of the ionization potential of solid, powder and film samples in air. This instrument thanks to an air-filled counter invented in 1979 by Uda and Kirihata,[12] is able to detect and measure low-energy electrons emitted into air from a solid surface, unlike other techniques, such as ultraviolet photoelectron spectroscopy (UPS), which necessitate of ultra-high vacuum.

A schematic view of the air counter and its working principle are represented in **Figure 3.7**.

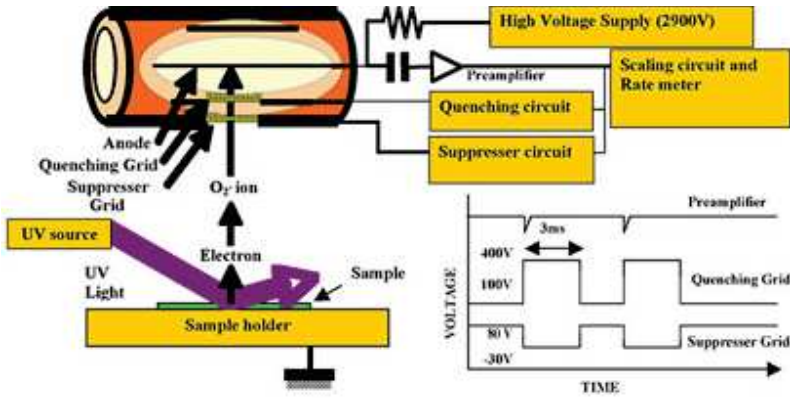


**Figure 3.7:** Scheme of a PYSA and voltage change during quenching time. Image taken from Riken Keiki website.[13]

When the sample, which is grounded, is irradiated with monochromatic UV light, if the energy of the UV photon is higher than the work function of the sample, a photoelectron is emitted from the surface. The electron is accelerated by the suppresser grid, which is kept at +80 V and by the quencher grid kept at +100V. During the drift to the counter, the electron is taken from an $O_2$ molecule forming a $O_2^-$ ion, which is accelerated again when entering in the inner cylinder of the open counter, since the anode is kept at a voltage +2.9 kV. The electron hitting $N_2$ molecules causes an electron avalanche and the formation of $N_2^+$ ions. The electron avalanche causes a reduction in the potential of the anode which is calculated as one electron entering the counter. Then the electron avalanche is quenched by the application for 3 ms of a more positive (+400 V) voltage to the quencher grid which causes a reduction of the electric field around the anode. During this quenching time also the potential of the suppressor grid is swept at negative potential to avoid the positive ions to go to the surface and new $O_2^-$ ions to enter into the counter. Then after the quenching time the initial voltages are restored back to the original value and a new photoelectron can be detected.[14]

For our measurements we employed a Riken Keiki AC-2 spectrometer. The measurements were done in collaboration with Thomas Mosciatti.

## 3.5. Organic field effect transistors

An organic field-effect transistor (OFET) is a three terminal device constituted by a source, a drain and a gate electrode, an active material (organic semiconductor) and a dielectric. An OFET operates like a capacitor where one plate is constituted by the gate electrode and the other plate is the channel between the source and drain electrode. According to the position of the different components, different geometries are possible as shown in **Figure 3.8**.[15]

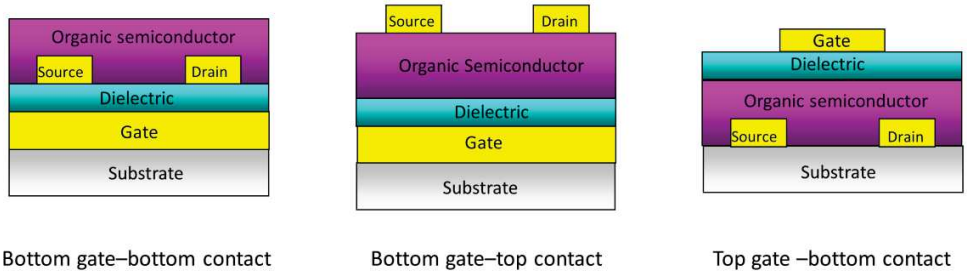


**Figure 3.8:** Different possible configurations of an OFET

The source and drain electrodes are usually high workfunction metals like gold. The gate can be a metal, but often highly doped Silicon is used and the thermally grown or sputtered $SiO_2$ on the top serves as dielectric. Other dielectric employed in OFETs are inorganic insulators ($Al_2O_3$, $Si_3N_4$) or polymeric insulators such as poly(methyl methacrylate) (PMMA) or CYTOP (an amorphous fluoropolymer).

The organic semiconductor can be classified as *n-type* semiconductor or *p-type* semiconductor in the case its HOMO or LUMO levels favor respectively the injection of electrons or holes.

In **Figure 3.9** a schematic representation of the working principle of an OFET and its operating regimes with the associated voltage-current plots are reported.

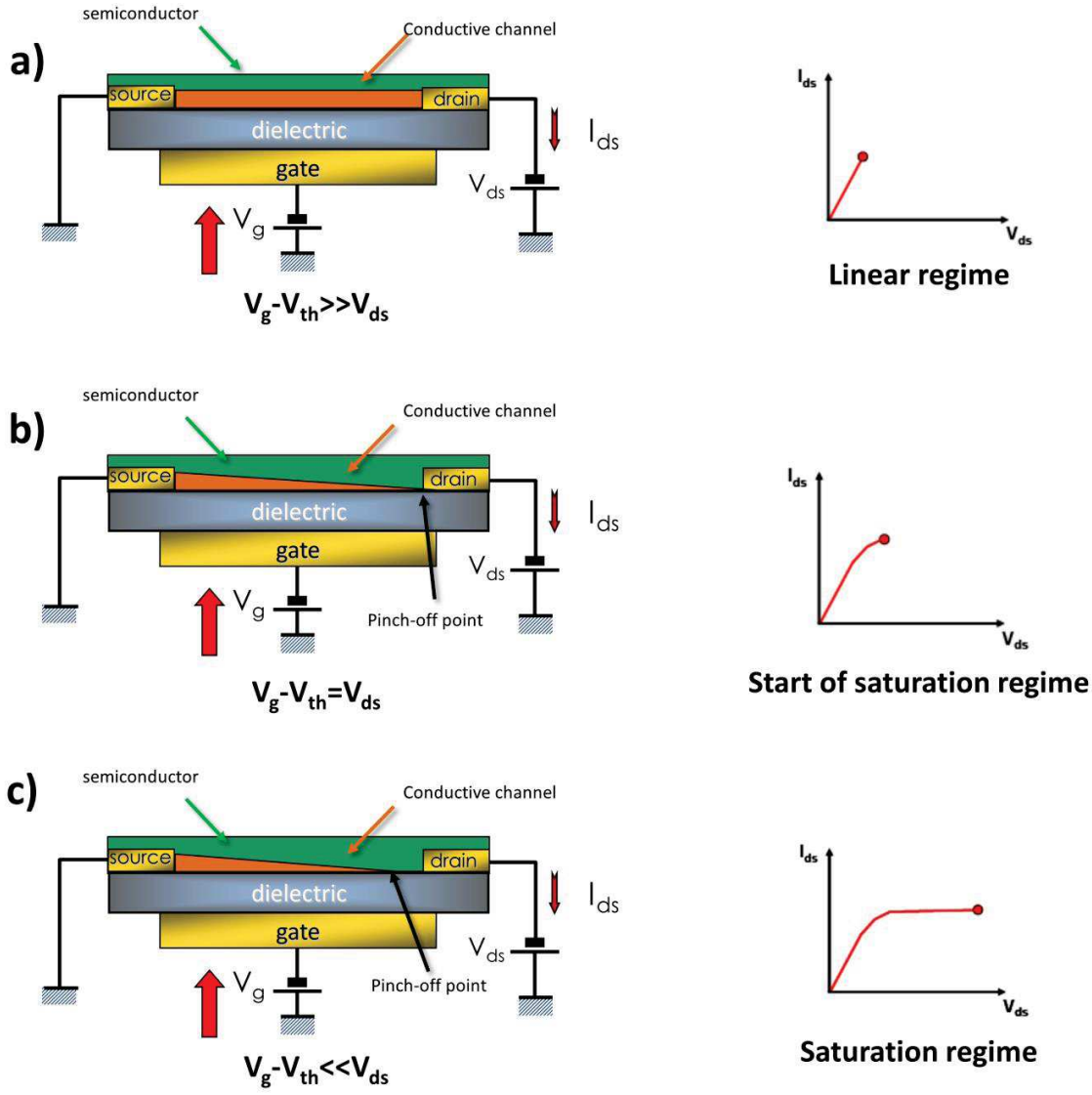


**Figure 3.9:** Operating principle of field effect transistors and correspondent Ids versus Vds current characteristic evolution. a)Linear regime, b) start of saturation regime, c) saturation regime. In the picture a p-type OFET is reported.

When applying a potential between the gate and the source ($V_g$), charges will be induced at the dielectric/semiconductor interface. However, not all of them are potentially *mobile* charges, because shallow traps have to be filled in the organic semiconductor before the conduction can take place. Therefore $V_g$ has to be higher than a threshold Voltage ($V_{th}$) and thus the effective applied gate voltage is $V_g$-$V_{th}$.

When a small source drain voltage ($V_{ds}$<<$V_g$-$V_{th}$) is applied a linear gradient of charge density will form from the injecting source electrode to the drain and the current flowing through the channel

will be proportional to the $V_{ds}$ bias (**Figure 3.9a**).The potential in the channel will also increase linearly from source ($x=0$, $V(x) = 0$) to drain ($x= L$ , $V(x)= V_d$). This is the so called *linear regime* and the $I_{ds}$ current is described by the equation:

$$I_{ds} = \frac{W}{L}\mu_{lin} C_i \left(V_g - V_{th}\right) V_{ds}$$

where $C_i$ is the capacitance of the dielectric, $\mu_{lin}$ is the field effect mobility, $W$ is the channel width and $L$ is the channel wavelength.

Increasing $V_{ds}$ to the point where $V_{ds}=V_g-V_{th}$ the potential at $x=L$ falls to 0 (point of pinch-off creating a depletion region next to the drain electrode (**Figure 3.9b**). At this point a charge space limited current $I_{ds}$ flows from the pinch-off point to the drain.

Increasing the $V_{ds}$ ($V_{ds}>>V_g-V_{th}$) does not lead to a further increase of the current but only to a shift of the pinch-off point towards the source electrode shortening the conductive channel (**Figure 3.9c**). In fact the potential at the pinch-off point remains equal to $V_g-V_{th}$. This is the *saturation regime* and it is described by the equation

$$I_{ds,sat} = \frac{W}{2L}\mu_{sat} C_i \left(V_g - V_{th}\right)^2$$

The typical current voltage characteristics of an OFET are reported in **Figure 3.10**. The output characteristic shows the variation of $I_{ds}$ with respect to $V_{ds}$ at different $V_g$. It is possible to distinguish the linear regime from the saturation regime (**Figure 3.10a**).

The transfer characteristics shown in **Figure 3.10b** and **3.10 c**, respectively in linear and saturation regime, are obtained measuring the $I_{ds}$ current, swapping the $V_g$ at a fixed $V_{ds}$.

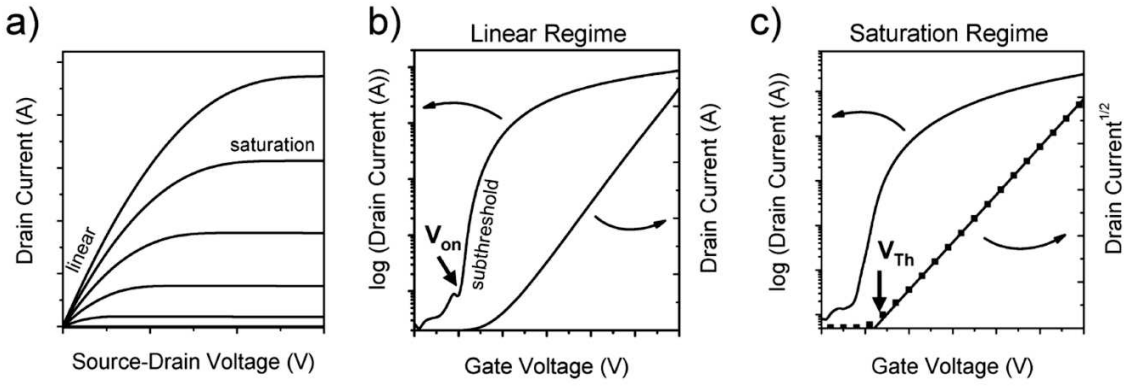


**Figure 3.10:** a) representative example of a) output characteristic, b) transfer characteristic in linear regime ($V_{ds}<<V_g-V_{th}$), c) transfer characteristic in the saturation regime ($V_{ds}>>V_g-V_{th}$). Image taken from ref. 15a.

The parameters, extracted from the transfer characteristics, which represent the figure of merit of OFETs are:

- $\mu$: the field effect mobility $\mu$ is average drift velocity of the charge carrier per applied electric field unit. In the linear regime it can be extracted from the following equation:

$$\mu_{lin} = \left( \frac{\partial I_{ds}}{\partial V_g} \right) \frac{L}{WC_i V_{ds}}$$

  In the saturation regime the mobility can be obtained by the plot of the square root of $I_{ds}$ vs $V_g$ by:

$$\mu_{sat} = \left( \frac{\partial \sqrt{I_{ds}}}{\partial V_g} \right)^2 \frac{2L}{WC_i}$$

- $V_{th}$: the threshold voltage is the minimum voltage to "turn on" the device that is to induce mobile charges in the channel.
- $I_{on}/I_{off}$: The $I_{on}/I_{off}$ ratio is indicative of the commutation performance of the device and is the ratio between the drain current in the on state at a particular $V_g$ and the drain current in the off state.

The preparation and characterization of OFETs reported in chapter 6 was performed in collaboration with Thomas Mosciatti. The electrical characterization was performed with a Keithley 2636A dual channel sourcemeter controlled by its software. The devices were connected to the Keithley by means of a Casacade Microtech M150 probe station using Süss probes with the help of a microscope. All the measurements were performed in nitrogen atmosphere in a Jacomex glovebox.

## 3.6. Raman spectroscopy

Raman spectroscopy[16] is a two-photon inelastic light-scattering event. Light scattered photons usually include mainly Rayleigh scattered light and a minority of Raman scattering. Rayleigh scattering is an elastic scattering which does not involve any loss in energy. The incident photon is momentarily absorbed by a transition from the ground state into a virtual state and a new photon is created by a transition from the virtual state back to the ground state and scattered (**Figure 3.11** in red). The intensity of the Rayleigh scatter is $10^{-3}$ lower than the incident beam. In Raman scattering the scattered photon is created by a transition from the virtual state to the first excited state of the

molecular vibration. The probability of Raman scattering is lower than that of Rayleigh scattering, therefore the intensity is $10^{-6}$ lower than the incident beam. This is an *inelastic scattering* since the molecule after the interaction with the photon will acquire a different vibrational energy and the scattered photon will have a different energy (different wavelength) form the incident photon. There are two different kind of Raman scattering. In the Stoke Raman scattering process (**Figure 3.11**, blue arrows) the molecule is promoted from a ground vibrational state to a higher energy excited vibrational state. The anti-Stokes scattering is due to some molecules which for thermal energy reasons can be present in an excited state as depicted in **Figure 3.11** (green arrows). Scattering from these states to the ground state involves transfer of energy to the scattered photon. Plotting the intensity of this "shifted" light versus frequency results in a Raman spectrum of the sample. Generally, Raman spectra are plotted with respect to the laser frequency such that the Rayleigh band lies at 0 $cm^{-1}$. The band positions of a Raman spectra expressed in $cm^{-1}$ will lie at frequencies that correspond to the energy levels of different functional group vibrations.

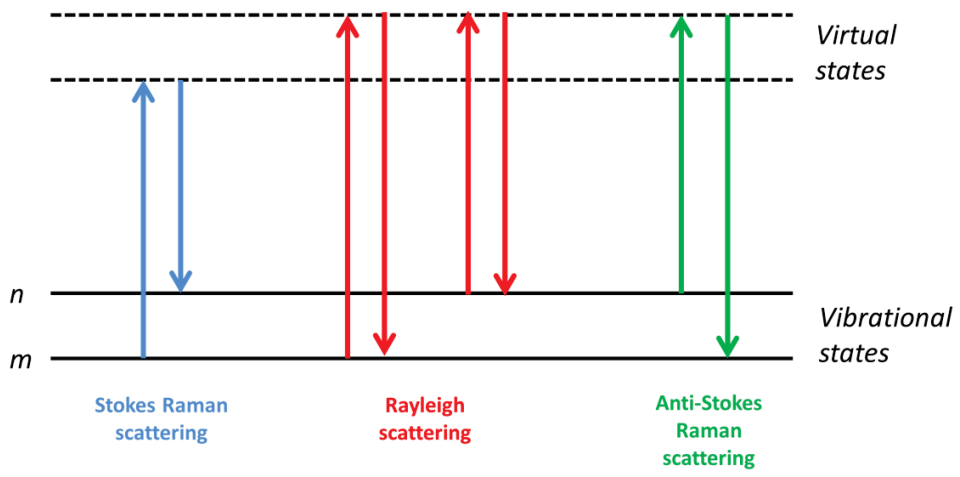


**Figure 3.11 :** schematic representation of different types of scattering

A Raman system is generally constituted by the following major components (**Figure 3.12**):

1. Excitation source (Laser).
2. Sample illumination system and light collection optics.
3. Wavelength selector (Filter or Spectrophotometer).
4. Detector (Photodiode array, CCD or PMT).

The sample under investigation, illuminated by UV, visible or infrared light generates Raman scattered light which is collected, upon elimination of elastic (Rayleigh) scattering by a notch filter, a holographic filter or double/triple spectrometers.

The wavelength selector is constituted by either dispersive spectrophotometers Czerny–Turner (CT) (which can be triple or double and in this case the notch filter is not necessary), or FT (Fourier transform spectroscopy based).Finally the Raman signal is detected by a photodiode array, charge-coupled devices (CCD) or photomultiplier tubes (PMT) in older apparatus.

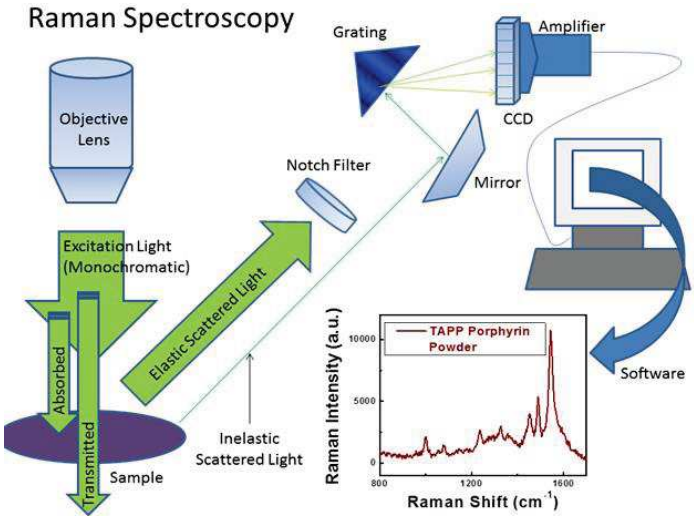


**Figure 3.12:** schematization of an apparatus for Raman spectrosocopy. Reproduced from http://www.chem.umd.edu/sharedinstrumentation/surface-analysis-center/.

In our studies a Renishaw microspectrometer in confocal mode and backscattering geometry with excitation energy of 488 nm, 514.5 nm and 633 nm was used . A Raman microspectrometer consists of a specially designed Raman spectrometer integrated with an optical microscope. With such an instrument the acquisition of spectra of microscopic samples or microscopic areas of larger samples is possible. A 100X objective with a numerical aperture (NA) of 0.95 was used for the characterization. This ensures a small laser spot size of less than 400 nm. The spectral resolution of the spectrometer is 2-3 $cm^{-1}$. The laser power was always below 1 mW to avoid damage. Raman measurements were performed and analyzed by Y. Shin at University of Manchester (group of Dr. Cinzia Casiraghi).

## 3.7. Scanning Electron Microscopy (SEM)

In scanning electron microscopy, a beam of electrons, generated thermoionically by a tungsten filament, with an energy ranging from 0.5 keV to 40 keV, is focused by two condenser lenses. Then the beam passes through scan coils which deflect the beam in the *x* and *y* axes so that it scans in a raster fashion over a rectangular area of the sample surface. Finally the beam goes through an

objective lens which focuses the beam on the surface sample (**Figure 3.13**). When the beam interacts with the sample many events occur which result in different signals generated from the interaction volume (usually the volume interacting with the beam extends from less than 100 nm to around 5 μm into the surface): secondary electrons (SE), back scattered electrons (BSE) and X-Rays. SE are produced when an incident electron excites an electron in the sample which moves towards the surface of the sample undergoing elastic and inelastic collisions until it reaches the surface. The SE can escape if its energy exceeds the surface work function. SE are collected by an electron detector, converted to photons via a scintillator, amplified in a photomultiplier, and converted to electrical signals and used to modulate the intensity of the image on the viewing screen.[17]

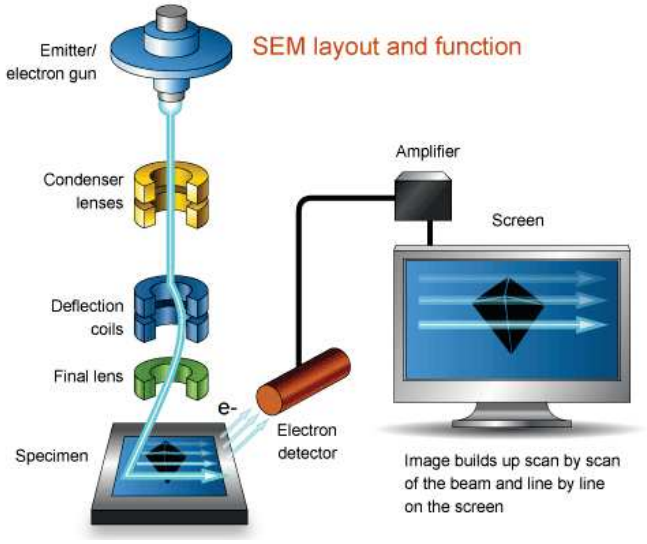


**Figure 3.13:** scheme of a SEM. Reproduced from http://www.ammrf.org.au

BSE are high energy electrons which give information about the atomic composition of the sample. They are produced through an elastic scattering interaction with the atoms in the sample that results in the electron being re-emitted from the specimen, with a large angle scattering (>90°). BSE are detected by a solid state diode mounted below the objective lens pole piece and centered around the optic axis.

X-rays are generated by the removal of an inner shell electron from the sample, causing a higher energy electron to fill the shell and release energy. X-Rays allow to identify the composition and measure the abundance of elements in the sample. X-Rays are collected by a energy dispersive X-Ray detector (EDX). All the system is in vacuum.

The images of the azobenzene crystals and the EDAX analysis were performed by Marco Squillaci with a Quanta FEG 450 (FEI®) system.

## 3.8. Transmission electron microscopy

The transmission electron microscope (TEM) operates with the same principle of a light microscope but, instead of using a light beam, an electron beam generated by thermoionic emission or field emission is employed as probe. A series of condensers allows the variation of the illumination aperture and the area of the sample under illumination. The electrons transmitted from the sample are collected through a lens system onto a fluorescent screen, coupled with an optical fiber to a CCD camera (**Figure 3.14**).[17] The TEM operates under vacuum because electrons are easily scattered at atmospheric pressure.

High-resolution transmission electron microscopy (HRTEM) uses both the transmitted and the scattered beams to create an interference image. HRTEM allows obtaining an image with atomic resolution. It has been extensively employed in the analysis of crystal structures and lattice imperfections in various kinds of advanced materials.

This technique has been used in this thesis work in order to characterize the quality of liquid phase exfoliated graphene. In fact with TEM it is possible to estimate the size of the graphene flakes and with HRTEM it is possible to estimate the thickness and the quality in terms of defects of the sheets.

In the present work High Resolution Transmission Electron Microscopy (HR-TEM) analysis was performed with a JEOL 2100 F microscope working at 200 kV, equipped with a Cs probe corrector and a GATAN Tridiem imaging filter. All the images and the statistical analysis were performed by Georgian Melinte (Institut de Physique et Chimie des Matériaux de Strasbourg (IPCMS)).

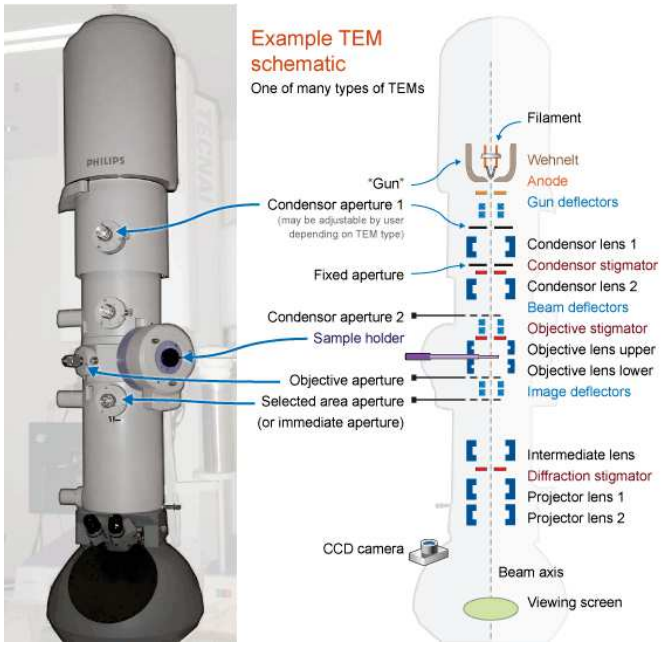


**Figure 3.14:** TEM scheme. Reproduced from Ref. 17.

## 3.9. Thermal desorption spectroscopy

Thermal desorption spectroscopy (TDS)[18] also known as Temperature programmed desorption (TPD) is a technique employed in order to determine kinetic and thermodynamic parameters concerning desorption processes. Molecules previously adsorbed on a particular surface are desorbed applying a programmed temperature rate on the substrate in ultra-high vacuum environment. The partial pressures of atoms and the mass of molecules evolving from the sample are measured by means of an ion gauge and a mass spectrometer (usually a quadrupole mass spectrometer is employed) respectively. The TPD measurement showed in chapter 7 were performed and analyzed by Dr. Artur Böttcher from Karlsruhe Institute of Technology.

## 3.10. References


1. Schmidtchen, F. P., Isothermal Titration Calorimetry in Supramolecular Chemistry. In *Analytical Methods in Supramolecular Chemistry*, Wiley-VCH Verlag GmbH & Co. KGaA: 2007; pp 55-78.
2. Freyer, M. W.; Lewis, E. A., Isothermal Titration Calorimetry: Experimental Design, Data Analysis, and Probing Macromolecule/Ligand Binding and Kinetic Interactions. In *Method Cell Biol.*, Dr. John, J. C.; Dr. H. William Detrich, III, Eds. Academic Press: 2008; Vol. Volume 84, pp 79-113.
3. (a) García-Fuentes, L.; Barón, C.; Quesada-Soriano, I.; Ramiro; Téllez-Sanz, *Thermodynamics of Molecular Recognition by Calorimetry*. INTECH Open Access Publisher: 2011; (b) MicroCal . ITC Data Analysis in Origin ® Tutorial Guide. MicroCal, L. N., MA **2004.**
4. Turnbull, W. B.; Daranas, A. H., On the Value of c: Can Low Affinity Systems Be Studied by Isothermal Titration Calorimetry? *J. Am. Chem. Soc.* **2003,** *125* (48), 14859-14866.
5. Schwarz Frederick, P.; Reinisch, T.; Hinz, H.-J.; Surolia, A., Recommendations on measurement and analysis of results obtained on biological substances using isothermal titration calorimetry (IUPAC Technical Report). In *Pure Appl. Chem.*, 2008; Vol. 80, p 2025.
6. Indyk, L.; Fisher, H. F., [17] Theoretical aspects of isothermal titration calorimetry. In *Methods Enzymol.*, Gary K. Ackers, M. L. J., Ed. Academic Press: 1998; Vol. Volume 295, pp 350-364.
7. Wiseman, T.; Williston, S.; Brandts, J. F.; Lin, L.-N., Rapid measurement of binding constants and heats of binding using a new titration calorimeter. *Anal. Biochem.* **1989,** *179* (1), 131-137.
8. Freire, E.; Schön, A.; Velazquez-Campoy, A., Chapter 5 Isothermal Titration Calorimetry: General Formalism Using Binding Polynomials. In *Methods Enzymol.*, Michael L. Johnson, J. M. H.; Gary, K. A., Eds. Academic Press: 2009; Vol. Volume 455, pp 127-155.
9. Gans, P.; Sabatini, A.; Vacca, A., Simultaneous Calculation of Equilibrium Constants and Standard Formation Enthalpies from Calorimetric Data for Systems with Multiple Equilibria in Solution. *J Solution Chem* **2008,** *37* (4), 467-476.
10. van der Heide, P., *X-ray Photoelectronm Spectroscopy. An Introduction to Principles and Practice*. Wiley: 2012.
11. Baikie, I. D.; Estrup, P. J., Low cost PC based scanning Kelvin probe. *Rev. Sci. Instrum.* **1998,** *69* (11), 3902-3907.
12. Kirihata, H.; Uda, M., Externally quenched air counter for low-energy electron emission measurements. *Rev. Sci. Instrum.* **1981,** *52* (1), 68-70.
13. Epifani, M.; Melissano, E.; Pace, G.; Schioppa, M., Precursors for the combustion synthesis of metal oxides from the sol-gel processing of metal complexes. *J. Eur. Ceram. Soc.* **2007,** *27* (1), 115-123.
14. Noguchi, T.; Nagashima, S.; Uda, M., An electron counting mechanism for the open counter operated in air. *Nuclear Instruments and Methods in Physics Research Section A: Accelerators, Spectrometers, Detectors and Associated Equipment* **1994,** *342* (2–3), 521-526.
15. (a) Zaumseil, J.; Sirringhaus, H., Electron and Ambipolar Transport in Organic Field-Effect Transistors. *Chem. Rev.* **2007,** *107* (4), 1296-1323; (b) Singh, T. B.; Sariciftci, N. S., PROGRESS IN PLASTIC ELECTRONICS DEVICES. *Annu. Rev. Mater. Res.* **2006,** *36* (1), 199-230.
16. Larkin, P. J., *INFRARED AND RAMAN SPECTROSCOPY: PRINCIPLES AND SPECTRAL INTERPRETATION*. Elsevier: 2011.
17. Lavina, S.; Negro, E.; Gliubizzi, R.; Depaoli, G.; Pace, G.; Di Noto, V., New hybrid inorganic-organic complexes based on poly (3-butylthiophene) and titanium tetrachloride: Synthesis, structure and conductivity. *Electrochim. Acta* **2007,** *52* (15), 5062-5070.
18. Schroeder, L. M. S.; Gottfried, M. Temperature-Programmed Desorption (TPD)_Thermal Desorption Spectroscopy (TDS). http://www.chemie.fu-berlin.de/~pcprakt/tds.pdf.

# 4. Complexation of cryptand 2.2.2: a bistable supramolecular switch studied by ITC

## 4.1. Introduction

One among the challenges in supramolecular chemistry[1] and more generally in the chemistry of complex multicomponent systems, is to quantify the contribution of non-covalent interactions to the free energy landscape of a given molecule upon its interaction with a binding partner. Such information is of paramount importance in biology and pharmacology, where the search is for the design of drugs binding to a given target in a reaction and giving a product of optimal stability.[2] Being able to correlate enthalpy and entropy changes to the binding affinity of investigated molecules when interacting with their binding partners can offer a clear picture of structure-energy relationships, which is particularly important for the design of new drugs and of functional supramolecular systems.[3]

The advent of highly sensitive titration micro-calorimeters in the late '80s opened the door to the successful extraction of thermodynamic parameters from simple experiments.[4] Isothermal titration calorimetry (ITC) is now an established and invaluable method for determining with a high degree of precision the thermodynamic parameters, association constants and stoichiometry of molecular interactions at equilibrium in solution.[5] Unlike other methods commonly employed for the characterization of equilibria (e.g. NMR, Raman, electronic absorption and fluorescence spectroscopy), ITC makes it possible to determine simultaneously and with high degree of precision the thermodynamic parameters and stoichiometry of a ligand-receptor interaction in a single experiment by measuring the increments of heat occurring during stepwise titration experiments.[6] ITC enables avoidance of the time consuming process of van 't Hoff analysis based on the

temperature dependence of equilibrium constants otherwise needed to acquire binding constants along with entropy and enthalpy values. As a result, ITC has been widely employed to explore biological systems[7] involving protein-ligand, protein-nucleic acid, and protein-protein interactions as well as to explore "model" systems for protein/metal ion interactions based on transition metal complexes of oligopeptides.[8] It has also been used to unveil supramolecular interactions involved in host-guest binding of a wide variety of synthetic receptors including crown ethers,[9] expanded-[10] and protonated-polyaza-[11] cryptands, cyclodextrins,[12] calixarenes and resorcin[4]arenes/cavitands,[13] cucurbiturils[14] and calixpyrroles,[15] as well as processes leading to oligomerisation or polymerisation *via* H-bonding,[16] and metal-ligand interaction in the field of coordination chemistry.[17] However, much of this work has been carried out in non-aqueous solvents. Surprisingly, only a few calorimetric measurements of any kind have been focussed to well-defined, simple aqueous systems involving assembly of alkali metal ion complexes, although the application of ITC to such a case was considered a useful means to further evaluate the merit of the technique.

This chapter is focused on the thermodynamics of the complexation of potassium ions by 1,10-diaza-4,7,13,16,21,24-hexaoxabicyclo[8.8.8]hexacosane (cryptand[2.2.2]) in aqueous media.

Cryptands, in their simplest form,[18] are synthetic macrobicyclic multidentate ligands that can host, amongst others, alkali and alkaline earth metal cations, usually in the form of 1:1 inclusion complexes. This capacity has recently been used as a "remote control" to trigger the in situ reversible conformational interconversion of oligoheterocyclic strands consisting of alternating pyridine and pyrimidine subunits,[19] as well as the operation of a dynamic switch between different self-assembled forms of guanine.[20] Thus, a detailed understanding of the thermodynamics of the involved reversible complexation reactions is fundamental to the analysis of such systems.

Towards this end we have performed different *in-situ* consecutive experiments, starting with the simple addition of an aqueous solution of potassium chloride to a solution of cryptand[2.2.2], followed by the consecutive addition of an acid and a base to trigger the reversible complexation/decomplexation process with the ultimate goal of monitoring quantitatively by ITC a bistable supramolecular system in action.

Due to differences in the free energy of solvation of the cations in various solvents, the stability of the complexes of [2.2.2] with alkali and alkaline-earth metal cations increases with decreasing solvent polarity.[18, 21] Nonetheless, because of its importance as a reference system, we decided to perform all experiments in water, thus engendering some particular problems associated with the use of a protic solvent. It must be noted that a solution of cryptand [2.2.2] in water is alkaline and that

the hydrolysis reaction involved means that in a dilute aqueous solution of [2.2.2] a significant fraction of the ligand is present in its monoprotonated form. Protonation is of course one means of inhibiting metal cation binding by the cryptand. Thus, in the present work we have defined the optimum conditions for determination of the complexation constant for a ligand which may undergo significant hydrolysis in water.

### 4.1.1.Experimental details

All reagents were purchased from Sigma-Aldrich and were of the highest purity available, and solutions were prepared with Millipore water (Milli-Q). Stock solutions of 4,7,13,16,21,24-hexaoxa-1,10-diazabicyclo[8.8.8]hexacosane (cryptand [2.2.2]), potassium chloride (KCl), hydrochloric acid (HCl) and 1,1,3,3-Tetramethylguanidine (TMG) were prepared in volumetric flasks to give a concentration of 1.0 M and further diluted to give the desired concentrations. KCl was dried by vacuum desiccation prior to use. 1H NMR spectra were recorded and analysed by Dr. Silvia Colella at 295 K using a Bruker Avance 400 spectrometer. The chemical shifts (δ) are given in ppm and the residual solvent peak was used as reference for calibration. Peaks are described as singlet (s), doublet (d), triplet (t), quartet (q), multiplet (m) or broad (b).

Isothermal titration calorimetry experiments were performed using a VP-ITC MicroCal titration calorimeter. Data fitting was performed using the HypΔH program.[22]

All experiments were performed at 298 K using degassed solutions. The concentration of the titrant has to be always at least 10 times higher than that of the titrand because the volume of the calorimetric pipette that contains the titrant is smaller than that of the sample cell. Heats of dilution for all reagents were determined in separate experiments and used to correct the raw ITC data. In all cases, tip diffusion errors required the first and sometimes the second titration points to be discarded.

In consecutive in-situ titration experiments for the second and third titration the concentration of the components present in the cell has to be calculated by taking into account that the VP-ITC works in overfilled mode and the concentrations of the components in the cell changes after every injection from the pipette into the cell (see section 4.5.2 of Appendix 1).

In appendix 1 it is possible to find all details of the experimental conditions used, the NMR experiments performed and the procedure employed in order to calculate the concentration for the consecutive titrations experiments.

## 4.2. Results and discussion

### 4.2.1. Determination of the starting conditions

Self-assembly of the complex $K[2.2.2]^+$ was studied initially as a direct reaction between the two components, that is, $K^+$ and cryptand [2.2.2], and also as a competition between potassium ion and the proton for the cryptand. This was done by firstly measuring the heat changes in the direct reaction of $K^+$ with [2.2.2], treating the resulting solution with a strong acid (HCl) to destroy the complex, and finally treating this solution with a strong base (1,1,3,3-tetramethylguanidine, TMG, p$K_a$ = 13.9[23]) to restore the complex along the path portrayed in **Figure 4.1**. The choice of HCl and TMG was aimed at avoiding further complications in the experiment since, neither chloride nor TMG or its conjugated acid can be included in the protonated cryptand.

The initial titrand was a solution 1.1 mM of cryptand [2.2.2] which was loaded in the sample cell while the titrants for the consecutive experiments were in the order: a solution 22 mM of potassium chloride, a solution 11.5 mM of HCl and a 20 mM solution of TMG.

Fitting of ITC data using the program HypΔH requires the development of a chemical model for the system studied.

While various crystal structure determinations on acid salts of [2.2.2] have shown that in the solid state the proton attached to cryptand-N may be directed *exo* or *endo* with respect to the cavity, in solution it is known that inversion at these centres (in the unprotonated species as well) is fast,[18, 24] so that the assumption was made that [2.2.2], $H[2.2.2]^+$ and $H_2[2.2.2]^{2+}$ could each be treated as a single species for a "slow" technique such as ITC. Since monoprotonation is considered to involve only one of the possible coordination sites of [2.2.2], it is conceivable that the species $KH[2.2.2]^{2+}$ could be formed but $^1$H NMR spectroscopic monitoring of the titration of a solution of $K[2.2.2]^+$ in $D_2O$ with DCl (see section 4.5.3 of appendix) showed that all changes could be accounted for in terms of the spectra of $K[2.2.2]^+$ and the two protonated forms of [2.2.2] only. Hence, the scheme reported in **Figure 4.1** is considered to fully describe the chemistry studied in the present work.

As the auto-ionisation of water is a rather well-studied reaction, literature values for $K_w$ (13.99)[25] and $\Delta H_w$ (13.4 kcal×mol$^{-1}$)[26] at zero ionic strength were incorporated as constants in the models for all systems but small errors may have resulted from the fact that the ionic strength, although low in all cases, did vary (from ~0.0002 – 0.003 M) as a result of the way the titrations were conducted.

Since cryptand protonation-deprotonation reactions were involved in all systems studied, the simple titration of [2.2.2] with HCl was used to provide values of the thermodynamic parameters for the two-protonation steps (the assumption being made that any protonation of ether-O sites could be ignored under the conditions used). The parameters describing the complexation of the potassium ion (logarithm of the stability constant $K_K$ , $LogK_K$, and the thermodynamic parameters) were in fact calculated by maintaining constant all the parameters concerning protonation/deprotonation reactions ($pK_{a1}$, $pK_{a2}$, enthalpies of protonation).

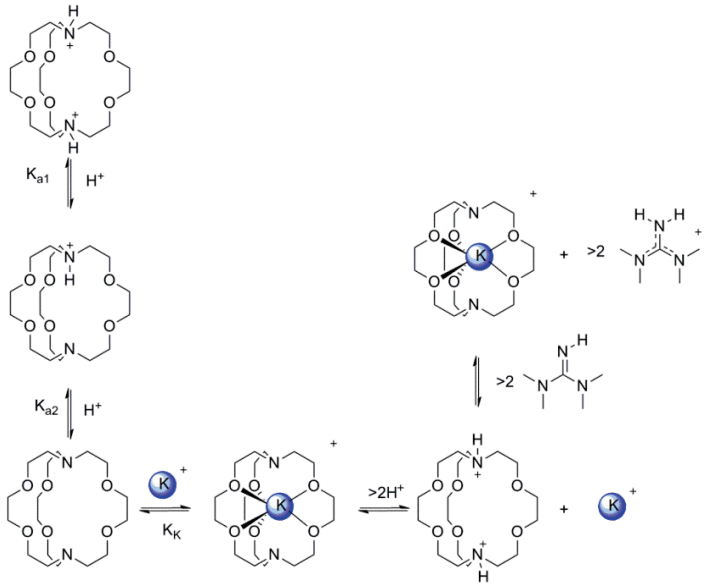


**Figure 4.1:** Stepwise in situ reversible assembly between cryptand[2.2.2] and cryptate K[2.2.2]$^+$. The blue sphere represents $K^+$.

## 4.2.2.Determination of $pK_{a1}$ and $pK_{a2}$

Since acidity constant values determined by ITC were not available, their measurement was made part of the present work to give a consistent data set for the treatment of $K^+$ complexation.

It is important to stress that since cryptand[2.2.2] is a base, its reaction with water has to be taken into account as well as those with $[H_3O]^+$ and $K^+$. Importantly, one of the long-known complications

in ITC analysis is to know the exact nature of the reacting species in solution[27], and thus to assign the observed heat changes to particular events. The complication of strong ion-pairing in weakly polar solvents, for example, has even proven to render some ITC data uninterpretable[28] and this is not the only complication arising in non-aqueous solvents.[15b]

In preliminary experiments 0.5 mM solutions of [2.2.2] were titrated with HCl in order to characterise the two-protonation steps.

The result of this experiment brought up some confusion related to the appearance of ITC end-points after addition of ~0.7 and 2.0 equivalents of acid (see **Figure 4.2**). If the literature values of the acidity constants for [2.2.2][24, 29] are used for a speciation calculation at this concentration, ~60 % of the added [2.2.2] would have been converted into its monoprotonated derivative along with an equivalent amount of hydroxide ion, so that the ITC results can be explained by the dominance initially of heat evolution due to the reaction $H^+ + OH^-$, which would of course reduce the accuracy of the determination of the enthalpy change for the first step of [2.2.2] protonation.

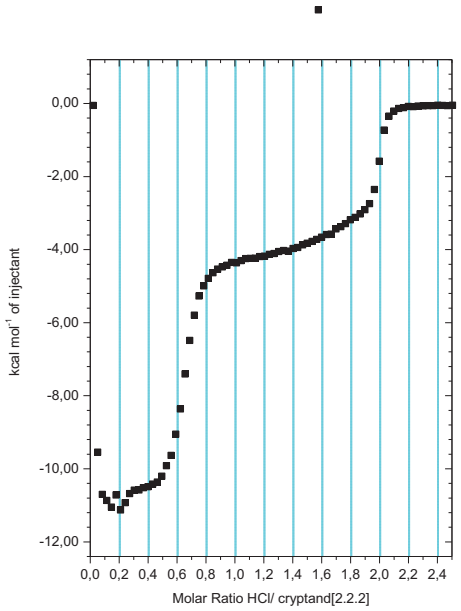


**Figure 4.2:** Isotherm curve for titration of a 0.5 mM solution of cryptand [2.2.2] with a 15 mM solution of HCl

Titrating instead a 1mM solution of cryptand[2.2.2] with a 30.2 mM solution of HCl the enthalpogram showed two apparent end-points at a molar ratio close to 1.0 and 2.0, indicating a negligible influence of the hydrolysis in the initial solutions of cryptand (see **Figure 4.3b**). The

values obtained for the protonation step parameters (**Table 4.1**) compare well with those obtained by other methods,[24, 29] where supporting electrolytes were employed to give an ionic strength of 0.1 M.

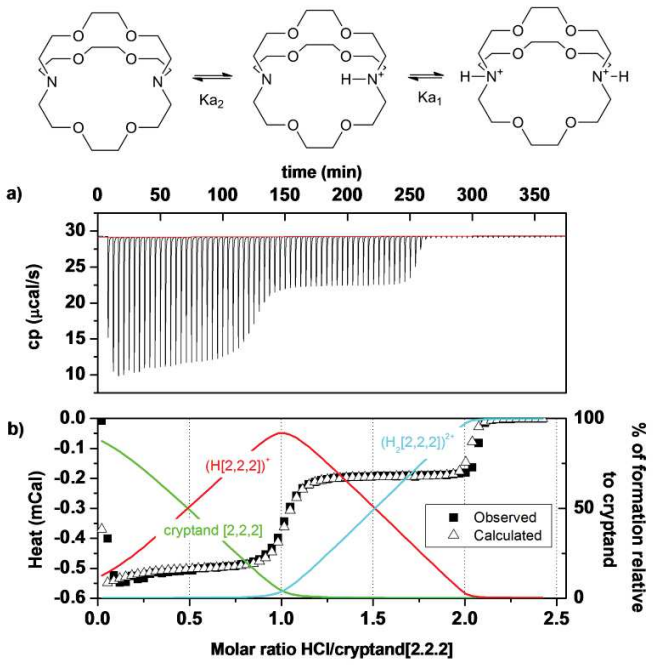


**Figure 4.3**: a) Representative ITC raw data for: interaction of cryptand [2.2.2] and HCl using a cryptand [2.2.2] solution 1.0 mM and HCl solution 30.2 mM; b) on the left Y axes: experimental (■) and calculated (△) heats for each injection; on the right Y axes: speciation curves relative to cryptand[2.2.2] (— free cryptand, — monoprotonated cryptand$(H[2.2.2])^+$, — diprotonated cryptand $(H_2[2.2.2])^{2+}$).

| **Titration** | **$H^+$+[2.2.2]®$(H[2.2.2])^+$** | | | | **$H^+$+$(H[2.2.2])^+$®$(H_2[2.2.2])^{2+}$** | | | |
|---|---|---|---|---|---|---|---|---|
| | $pK_{a2}$ | ΔH° (kcal mol$^{-1}$) | ΔG° (kcal mol$^{-1}$) | ΔS° (cal mol$^{1}$ K$^{-1}$) | $pK_{a1}$ | ΔH° (kcal mol$^{-1}$) | ΔG° (kcal mol$^{-1}$) | ΔS° (cal mol$^{-1}$ K$^{-1}$) |
| **Literature**[21, 29-30] | 9.60 ±0.05[21] | | | | 7.28±0.05[21] | | | |
| | 10.00±0.01[30] | | | | 7.53 ±0.04[30] | | | |
| | 9.71[29] | -10.8[29] | -13.25[29] | 8.2[29] | 7.31[29] | -4.5[29] | -9.95[29] | 18.3[29] |
| **[2.2.2]+HCl** | *9.1±0.4* | *-11.02±0.01* | *-12.41±0.54* | *4.67±1.78* | *6.4 ±0.7* | *-4.27±0.1* | *-8.74±0.95* | *14.94±3.11* |

*- The Gibbs Energy (ΔG°) and entropy (ΔS°) energy have been calculated using the classic thermodynamic equations* $\Delta G^\circ = -RT\ln K$ *and* $\Delta S = \frac{\Delta H^\circ - \Delta G^\circ}{T}$ *The errors are generated by the fitting process of the program HypΔH.*

**Table4.1:** thermodynamic parameters for the protonation of cryptand[2.2.2.] obtained by ITC experiments compared to the one in literature.

Since experiments of protonation of cryptand [2.2.2] at a concentration 1 mM led to ITC end point values close to 1 and 2 equivalents of acid (**Figure 4.3b**), all further experiments were performed at

this concentration. However, this did not completely exclude the effects of ligand hydrolysis (at $10^{-3}$ M, ~20 % conversion to $H[2.2.2]^+$ is still expected and has to be taken into account).

### 4.2.3. Reversible *in-situ* complexation of potassium ions by cryptand [2.2.2.]

After the determination of $pK_{a1}$ and $pK_{a2}$ and their related enthalpy changes, the study of the reversible $K^+$ complexation/decomplexation by cryptand [2.2.2] was performed by *in situ* consecutive experiments, monitoring by ITC the pH modulated switching.

First, the simple complexation of cryptand [2.2.2] with potassium ion in water was executed by titrating with a 20 mM potassium chloride a 1.1 mM cryptand [2.2.2] solution. The raw ITC data and the observed and calculated heat as function of the molar ratio KCl/cryptand are portrayed in **Figure 4.4**. They reveal again that any influence of the cryptand hydrolysis is hidden within the effects arising from the $K^+$ complexation. Here, the cryptand protonation parameters determined from the preceding experiment were used as fixed constants (along with $K_w$ and $\Delta H_w$) in the fitting in order to define the equilibrium constant and enthalpy changes for the potassium complex. While the values obtained (**Table 4.2**) were again in good agreement with literature data (ionic strength 0.05 M or 0.1M),[21, 29, 31] reversal of the initial ligand hydrolysis during the titration had a significant influence on the heat changes and the value found for $K_K$ indicates that at a concentration near $10^{-3}$ M, any dissociation of the complex would be slight.

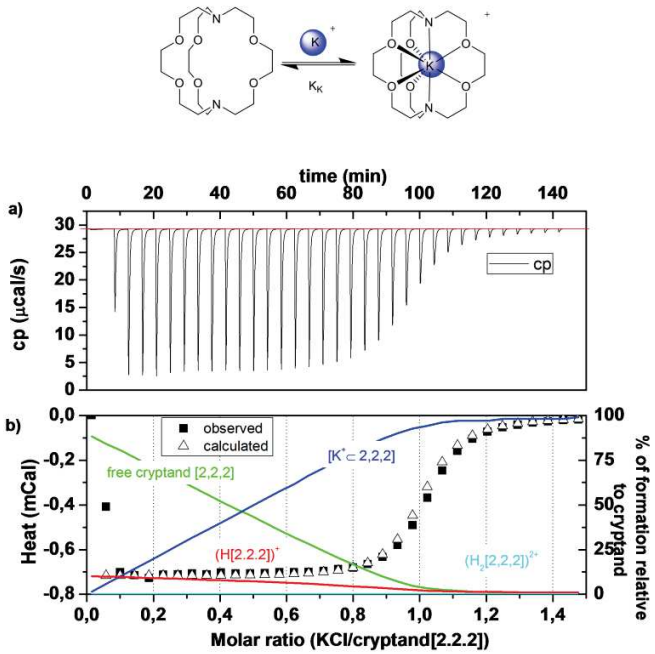


**Figure 4.4**: a) Representative ITC raw data for the interaction of KCl and cryptand [2.2.2] showing 34 consecutive injections of 3 µL; b) on the left Y axes: experimental (■) and calculated (△) heats for each injection; on the right Y axes: speciation curves relative to cryptand[2.2.2] (— cryptate $K[2.2.2]^+$, — free cryptand, — monoprotonated cryptand$(H[2.2.2])^+$, — diprotonated cryptand $(H_2[2.2.2])^{2+}$).

For this reasons a better way to perform the titration could be to add HCl to a solution of the complex. This experiment corresponds to the second *in situ* consecutive titration, carried out by titrating a 11.5 mM solution of HCl into the sample cell containing now all the cryptand in its cryptate form. The protonation of the cryptand causes the displacement of the potassium ion thus affecting in particular the first part of the titration, as it is evident by comparing **Figures 4.3** and **4.5**. Indeed, the results obtained from the deceptively simple raw ITC data curve for this reverse titration keeping all the other parameters as fixed constants (**Figures 4.5**) provides values still within the error bar of the ones reported in literature (see **Table 4.2**).[21]

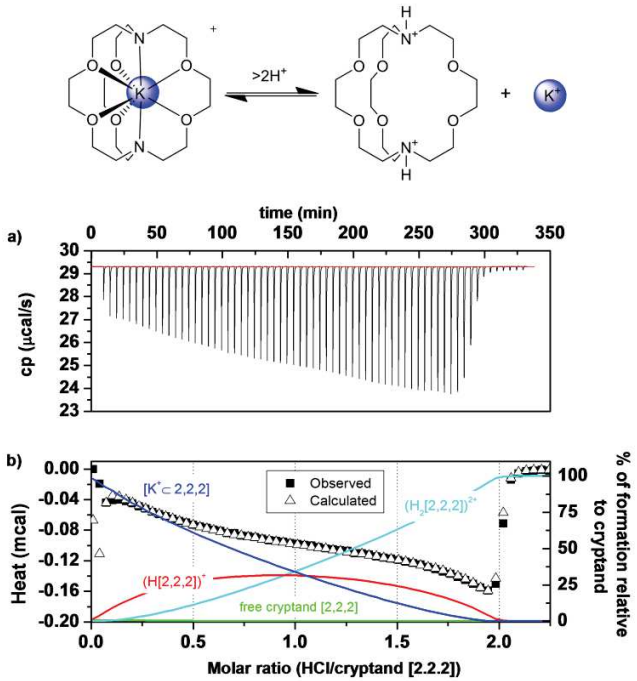


**Figure 4.5**: a) Representative ITC raw data for the interaction of cryptate $K[2.2.2]^+$ and HCl; b) on the left Y axes: experimental (■) and calculated (△) heats for each injection; on the right Y axes: speciation curves relative to cryptand[2.2.2] (— cryptate $K[2.2.2]^+$, — free cryptand, — monoprotonated cryptand$(H[2.2.2])^+$, — diprotonated cryptand $(H_2[2.2.2])^{2+}$.

| **Titration** | **[2.2.2]+KCl®K[2.2.2]$^+$** | | | |
|---|---|---|---|---|
| | $LogK_K$ | ΔH° (kcal mol$^{-1}$) | ΔG° (kcal mol$^{-1}$) | ΔS° (cal mol$^{-1}$ K$^{-1}$) |
| **Literature**[21, 29-30] | 5.4±0.4 [21] | -11.4±0.2[31a] | | -14.1±2[31a] |
| | 5.58[29] | -11[29] | -7.61[29] | -11.5[29] |
| **[2.2.2]+KCl** | *5.5 ±0.1* | *-10.78±0.01* | *-7.50±0.14* | *-11.00±0.48* |
| **K[2.2.2]$^+$ + HCl** | *5.8±0.1* | *-11.06±0.01* | *-7.92±0.14* | *-10.56±0.49* |
| **K$^+$+($H_2$[2.2.2])$^{2+}$ + TMG** | *4.9±0.1* | *-10.43±0.01* | *-6.68±0.14* | -12.55±0.48 |

**Table 4.2** Selected thermodynamic parameters of the *in situ* reversible $H^+$ dependent assembly between cryptand [2.2.2] and $K^+$ :

In order to reassemble the potassium ion complex of the cryptand, *in situ* deprotonation was performed by titrating the $(H_2[2.2.2])^{2+}$ solution in the presence of potassium ions, with a 20 mM solution of TMG. **Figure 4.6** displays (a) the raw ITC data and (b) the observed and calculated step reaction heats. In this case the enthalpogram clearly shows two inflection points. The first inflection point, at a molar ratio base/cryptand of ca. 0.3, corresponds to the reaction of the acid in excess from the previous titration (**Figure 4.5**) on addition of the base.

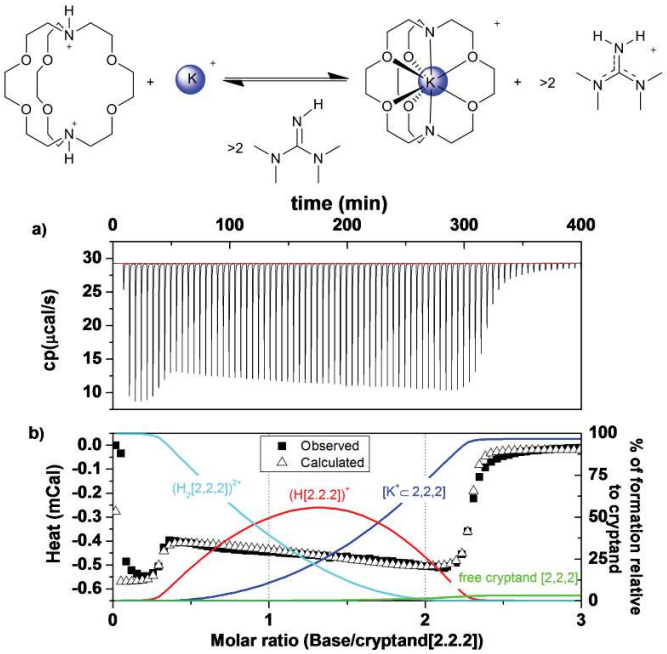


**Figure 4.6:** a) Representative ITC raw data for the deprotonation of the cryptand [2.2.2] in the presence of the potassium cation; b) on the left Y axes: experimental (■) and calculated (△) heats for each injection; on the right Y axes: speciation curves relative to cryptand[2.2.2] (— free cryptand, — monoprotonated cryptand species $(H[2.2.2])^+$, — diprotonated cryptand $(H_2[2.2.2])^{2+}$, — cryptate $K[2.2.2]^+$).

In fact, if we perform the second experiment (**Figure 4.5**) stopping exactly the titration at a molar ratio equivalent to two (to avoid the excess of acid), in this case in the third consecutive titration, the first part of the curve due to the neutralization of the acid with the base is not observed (**Figure 4.7**). The second inflection point at a molar ratio 2.27 is characteristic of the completion of the process of the deprotonation of the second nitrogen atom and inclusion of the potassium ion (see speciation curves in **Figure 4.6b**). Also in this case the curve is not a simple bi-sigmoidal curve because the parallel inclusion of the potassium ion is occurring. While hydrolysis of a solution of [2.2.2] dihydrochloride may be less extensive than that of the free base, titration with alkali rather than acid can involve greater problems of reagent purity.

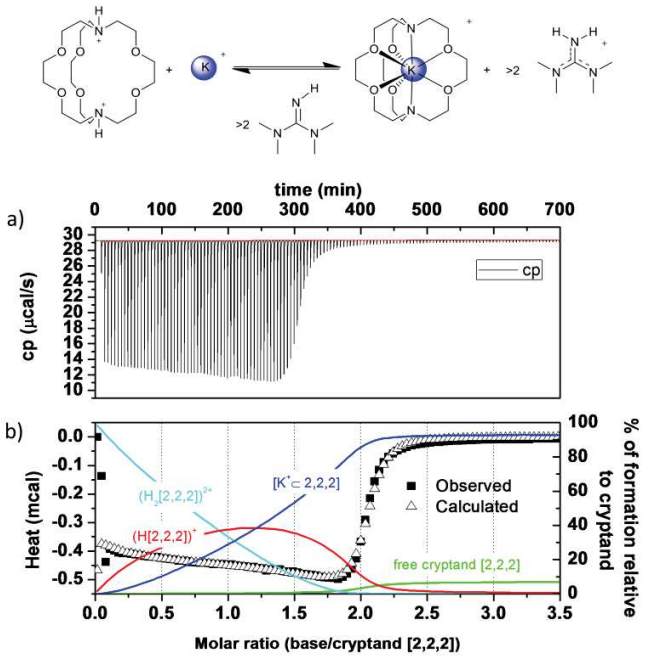


**Figure 4.7:** a) Representative ITC raw data for the deprotonation of the cryptand [2.2.2] in the presence of the potassium cation, starting without an excess of HCl; b) on the left Y axes: experimental (■) and calculated(△)heats for each injection; on the right Y axes: speciation curves relative to cryptand[2.2.2] (— free cryptand, — monoprotonated cryptand species $(H[2.2.2])^+$, — diprotonated cryptand $(H_2[2.2.2])^{2+}$, — cryptate $K[2.2.2]^+$).

The use of a base such as TMG, chosen both to avoid cryptand inclusion reactions and because it is more easily obtained in a pure form than is guanidine itself, illustrates another problem in that additional thermodynamic parameters are required to describe the complete system. For TMG, an approximate $pK_a$ is available[23] but its heat of neutralization is not known, although it is expected to be similar to that of guanidine and thus close to that of $OH^-$.[32] Indeed, the value of the association constant of the potassium ion ($LogK_K$), determined by keeping all the parameters constant except the enthalpy of protonation of TMG and the enthalpy of formation of the cryptate complex, is less accurate than the one found with previous titrations (see **Table 4.2**).

Moreover the value obtained for the heat of neutralisation of TMG is very high (13.91 ± 0.01 $kcal \times mol^{-1}$). We can conclude that the last result is not of great significance in the absence of a precise $pK_a$ value for aqueous media.

## 4.3. Conclusions

We have shown that ITC can be used to monitor the reversible process of complexation/decomplexation in a genuinely bistable supramolecular system in which the pH change is used as a remote control. As a model system we have chosen the complexation of 1,10-diaza-4,7,13,16,21,24-hexaoxabicyclo[8.8.8] hexacosane (cryptand [2.2.2]) by potassium ion. Its decomplexation followed by a recomplexation was triggered by subsequent addition of a strong acid and a strong base, respectively. In all the subsequent titrations it was possible to determine the association constant and the thermodynamic parameters relative to the process of complexation of potassium ion by cryptand [2.2.2]. We emphasize that the protic nature of water as a medium engenders complications in the analysis of equilibria involving the binding of acidic and basic substrates which mean that in the present case a cryptand concentration of at least 1 mM is necessary to obtain optimum precision of the derived thermodynamic parameters.

The results obtained by ITC for the protonation and complexation (by $K^+$) of cryptand [2.2.2] are in agreement with those reported in the literature, based on studies carried out with other techniques. Even though it is known that the precision reached by other methods in the calculation of the stability constant (i.e. potentiometric methods) can be higher, the big advantage of ITC is the possibility to determine all the thermodynamics parameters in a single set of measurements. The separation of enthalpic and entropic contributions to a reaction free energy that is readily obtained by ITC measurements is instrumental for assessing the factors that may influence host-guest recognition. Unfortunately, where only free energies (equilibrium constants) are known, there is a tendency to emphasize influences such as bonding and solvation considered as contributions to an enthalpy change, whereas there are actually many instances where the entropy change dominates that of enthalpy as a contribution to the overall Gibbs free energy.[33] Recognition of this can provide a rather different perspective on the nature of the equilibrium involved. A comparison of the binding of one proton or one potassium ion by [2.2.2] is interesting in that even though the guest binding interactions are rather different, the enthalpy change in the reactions is similar while the entropy change is positive for protonation and negative for $K^+$ binding. The entropy decrease on $K^+$ binding has been ascribed to enhanced solvent structuring about the cation masked by the organic sheath of the cryptand ligand,[18] an argument which implies that $K^+$ binding might be simply enhanced by functionalising the exterior of [2.2.2] with hydrophilic units.

## 4.4. References


1. (a) Lehn, J. M., Supramolecular Chemistry. *Science* **1993,** *260* (5115), 1762-1763; (b) de Greef, T. F. A.; Meijer, E. W., Materials science: Supramolecular polymers. *Nature* **2008,** *453* (7192), 171-173; (c) Desiraju, G. R., Hydrogen bridges in crystal engineering: Interactions without borders. *Acc. Chem. Res.* **2002,** *35* (7), 565-573.
2. Freire, E.; Ruben, A. J.; Kiso, Y., Overcoming roadblocks in lead optimization: A thermodynamic perspective. *Chem Biol Drug Des* **2006,** *67* (1), 2-4.
3. (a) Riley, K. E.; Hobza, P., On the Importance and Origin of Aromatic Interactions in Chemistry and Biodisciplines. *Acc. Chem. Res.* **2012,** *46* (4), 927-936; (b) Asensio, J. L.; Ardá, A.; Cañada, F. J.; Jiménez-Barbero, J., Carbohydrate–Aromatic Interactions. *Acc. Chem. Res.* **2012,** *46* (4), 946-954.
4. (a) Wiseman, T.; Williston, S.; Brandts, J. F.; Lin, L. N., Rapid Measurement of Binding Constants and Heats of Binding Using a New Titration Calorimeter. *Anal Biochem* **1989,** *179* (1), 131-137; (b) Brandts, J. F.; Lin, L. N.; Wiseman, T.; Williston, S.; Yang, C. P., An Instrument for Rapid-Determination of Binding Constants for Biomolecules. *Am Lab* **1990,** *22* (8), 30-41; (c) Wadso, I., Trends in isothermal microcalorimetry. *Chem. Soc. Rev.* **1997,** *26* (2), 79-86.
5. (a) Falconer, R. J.; Collins, B. M., Survey of the year 2009: applications of isothermal titration calorimetry. *J Mol Recognit* **2011,** *24* (1), 1-16; (b) Arranz-Mascaros, P.; Bazzicalupi, C.; Bianchi, A.; Giorgi, C.; Godino-Salido, M. L.; Gutierrez-Valero, M. D.; Lopez-Garzon, R.; Savastano, M., Thermodynamics of Anion-pi Interactions in Aqueous Solution. *J Am Chem Soc* **2013,** *135* (1), 102-105.
6. Schmidtchen, F. P., Isothermal Titration Calorimetry in Supramolecular Chemistry. In *Analytical Methods in Supramolecular Chemistry*, Wiley-VCH Verlag GmbH & Co. KGaA: 2007; pp 55-78.
7. (a) Ball, V.; Maechling, C., Isothermal Microcalorimetry to Investigate Non Specific Interactions in Biophysical Chemistry. *Int J Mol Sci* **2009,** *10* (8), 3283-3315; (b) Ladbury, J.; Haq, I., Drug-DNA recognition: energetics and implications for design. *J Mol Recognit* **2000,** *13* (4), 188-197.
8. (a) Grossoehme, N.; Spuches, A.; Wilcox, D., Application of isothermal titration calorimetry in bioinorganic chemistry. *J Biol Inorg Chem* **2010,** *15* (8), 1183-1191; (b) Hatcher, L. Q.; Hong, L.; Bush, W. D.; Carducci, T.; Simon, J. D., Quantification of the binding constant of copper(II) to the amyloid-beta peptide. *J Phys Chem B* **2008,** *112* (27), 8160-8164; (c) Hong, L. A.; Carducci, T. M.; Bush, W. D.; Dudzik, C. G.; Millhauser, G. L.; Simon, J. D., Quantification of the Binding Properties of Cu2+ to the Amyloid Beta Peptide: Coordination Spheres for Human and Rat Peptides and Implication on Cu2+-Induced Aggregation. *J Phys Chem B* **2010,** *114* (34), 11261-11271.
9. (a) Turnbull, W. B.; Daranas, A. H., On the value of c: Can low affinity systems be studied by isothermal titration calorimetry? *J Am Chem Soc* **2003,** *125* (48), 14859-14866; (b) Rawat, N.; Gujar, R. B.; Murali, M. S.; Tomar, B. S.; Manchanda, V. K., Thermodynamics of complexation of Sr(II) and Ba(II) by 18 crown 6 in water–ethanol binary mixture using titration calorimetry. *Thermochim. Acta* **2009,** *488* (1–2), 21-26; (c) Izatt, R. M.; Bradshaw, J. S.; Nielsen, S. A.; Lamb, J. D.; Christensen, J. J., Thermodynamic and Kinetic Data for Cation Macrocycle Interaction. *Chem Rev* **1985,** *85* (4), 271-339.
10. (a) Pederson, A. M. P.; Ward, E. M.; Schoonover, D. V.; Slebodnick, C.; Gibson, H. W., High-Yielding, Regiospecific Synthesis of cis(4,4 ')-Di(carbomethoxybenzo)-30-crown-10, Its Conversion to a Pyridyl Cryptand and Strong Complexation of 2,2 '- and 4,4 '-Bipyridinium Derivatives. *J Org Chem* **2008,** *73* (22), 9094-9101; (b) Pederson, A. M. P.; Vetor, R. C.; Rouser, M. A.; Huang, F.; Slebodnick, C.; Schoonover, D. V.; Gibson, H. W., A new functional bis(m-phenylene)-32-crown-10-based cryptand host for paraquats. *J Org Chem* **2008,** *73* (14), 5570-5573.
11. (a) Amendola, V.; Alberti, G.; Bergamaschi, G.; Biesuz, R.; Boiocchi, M.; Ferrito, S.; Schmidtchen, F. P., Cavity Effect on Perrhenate Recognition by Polyammonium Cages. *Eur J Inorg Chem* **2012,** (21), 3410-3417; (b) Mateus, P.; Bernier, N.; Delgado, R., Recognition of anions by polyammonium macrocyclic and cryptand receptors: Influence of the dimensionality on the binding behavior. *Coord. Chem. Rev.* **2010,** *254* (15–16), 1726-1747.
12. (a) Inoue, Y.; Rekharsky, M. V., Complexation thermodynamics of cyclodextrins. *Chem Rev* **1998,** *98* (5), 1875-1917; (b) Bouchemal, K.; Mazzaferro, S., How to conduct and interpret ITC experiments accurately for cyclodextrin–guest interactions. *Drug Discovery Today* **2012,** *17* (11–12), 623-629.
13. (a) Danil de Namor, A. F.; Cleverley, R. M.; Zapata-Ormachea, M. L., Thermodynamics of Calixarene Chemistry. *Chem Rev* **1998,** *98* (7), 2495-2526; (b) Hornung, J.; Fankhauser, D.; Shirtcliff, L. D.; Praetorius, A.; Schweizer, W. B.; Diederich, F., Cycloalkane and Alicyclic Heterocycle Complexation by New Switchable Resorcin[4]arene-Based Container Molecules: NMR and ITC Binding Studies. *Chem.-Eur. J.* **2011,** *17* (44), 12362-12371; (c) Corbellini, F.; Di Costanzo, L.; Crego-Calama, M.; Geremia, S.; Reinhoudt, D. N., Guest Encapsulation in a Water-Soluble Molecular Capsule Based on Ionic Interactions. *J Am Chem Soc* **2003,** *125* (33), 9946-9947; (d) Sgarlata,

C.; Bonaccorso, C.; Gulino, F. G.; Zito, V.; Arena, G.; Sciotto, D., Stereochemistry and thermodynamics of the inclusion of aliphatic and aromatic anionic guests in a tetracationic calix[4]arene in acidic and neutral aqueous solutions. *New J Chem* **2009,** *33* (5), 991-997; (e) Dionisio, M.; Oliviero, G.; Menozzi, D.; Federici, S.; Yebeutchou, R. M.; Schmidtchen, F. P.; Dalcanale, E.; Bergese, P., Nanomechanical Recognition of N-Methylammonium Salts. *J Am Chem Soc* **2012,** *134* (4), 2392-2398.

14. (a) Biedermann, F.; Uzunova, V. D.; Scherman, O. A.; Nau, W. M.; De Simone, A., Release of High-Energy Water as an Essential Driving Force for the High-Affinity Binding of Cucurbit[n]urils. *J Am Chem Soc* **2012,** *134* (37), 15318-15323; (b) Biedermann, F.; Vendruscolo, M.; Scherman, O. A.; De Simone, A.; Nau, W. M., Cucurbit[8]uril and Blue-Box: High-Energy Water Release Overwhelms Electrostatic Interactions. *J Am Chem Soc* **2013,** *135* (39), 14879-14888.

15. (a) Sessler, J. L.; Gross, D. E.; Cho, W. S.; Lynch, V. M.; Schmidtchen, F. P.; Bates, G. W.; Light, M. E.; Gale, P. A., Calix[4]pyrrole as a chloride anion receptor: Solvent and countercation effects. *J Am Chem Soc* **2006,** *128* (37), 12281-12288; (b) Valik, M.; Kral, V.; Herdtweck, E.; Schmidtchen, F. P., Sulfoniumcalixpyrrole: the decoration of a calix[4] pyrrole host with positive charges boosts affinity and selectivity of anion binding in DMSO solvent. *New J Chem* **2007,** *31* (5), 703-710.

16. De Greef, T. F. A.; Smulders, M. M. J.; Wolffs, M.; Schenning, A. P. H. J.; Sijbesma, R. P.; Meijer, E. W., Supramolecular Polymerization. *Chem Rev* **2009,** *109* (11), 5687-5754.

17. Ostermeier, M.; Berlin, M. A.; Meudtner, R. M.; Demeshko, S.; Meyer, F.; Limberg, C.; Hecht, S., Complexes of Click-Derived Bistriazolylpyridines: Remarkable Electronic Influence of Remote Substituents on Thermodynamic Stability as well as Electronic and Magnetic Properties. *Chem.-Eur. J.* **2010,** *16* (33), 10202-10213.

18. Lehn, J.-M., Cryptates - Chemistry of Macropolycyclic Inclusion Complexes. *Acc. Chem. Res.* **1978,** *11* (2), 49-57.

19. Barboiu, M.; Lehn, J.-M., Dynamic chemical devices: Modulation of contraction/extension molecular motion by coupled-ion binding/pH change-induced structural switching. *P Natl Acad Sci USA* **2002,** *99* (8), 5201-5206.

20. (a) Spada, G. P.; Pieraccini, S.; Masiero, S.; Pandoli, O.; Samori, P., Reversible interconversion between a supramolecular polymer and a discrete octameric species from a guanosine derivative by dynamic cation binding and release. *Org Lett* **2006,** *8* (14), 3125-3128; (b) Ciesielski, A.; Lena, S.; Masiero, S.; Spada, G. P.; Samori, P., Dynamers at the Solid-Liquid Interface: Controlling the Reversible Assembly/Reassembly Process between Two Highly Ordered Supramolecular Guanine Motifs. *Angew Chem Int Edit* **2010,** *49* (11), 1963-1966.

21. Lehn, J.-M.; Sauvage, J. P., [2]-Cryptates - Stability and Selectivity of Alkali and Alkaline-Earth Macrobicyclic Complexes. *J Am Chem Soc* **1975,** *97* (23), 6700-6707.

22. Gans, P.; Sabatini, A.; Vacca, A., Simultaneous calculation of equilibrium constants and standard formation enthalpies from calorimetric data for systems with multiple equilibria in solution. *J Solution Chem* **2008,** *37* (4), 467-476.

23. Taft, R. W.; Yang, H. B., Concerning contrasting effects of base structure on hydrogen-bonded ion-pair and hydrogen-bonded complex formation. *J Am Chem Soc* **1971,** *93* (5), 1310-1311.

24. Pizer, R., The dynamics of cryptand protonation. *J Am Chem Soc* **1978,** *100* (13), 4239-4241.

25. Bandura, A. V.; Lvov, S. N., The Ionization Constant of Water over Wide Ranges of Temperature and Density. *J. Phys. Chem. Ref. Data* **2006,** *35* (1), 15-30.

26. Grenthe, I.; Ots, H.; Ginstrupp, M., *Acta Chem. Scand.* **1970,** *24*, 1067-1080.

27. Zhang, Y.; Akilesh, S.; Wilcox, D. E., Isothermal titration calorimetry measurements of Ni(II) and Cu(II) binding to His, GlyGlyHis, HisGlyHis, and bovine serum albumin: A critical evaluation. *Inorg Chem* **2000,** *39* (14), 3057-3064.

28. Gross, D. E.; Schmidtchen, F. P.; Antonius, W.; Gale, P. A.; Lynch, V. M.; Sessler, J. L., Cooperative binding of calix[4]pyrrole-anion complexes and alkylammonium cations in halogenated solvents. *Chem.-Eur. J.* **2008,** *14* (26), 7822-7827.

29. Anderegg, G., Thermodynamics of Metal Complexing with Polyoxadiazamacrocyclic Compounds. *Helv Chim Acta* **1975,** *58* (4), 1218-1225.

30. Arnaud-Neu, F.; Spiess, B.; Schwing-Weill, M.-J., Stabilité en solution aqueuse de complexes de métaux lourds avec des ligands diaza-polyoxamacrocycliques. *Helv Chim Acta* **1977,** *60* (8), 2633-2643.

31. (a) Kauffmann, E.; Lehn, J.-M.; Sauvage, J. P., Enthalpy and Entropy of Formation of Alkali and Alkaline-Earth Macrobicyclic Cryptate Complexes. *Helv Chim Acta* **1976,** *59* (4), 1099-1111; (b) Gutknecht, J.; Schneider, H.; Stroka, J., Cryptate Formation in Non-Aqueous Solvents - New Aspects in Single-Ion Thermodynamics. *Inorg Chem* **1978,** *17* (12), 3326-3329.

32. Fabbrizzi, L.; Micheloni, M.; Paoletti, P.; Schwarzenbach, G., Protonation processes of unusual exothermicity. *J Am Chem Soc* **1977,** *99* (17), 5574-5576.

33. (a) Schmidtchen, F. P., Reflections on the construction of anion receptors: Is there a sign to resign from design? *Coord. Chem. Rev.* **2006,** *250* (23–24), 2918-2928; (b) Schmidtchen, F. P., Hosting anions. The energetic perspective. *Chem. Soc. Rev.* **2010,** *39* (10), 3916-3935; (c) Ursu, A.; Schmidtchen, F. P., Selective Host–Guest Binding of Anions without Auxiliary Hydrogen Bonds: Entropy as an Aid to Design. *Angew Chem Int Edit* **2012,** *51* (1), 242-246.

# 4.5. Appendix 1

## 4.5.1. ITC measurements

Isothermal titration calorimetry experiments were performed using a VP-ITC MicroCal titration calorimeter. Data fitting was performed using the HypΔH program[1]. In the following subsections the models and the experimental ITC procedure are reported.

**Cryptand [2.2.2]+HCl**

Solution 0.5 mM of cryptand [2.2.2]

A solution 15.1 mM of HCl in Milli-Q water was degassed in vacuum for 15 minutes and drawn into the calorimeter's pipet. A 0.5 mM solution of cryptand [2.2.2] was degassed in vacuum and loaded into the sample cell. After equilibrating the cell at 25 °C, the pipet was stirred at 307 rpm and the titrant solution added into the sample cell as 1×1.00 μL followed by 72• ×1.50 μL injections every 300 s.

Solution 1 mM of cryptand [2.2.2]

A solution 30.2 mM of HCl in Milli-Q water was degassed in vacuum for 15 minutes and drawn into the calorimeter's pipet. A 0.98 mM solution of cryptand [2.2.2] was degassed in vacuum and loaded into the sample cell. After equilibrating the cell at 25 °C, the pipet was stirred at 307 rpm and the titrant solution added into the sample cell as 1×1.00 μL followed by 72• ×1.50 μL injections every 300 s.

**[2.2.2] + KCl (1$^{st}$ titration)**

In a typical procedure, the calorimeter was rinsed with Milli-Q water prior to use, and the titrand solution (1.100 mM [2.2.2] in Milli-Q water) as well as titrant solution (22.00 mM KCl in Milli-Q water) were degassed in vacuum for 15 min. Degassed Milli-Q water (1.75 mL) was loaded into the reference cell, the titrand solution (1.75 mL) loaded into the sample cell, and the titrant solution drawn into the calorimeter's pipet. After equilibrating the cell at 25°C, the titrant solution was added to the sample cell in 34 consecutive injections of 3.00 μL every 240 s with continuous rotation of the

pipette at 307 rpm.in order to have a homogenous content in the cell. The model used to fit the experimental data set included the presence of monoprotonated and deprotonated form of cryptand [2.2.2].

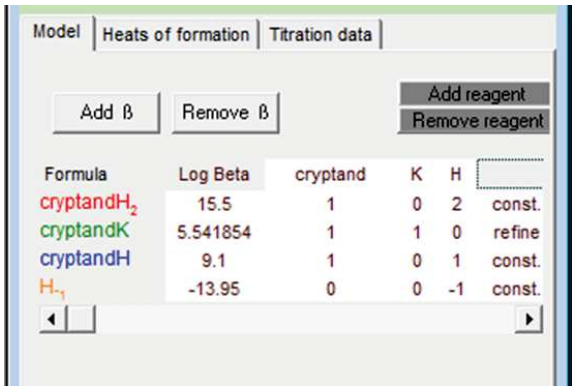


Figure S1: Model used for the fitting in HypDH for the [2.2.2] + KCl (1st titration)

**[K [2.2.2]$^+$]Cl$^-$ + HCl (2nd titration)**

After completion of the KCl addition to [2.2.2], the calorimeter's pipet was cleaned and rinsed with Milli-Q water, while the K([2.2.2])$^+$ cryptate solution was kept in the sample cell after removing the excess volume with a syringe (in order to have always equal volumes in the reference and sample cell). HCl was used to trigger release of $K^+$ by protonation of the cryptate nitrogen atoms. The titrant solution of 11.50 mM HCl was degassed in vacuum for 15 min. and drawn into the calorimeter's pipet. As a consequence of step 1, the formal initial concentration of cryptand in this second experiment was 1.024 mM rather than 1.100 mM. (See Section 4.5.2 below). After equilibrating the cell at 25°C, the pipet was stirred at 307 rpm and the titrant solution was added to the sample cell as 1×1.00 µL followed by 66×4.00 µL injections every 300 s. The model developed using HySS is shown in figure S2.

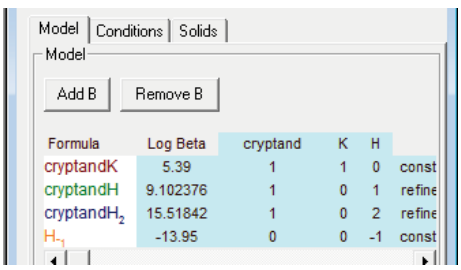


Figure S2: Model used for the fitting in HypDH for the [K([2.2.2])]Cl + HCl (2nd titration):

**$(H_2[2.2.2])^{2+}$ TMG (3rd titration) in presence of $K^+$ ions**

After completion of step 2, the pipet was cleaned and rinsed with Milli-Q water, while the $(H_2[2.2.2])^{2+}$ solution containing potassium ions was kept in the sample cell (from which the excess volume was withdrawn), so allowing re-entry of potassium ions into the cryptand following addition in this third step of tetramethylguanidine to deprotonate the cryptate. The titrant solution (20 mM aqueous tetramethylguanidine) was degassed in vacuum for 15 min. then drawn into the calorimeter's pipet. The formal initial concentration of cryptand was now 0.85mM. After equilibrating the cell at 25°C, the pipet was stirred at 307 rpm and the titrant solution was added into the sample cell as 1×1.00 μL followed by 83×2.00 μL injections every 300 s.

## 4.5.2. Calculation of the concentration in the cell of the reagents for the second and third titration[2]

The VP-ITC microcalorimeter works in an overfilled mode. In fact even though the total volume of the cell is 1.75 ml the working volume *V* is only 1.40 ml, the volume of the coin-shaped part of the cell. When a volume ΔV is injected from the pipette into the cell, since the cell is overfilled, a volume ΔV is displaced from the working volume to the inactive part of the cell. If at the beginning of the titration the initial concentration of cryptand [2.2.2] is $C_0$, after the injection the concentration of the molecules in the working volume decreases to $C_f$ and in the displaced volume ΔV the concentration is an average of the initial concentration $C_0$ and the present concentration $C_f$ in the active volume. Given that the mass of cryptand is constant, the mass balance is given by the equation:

$$C_0 V = C_f V + \frac{1}{2}(C_0 + C_f)\Delta V$$

It follows that:

$$C_f = C_0 \left( \frac{1 - \frac{\Delta V}{2V}}{1 + \frac{\Delta V}{2V}} \right)$$

Using the same assumption, the formal concentration of cryptand, $L_f$, in the cell after each injection can be calculated. If $L_0$ is the concentration of the ligand that we inject and we suppose that everything goes in the working volume, the new concentration $L_f$ will be:

$$L_0V = L_fV + \frac{1}{2}L_f\Delta V$$

$$L_f = L_0\left(\frac{1}{1+\frac{\Delta V}{2V}}\right)$$

### 4.5.3.NMR studies

[2.2.2]

$^1$H-NMR ($D_2O$, δ): 3.65 (t, broad, 12H, -$OCH_2$-), 3.63 (s, 12H, -$CH_2CH_2O$-), 2.83 (t, 12H, J =5.6Hz, -$NCH_2$-).

[2.2.2] + 1eqHCl

$^1$H-NMR ($D_2O$, δ): 3.67 (t, broad, 12H, -$OCH_2$-), 3.64 (s, 12H, -$CH_2CH_2O$-), 2.97 (s, broad, 12H, -$NCH_2$-).

[2.2.2] + 2eqHCl

$^1$H-NMR ($D_2O$, δ): 3.87 (t, 12H, J = 4.8Hz, -$OCH_2$-), 3.74 (s, 12H, -$CH_2CH_2O$-), 3.59 (t, 12H, J =4.8Hz, -$NCH_2$-).

[2.2.2] + 1eqKCl

$^1$H-NMR ($D_2O$, δ): 3.61 (s, 12H, -$CH_2CH_2O$-), 3.56 (t, broad, 12H, -$OCH_2$-), 2.52 (t, broad, 12H, -$NCH_2$-).

[2.2.2] + 1eqKCl + 1eqHCl

$^1$H-NMR ($D_2O$, δ): 3.84 (s, broad), 3.71 (s, broad), 3.60 (s), 3.56 (t), 3.52 (s, broad), 2.52 (t).

[2.2.2] + 1eqKCl + 2eqHCl

$^1$H-NMR ($D_2O$, δ): 3.87 (t, 12H, J = 4.8Hz, -$OCH_2$-), 3.74 (s, 12H, -$CH_2CH_2O$-), 3.59 (t, 12H, J = 4.8Hz, -$NCH_2$-)

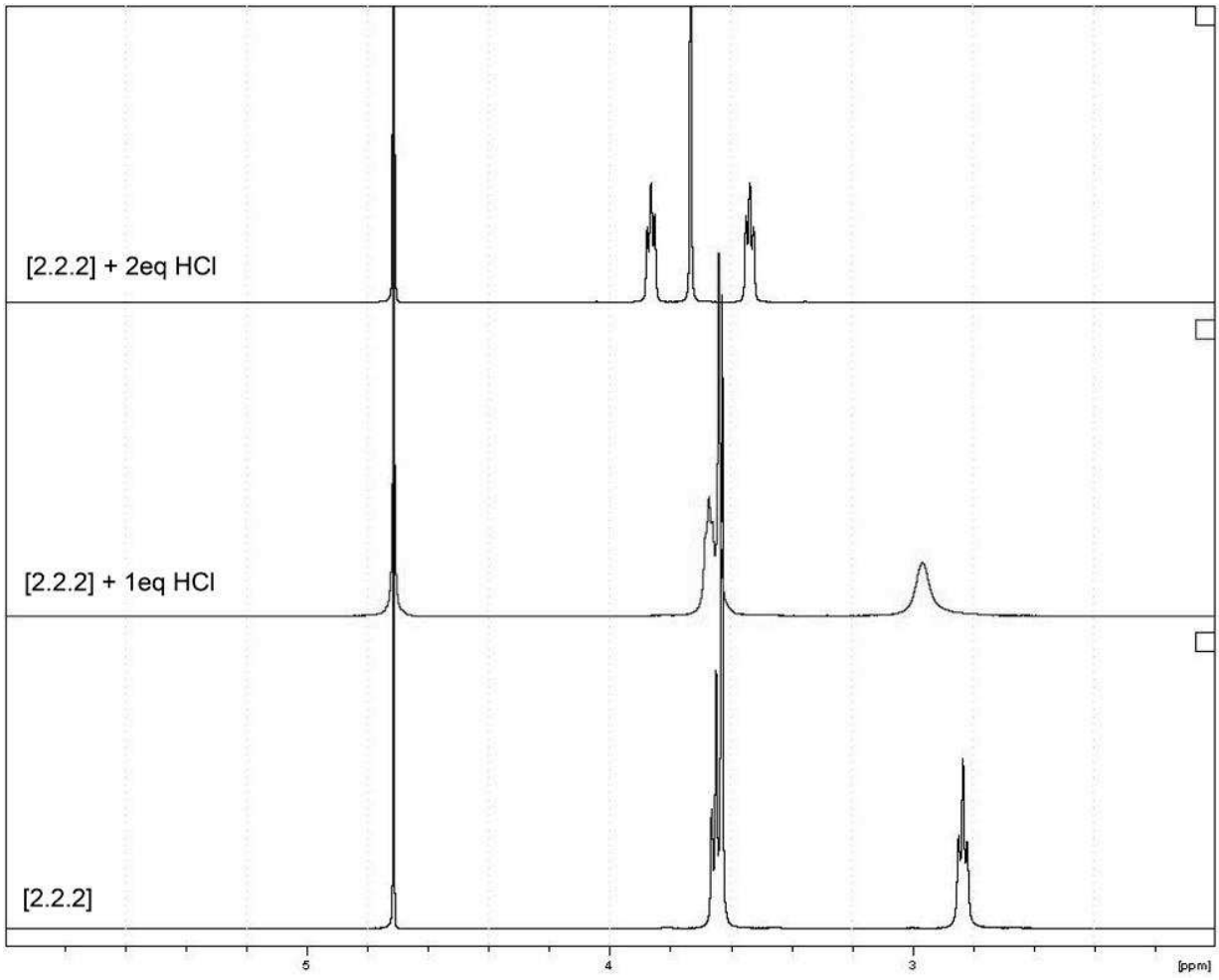
[2.2.2] + 2eq HCl
[2.2.2] + 1eq HCl
[2.2.2]
5
4
3
[ppm]

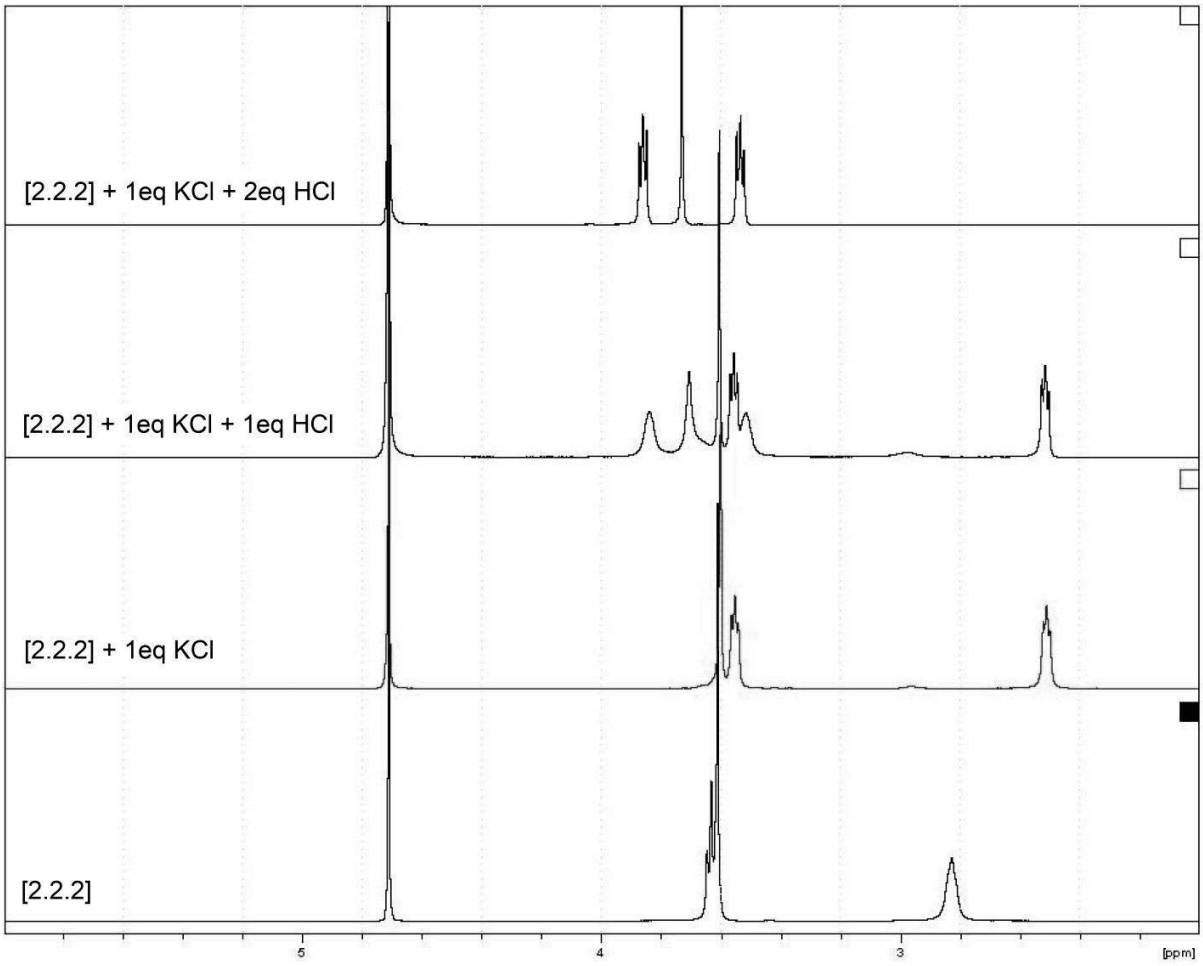


Although, in some of the spectra of mixtures, peak broadening due to exchange is apparent, the only species required to fully explain the spectra are the cryptand, its mono- and di-protonated forms and its potassium ion complex. There is no evidence for a monoprotonated form of the potassium complex.

1. P. Gans, A. Sabatini and A. Vacca, *J Solution Chem*, 2008, **37**, 467-476.

2. *ITC Data Analysis in Origin , Tutorial Guide Microcal*.

# 5. Exploitation of supramolecular interactions for the production of liquid-phase exfoliated graphene

## 5.1. Introduction

Graphene is a two dimensional material possessing unique optical, electrical[1] and mechanical[2] properties. Two approaches are possible for the production of graphene: a *bottom-up* approach starting from smaller building blocks or a *top-down* approach which exploits graphite as starting material.[3] Among the *top-down* approaches, an easily up-scalable one consists of the exfoliation of graphite in liquid media by making use of ultrasonication.[4] The liquid-phase exfoliation (LPE) method is becoming more and more interesting and popular because it is extremely versatile: it can be used to deposit graphene in a variety of environments and on different substrates not accessible using mechanical cleavage or growth methods.[5] The LPE process consists of three stages: *(i)* dispersion of graphite in the chosen solvent, *(ii)* sonication, and *(iii)* purification through centrifugation.[6] Exfoliation of graphite occurs thanks to shear forces and cavitation, acting on the bulk material during ultrasonication.[7] The choice of the solvent is crucial since, after exfoliation, the solvent–graphene interaction needs to balance the attractive forces between graphene sheets.

It has been widely studied and proved that liquid media having surface tension around 40 mJ $m^{-2}$,[4] like N-Methyl-2-pyrrolidone (NMP), are the best choice for exfoliation technique, since they minimize the interfacial energy between the solvent and graphene and thus allowing for the overcoming of the van der Waals forces between adjacent graphene layers. Recently, it has been shown that the addition of small organic molecules and/or polymers,[8] featuring a high affinity for the surface of graphene, during LPE of graphite can harness both the yield of exfoliation and quality of graphene and, in particular cases can confer additional properties to the exfoliated material.[9] In particular in our group it was possible to obtain an improvement in the exfoliation yield and in the percentage of mono- and bilayer graphene flakes produced by addition of simple alkane molecules

such as 1-phenyloctane and arachidic acid.[10] This was possible by mastering the supramolecular approach since it is known that the correspondence between the zig-zag alternation of methylene group of alkanes and the honeycomb structure of graphene leads to a stabilization energy of 64meV for each methylene group.[11]

A deeper study revealed that, by employing fatty acids with different lengths as stabilizing agents during the exfoliation process, the efficiency of the exfoliation in terms of concentration of exfoliated graphene was proportional to the length of the employed fatty acid.[12]

In view of the fact that in a recent computational prediction our collaborators Conti and Cecchini had reported that fully chlorinated compounds could exhibit a greater energy of adsorption on graphene than the respective hydrogenated derivatives,[13] we decided to investigate if the use of perchlorinated molecules as exfoliating agents could further improve the quality of the LPE graphene.

Since long perchlorinated hydrocarbons are unstable at room temperature and ambient pressure and because of this reason in literature only chains up to butane are possible to find,[14] we decided to explore the use of aromatic stabilizing agents. π-π interactions have been already exploited in order to stabilize graphene in aqueous solvents by making use of aromatic molecules bearing amphiphilic moieties.[15]

Therefore in this work we have explored the possibility of taking advantage of π-π interactions to improve the quality and quantity of graphene dispersions. We have employed in particular a coronene molecule, one of the most common polycyclic aromatic hydrocarbon (PAH) [16] and we have investigated how the functionalization of these molecules with chlorine atoms could affect the exfoliation process, improving the interactions with graphene sheets. For this purpose, a perchlorinated coronene synthetized by the group of Prof. K. Müllen (Max Planck Institute, Mainz) has been employed as surfactant in comparison to a simple coronene molecule. The LPE experimental work has been preceded by theoretical calculations performed by the group of Dr. M. Cecchini at I.S.I.S., Strasbourg.

Thermal desorption spectroscopy (TDS) performed by Dr. A. Böttcher, in the group of Prof. Manfred Kappes at the Karlsruhe Institute of Technology (KIT) has been employed to measure experimentally the desorption energy of the molecules from the graphene/graphite surface in order to confirm the theoretical experiments.

## 5.2. Experimental details

Coronene and perchlorinated coronene used for exfoliation were synthetized by the group of Prof. K. Müllen. Graphite powder (product number (p.n.) 332461), *ortho*-dichlorobenzene (*o*-DCB, *p.n.*240664) were acquired from Sigma-Aldrich and used without further treatment.

***Preparation of Graphene by Exfoliation of Graphite:*** Graphite flakes were sonicated for 6 hours in *o*-DCB in presence of the PAHs in a thermostated bath at 40 °C keeping the percentage of graphite flakes always constant (1% weight). At the end of sonication the samples were decanted for 20 min and the upper part of each dispersion was collected and centrifuged for 30 min at 5000 rpm, 15 min at 8000 rpm and finally 15 min at 10000 rpm (Eppendorf 5804, rotor F-34-6-38) obtaining homogeneous dispersions.

***Characterization of LPE graphene:*** The dispersions and the starting solutions of PAHs were characterized by UV-Vis absorption and fluorescence spectroscopy using a Jasco V670 spectrophotometer and a Jobyn Hivon Horiba Fluorolog®-3 employing microquartz cuvette in order to decrease the optical pathway and avoid inner filter effects. For dilutions experiments cuvettes with 1 cm optical pathway were used.

High Resolution Transmission Electron Microscopy (HR-TEM) analysis was performed with a JEOL 2100 F microscope working at 200 kV, equipped with a Cs probe corrector and a GATAN Tridiem imaging filter by G. Melinte member of Prof. O. Ersen group (Institut de Physique et Chimie des Matériaux de Strasbourg (IPCMS)). For the analyses, for each sample, a drop of graphene dispersion was deposited on a TEM grid covered by a lacey carbon membrane. The as-prepared grids were kept overnight under high vacuum to allow the evaporation of the solvent.

Micro Raman measurements were carried out with a Witec spectrometer in confocal mode and backscattering geometry with excitation energy of 488 nm, 514.5 nm and 633 nm. A 100X objective with a NA of 0.95 was used for the characterization. This ensures a small laser spot size of around 400 nm. The spectral resolution of the spectrometer amounts to 2–3 $cm^{-1}$. The laser power was well below 1 mW to avoid damage. Around 50 flakes drop-cast on a silicon substrates were analyzed and the shape of the 2D peak and intensity (as height) ratio between D and G peak, I(D)/I(G) were analyzed. In particular, the 2D peak was fitted with a Lorentzian lineshape and the coefficient of determination, R2, was used to discriminate between 1 layer (symmetric peak) and restacked or thin layers (asymmetric 2D peak). This allows deriving qualitative information on the thickness

distribution and the amount of defects. The Raman characterization was carried out by Y. Shin at the Nanoscience and Spectroscopy Lab of Dr. C. Casiraghi at University of Manchester.

The concentration of the dispersions was determined by heating the graphene dispersion previously mixed with chloroform at 50°C in order to desorb the molecules from the graphene sheets and filtering the mixture through a polytetrafluoroethylene (PTFE) membrane with 0.1μm pore size.

***Theoretical calculations:*** Modeling was performed to study in which extend the chlorination of polycyclic aromatic hydrocarbons improves the affinity for graphene. The adsorption energy for graphene of hydrogenated and PAHs was evaluated using a force field model of interactions.[17] The atom typing of hydrogenated and perchlorinated PAHs was performed via the ParamChem Web server (version 0.9.7),[18] which generates parameters for CGenFF version 2b8.[17] The graphene substrate was modeled using a squared 610 carbons polyaromatic molecule with dangling hydrogens. The carbon atoms of graphene were parameterized using the atom type CG2R61 (aromatic carbon) with zero charge if internal and −0.115 e.u. on the edge. Hydrogens were parameterized with the atom type HGR61 (aromatic hydrogen) with a partial charge of +0.115 e.u.. For the calculation of the desorption energy, the adsorbate in complex with the substrate was energy minimized by 1000steps of the steepest descent (SD) followed by an adopted basis Newton−Raphson (ABNR) optimization until convergence to an energy gradient of 10−8 kcal $mol^{-1}$ $Å^{-1}$. All calculations were performed using the CHARMM software.[19]

***Thermal desorption spectroscopy:*** Thermal desorption of coronene and perchlorocoronene from freshly cleaved HOPG was studied by temperature resolved mass spectrometry (quadrupole mass spectrometer, Extrel, 70 eV electron impact ionization, typical mass resolution $m/\Delta m \sim 300$). For this, the flux of desorbed species was monitored while linearly increasing the sample temperature at a constant heating rate ($\beta$ = 2.5 K $s^{-1}$). TDS measurements were performed and analyzed by Dr. A. Böttcher, in the group of Prof. Manfred Kappes at the Karlsruhe Institute of Technology (KIT).

## 5.3. Results and discussion

### 5.3.1.Theoretical calculations

Müllen and coworkers recently showed a general protocol for the controlled edge chlorination of nanographenes (i.e.PAHs) and graphene nanoribbons[20]. The chlorination confers to these materials a

high degree of solubility with respect to hydrogen terminated ones.[21] Moreover, the control over the size and the precise control on the chlorination allow the tuning of the optical band gap making these materials appealing for organic electronic applications. It had been computationally predicted by Conti and Cecchini[13] that the halogenation of alkyl chains and benzene should increase the affinity of the molecules for graphene, due to a larger polarizability of halogens compared to carbon. Moreover the adsorption energy of the molecules should increase with the increasing number of halogenated atoms present in the molecule. For this reason similar calculations were performed by Conti on the molecules reported in Müllen's paper and on perchlorocoronene. In **Figure 5.1** the chemical structures of the investigated PAHs are shown.

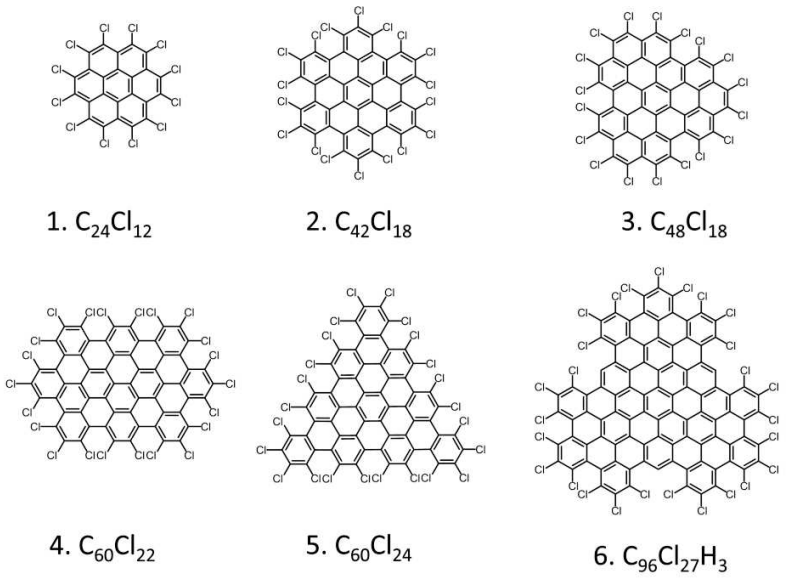


**Figure 5.1 :** Perchlorocoronene and chlorinated nanographene reproduced from reference [20].

In **Table 5.1** the calculated adsorption energies of the chlorinated PAHs on graphene compared to their hydrogenated counterparts are reported.

| Molecule | Chemical formula | $E_{ads}$ hydrogenated (kcal mol$^{-1}$) | $E_{ads}$ Chlorinated (kcal mol$^{-1}$) | $\Delta E_{ads}$ (kcal mol$^{-1}$) |
|---|---|---|---|---|
| **1** | $C_{24}Cl_{12}$ | -36.1 | -45.2 | -9.1 |
| **2** | $C_{42}Cl_{18}$ | -61.6 | -56.2 | 5.3 |
| **3** | $C_{48}Cl_{18}$ | -69.3 | -78.0 | -8.8 |
| **4** | $C_{60}Cl_{22}$ | -86.5 | -89.4<br>-76.8 | -2.8<br>9.7 |
| **5** | $C_{60}Cl_{24}$ | -87.4 | -84.2 | 3.2 |
| **6** | $C_{96}Cl_{27}H_3$ | -136.0 | -133.3 | 2.7 |

**Table 5.1 :** Calculated adsorption energy for the chlorinated nanographenes reported in figure 5.1 and the corresponding hydrogenated molecules. The difference in adsorption energy between hydrogenated and chlorinated compounds is reported in the last column. Negative values of $\Delta E_{ads}$ imply an increase in adsorption energy. For molecule 4 different adsorption energy correspond to different geometries of the adsorbate.

Plotting the adsorption energy of the molecules as a function of the number of carbons present in the molecules, as shown in **Figure 5.2**, it was clear that, while for the hydrogenated molecules there was a linear correlation between the adsorption energy and the size, this was not the case for chlorinated molecules. Moreover, only in two out of six cases (molecules **1** and **3**) the adsorption energy of PAHs was significantly increased by the functionalization with chlorinated atoms.

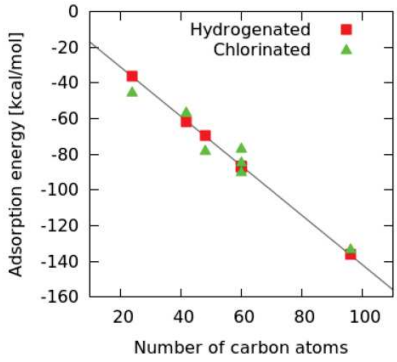


**Figure 5.2 :** Energy of adsorption of hydrogenated (red) and chlorinated (green) nanographenes as function of number of carbon (i.e. size). The adsorption energy of hydrogenated nanographenes on graphene increases linearly with increasing of the molecule size.

The cause for this was found in the crystal structure of the PAHs. In fact, as reported by Müllen,[20] for some of the molecules (molecule **2**, **5** and **6**) a high level of distortion from planarity has been observed. The geometries of perchlorocoronene and molecule **2** adsorbing on graphene are reported in **Figure 5.3**. The strong deviation from planarity of molecule **2** (**Figure 5.3b**) is responsible for the decrease in binding affinity for graphene compared to the correspondent fully planar hydrogenated compound.

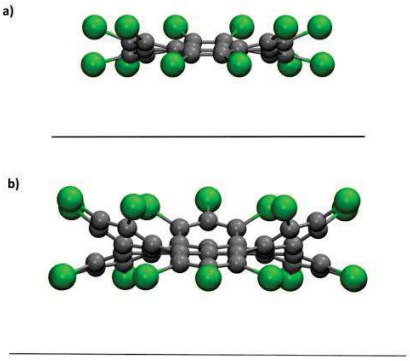


**Figure 5.3 :** Side-view of the optimized geometries for the adsorption of a) coronene and b) molecule 2 ($C_{42}Cl_{18}$) on graphene (represented with a grey line). The green spheres represent the chlorine atoms while the grey spheres represent the carbon atoms.

The distortion is induced by the accommodation of the chlorine atoms in the molecules. While for molecules **1** and **3** the chlorine are equally distributed at the edges (**Figure 5.4a**) severe steric hindrance of the inner chlorine atoms for molecules **2**, **5** and **6** (**Figure 5.4b**) forces the outer benzene rings of the carbon framework to flip up and down in an alternating manner with a stronger distortion.

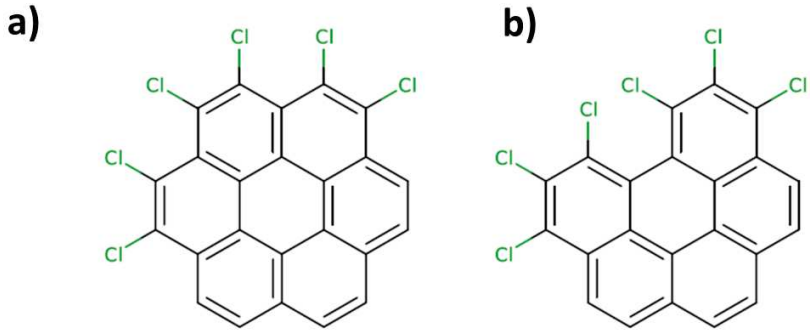


**Figure 5.4 :** Different arrangement of chlorine atom at the edges of PAHs. a) Arrangement typical for a perchlorocoronene and molecule 3; b) arrangement for chlorine atoms typical of molecule 2, 4, 5 and 6.

In the case of perchlorocoronene, the molecule is only slightly distorted thus, allowing still a good interaction of the core of the molecule and of the chlorine atoms with graphene. It was observed that the adsorption energy of perchlorocoronene on graphene was higher than the one calculated for hydrogenated coronene. The main contribution to this interaction was find to be the *polarizability* of chlorine respect to carbon which should enhance the strength of the dispersion interactions with graphene.[22]

We decided to employ perchlorocoronene and coronene as exfoliating agents in order to find out if the difference in adsorption energy on graphene could be translated in a difference in the quality and quantity of the exfoliation outcome. Among all the chlorinated/hydrogenated pairs studied, we specifically chose this couple in view of the higher solubility of this molecule due to the small size.

## 5.3.2. Exfoliation

To test the effective improvement given by the presence of coronene and perchlorocoronene in the exfoliation process, we prepared LPE dispersions by adding in a vial graphite powder in *orto*-dichlorobenzene (*o*-DCB) solvent in presence of the two PAHs. o-DCB was chosen due to the good solubility of both coronene and perchlorocoronene in this solvent. Moreover blank experiments, i.e. dispersions prepared in absence of surfactants were performed. The calculation of the approximate amount of molecules to add for the exfoliation was made on the assumption that graphite powder is a single rectangular graphene sheet with area $S_{graphene}$. Scanning tunneling microscopy (STM) studies were reported in literature[23] on the coronene self-assembly on highly oriented pyrolytic graphite (HOPG) revealing that this molecules adopt a supramolecular structure characterized by a 6-fold geometry and the area occupied by each coronene molecule $A_{stabilizer}$ is 1.09±0.19 nm$^2$. From this we calculated the mass of molecules $M_{intercal.}$ necessary to form a densely packed monolayer on graphene as:

$$M_{intercal.} = \left( \frac{\left( \frac{S_{graphene}}{A_{stabilizer}} \right)}{N_A} \right) \times Mw_{stabilizer}$$

where:

$$S_{graphene} = G_{unit\ cell} \times \left( \frac{M_{graphite\ powder} \times N_A}{2 \times M_{C\ atom}} \right) \times 2$$

being $G_{unit\ cell}$=0.052±0.004 nm$^2$ the unit cell of graphene, $M_{C\ atom}$ the mass of carbon, $Mw_{stabilizer}$ the molecular weight of the coronene and perchlorocoronene, $M_{graphite\ powder}$ the mass of graphite and $N_A$ the Avogadro number. Despite several attempts to perform STM of perchlorocoronene on HOPG no clear evidence of the self-assembly of the chlorinated molecules was obtained. Therefore we used for our calculations the same unit cell of simple coronene. In **Table 5.2** the quantities of material employed are reported. Given that the effective surface area of graphene is much less than the unreal hypothesis of a single graphene sheet, we used only 2% of molecules needed to cover the "ideal" graphene surface.

| Sample | Mass of graphite (mg) | Volume of solvent (ml) | Mass of molecule (mg) |
|---|---|---|---|
| **Graphene exfoliated with coronene in o-DCB** | 130.4±0.2 | 10 | 3.2±0.1 |
| **Graphene exfoliated with perchlorocoronene in o-DCB** | 130.5±0.1 | 10 | 7.5±0.1 |
| **Graphene in o-DCB** | 131±0.2 | 10 | 0 |

**Table 5.2 :** masses of graphite, solvent and molecules used for the exfoliation

After the LPE procedure schematized briefly in **Figure 5.5** and described in the experimental details, we obtained stable dispersions which resulted to be very stable. In fact after 4 months there was no sign of precipitation.

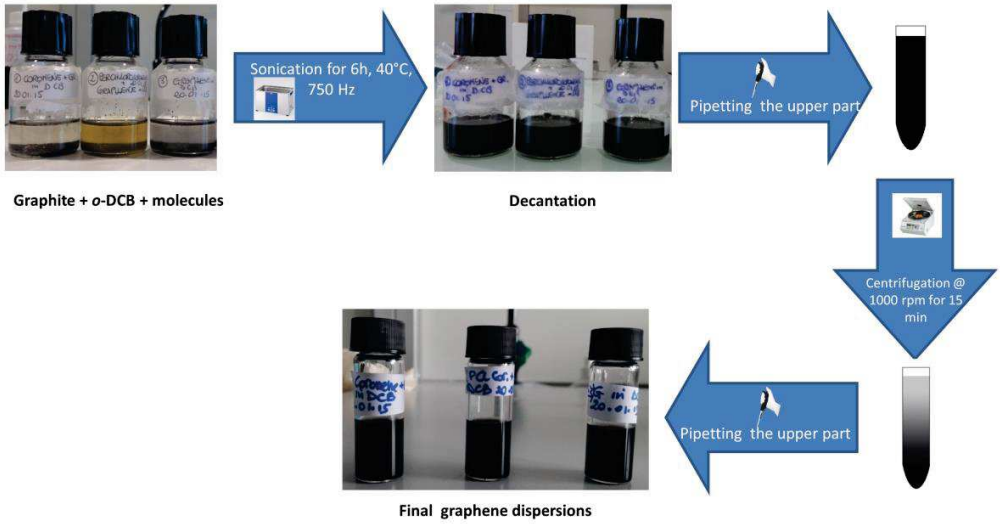


**Figure 5.5:** Scheme of the LPE exfoliation procedure starting from the preparation of the vials with graphite powder, solvent and molecules, then sonication, followed by decantation. Finally after centrifugation the final dispersion were obtained. In each photo the vials correspond, going from left to right, to the exfoliations in presence of coronene, perchlorocoronene and blank experiment.

The dispersions were analyzed by UV-Vis absorption and fluorescence spectroscopy. The characteristic absorption and the emission spectra for the two dispersions prepared in presence of coronene and perchlorocoronene are reported in **Figure 5.6** as a comparison with the pristine solutions of the molecules in *o*-DCB. The final suspensions contained a large excess of surfactants, as evident from the absorption spectra (**Figure 5.6a** and **5.6c**). In fact the UV-Vis absorbance spectra of the dispersions show a superposition of the typical coronene and perchlorocoronene absorption bands with the uniform decaying light dispersion of graphene sheets in the dispersions.[4] It is possible to see from **Figure 5.6b** and **5.6d** that the emission of the molecules in the dispersions

is attenuated compared to the one of the pristine solutions of the molecules. This can be attributed to two factors: on the one hand to a quenching process[24] of the graphene and on the other end to the overall process of production (decantation+ centrifugation) of LPE graphene which reduces the quantity of perchlorocoronene and coronene present in the final dispersions.

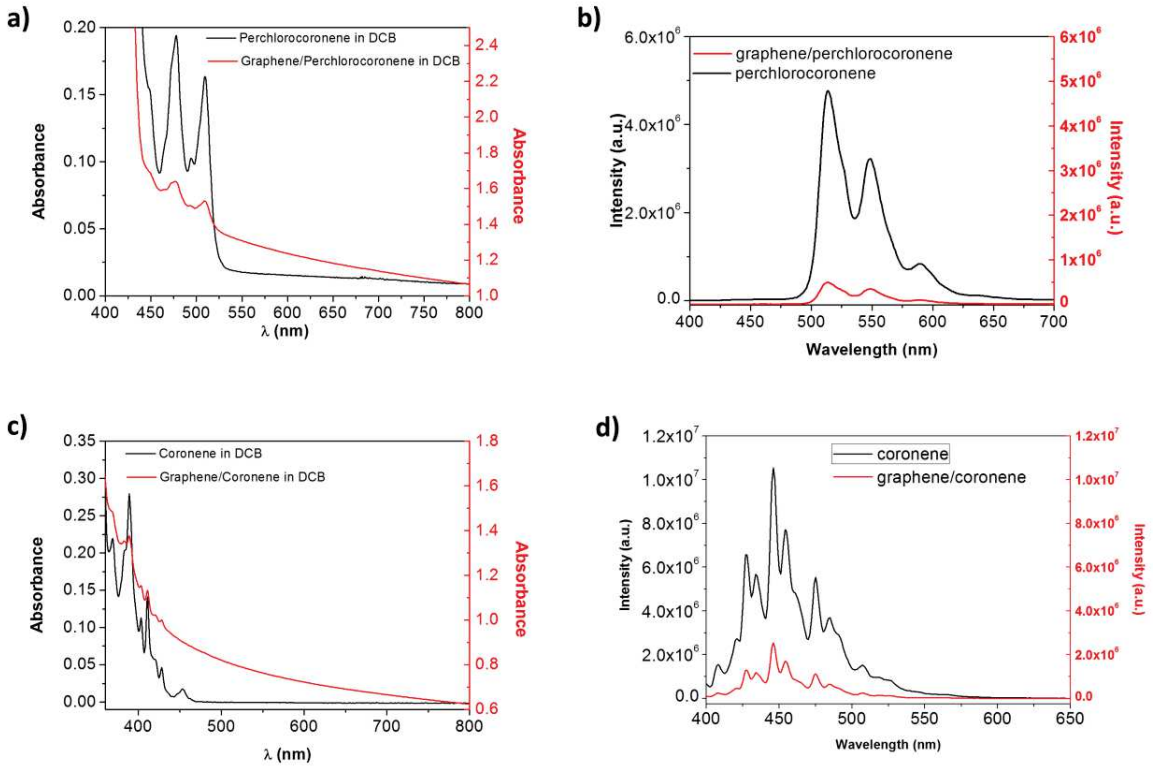


**Figure 5.6:** a) absorbance and b) fluorescence emission spectra of perchlorocoronene initial solution (black) and of the final dispersion of LPE graphene (red) in presence of perchlorocoronene; c) absorbance and d) fluorescence emission spectra of coronene initial solution (black) and of the final dispersion of LPE graphene (red) in presence of coronene. All the spectra were performed with cuvette of path wavelength 3mm x3mm in order to minimize inner filter effects.

Each dispersion was diluted several times and for each dilution the absorption spectrum was recorded. Plotting the absorbance at 660 nm divided by the cell path length versus the relative concentration (with respect to the initial solution) it was possible to observe that all the dispersions followed the Lambert-Beer behavior (**Figure 5.7**).

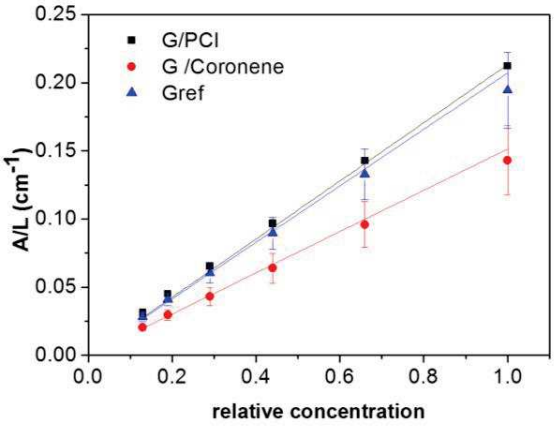


**Figure 5.7 :** Lambert Beer behavior for the three dispersions: graphene in o-DCB in presence of perchlorocoronene molecules (black), graphene in o-DCB in presence of coronene molecules (red) and blank experiments (blue).

The concentration of the dispersions was calculated filtering a known volume of the dispersions through a PTFE membrane with 0.1 μm pore size and also from the absorption spectrum using as absorption coefficient $\alpha$= 2460 $mLmg^{-1}m^{-1}$ value for $\lambda$= 660 nm reported by Hernandez et coworkers.[4] The values obtained with the two different methodologies are reported in **Table 5.3**. The values calculated from the absorbance spectra were slightly higher to the one determined by weight, nevertheless they showed a similar trend. The presence of perchlorocoronene didn't affect the final concentration of the dispersions which was very close to the one of blank samples. Instead, dispersions obtained exfoliating in presence of coronene presented a lower concentration, although the quality of the dispersions was improved (see below).

| **Concentration** | **Perchlorocoronene/G (μg/mL)** | **Coronene/G (μg/mL)** | **Ref (μg/mL)** |
|---|---|---|---|
| **From absorbance** | 171±1 | 114±20 | 154±22 |
| **From mass weight** | 128±2 | 95±6 | 135±6 |

**Table 5.3 :** Average concentration for the graphene dispersions produced by LPE calculated by weight and from the absorbance.

TEM and HRTEM analysis of the dispersions provided information about the quality of the graphene dispersions produced in terms of the percentage of single layer graphene (SLG) flakes present in the dispersion and of average size of flakes. A statistical analysis of the number of layers per flake in the dispersions is reported in the histogram in **Fig. 5.8a.**

The amount of monolayers obtained in DCB was 1% while it reached 9% in coronene and 12% in perchlorocoronene, showing that aromatic compounds improve the quality of the exfoliation and more particularly perchlorocoronene. Moreover from the distributions it is possible to see that DCB dispersions were made mostly of three-layer flakes while DCB/perchlorocoronene and DCB/coronene dispersion were mainly constituted by bilayer flakes. In the case of perchlorocoronene dispersions the number of flakes with more than 5 layers was much lower than in the other two types of dispersions (as it is possible to see in **Figure 5.9** where some HRTEM images are reported) confirming the better quality achieved using this stabilizer. Moreover TEM analysis allowed the calculation of the average lateral size of graphene sheets. The lateral size of graphene sheets showed an asymmetrical distribution (see **Figure 5.8b**) which was fitted with a Log-Normal function, a continuous probability distribution commonly used to study fragmentation processes and already employed in the analysis of lateral size distributions of exfoliated 2D materials.[25] The lateral size of the flakes was estimated to be 326±10 nm, 368±10 nm and 475±17 nm for graphene exfoliated in *o*-DCB/perchlorocoronene, *o*-DCB/coronene and *o*-DCB, respectively. The lateral size of the flakes in the case of o-DCB/perchlorocoronene LPE graphene was slightly lower than o-DCB/coronene and o-DCB graphene which can be attributed to the fact that usually graphite exfoliation via sonication produces on average flakes with lateral sizes that increase with the number of layers.

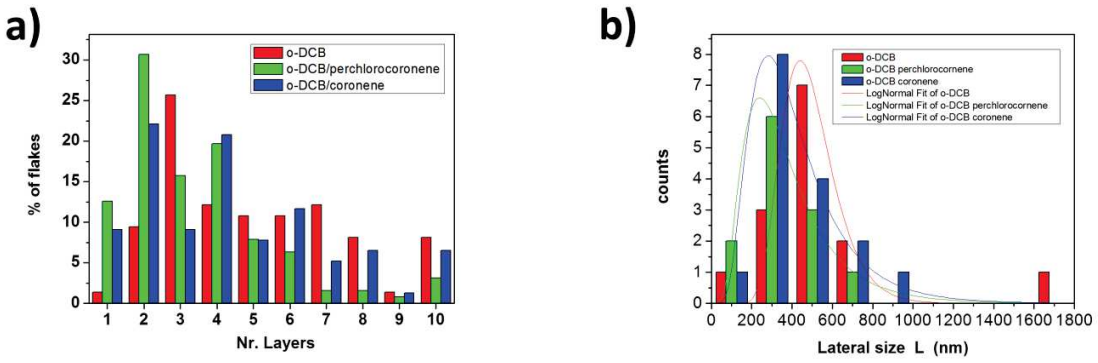


**Figure 5.8:** Statistical analysis of TEM and HR-TEM results of graphene exfoliated in o-DCB (red), in presence of perchlorocoronene (green) and in presence of coronene (blue). a) Histogram of the distributions of the flake thickness; b) histogram of the lateral flakes size distributions fitted with a Lognormal distribution.

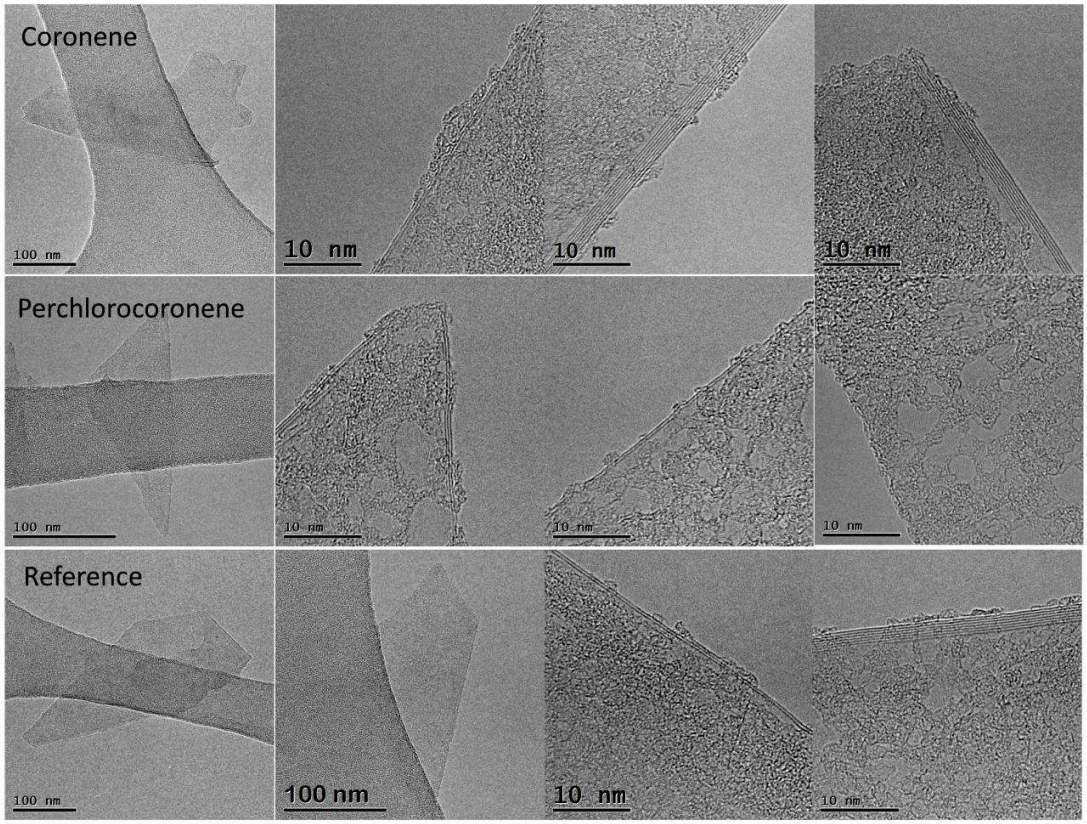


**Figure 5.9 :** TEM and HR-TEM images of graphehe flakes for the three dispersion studied. It is possible to observe graphene flakes with more than 5 layer s for coronene and reference samples while they are almost absent for perchlorocoronene samples.

The quality of the three graphene dispersions was also analyzed by means of microRaman spectroscopy by the group of Dr. Cinzia Casiraghi in Manchester University. The first order Raman spectrum of LPE graphene is characterized by the G and D peak at about 1580 $cm^{-1}$ and 1400 $cm^{-1}$ respectively. The D peak is activated by defects and in LPE graphene, mostly by edge size defects due to the small size of the flakes. Typically, in LPE graphene, the more the graphene is exfoliated, i.e. more SLG sheets are present, the more edge defects there are. I(D)/I(G) ratio is used for estimating the concentration of defects. So in this case, the smaller the number of graphene layers per flake is, the higher the I(D)/I(G) ratio will be and as it is possible to see in **Figure 5.10** this was the general trend of the three graphene dispersions studied. The second order Raman spectrum is very important because it allows a qualitative identification of the thickness of the flakes through the 2D shape of the peak. In mechanical exfoliated graphene this peak is a single and intense peak while in LPE it can assume complicate line shapes because of re-aggregation and folding. Higher the

R2_2D values (fitting coefficient of Lorentzian lineshape for 2D peak) are, thinner the flakes are and they have higher defects (edge) concentrations and therefore higher I(D)/I(G) ratio, as it is possible to see in **Figure 5.10**.

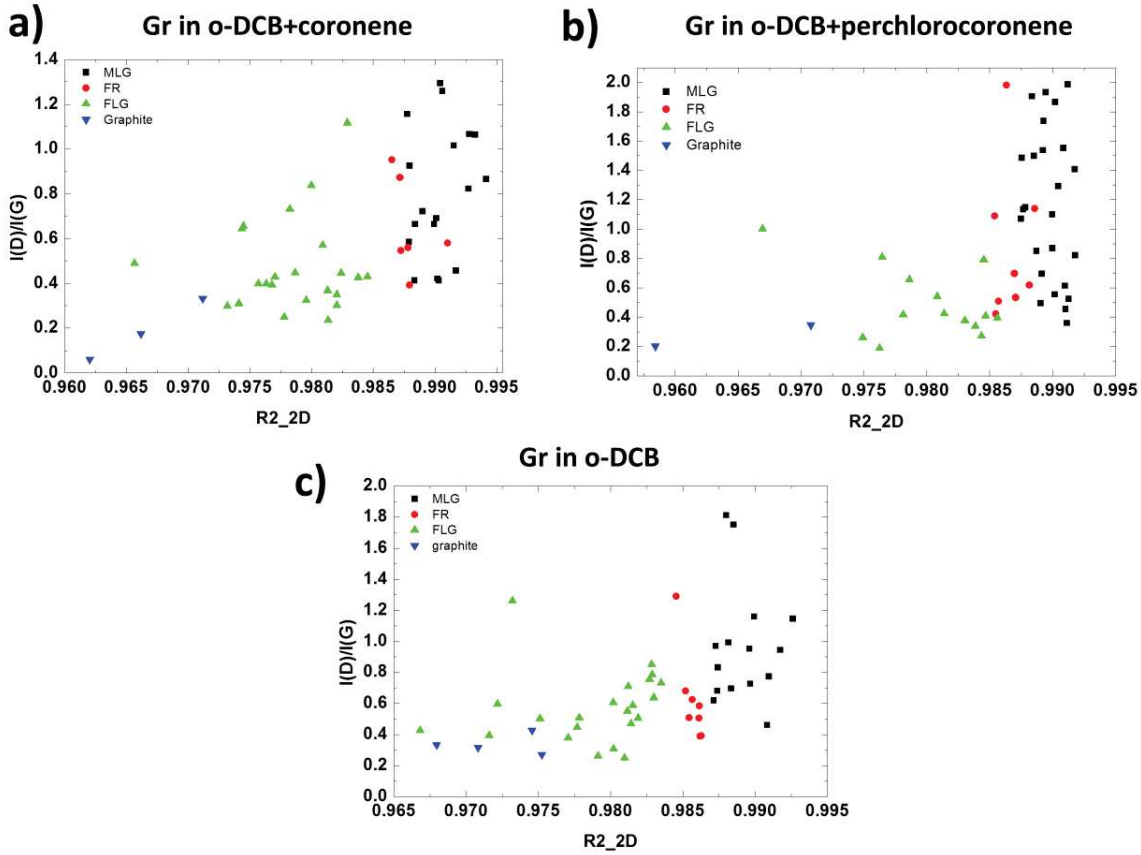


**Figure 5.10 :** Raman statistical analysis of graphene dispersions. I(D)/I(G) ratio plotted versus the coefficient of Lorentzian fitting of 2D peak for a) graphene exfoliated in o-DCB in presence of coronene; b) graphene exfoliated in o-DCB in presence of perchlorocoronene; c) reference sample. In black monolayer graphene, in red re-stacked layers, in green few layer graphene (less than 7 layers) and in blue graphite.

The analysis of the 2D line shape allowed calculating the percentage of monolayers (SLG), few layer graphene (FLG) and graphite, which is reported in summary in **Table 5.4**. The percentage of monolayer graphene amounts to approximately 51% in the case of LPE graphene exfoliated in presence of perchlorocoronene which is higher than the one in LPE in presence of coronene (36%). This is in agreement with TEM results. The percentage are higher in view of the fact that in TEM analysis, due to the high amount of molecules adsorbed on the graphene sheets, it is not always easy to count and distinguish the edges, underestimating the monolayers present in the sample. Raman analysis confirmed that the presence of graphitic material is lower in the o-DCB/perchlorocoronene graphene dispersion.

| Sample | SLG (%) | FLG (%) | Graphite (%) | Total (%) |
|---|---|---|---|---|
| **o-DCB** | 31 | 61 | 8 | 100 |
| **o-DCB/perchlorocoronene** | 51 | 44.9 | 4.1 | 100 |
| **o-DCB/coronene** | 36 | 58 | 6 | 100 |

**Table 5.4 :** Percentage of single layer (SLG), few layers (FLG ) and graphite for the three kind of dispersions.

## 5.3.3. Thermal desorption spectroscopy

Thermal desorption spectroscopy (TDS) was performed in order to determine the activation energy for desorption of coronene and perchlorocoronene from a HOPG surface. These experiments were performed and analyzed by Dr. Artur Böttcher.

In **Figure 5.11** the thermal desorption spectra for different coverages $\Theta_0$ of coronene and perchlorocoronene are reported.

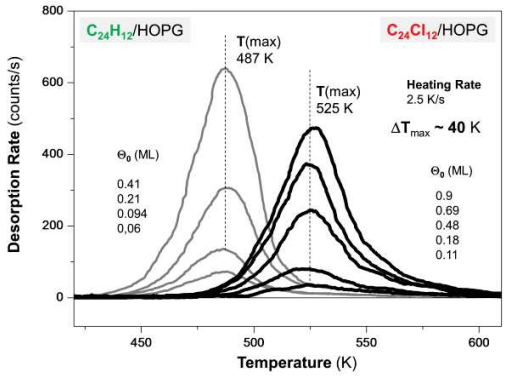


**Figure 5.11 :** Thermal desorption spectra of coronene (left) and perchlorocoronene (right) from the HOPG surface for different coverages. Coverages $\Theta_0$ in monolayers (ML) are reported for coronene (0.06, 0.094, 0.21, 0.41) and perchlorocoronene (0.11, 0.18, 0.48, 0.69, 0.9). The rate of desorption was in both cases β= 2.5 K $s^{-1}$.The TDS spectra were performed and analyzed by Dr. Artur Böttcher.

It was possible to observe a desorption peak maximum $T_{\max}$ at 487K for coronene and at 525K for perchlorocoronene, which were coverage independent. This feature together with the shape of the TD spectra was indicative of a 1st order kinetic process. The desorption rate of some adsorbates from a solid surface can be described by the following *Polanyi-Wigner* equation:

$$-\frac{d\Theta(t)}{dt} = \nu \cdot \Theta^n(t) \cdot exp\left(-\frac{E_a}{kT(t)}\right)$$

where $\nu$ is the pre-exponential factor, $\Theta$ is the surface coverage, $k$ is the Boltzmann constant, $T$ the temperature, $E_a$ is the activation energy for desorption, $n$ is the kinetic order.

Assuming that the activation parameters are independent from the surface coverage and the desorption follows a first order kinetics from the previous equation it is possible to obtain the *Redhead equation*:

$$E_a = kT_{\max}[\ln\left(\frac{\nu T_{\max}}{\beta}\right) - 3.64]$$

where $T_{\max}$ is the peak maximum and $\beta$ is the rate constant with which the sample is heated. Using a pre–exponential factor $\nu = 2 \cdot 10^{14}\ s^{-1}$ it was possible to determine the activation energy $E_a$ that resulted to be 1.45 eV for coronene and 1.57 eV for perchlorocoronene. Therefore, we can conclude that the interaction of perchloronene with graphene is stronger, presumably due to interaction of polar C-Cl bonds with π electrons of the HOPG substrate. These results confirmed the theoretical calculations.

## 5.4. Conclusions

In conclusion, in this work we showed that employing perchlorinated coronene as dispersion-stabilizing agent in LPE of graphite in *o*-DCB it is possible to improve the quality of graphene produced in terms of monolayers compared with a simple coronene. The reason for this capacity is the higher adsorption energy of perchlorinated coronene compared to the hydrogenated counterpart, as confirmed by theoretical calculations and by thermal desorption spectroscopy. The higher adsorption energy is caused by the higher polarizability of the chlorine atoms compared to carbon which increases the dispersion interactions between graphene and the molecule. We believe that through this theoretical model it will be possible to rationalize the design of new graphene surfactants, by predicting in a short time out of a set of commercial or synthesizable molecules, the ones having higher affinity with graphite and therefore allowing the direct LPE with this targeted molecules. This approach can reduce the time and the cost of experiments and boost the LPE technique towards upscalable procedures.

## 5.5. References


1. (a) Morozov, S. V.; Novoselov, K. S.; Katsnelson, M. I.; Schedin, F.; Elias, D. C.; Jaszczak, J. A.; Geim, A. K., Giant intrinsic carrier mobilities in graphene and its bilayer. *Phys Rev Lett* **2008,** *100* (1), 016602; (b) Bolotin, K. I.; Sikes, K. J.; Jiang, Z.; Klima, M.; Fudenberg, G.; Hone, J.; Kim, P.; Stormer, H. L., Ultrahigh electron mobility in suspended graphene. *Solid State Commun.* **2008,** *146* (9–10), 351-355.
2. Frank, I. W.; Tanenbaum, D. M.; van der Zande, A. M.; McEuen, P. L., Mechanical properties of suspended graphene sheets. *J. Vac. Sci. Technol., B* **2007,** *25* (6), 2558-2561.
3. Ciesielski, A.; Samorì, P., Graphene via sonication assisted liquid-phase exfoliation. *Chem Soc Rev* **2014,** *43* (1), 381-98.
4. Hernandez, Y.; Nicolosi, V.; Lotya, M.; Blighe, F. M.; Sun, Z.; De, S.; McGovern, I. T.; Holland, B.; Byrne, M.; Gun'Ko, Y. K.; Boland, J. J.; Niraj, P.; Duesberg, G.; Krishnamurthy, S.; Goodhue, R.; Hutchison, J.; Scardaci, V.; Ferrari, A. C.; Coleman, J. N., High-yield production of graphene by liquid-phase exfoliation of graphite. *Nat Nano* **2008,** *3* (9), 563-568.
5. Bonaccorso, F.; Lombardo, A.; Hasan, T.; Sun, Z.; Colombo, L.; Ferrari, A. C., Production and processing of graphene and 2d crystals. *Mater. Today* **2012,** *15* (12), 564-589.
6. Ciesielski, A.; Samori, P., Graphene via sonication assisted liquid-phase exfoliation. *Chem. Soc. Rev.* **2014,** *43* (1), 381-98.
7. Cravotto, G.; Cintas, P., Sonication-Assisted Fabrication and Post-Synthetic Modifications of Graphene-Like Materials. *Chem.–Eur. J.* **2010,** *16* (18), 5246-5259.
8. (a) Liang, Y. T.; Hersam, M. C., Highly Concentrated Graphene Solutions via Polymer Enhanced Solvent Exfoliation and Iterative Solvent Exchange. *J. Am. Chem. Soc.* **2010,** *132* (50), 17661-17663; (b) Xu, L.; McGraw, J.-W.; Gao, F.; Grundy, M.; Ye, Z.; Gu, Z.; Shepherd, J. L., Production of High-Concentration Graphene Dispersions in Low-Boiling-Point Organic Solvents by Liquid-Phase Noncovalent Exfoliation of Graphite with a Hyperbranched Polyethylene and Formation of Graphene/Ethylene Copolymer Composites. *J. Phys. Chem. C* **2013,** *117* (20), 10730-10742.
9. Schlierf, A.; Samorì, P.; Palermo, V., Graphene-organic composites for electronics: optical and electronic interactions in vacuum, liquids and thin solid films. *J. Mater. Chem. C* **2014,** *2* (17), 3129-3143.
10. Ciesielski, A.; Haar, S.; El Gemayel, M.; Yang, H.; Clough, J.; Melinte, G.; Gobbi, M.; Orgiu, E.; Nardi, M. V.; Ligorio, G.; Palermo, V.; Koch, N.; Ersen, O.; Casiraghi, C.; Samorì, P., Harnessing the Liquid-Phase Exfoliation of Graphene Using Aliphatic Compounds: A Supramolecular Approach. *Angew. Chem. Int. Ed.* **2014,** *53* (39), 10355-10361.
11. Bléger, D.; Kreher, D.; Mathevet, F.; Attias, A.-J.; Schull, G.; Huard, A.; Douillard, L.; Fiorini-Debuischert, C.; Charra, F., Surface Noncovalent Bonding for Rational Design of Hierarchical Molecular Self-Assemblies. *Angew. Chem.* **2007,** *119* (39), 7548-7551.
12. Haar, S.; Ciesielski, A.; Clough, J.; Yang, H.; Mazzaro, R.; Richard, F.; Conti, S.; Merstorf, N.; Cecchini, M.; Morandi, V.; Casiraghi, C.; Samorì, P., A Supramolecular Strategy to Leverage the Liquid-Phase Exfoliation of Graphene in the Presence of Surfactants: Unraveling the Role of the Length of Fatty Acids. *Small* **2015,** *11* (14), 1691-1702.
13. Conti, S.; Cecchini, M., Accurate and Efficient Calculation of the Desorption Energy of Small Molecules from Graphene. *J. Phys. Chem. C* **2015,** *119* (4), 1867-1879.
14. Cioslowski, J.; Liu, G. H.; Moncrieff, D., Theoretical thermochemistry of homolytic C-C and C-Cl bond dissociations in unbranched perchloroalkanes. *J. Phys. Chem. A* **1998,** *102* (48), 9965-9969.
15. (a) Schlierf, A.; Yang, H.; Gebremedhn, E.; Treossi, E.; Ortolani, L.; Chen, L.; Minoia, A.; Morandi, V.; Samori, P.; Casiraghi, C.; Beljonne, D.; Palermo, V., Nanoscale insight into the exfoliation mechanism of graphene with organic dyes: effect of charge, dipole and molecular structure. *Nanoscale* **2013,** *5* (10), 4205-4216; (b) Yang, H.; Hernandez, Y.; Schlierf, A.; Felten, A.; Eckmann, A.; Johal, S.; Louette, P.; Pireaux, J. J.; Feng, X.; Müllen, K.; Palermo, V.; Casiraghi, C., A simple method for graphene production based on exfoliation of graphite in water using 1-pyrenesulfonic acid sodium salt. *Carbon* **2013,** *53*, 357-365; (c) Schlierf, A.; Cha, K.; Schwab, M. G.; Samorì, P.; Palermo, V., Exfoliation of graphene with an industrial dye: teaching an old dog new tricks. *2D Mater.* **2014,** *1* (3), 035006.
16. Randić, M., Aromaticity of Polycyclic Conjugated Hydrocarbons. *Chem. Rev.* **2003,** *103* (9), 3449-3606.
17. Vanommeslaeghe, K.; Hatcher, E.; Acharya, C.; Kundu, S.; Zhong, S.; Shim, J.; Darian, E.; Guvench, O.; Lopes, P.; Vorobyov, I.; Mackerell, A. D., CHARMM general force field: A force field for drug-like molecules compatible with the CHARMM all-atom additive biological force fields. *J. Comput. Chem.* **2010,** *31* (4), 671-690.

18. (a) Vanommeslaeghe, K.; MacKerell, A. D., Automation of the CHARMM General Force Field (CGenFF) I: Bond Perception and Atom Typing. *J. Chem. Inf. Model.* **2012,** *52* (12), 3144-3154; (b) Vanommeslaeghe, K.; Raman, E. P.; MacKerell, A. D., Automation of the CHARMM General Force Field (CGenFF) II: Assignment of Bonded Parameters and Partial Atomic Charges. *J. Chem. Inf. Model.* **2012,** *52* (12), 3155-3168.
19. Brooks, B. R.; Brooks, C. L.; Mackerell, A. D.; Nilsson, L.; Petrella, R. J.; Roux, B.; Won, Y.; Archontis, G.; Bartels, C.; Boresch, S.; Caflisch, A.; Caves, L.; Cui, Q.; Dinner, A. R.; Feig, M.; Fischer, S.; Gao, J.; Hodoscek, M.; Im, W.; Kuczera, K.; Lazaridis, T.; Ma, J.; Ovchinnikov, V.; Paci, E.; Pastor, R. W.; Post, C. B.; Pu, J. Z.; Schaefer, M.; Tidor, B.; Venable, R. M.; Woodcock, H. L.; Wu, X.; Yang, W.; York, D. M.; Karplus, M., CHARMM: The biomolecular simulation program. *J. Comput. Chem.* **2009,** *30* (10), 1545-1614.
20. Tan, Y.-Z.; Yang, B.; Parvez, K.; Narita, A.; Osella, S.; Beljonne, D.; Feng, X.; Müllen, K., Atomically precise edge chlorination of nanographenes and its application in graphene nanoribbons. *Nat Commun* **2013,** *4*.
21. Hughes, J. M.; Hernandez, Y.; Aherne, D.; Doessel, L.; Müllen, K.; Moreton, B.; White, T. W.; Partridge, C.; Costantini, G.; Shmeliov, A.; Shannon, M.; Nicolosi, V.; Coleman, J. N., High Quality Dispersions of Hexabenzocoronene in Organic Solvents. *J. Am. Chem. Soc.* **2012,** *134* (29), 12168-12179.
22. Israelachvili, J., *Intermolecular and Surface Forces, Third Edition*. Academic Press: 2010.
23. Zhang, H.-X.; Chen, Q.; Wen, R.; Hu, J.-S.; Wan, L.-J., Effect of Polycyclic Aromatic Hydrocarbons on Detection Sensitivity of Ultratrace Nitroaromatic Compounds. *Anal. Chem.* **2007,** *79* (5), 2179-2183.
24. Kim, J.; Cote, L. J.; Kim, F.; Huang, J., Visualizing Graphene Based Sheets by Fluorescence Quenching Microscopy. *J. Am. Chem. Soc.* **2010,** *132* (1), 260-267.
25. Kouroupis-Agalou, K.; Liscio, A.; Treossi, E.; Ortolani, L.; Morandi, V.; Pugno, N. M.; Palermo, V., Fragmentation and exfoliation of 2-dimensional materials: a statistical approach. *Nanoscale* **2014,** *6* (11), 5926-5933.

# 6. Preparation of optically switchable asymmetric electrodes: towards multifunctional devices

## 6.1. Introduction

In the past years the performances of organic field-effect transistors (OFETs) have improved considerably through careful synthesis of ad-hoc organic/polymeric semiconductors, the control over their self-assembly on surfaces via solution processing using sophisticated approaches, the tailoring of all interfaces of a device via chemical functionalization and the optimization of the energetics of all components reaching field-effect mobilities exceeding 45 $cm^2 V^{-1} s^{-1}$.[1]

Such high mobilities indeed require an optimal charge injection at the electrode-semiconductor interface which can be achieved by tuning the Schottky barrier through a modification of the work function of the electrodes.[2] Among the various strategies employed to optimize the work function, the functionalization of the electrodes with self-assembled monolayers (SAMs) of polar molecules is particularly versatile considering the wide range of molecules available and their ability to modify not only the electrode work function but also its wettability.[3]

Another great possibility of OFETs is the potential to incorporate stimuli responsive components (light, magnetic field, environment), paving the way towards multi-responsive devices.[4]

It has been demonstrated that incorporation of photochromic molecules in the device can confer a light responsive nature to OFETs, by modulation of different types of physico-chemical properties.[5]

Photochromic molecules are in fact extensively studied organic molecules which upon application of specific light stimuli can undergo isomerization between at least two (meta)stable states, which

exhibit, in addition to different spectral features, very different chemico-physical properties at the molecular level (refractive index, dielectric constant, oxidation/reduction potential, and geometrical structure).[6]

For example upon blending the organic semiconductor with diarylethenes, a well-known class of photochromic molecules, it is possible to modulate the *charge transport* by tuning the energy levels of the molecule in the film by light irradiation at different wavelengths thereby creating/removing traps from the semiconductor blend.[7]

The incorporation of photochromic molecules at the electrode-semiconductor interface by functionalizing the electrode with a SAM comprising photochromic molecules allows instead a tuning of the *charge injection*. It has been shown that by functionalizing source and drain electrodes with an azobenzene SAM the injection can be modulated through a variation of the tunneling barrier switching the molecule from the *trans* to the *cis* state and *viceversa.*[8] Molecular junctions with a SAM of diarylethene based-switches[9] showed a modulation of the current upon light illumination, due to a change in the conjugation of diarylethene from the open (not-conjugated) to the closed form (conjugated form), which could let think to a possible application in OFETs.

Another further step in order to increase the number of tuning functionalities in the same device could be the possibility to modulate in an independent way the injection of source and drain electrode. Liscio et al. have demonstrated that an easy and potentially up-scalable way to functionalize source and drain electrode pairs with two different SAMs is a three steps process which involves the adsorption of the most stable SAM forming molecule on the gold electrodes, the electrochemical desorption of the SAM from one of the two electrodes and the successive adsorption of the second SAM on the gold electrode left exposed by desorption.[10] In this way it is possible to produce asymmetric electrode pairs having different charge injection properties.

In the present work we will show the possibility of combining the two strategies described above in order to increase the possible switching combinations in the same device. We will demonstrate, in particular, that it is possible to functionalize adjacent interdigitated electrodes with two different photochromic SAMs by a process combining chemisorption and selective electrochemical desorption. The molecules designed for this purpose belong to two different photochromic classes, azobenzene and diarylethene.

Through UV-Vis absorption experiments of mixtures of the two photochromic molecules in solution we will show the possibility of switching one type of molecule without affecting the other.

First attempts of integration of the asymmetric electrodes in OFETs in order to transduce the asymmetry in the electrodes in an asymmetric electrical behavior of the device are presented. In fact through an appropriate irradiation at different wavelengths it can be possible to modulate the charge injection of each electrode independently thus increasing the number of independent stimuli to which the device can respond.

## 6.2. Experimental details

***Materials:*** Biphenylthioacetate azobenzenes (AZO, **Figure 6.1a**) were synthetized by the group of Prof. Marcel Mayor using the procedure already reported in literature[11] and used as received. The group of Prof. Stefan Hecht provided diarylethenes thioacetate with a thioacetate group in para (p-tDAE, **Figure 6.1b**) or meta (m-tDAE, **Figure 6.1c**) position functionalized with tert butyl groups.

Ethanol (CHROMANORM), chloroform, toluene (CHROMASOLV Plus), potassium hydroxide (KOH) were purchased from Sigma Aldrich.

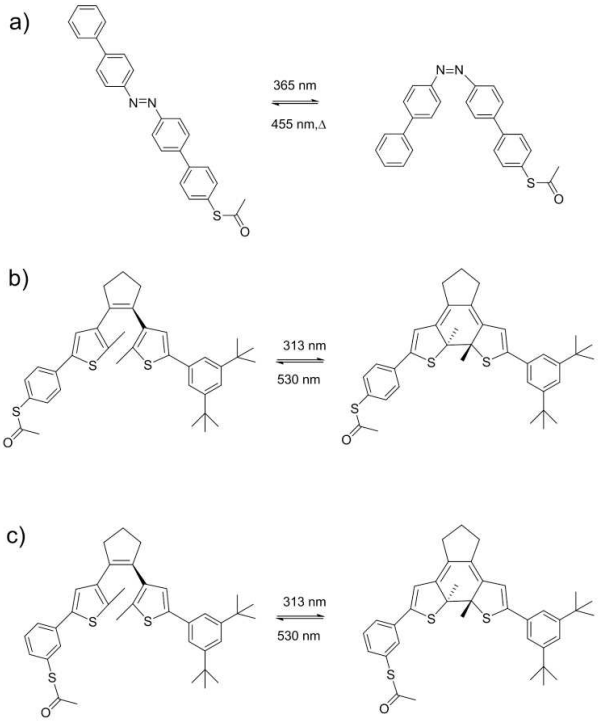


**Figure 6.1 :** Molecules employed in our study: a) biphenyl azobenzene thioacetate (AZO); b) diarylethene with thioacetate group in *para* (p-tDAE); c) diarylethene with thioacetate group in *meta* (m-tDAE)

***Preparation of the substrates:*** The interdigitated electrodes for desorption experiments and XPS analysis were prepared evaporating on $Si^{n++}/SiO_2$ substrates (Fraunhofer institute) 1.5 nm of an adhesion layer of chromium followed by 30 nm of gold using a shadow mask.
Semi-transparent substrates were prepared for UV-Vis absorption experiments evaporating 3 nm of chromium followed by 15 nm of gold on quartz slides (SCIENCE SERVICES GmbH). Semitransparent interdigitated electrodes were prepared in the same way by application of a shadow mask.
Both $Si^{n++}/SiO_2$ and quartz substrate were cleaned by sonication in acetone, isopropanol and UV-ozone treatment prior to use.
Substrates of epitaxial Au(111) (300 nm) on mica were purchased from Georg Albert PVD and ozone treated prior to use.

**Preparation of solutions for UV-Vis spectroscopy:** $1.25\times10^{-5}$ M solution of m-tDAE in opened form in toluene was prepared drying the THF mother solution, adding toluene and diluting to the desired concentration. A 1 mM solution of p-tDAE in chloroform was prepared in the same way. A $1.25\times10^{-5}$ M solution of biphenyl-AZO in *trans* form was prepared from a 0.5 mM mother solution. The mixed solution ($1.25\times10^{-5}$ M m-tDAE + $1.25\times10^{-5}$ M biphenyl-AZO) in toluene is prepared mixing two solution of DAE and AZO of doubled concentration in ratio 1:1.

***Preparation of the Azobenzene SAMs:***
In a 50 ml round bottom flask a small quantity (~ 0.25 mg) of byphenyl azobenzene and 20 mL of ethanol are added. Byphenyl azobenzene is not soluble in ethanol at room temperature). Immediately after a UV-Ozone cleaning treatment (5 min of ozone generation + 25 minutes of incubation) the substrate is immersed in the flask and the flask is kept for 24 hours at 70 °C under reflux in a dark environment. The azobenzene at this temperature partially dissolves in ethanol and a SAM of biphenyl azobenzene molecules forms on the gold. The sample is then removed from the flask, rinsed with warm ethanol and chloroform and sonicated for 15 minutes in chloroform in order to be sure to have removed all the physisorbed molecules and crystals and dried under nitrogen flux.

***Preparation of t-DAE SAM:*** The substrate is immersed in a 1 mM solution of t-DAE for at least 36 hours. Subsequently it is rinsed with warm ethanol, chloroform and dried under nitrogen flux.

***UV-Vis experiments:*** UV-Vis absorbance spectra of solutions and SAMs were recorded with a UV-Vis Jasco V-650 spectrophotometer. The spectra concerning the switching of the self-assembled monolayers were recorded in nitrogen atmosphere irradiating the sample in-situ.
Irradiation was performed using the following light sources.

- LED with wavelength 310 ± 5 nm (UVTOP310 by Roithner Laser Technik Gmbh);
- UV lamp with centered wavelength 312 nm;
- Fiber coupled LEDs with wavelengths 365 nm, 455 nm, 530 nm (ThorLabs).

***Electrochemical desorption experiments:*** The electrochemical desorption was performed with a homemade set-up using a probe station and applying different potentials (using a Keithley 2636A dual channel sourcemeter controlled by the associate software) from a gold tip connected to the electrode using as counter electrode a gold coil and as electrolyte a 50mM solution of potassium hydroxide in Ethanol.

***XPS experiments:*** XPS analyses were carried out on a Thermo Scientific K-Alpha X-ray photoelectron spectrometer with a base pressure of ~$10^{-8}$ mbar and an Al anode as the X-ray source (x-ray radiation of 1486 eV). Spot sizes between 30 μm and 400 μm were used. Survey spectra are an average of 10 scans with a pass energy of 200.00 eV and a step size of 1 eV. High-resolution spectra are an average of 10 scans (or even 50 or 100 when needed) with a pass energy of 50.00 eV and a step size of 0.10 or 0.05 eV.

***SEM characterization:*** SEM images were acquired with Quanta FEG(FEI®) using the secondary electron detector with 5 kV acceleration.

***Device fabrication:*** Semi-transparent interdigitated electrodes on quartz slides were prepared evaporating 3 nm of chromium followed by 15 nm of gold (SCIENCE SERVICES GmbH) by means of a shadow mask. In each sample there are 8 pairs of interdigitated electrodes with channel lengths of 120, 100, 80 and 60 μm and channel width W=10000 μm.
After being ozone treated they underwent the procedure for the formation of an AZO SAM. Then, for each pair of interdigitated electrodes an electrochemical desorption experiment was performed on one of the two electrodes as described in detail in section 6.3.4. The substrate was then immersed in a 1mM p-tDAE solution for 36 h. After cleaning, the substrates were transferred to the glovebox

and 520µl of a 5mg/ml solution of P(NDI2OD-T2) (purchased from Polyera) in chloroform were spin coated on it. Then the sample was annealed at 60° for 2h and cooled down at room temperature. Afterwards, 1020 µl of Cytop/Cytop-solvent (purchased from Asahi glass, code: CTL-809M) solution in ratio 9/1 were deposited on top of the organic semiconductor and the sample was annealed for 4 h at 70 °C. Profilometer measurements revealed that the average film thickness of P(NDI2OD-T2) film was 60 nm while Cytop layer was 700 nm thick. Finally 100 nm of aluminum were deposited on top as gate electrode. As reference samples also devices bearing AZO SAMs, p-tDAE SAMs and monophenylthiol (MPT) SAMs on both electrodes were prepared. MPT SAM was formed on the electrodes immersing the sample in a 5 mM solution of MPT in EtOH for 12 hours. Samples without any functionalization of the electrodes were also prepared.

The electrical characterization was performed with a Keithley 2636A dual channel sourcemeter controlled by the proprietary software.

Irradiation of devices was performed from the underside with a Polychrome V (Till Photonics) tunable light source providing a monochromatic light beam (± 15 nm) for different wavelengths.

The device fabrication, the electrical characterization and the workfunction measurements were performed in collaboration with Thomas Mosciatti.

## 6.3. Experimental results and discussion

### 6.3.1. Independent switching of AZO and tDAE in solution: proof of concept

The UV-Vis spectra of the switching in solution of m-tDAE, are reported in **Figure 6.2**.

The m-t DAE in the open form is characterized by the presence of a shoulder peak at 310 nm. Irradiating at this wavelength it is possible to convert the open form to the fully conjugated closed form which shows a peak in the visible region at ca. 530 nm and a double peak in the UV region at ca. 365 nm. This form can be converted back to the open form just by irradiation with light in the range of the band centered at 530 nm.

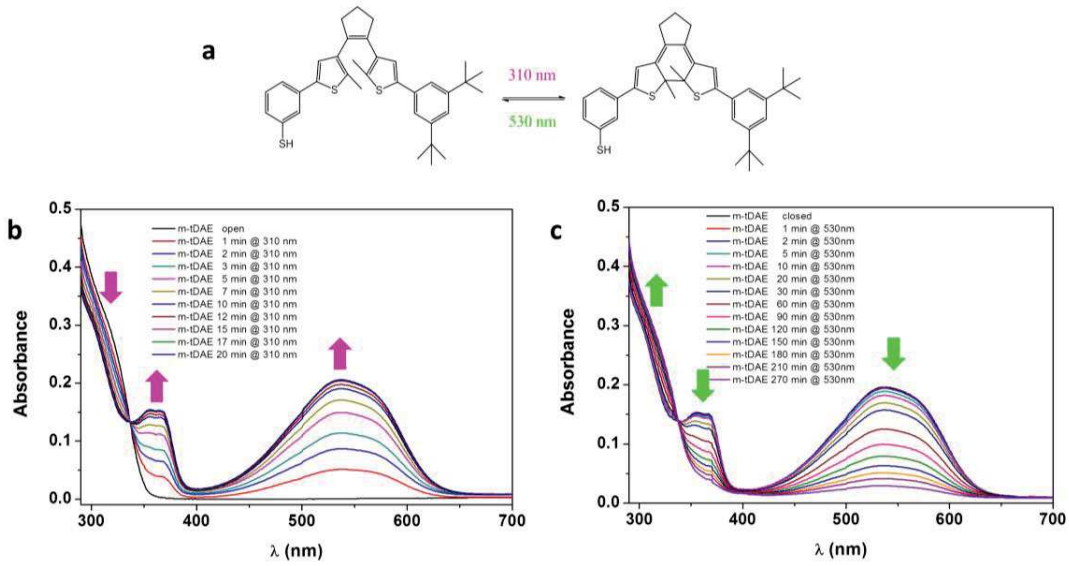


**Figure 6.5 :** a) Scheme of the switching of m-tDAE from the opened to the closed form. b) UV-Vis absorbance spectra recorded while irradiating at 310 nm. The formation of the closed form is characterized by the appearance of a broad peak with maximum at 534 nm and a peak at ca. 355 nm (violet arrows). c) UV-Vis absorbance spectra recorded while irradiating *ex situ* at 530 nm. The opened form is characterized by the appearance of a peak at about 315 nm. The green arrows indicate the appearance of the peak at 315 nm characteristic of the opened form and the disappearance of the peaks at 534 nm and 355nm typical of the closed form.

The two isomeric states of diarylethene are thermodynamically stable and reversible, but it is known that prolonged UV-irradiation of diarylethenes with thiophene rings can cause the formation of a byproduct which is a condensed moiety with two six membered heterocyclic rings. The new product has similar features to the closed form but the peak around 500 nm is blue-shifted and less intense. The byproduct cannot undergo reversible isomerization, and thus its formation is not suitable for our aim.[12]

The p-tDAE molecule presents similar features in the open and closed form but all the UV-Vis spectra are red shifted of about 10 nm (see **Figure 6.3**).

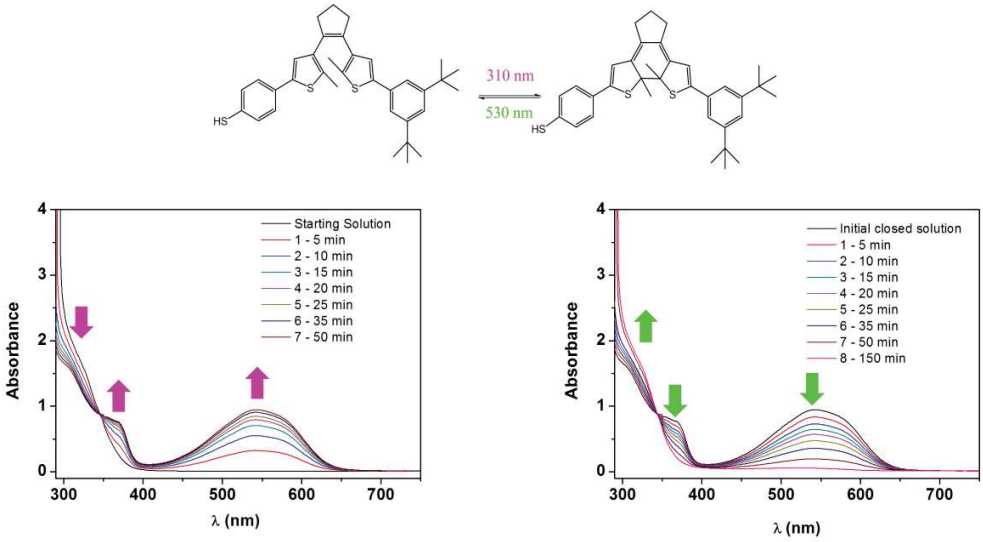


**Figure 6.3** : a) Scheme of the switching of p-tDAE form the opened to the closed form. b) UV-Vis absorbance spectra recorded while irradiating at 310nm. The formation of the closed form is characterized by the appearance of a broad peak with maximum at 541 nm and a peak at ca. 370 nm (violet arrows). c) UV-Vis absorbance spectra recorded while irradiating *ex situ* at 530nm. The opened form is characterized by the appearance of a peak at about 313 nm. The green arrows indicate the appearance of the peak at 315 nm characteristic of the opened form and the disappearance of the peaks at 541 nm and 370 nm typical of the closed form.

The UV-Vis absorbance spectra of the switching in solution of the azobenzene is reported in **Figure 6.4**. The *trans* form of the biphenyl azobenzene shows an absorbance band at 365 nm (characteristic of a $\pi$-$\pi^*$ transition) and a weaker forbidden $n$-$\pi^*$ band at around 450 nm. Irradiating at 365 nm the isomerization to the *cis* form occurs and the band at 365 disappears while the band at 450 nm becomes more pronounced (**Figure 6.4b**). It is possible to go back to the *trans* form by irradiation at 455 nm (**Figure 6.4c**) or thermally.

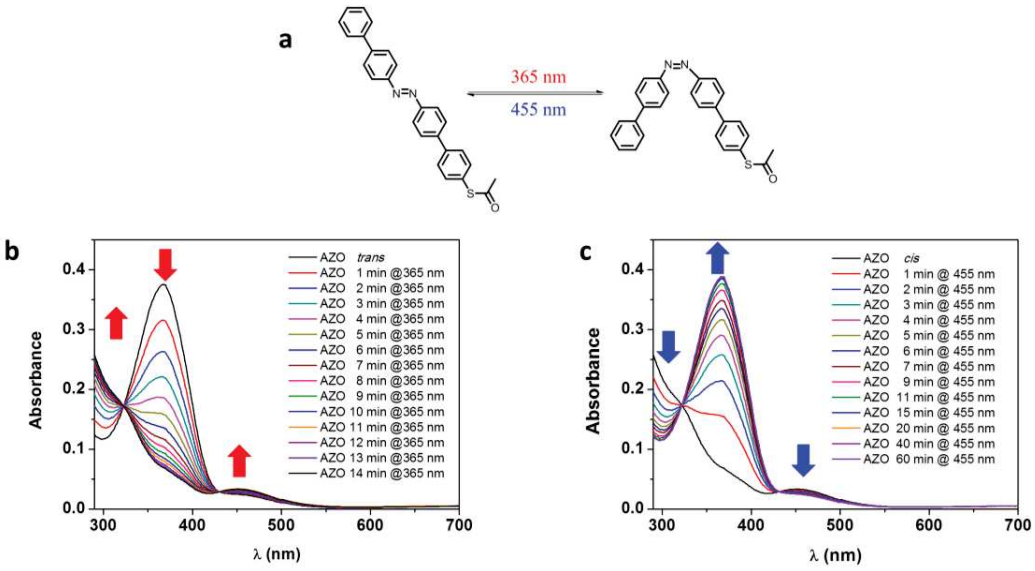


**Figure 6.4** : a) Scheme of the switching of the azobenezene from *trans* to *cis* and vice versa and wavelength used for switching; b) UV-Vis absorption spectra from the trans to the cis form irradiating at 365 nm; c) UV-Vis absorption spectra from the cis to the trans form irradiating at 455nm.

In order to study the independent switching of diarylethenes in presence of azobenzenes preliminary tests were performed to see if the diarylethene switches at the characteristic switching wavelengths of azobenezene that is 365 and 455 nm. The same principle was applied for azobenzenes.

From these experiments it was possible to conclude that AZO and m-t DAE molecules can be switched independently except when the azobenzene molecule is in its *cis* state, when it will switch back to *trans* at the DAE switching wavelengths, as reported in **Figure 6.5d** and **6.5e**. Also, the DAE closed to open switch will occur at the azobenzene switching wavelengths, but with much lower quantum yield. A summary of all the switching experiments is reported in **Table 6.1**.

These experiments demonstrate that, despite some switching combinations cannot be possible; there is still a margin for possible combinations. In **Figure 6.6** an example of possible independent switches in a solution containing both azobenzene and diarylethene molecules is reported.

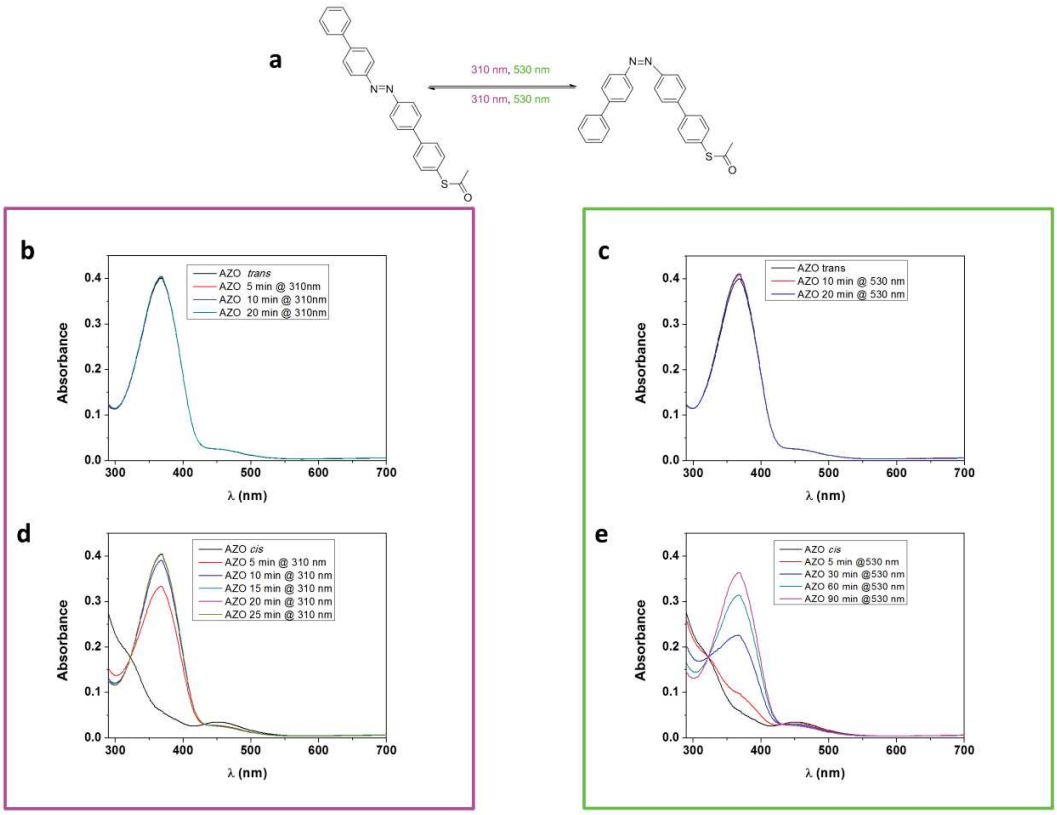


**Figure 6.5 :** a) Scheme of the switching of azobenzene at 310 nm at 530 nm from *trans* to *cis* and *cis* to *trans*. b) trial to switch azobenzene from *trans* to *cis* at 310 nm; c) trial to switch azobenzene from *trans* to *cis* at 530 nm; d) switching of the azo at 310 from *cis* to *trans* , e) switching of azobenene from *cis* to *trans* at 530 nm.

| | Switching wavelength (nm) | Diarylethene | | Azobenzene | |
|---|---|---|---|---|---|
| | | Open → Closed | Closed → Open | *Trans → Cis* | *Cis → Trans* |
| Diarylethene switching wavelengths | 310 | YES ✓ | NO ✓ | NO ✓ | YES ✗ |
| | 530 | NO ✓ | YES ✓ | NO ✓ | YES ✗ |
| Azobenzene switching wavelengths | 365 | NO ✓ | YES (>1h) ? | YES (15min) ✓ | NO ✓ |
| | 455 | NO ✓ | YES (>2h) ? | NO ✓ | YES (40 min) ✓ |

**Table 6.1 :** Possible switching combinations of the diarylethene and azobenzene molecules in solution. "YES" means the molecule switches at the indicated wavelength, "NO" means it does not. Green ticks indicate where the behavior is desirable; red crosses where the behavior is not (i.e. a switch at the wavelength used to switch the other molecule).

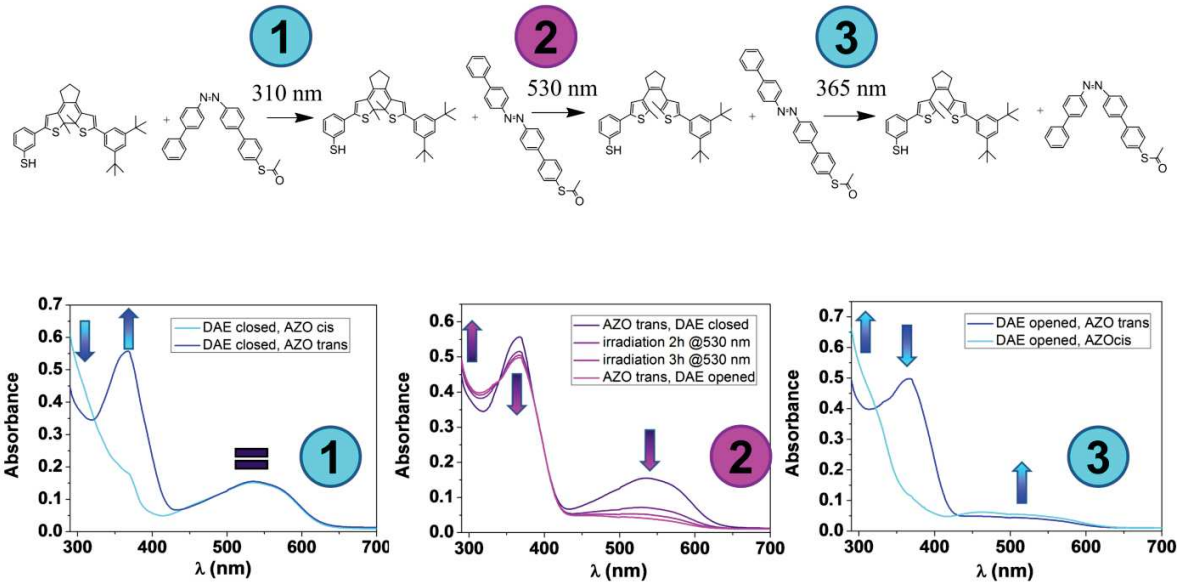


**Figure 6.6 :** Switching of a solution containing diarylethene and azobenzene molecules. The starting solution is in the form m-tDAE closed/AZO cis and has been irradiated first at 310 nm passing to the form AZO trans / m-t DAE closed. Then irradiating at 530 nm it is possible to switch to the form AZO trans/m-tDAE open and finally irradiating at 365 nm it is possible to go to the form AZO cis / ,m-tDAE open covering all the possible combination of AZO/m-tDAE

These experiments were not repeated for the p-tDAE which exhibits spectral features extremely similar to those of m-tDAE, thus the same switching behavior is expected.

## 6.3.2. Switching of the molecules on the surface

The formation of a nicely packed SAM formed by AZO molecules on Au111 had already been demonstrated in previous studies[13] by STM measurements. AZO SAMs show, both in *trans* and *cis* form, an herringbone structure with a unit cell containing two molecules and with the following parameters: a = 6.5±0.5 Å, b = 8.9±0.5 Å, α = 84°±5°.

The protocol used previously in our group to obtain AZO SAMs was the immersion of the substrate for 24 h in chloroform or toluene solutions of AZO at room temperature.

In order to increase the size of the 2D crystalline domains, lately other approaches were undertaken in our group, like increasing the temperature of the AZO solution or the use of a poor solvent such as ethanol. In fact it has been demonstrated that higher temperatures can help in the migration of gold adatoms which are formed as a result of the reconstruction of Au surface during chemisorption and usually inhibit the formation of bigger domains.[14] The role of the solvent is still not clear, but the use of polar, poor solvents seems to produce densely packed SAMs with a few defects.[15]

As it is possible to see in **Figure 6.7** it was found that the formation of the largest 2D crystal domains is reached immersing the SAM in a solution of AZO SAM in EtOH at 70°C under reflux overnight without deprotecting the thioacetate group.

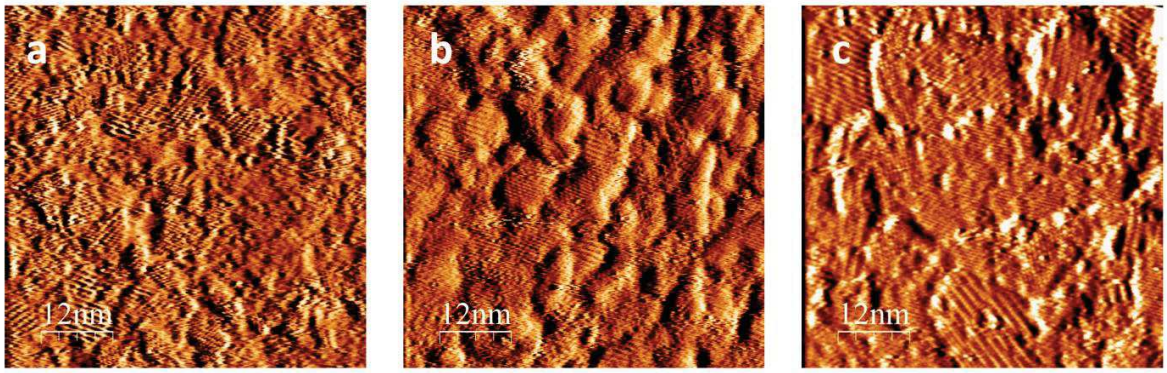


**Figure 6.7 :** STM images of AZO SAMs on Au 111 prepared incubating a substrate of Au(111) on mica overnight a) in AZO solution of Chloroform at room temperature; b) in AZO solution of toluene at 50 °C; c) in AZO solution of EtOH at 70 °C. The STM images were recorded by Dr. Mohamed El Garah and the samples were prepared by Dr. Karl Börjesson.

However, this procedure leads to the formation of big crystals on gold surface, as shown in Fig. 5.8. EDAX analysis performed by Marco Squillaci (**Figure 6.8d**) revealed that these crystals are composed by azobenzene molecules, since they are constituted just by C, S, O and N. They can be removed by sonication in chloroform for a few minutes, without destroying the SAM.

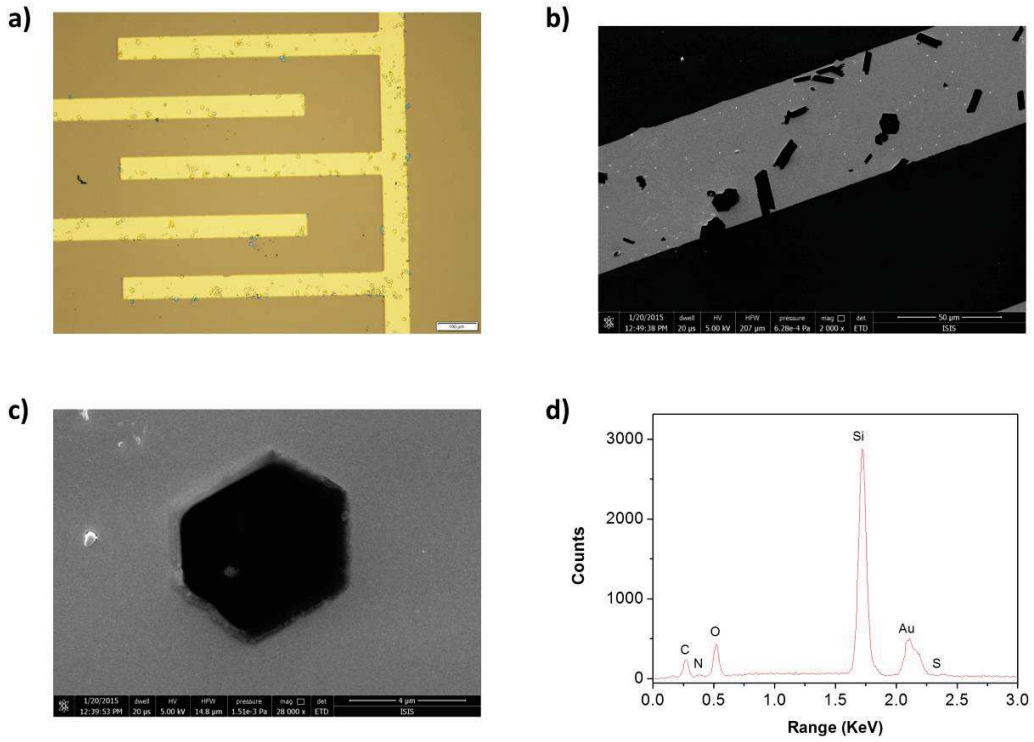


**Figure 6.8 :** (a) Optical and (b,c) SEM images of a device after immersion in azobenzene solution at 70 °C overnight and after rinsing; d) EDAX analysis on the crystal shown in panel c). SEM images and EDAX analyses were performed by Marco Squillaci.

In **Figure 6.9** the switching of the azobenzene SAM recorded by UV-Vis absorption spectroscopy is reported. The switching is not clearly visible directly in the spectra due to the strong absorption of gold, but by observing differences in consecutive spectra it is possible to observe the characteristic peaks. The spectra in blue have been obtained by subtracting the spectra recorded after UV irradiation at 365 nm from the initial spectrum of the AZO SAM in the *trans* form. It is possible to see a negative peak around 350 nm which corresponds to the decrease of the characteristic peak of the *trans* form of azobenzene upon irradiation with UV light (365 nm). The switching of the azobenzene to the *cis* forming applying an irradiance 2.11 mW/cm$^2$ was complete after 6 min.

Irradiating with 455 nm light, the peak at 350 nm re-appeared as illustrated by a positive peak in the spectrum after subtraction of the *cis* spectrum. It was possible to switch back the AZO at the *cis* form irradiating again at 365 nm. In these spectra it is possible to observe the evolution another small peak at around 270 nm which is characteristic of the *cis* form of the azobenzene which was not possible to record in solution due to the strong absorption of toluene below 300 nm.

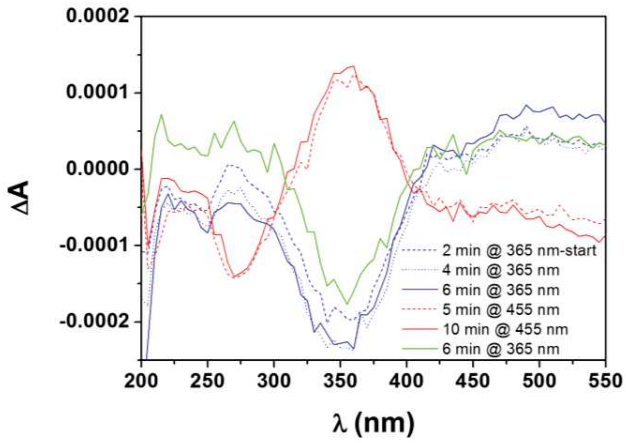


**Figure 6.9 :** Absorption spectra of the reversible switching of the azobenzene SAM on gold. The SAM has been switched first with 365nm light from *trans* to *cis* and 6 min are necessary to complete the switching (blue lines). The switching back to the *trans* form has been achieved irradiating with 455 nm light (red lines). Finally AZO SAM has been switched back again to *cis* form (green line).

The XPS analysis performed after the UV-Vis spectroscopy experiments shows that the switched AZO molecules are effectively bounded to gold. In fact it is possible to distinguish in the S2p peak (**Figure 6.10a**) a doublet with the main peak centered at 161.9 eV which corresponds to the sulphur chemisorbed on gold. The S2p peak in general can be decomposed in different contributions, each one being described by a doublet whose peaks, $S2p_{1/2}$ and $S2p_{3/2}$, have intensity ratio 2:1 and a spin orbit split of c.a. 1.2 eV.[16] Moreover also the nitrogen (**Figure 6.10c**) and carbon (**Figure 6.10b**) peak respectively at 399.2 eV and 184.3 eV are in agreement with previous XPS experiments performed on the same kind of SAM.[13]

The knowledge of the work function of the gold functionalized by AZO SAM is fundamental in view of the application of this system in a device. Kelvin probe measurement of AZO SAMs were already performed in our group showing that the WF for *trans*-AZO functionalized gold is 5.15±0.02 eV, while for the same AZO after illumination for 60 min at 365 nm is 5.22 ±0.02 eV.[17]

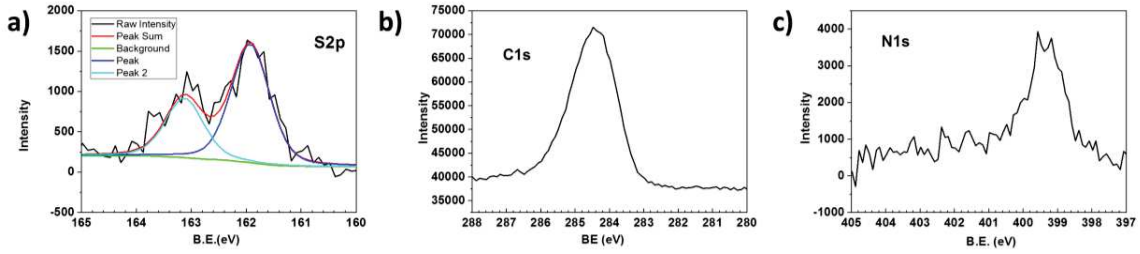


**Figure 6.10 :** a) S2p spectrum b) C1s spectrum, and c) N1s spectrum of an AZO SAM.

Concerning the diarylethene, the p-tDAE was studied in the self-assembled monolayer form because parallel studies in our group had shown good switching performance when employed in OFETs (see section 6.3.5.2), even though this was unexpected. In fact when the thiol unit is in *para* position there should be a strong coupling between the molecule and the gold substrates and therefore a mixing of the orbital states which, it has been predicted, should prevent the molecule to switch to the closed form.[18]

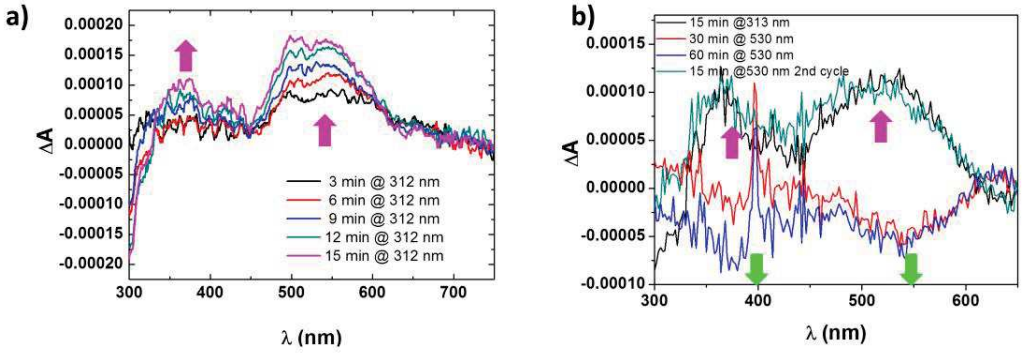


**Figure 6.11** Switching of p-tDAE SAM formed in the open form. a) switching from open to closed form irradiating with 312 nm lamp. The switching is complete after 15 min; b) cycle of irradiation: 15 min with 312 lamp (black line) in order to switch from open to closed form, switching back to the open form with 530 nm LED irradiating for 30 min (red line) and 1 hour (blue line), switching back to the closed form (2nd cycle) ( green line); subtraction of p-tDAE spectra in closed form from p-tDAE spectra in open form (black line) and viceversa (red line) in solution

The switching was confirmed also by UV-Vis spectroscopy. Upon irradiation of a p-tDAE SAM on a semitransparent Au-quartz substrate by 312 nm light, it was possible to follow, the increase of the peak at 540 nm and, for the first time in literature, also of the peak at 365 nm typical of the *closed* form. Twelve minutes of irradiation at 0.14 mW/cm$^2$ were enough to achieve the maximum switching from o-DAE to c-DAE (**Figure 6.11a**). It is more challenging to see the switching back after irradiation at 530 nm (0.42 mW/cm$^2$) due to the fact that reaction from closed to open form has a lower quantum yield and the baseline of the spectrophotometer is not stable over long periods of time. Anyhow a partial switch back of the molecule was monitored upon 1 hour of irradiation (**Figure 6.11b**).

STM experiments performed on chemisorbed p-tDAE did not detect any 2D crystalline domain, and so we turned to XPS to confirm order in the monolayer.

XPS analysis showed that, despite the unsuccessful detection of the SAM by STM, the molecules are present and bounded to gold, as we already know from UV-Vis.

A typical S2p XPS spectrum recorded for the p-tDAE SAM is reported in **Figure 6.12**. It can be deconvoluted in three doublets, which correspond to different chemical species of sulphur. As for the AZO SAM the peak around 162 eV corresponds to the sulphur chemisorbed on gold while the peak at 163.4 eV is characteristic of the sulphur belonging to the thiophene moiety. The peak at 161 eV can appear sometimes in thiol SAMs spectra. The origin of this feature is still under investigation but the most accredited hypothesis attributes this peak to atomic sulfur formed by the C-S bond cleavage[19] or isolated sulphur in sp configuration.[20]

a)

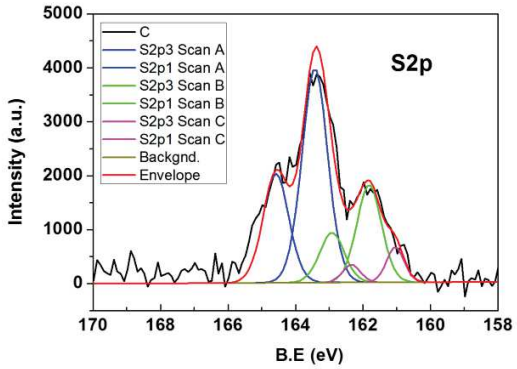


b)

| Name | Peak BE (eV) | FWHM (eV) | Area (P) CPS.eV | Atomic % |
|---|---|---|---|---|
| S2p3 Scan A | 163.42 | 0.9 | 3855.95 | 32.25 |
| S2p1 Scan A | 164.58 | 0.9 | 1969.66 | 32.27 |
| S2p3 Scan B | 161.82 | 0.86 | 1685.04 | 14.08 |
| S2p1 Scan B | 162.92 | 0.86 | 860.74 | 14.09 |
| S2p3 Scan C | 161.04 | 0.62 | 437.61 | 3.65 |
| S2p1 Scan C | 162.34 | 0.62 | 223.54 | 3.66 |

**Figure 6.12 :** a) S2p XPS spectra recorded for p-tDAE SAM. The black line represents the raw data as recorded. The peak has been deconvoluted in three doublets: doublet A (pink) corresponds to isolated sulphur or C-S cleaved sulphur; doublet B (blue) corresponds to sulphur chemisorbed on gold; doublet C is assigned to S belonging to thiophene moiety. The red line is the global fitting obtained by the sum of the three doublets. b) Summary of the peaks resulting from the deconvolution of the S2p peak of DAE SAM. For each peak, the binding energy, the full width at half maximum (FWMH), the area and the percentage are reported.

The latter theory implies a poorly ordered monolayer, which could explain the impossibility of mapping ordered region with STM.[21]

As it is possible to see from **Figure 6.12b** the ratio between peak A (thiophene sulphur) and peak B (thiol sulphur) is close to 2, as expected since in one molecule there are two thiophene units and just one thiol.

The workfunction (WF) of gold functionalized by p-tDAE SAM was determined by photoelectron yield spectrometer in air (PYSA). The measurement were performed and analyzed by Thomas Mosciatti. p-tDAE SAM in open and closed form were prepared and the photoelectron yield spectra

measured are reported in **Figure 6.13a**. The spectra were recorded from 4.0 eV to 5.25 eV which corresponds to a range from 310 nm to 229.6 nm and this could lead to an isomerization of the DAE from open to closed form. By keeping the power of the beam at 50 nW and for a short time (10 s) this potential problem was prevented. In fact measuring the spectra three times consecutively no change was observed. The WF of gold functionalized with p-tDAE in open form extracted from PYSA data is 4.5 ±0.05 eV, while for the gold with p-tDAE in the closed form is 4.62 ± 0.05 eV. The shift is of just 120 meV.

The measurements of the same samples with single point Kelvin probe revealed a difference in WF between the closed and open form of 125 ± 24 mV, with the functionalized closed p-tDAE gold presenting the higher WF (**Figure 6.13b**), in perfect agreement with the one extrapolated from PYSA measurements.

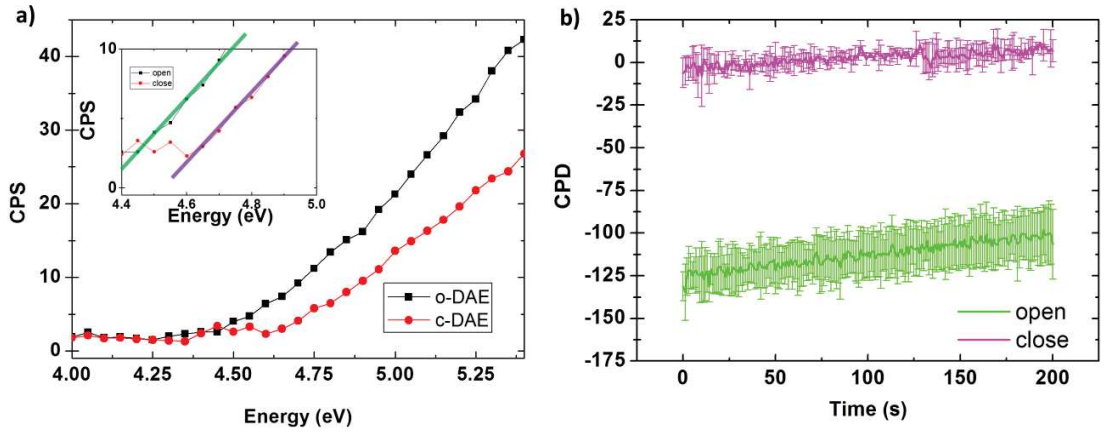


**Figure 6.13 :** a) Photoelectron yield spectra of open p-tDAE (black) and closed p-tDAE (red). Work function shift is highlighted in the inset b). Kelvin probe 200 sec measure of open p-tDAE (violet) and closed p-tDAE (green) functionalized gold reporting average and standard deviation of all measures performed for both SAM. Analysis and measurements performed by Thomas Mosciatti.

## 6.3.3. Competitive chemisorption experiments

A study of competitive chemisorption was performed in order to determine which SAM, the byphenyl azobenzene SAM or the p-DAE diarylethene SAM, has higher affinity for gold. This step is very important for the fabrication of asymmetric electrodes, as it determines which of the two SAMs has to be chemisorbed on the electrodes first and then electrochemically desorbed from one of them. The adsorption of the second SAM on the electrochemically cleaned electrode must not displace the SAM already present on the other electrode.

For this experiment epitaxial Au(111) on mica was employed. One substrate was subjected to the preparation protocol of the AZO SAM while the other to the p-tDAE one. After rinsing, both substrates where cut and one of the two parts of each sample underwent the procedure of formation of the opposite SAM as depicted schematically in **Figure 6.14**, whilst the other part was retained for analysis.

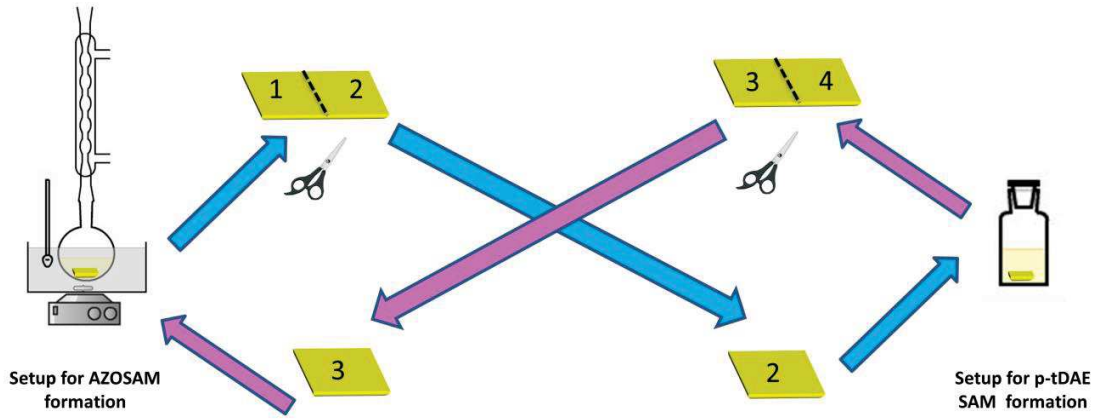


**Figure 6.14 :** Schematic representation of the experiment of competitive adsorption. Blue arrow pathway lead to the formation of sample 1 (AZO SAM) and sample 2 (AZO SAM immersed in a p-tDAE solution for 36 h and then rinsed). Pink arrow pathway lead to the formation of sampe 4 (p-tDAE SAM) and sample 3 (p-tDAE SAM, then subjected to process for AZO SAM formation).

The four samples thus obtained were:

- SAMPLE 1:sample with biphenyl azobenzene SAM (AZO SAM);
- SAMPLE 2: sample with a biphenyl azobenzene SAM immersed in a p-tDAE solution for 36 hours;
- SAMPLE 3: p- diarylethene SAM immersed for 24 hours in an azobenzene solution at 70°C;
- SAMPLE 4: p-diarylethene SAM.

A XPS survey of the four samples was performed in three different points of each sample and the average for each sample is reported in **Table 6.2**.

| Sample | N% | S% | C% | O% | Au% |
|---|---|---|---|---|---|
| 1 AZOSAM | 3.2 | 1.4 | 60.9 | 9 | 25.5 |
| 2 AZO SAM in p-DAE solution | 2.9 | 1.2 | 61.1 | 9.01 | 25.7 |
| 3 P-DAESAM in AZO solution | 5.1 | 2.28 | 60.4 | / | 32.2 |
| 4 P-DAE SAM | / | 2.2 | 51.6 | 4.4 | 43.2 |

**Table 6.2 :** percentage of N, S, C, O, Au element extracted from XPS survey on each sample employed for the study of competitive adsorption. Each value is the average of data taken in three different points of each sample.

Nitrogen is the key element which allows us to understand which SAM is present on the gold surface. As expected, in the p-tDAE SAM (sample 4) the nitrogen was absent while sample 1 AZO SAM presented a N:S ratio of 2.2 which is close to the expected value of 2. In sample 3, which underwent a competitive adsorption experiment applying first the p-tDAE SAM protocol formation followed by the AZO SAM protocol, it is immediately evident from the survey that there are molecules of azobenzene present on the surface. Moreover, the ratio N:S is close to 2 which could be an indication that the p-tDAE SAM formed in the first step had been partially displaced by the AZO molecules. Sample 2, which underwent the opposite competitive adsorption experiments still shows a N:S ratio of 2:1 which can suggest that the AZO SAM was not altered by the presence of p-tDAE molecules.

Another key element is given by the HRXPS spectra of the sulphur which, as already shown, have different features in the two SAMs. In **Figure 6.15** the S2p spectra of all four samples and the tables with the feature of the peaks resulted from fitting are shown. Comparing sample 2 (**Figure 6.15b**) to the reference sample for AZO SAM (**Figure 6.15a**) it is evident that the S2p peak in sample 2 has not changed after immersion in the p-tDAE solution, meaning that the AZO SAM was not affected by diarylethene molecules.

On the other hand, as reported in **Figure 6.15c**, the sample covered with p-tDAE SAM once subjected to the protocol of formation of an AZO SAM, does not show anymore a S2p peak with similar features to the one of a classical p-tDAE SAM (**Figure 6.15d**), while it has a shape and an intensity more similar to the spectrum of an AZO SAM.

It was difficult to deconvolute the S2p peak of sample 3 since most probably it is defined by the contribution of both SAM molecules.

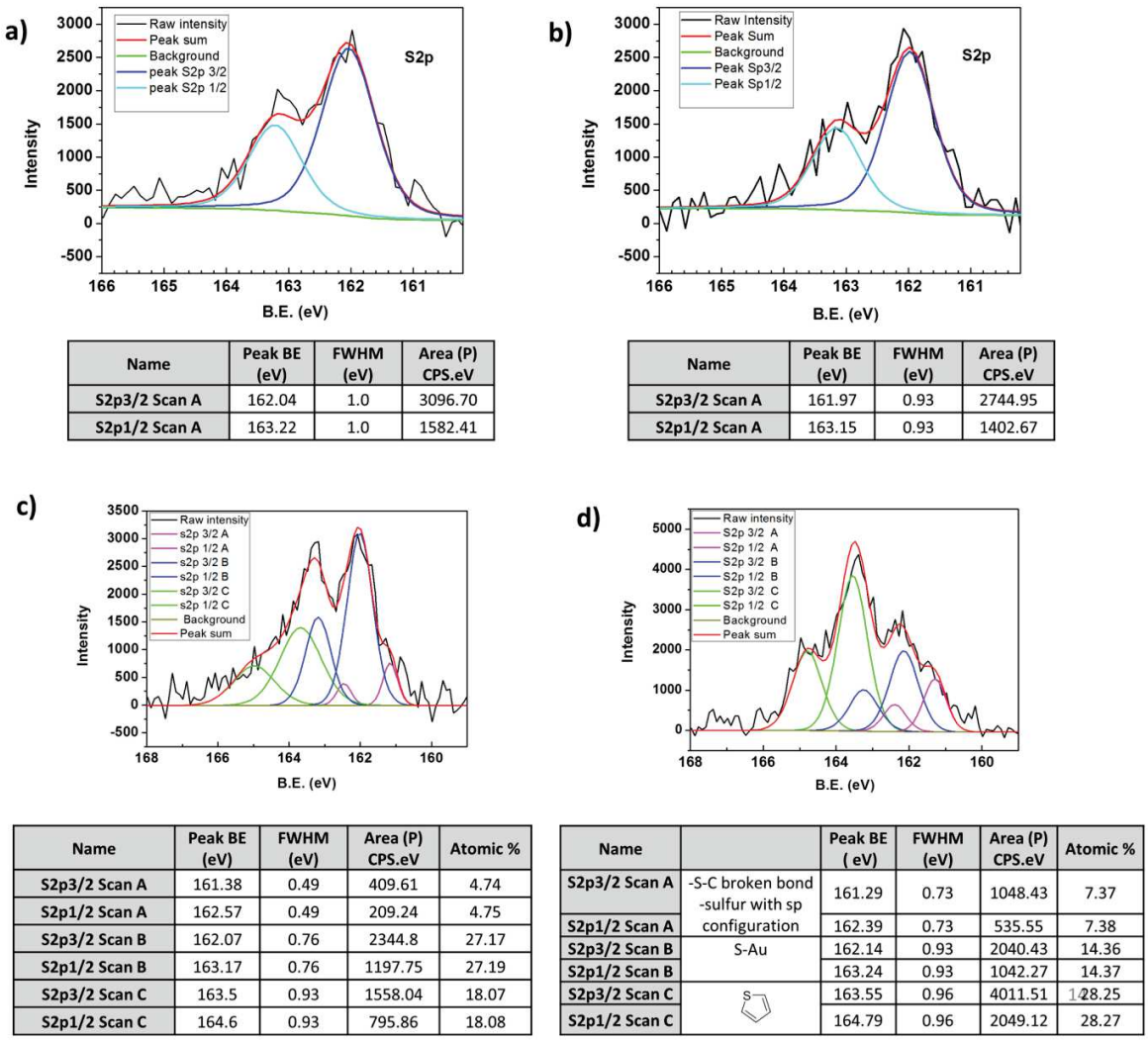


| Name | Peak BE (eV) | FWHM (eV) | Area (P) CPS.eV |
|---|---|---|---|
| S2p3/2 Scan A | 162.04 | 1.0 | 3096.70 |
| S2p1/2 Scan A | 163.22 | 1.0 | 1582.41 |

| Name | Peak BE (eV) | FWHM (eV) | Area (P) CPS.eV |
|---|---|---|---|
| S2p3/2 Scan A | 161.97 | 0.93 | 2744.95 |
| S2p1/2 Scan A | 163.15 | 0.93 | 1402.67 |

| Name | Peak BE (eV) | FWHM (eV) | Area (P) CPS.eV | Atomic % |
|---|---|---|---|---|
| S2p3/2 Scan A | 161.38 | 0.49 | 409.61 | 4.74 |
| S2p1/2 Scan A | 162.57 | 0.49 | 209.24 | 4.75 |
| S2p3/2 Scan B | 162.07 | 0.76 | 2344.8 | 27.17 |
| S2p1/2 Scan B | 163.17 | 0.76 | 1197.75 | 27.19 |
| S2p3/2 Scan C | 163.5 | 0.93 | 1558.04 | 18.07 |
| S2p1/2 Scan C | 164.6 | 0.93 | 795.86 | 18.08 |

| Name | | Peak BE ( eV) | FWHM (eV) | Area (P) CPS.eV | Atomic % |
|---|---|---|---|---|---|
| S2p3/2 Scan A | -S-C broken bond -sulfur with sp configuration | 161.29 | 0.73 | 1048.43 | 7.37 |
| S2p1/2 Scan A | | 162.39 | 0.73 | 535.55 | 7.38 |
| S2p3/2 Scan B | S-Au | 162.14 | 0.93 | 2040.43 | 14.36 |
| S2p1/2 Scan B | | 163.24 | 0.93 | 1042.27 | 14.37 |
| S2p3/2 Scan C |  | 163.55 | 0.96 | 4011.51 | 28.25 |
| S2p1/2 Scan C | | 164.79 | 0.96 | 2049.12 | 28.27 |

**Figure 6.15** : S2p spectra for all the samples of the competitive adsorption experiment and relative table with the features (area, peak Binding energy, FWMH and atomic %) of all the peaks resulting from deconvolution. A) sample 1 AZO SAM; b) sample 2: sample first subjected to AZOSAM protocol and then,p-tDAE SAMprotocol formation; c) sample 3 : sample first subjected to p-tDAE SAM protocol and then,AZO SAM protocol formation; d) p-tDAE SAM.

Another element which can help in the discrimination of the two SAMs is the percentage of Au. In fact the percentage of detected gold on an AZO SAM was always around 25% while that of a p-tDAE SAM was in a range of 50%. This could be related to a higher packing of the AZO SAM on the surface compared to the p-tDAE SAM or to the greater length of the AZO molecule, inducing a less intense signal from the substrate.

In conclusion, it is possible to state that the AZO SAM has higher affinity on gold than p-tDAE SAM. For these reasons it has to be the first SAM to be adsorbed on the asymmetric electrodes.

## 6.3.4. Preparation of the asymmetric electrodes

Samples with AZO SAMs on interdigitated electrodes were prepared using the protocol described in the experimental details. After placing the sample in a 50 mM potassium hydroxide/EtOH solution, on one electrode of each pair of interdigitated electrodes a potential was applied with respect to a counter electrode in order to desorb the SAM. After desorption the samples were immersed in a 1 mM solution of p-tDAE (see scheme in **Figure 6.16**) We explored both positive and negative desorption potential in order to determine the most effective ones in the removal of the azobenzene SAM.

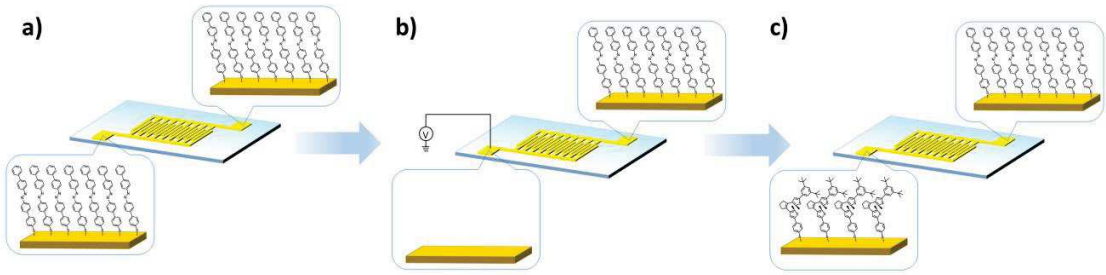


**Figure 6.16 :** schematic representation of the preparation of asymmetric electrodes a) first step: formation of the AZO SAM following the protocol described in the experimental details; b) second step: electrochemical removal of the AZO SAM from one of the electrodes; c) third step immersion of the sample in a p-tDAE solution for 36 h in order to form the p-tDAE SAM on the electrode electrochemically cleaned in the previous step.

In fact it is known that applying negative or positive potentials on an electrode covered with a thiolated SAM in presence of an electrolyte it is possible respectively to reduce or oxidize the thiol layer from a gold surface, causing its desorption.[22]

The reductive desorption has been extensively studied since many years and the half electrochemical reaction which describes the mechanism of desorption is:

$$Au - SR + 1e^- \rightarrow Au(0) + RS^-$$

The mechanism of oxidative desorption is less understood and there are various hypotheses. One of the mechanisms is described by a three-electron reaction which has as product sulphonic acid.

$$Au - SR + 2H_2O \rightarrow RSO_2H + 3e^- + 3H^+$$

Despite of the different mechanisms proposed, in general all the studies agree on the fact that in the oxidative process the reaction first takes place with the oxidative cleavage of the sulphur –gold bond followed by further oxidation of the sulphur.[23]

As a proof of the achieved desorption, on the two pads of each couple of electrodes, XPS analysis was performed recording the survey, the sulphur S2p and nitrogen N1s peak.

The application of a positive potential of +2V was the most effective for the removal of the azobenzene SAM, as reported in summary in **Table 6.3** while when applying negative the desorption of the azobenzene was achieved only for -2.5 V, even if not completely in one case .

| Device | Voltage applied (V) | Presence of Nitrogen |
|---|---|---|
| **120A** | +2 | NO |
| **100B** | +2 | NO |
| **120C** | -1.4 | YES |
| **100D** | -2.5 | Small N peak (almost complete desorption |
| **80E** | -2.5 | NO |
| **80G** | -1.4 | YES |

**Table 6.3 :** devices present on the $Si/SiO_2$ substrate and different potential applied to one of the electrode (denominated left electrode), and response of presence of nitrogen from XPS analysis.

We focused our attention on the devices 120A and 120B where, applying a +2V potential, the desorption was complete.

As it is shown in **Figure 6.17** on both devices in the pad of the electrode, where the desorption experiment was performed, the signal of nitrogen N1s peak was absent, while the sulphur peak shape was more similar to the one of the p-tDAE SAM, even though not exactly the same. Interestingly the peak at 161 eV is more pronounced, meaning that maybe there is a more disordered SAM. This could be explained by the fact that the application of potential can cause, apart from the desorption of the SAM also a rearrangement of the gold surface.[24]

On the same devices we performed an XPS line scan recording the Au4f and N1s peak in different points along a line crossing the interdigitated electrodes.

In **Figure 6.18a** the line scan of device 100 B is shown and the area of the Au4f and N1s peak is reported as function of the distance (**Figure 6.18b**). Similar results have been obtained for device 120A.

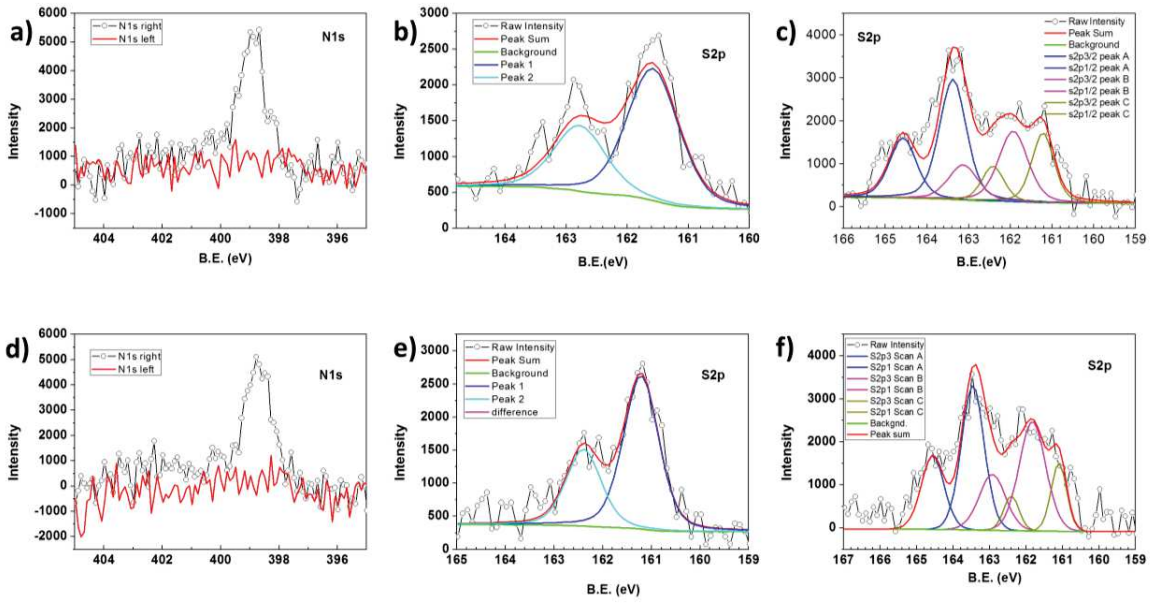


**Figure 6.17 :** XPS HR spectra of samples 100B (top raw) and 120 A (bottom raw). N1s (*a)* and *d)* black line) and S2p peak (*b)* and *e)*) of the pad not subjected to electrochemical desorption; N1s (*a)* and *d)* red line) and S2p peak (*c)* and *f)*) of the pad which were electrochemical desorbed upon application of a +2V potential.

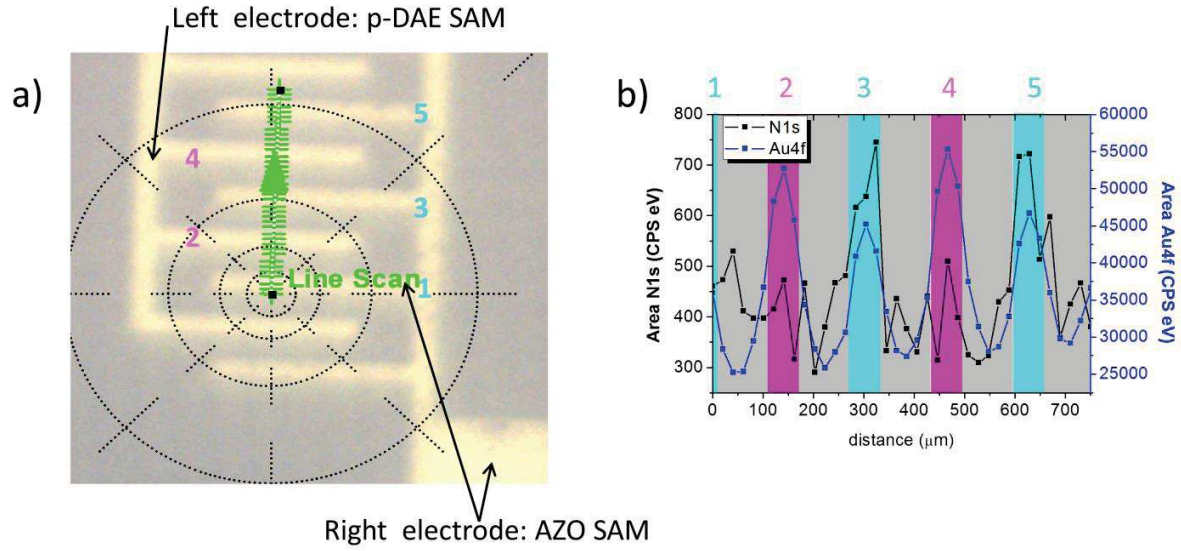


**Figure 6.18:** a) XPS line scan performed on device 100B; b) area of the N1s and Au4f peak reported versus the distance following the arrow in picture a).

It was possible to see that the nitrogen peak decreases where the desorption has occurred (pink areas). An alternative way to distinguish the two electrodes is the monitoring of the intensity of the

Au peaks. In fact, the signal of the gold electrodes where the AZO SAM is adsorbed, is lower compared to the one of the electrode on which the pDAE SAM is present maybe due to the higher packing of the AZO SAM.

Interestingly the Au peak never goes to 0 when the XPS beam is scanning a point in-between the electrodes (grey areas in **Figure 6.18b**) even though the distance between the electrodes is in this case 100µm and the nominal beam size of the XPS is 30 µm. This can be due to a problem of focus of the XPS beam which has a nominal spot size of 36 $\mu m^2$.

## 6.3.5. Incorporation of asymmetric electrodes in a device

After demonstrating the possibility of building asymmetric electrodes bearing two different SAMs, we implemented them in organic field-effect transistors (OFETs). Among all the possible OFETs configurations we chose bottom contact top gate configuration. A device schematization is reported in **Figure 6.19**. Top gate configuration was chosen because it is the most suitable one in order to account for modification in the charge injection or work function induced by a switching of the SAMs. In fact in this configuration it is possible to extract or inject carriers taking advantage of the whole functionalized surface of source and drain electrodes.

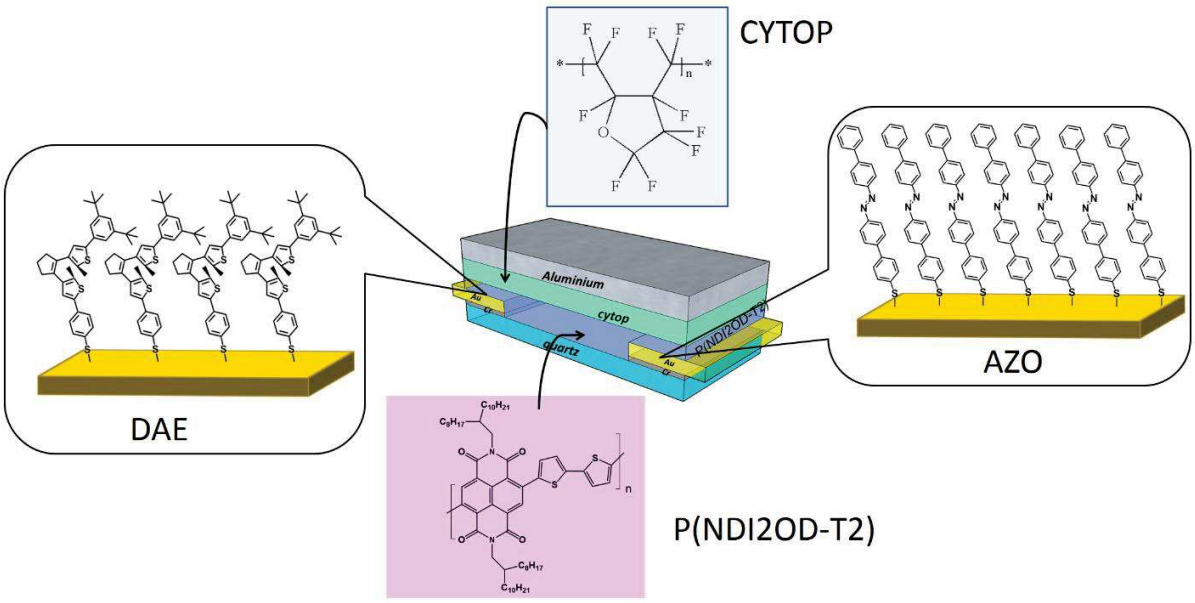


**Figure 6.19 :** Scheme of the bottom contact top gate geometry OFET with asymmetric electrodes. The formulae of CYTOP (light blue) and P(NDI2OD-T2) (pink) are reported.

The OFET was built on a transparent quartz substrate and semitransparent gold electrodes 15 nm thick with an adhesion layer of chromium were evaporated on the top. The transparency of both

substrate and electrodes was required because in this configuration the device was illuminated from the bottom with a monochromator coupled with an optical fiber to perform the switching of the SAMs. The organic semiconductor spin coated on the top of the electrodes is a *n-type* semiconductor, *P(NDI2OD-T2)* known for its high performance[25] especially in the top gate configuration.[26] Finally a 700±50 nm of dielectric CYTOP was spun over the semiconductor and an aluminium gate electrode was evaporated on top.
Reference samples were also prepared by varying the coating on the electrodes, in particular:

- OFETs with AZO SAM on both electrodes (FULL AZO);
- OFETs with p-tDAE SAM on both electrodes (FULL DAE);
- OFETs bearing a monophenyl thiol SAM on source and drain electrodes which is not switchable by light (BLANK 1);
- OFETs without SAMs on the electrode (BLANK 2).

The preparation and characterization of the devices was done in collaboration with Thomas Mosciatti.

#### 6.3.5.1. OFETs with AZO SAMs on both electrodes

The response of the AZO SAM to different light stimuli in a device was first checked in the devices where this SAM was present on both electrodes. First of all the symmetry of this devices was proved by recording the transfer characteristics at $V_d$=10 V and $V_d$=40 V and choosing as source (i.e. grounding) alternately one of the two electrodes. As expected the curves due to the symmetry of the electrodes change only slightly (**Figure 6.20a** and **6.21a**). Upon irradiation of the device originally in *trans* form with a 365 nm light the AZO SAM should switch to the *cis* form causing a change in current of the device (**Figure 6.20b**). In fact it was possible to observe an increase in the current in transfer characteristics, accompanied by an increase in mobility of 27% after 15 min of irradiation both in linear and saturation regime (**Figure 6.20d**). This result is in line with previous studies in our group where an increase of the current of 20% was observed in a bottom contact bottom gate configuration device with electrodes covered by AZO SAM but with a different organic semiconductor.[8] The increase of the current can be attributed to a decrease of the tunneling barrier resistance due to a decrease of the SAM thickness.

Surprisingly, irradiating the same device with 455 nm light for more than one hour did not lead to any switch back (**Figure 6.20c**) which could be explained by a mechanical interference with the back-reaction. The molecules switching from the *trans* to the *cis* form leave some empty space which can be filled by the alkyl chains of *P(NDI2OD-T2)* , being morphologically a rather amorphous material.[27]

After 44 hours in the dark the same OFET was tested again. A recover of almost 50% towards the starting maximum $I_{DS}$ current was observed. This corroborates our hypothesis of structural impediment which with time was overcome slightly.

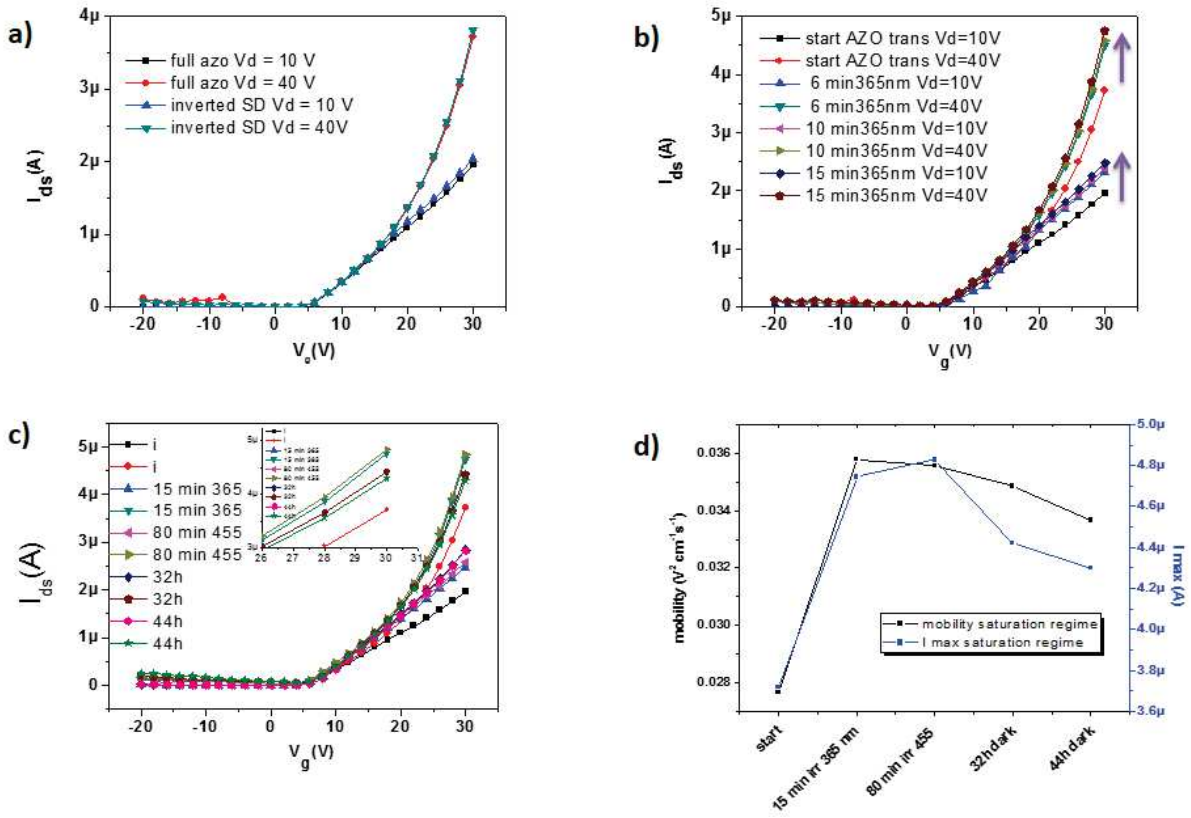


**Figure 6.20 :** Electrical characterization of a device with both electrodes covered by AZO SAMs of channel length 80 µm. a) transfer characteristics in linear ($V_d$=10 V) and saturation regime ($V_d$=40 V) grounding alternatively one of the two electrodes; b) transfer characteristics before and after irradiation of the device with 365 nm light ; c) transfer characteristic in linear and saturation regime starting from *trans* form, after 15 min irradiation with 365 nm, after irradiation with 455 nm light for 80 min and finally after 32 and 44 hours in the dark; d) mobility and maximum drain current in saturation regime plotted for all the transfer curves depicted in fig.c).

AZO in *trans* form should not be affected by irradiation wavelengths characteristic of the switching of a p-tDAE molecules, i.e. 313 nm and 530 nm, as already shown in solution (see **Table 6.1**). If this is true also for SAMs, irradiating the device at these wavelengths should not alter the performance of the OFET. Indeed the experimental results showed no change in the transfer characteristics of a FULL AZO device in the *trans* form upon irradiation with these wavelengths (**Figure 6.21b**). Unfortunately it was not possible to probe the effect of the p-tDAE characteristic switching wavelength on the *cis* form of the device since the SAM seemed blocked in this form as explained above.

For all these devices there was no significant threshold voltage ($V_{th}$) shift.

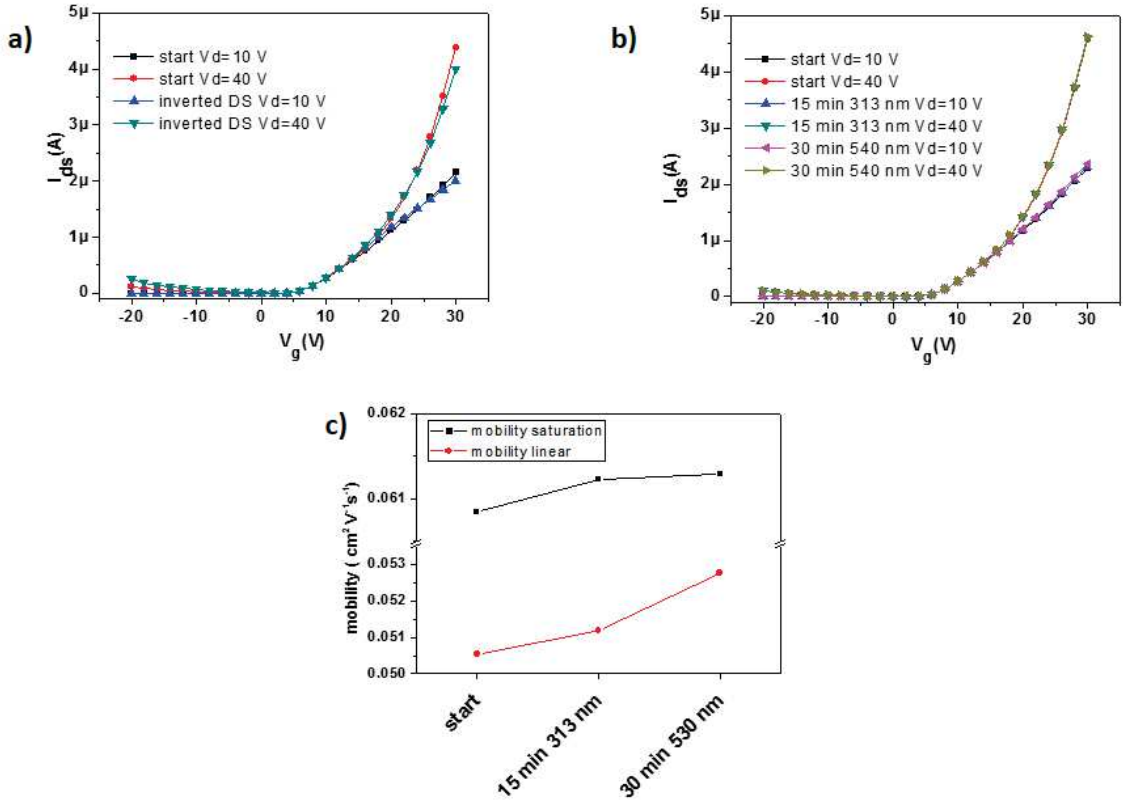


**Figure 6.21 :** Electrical characterization of a device with both electrodes covered by AZO SAMs of channel length 120 µm. a) transfer characteristics in linear ($V_d$=10 V) and saturation regime ($V_d$=40 V) grounding alternatively one of the two electrodes; b) transfer characteristics of the device in the initial state and after subsequent irradiation in the order at 365 nm and 530 nm; c) mobility in the linear and saturation regime extracted from the transfer characteristics in panel b).

### 6.3.5.2. OFETs with p-tDAE SAM on both electrodes

The second class of devices analyzed was the one with p-tDAE SAM on both electrodes.

Also in this case the devices are completely symmetric (**Figure 6.22a**). Irradiating with 313 nm light there was a dramatic change in the transfer characteristics (**Figure 6.22b** and **6.22c**) with an increase of the source drain current of about 50% for saturation regime and 70% for linear regime (**Figure 6.22d**).

Also in this case $V_{th}$ is not affected by irradiation. The increase in mobility can be assigned to the switching of the molecule from a non- conjugated (open) form to a fully conjugated (closed) one, with consequent decrease of the tunneling barrier. It was possible to switch back the p-tDAE to the open form thus recovering the initial transfer characteristics by irradiating the device for 20 min with green light (**Figure 6.22 b** and **6.22c**).

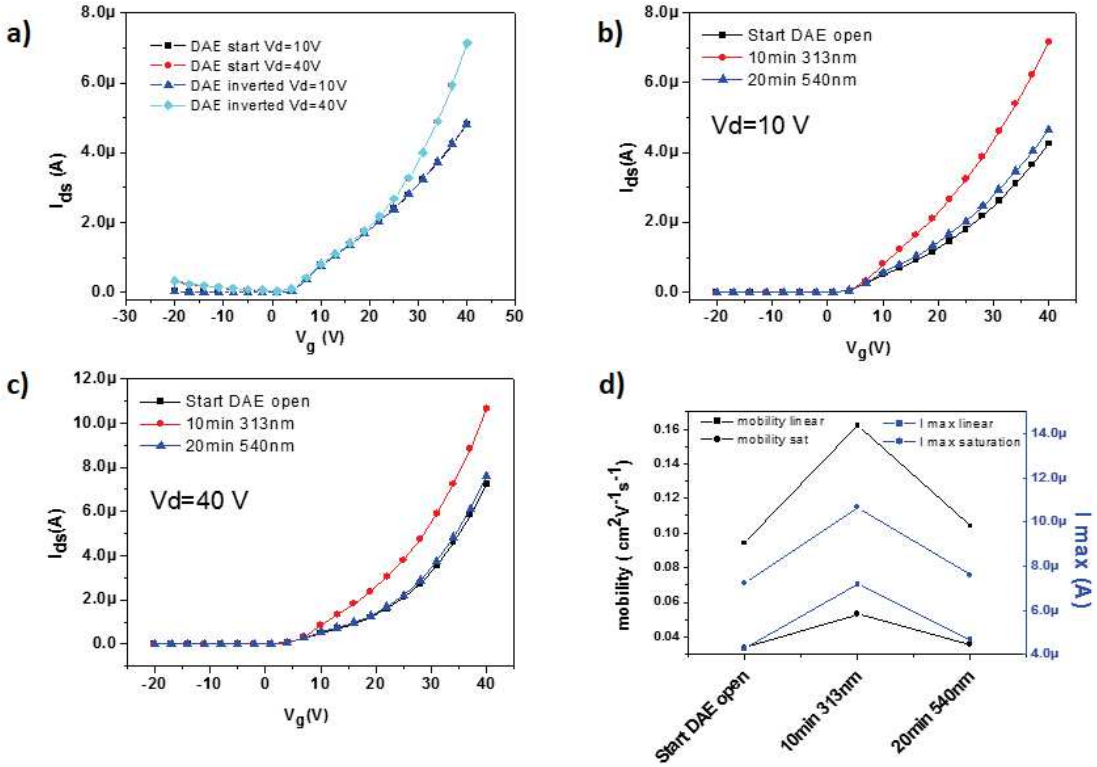


**Figure 6.22 :**Electrical characterization of a device with both electrodes covered by AZO SAMs of channel length 100 µm; a) transfer characteristics in linear ($V_d$=10 V) and saturation regime ($V_d$=40 V) grounding alternatively one of the two electrodes; b) transfer characteristics in the linear regime showing a switching cycle of diarylethene: start(black), transfer after illumination at 313 nm (red) and transfer after illumination at 530 nm (blue); c) transfer characteristics in saturation regime showing a switching cycle of diarylethene: start (black), transfer after illumination at 313 nm (red) and transfer after illumination at 530 nm (blue); d) mobility and maximum drain current in saturation regime plotted for all the transfer curves depicted in fig. b) and c).

The open form of diarylethene in solution is not affected by the switching wavelengths of AZO (see **Table 6.1**). It was revealed that this statement is true also for the p-t DAE in the SAM form by irradiation of a device with DAE in the open form first with 365 nm light and then with 455 nm irradiation. No change in the transfer characteristics was observed (**Figure 6.23a**).

On the contrary after switching the SAM to the closed form and irradiating with 365 nm a slight decrease of the source drain current and an unexpected change in the shape of the transfer characteristics both in linear and saturation regime were registered (**Figure 6.23b** and **c**). The decrease in current could be assigned to the fact that the closed p-tDAE can switch back to the open form when irradiated with 365 nm wavelength. However, we could not state what was the reason for a change in shape of the transfer curve and why after this switching it was not possible to go back to the initial state irradiating with 530 nm wavelength.

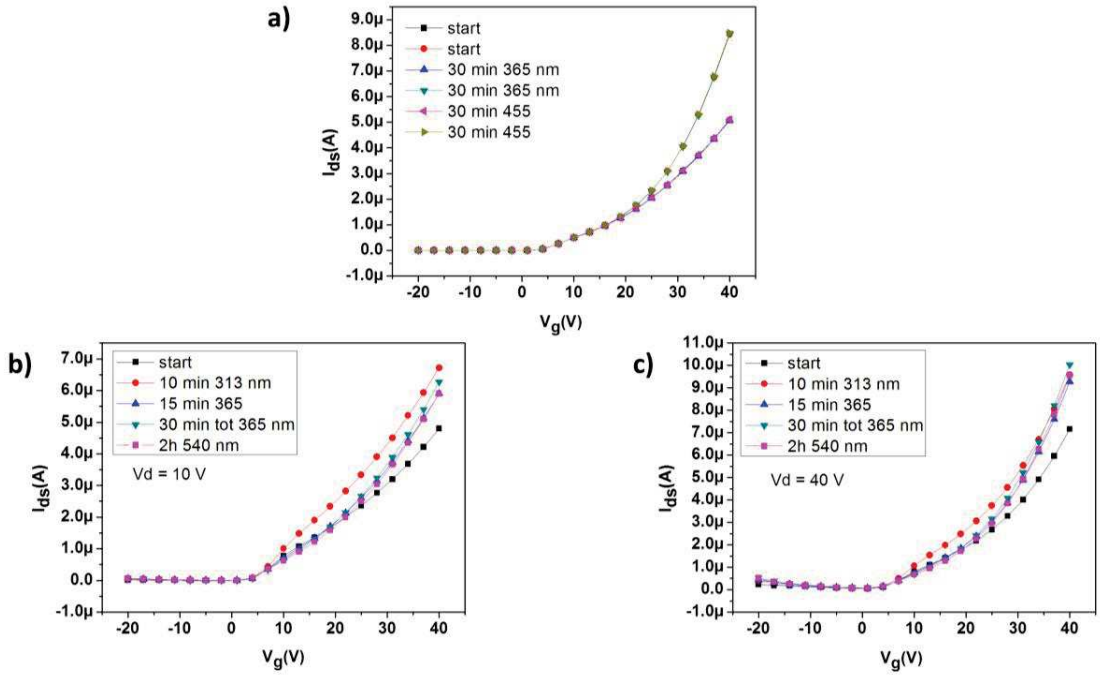


**Figure 6.23 :** Electrical characterization of a device with both electrodes covered by p-tDAE SAMs of channel length 100 µm; a) transfer characteristics starting from the open form and then irradiating subsequently at 365 and 455 nm; c) transfer characteristics in linear regime starting from the device with the p-tDAE in open form, then irradiating at 313 nm to switch it to the closed form followed by an irradiation at 365 nm which causes a decrease of the current and a change in shape followed by irradiation at 540 nm in order to try to recover the initial conditions.

### 6.3.5.3. OFETs with asymmetric electrodes

After the analysis of OFETs bearing the AZO and p-tDAE SAMs on both electrodes we performed the switching of OFETs with asymmetric electrodes. The starting form of SAMs was *trans* for the azobenzene and *open* for the diarylethene. Setting as source alternately the electrode bearing the AZO SAM and the p-tDAE SAM and recording each time the transfer characteristics using the same parameters, different curves were obtained as reported in **Figure 6.25a**. In particular it was noticed that when the electrode functionalized with AZO SAM was grounded, the source–drain current was lower. This can be explained by the workfunction of the two different gold electrodes. In fact as reported in **Figure 6.24** when the AZO coated electrode is grounded (being the source of the electrons) the electrons have to overcome a higher injection barrier than when the DAE coated electrode is grounded to be injected in the LUMO level of the semiconductor. We can conclude that the asymmetry in the functionalization is transferred also in an asymmetry of the electrical properties of the device.

On one of the prepared samples we tried to switch the diarylethene SAM from the open to the closed form, by irradiating at 313 nm. As for the sample where both electrodes were covered with p-tDAE SAM an increase in the source-drain current was recorded (**Figure 6.25b**). It was shown that also in this case 10 minutes of irradiation were sufficient to reach the compete switching since after prolonged irradiation there was no relevant increase of current (**Figure 6.25b**). The increase in current was estimated to be of 21 % in the saturation regime and 15 % in the linear regime, while the mobility increase was 10% in the linear regime and 25% in the saturation regime (**Figure 6.25d**). Surprisingly when irradiating with 530 nm wavelength (**Figure 6.24c**) there was no recover of the original values of transfer characteristics as in the case of the device bearing diarylethene molecules on both electrodes. The only difference in this case is that the electrode was subjected to an electrochemical desorption which can cause modification in the gold itself which can be translated in a different packing of the molecule.[24]

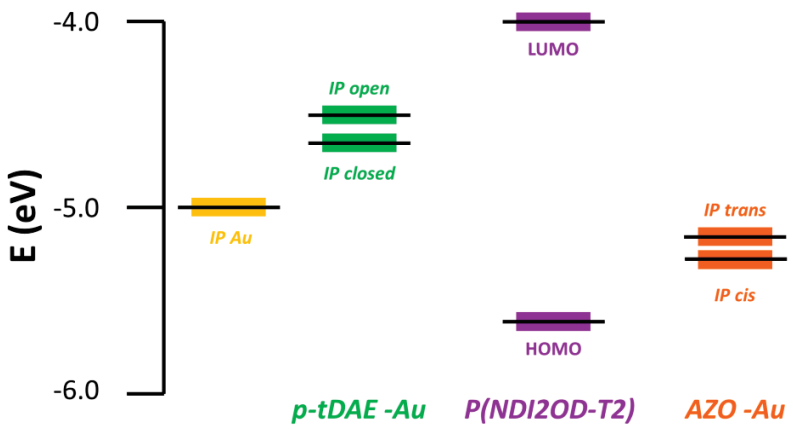


**Figure 6.24 :** Scheme of the energy levels of the organic semiconductor under study and the workfunction of the electrodes functionalized with AZO and p-tDAE. Electrons are injected from the Fermi level of the metal into the LUMO level of the semiconductor overcoming an intrinsic energy barrier. It is possible to see that the barrier is higher in the case of the azobenzene SAM.

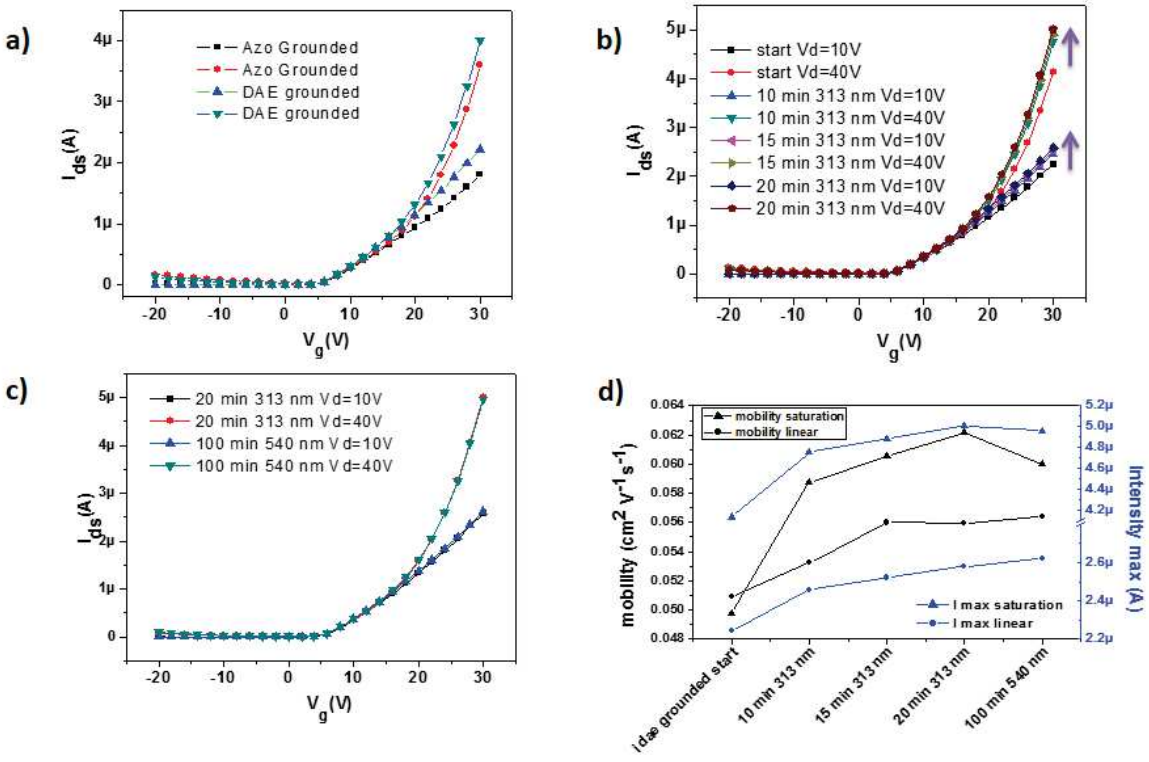


**Figure 6.25 :** Electrical characterization of a device with asymmetric electrodes of channel length 120 µm. a) transfer characteristics in linear ($V_d$=10 V) and saturation regime ($V_d$=40 V) grounding alternatively one of the two electrodes; b) transfer characteristics of the device in the initial state and after irradiation at 313 nm; c) transfer characteristics of the device fter subsequent irradiation at 530 nm; d) mobility and maximum source-drain current measured for the different step of irradiation.

We tried then starting from a new device to switch the azobenzene SAM irradiating at 365 nm (**Figure 6.26a**) Non-linear transfer characteristics with a decrease in drain-source registered current arose from difficult charge injection at low drain voltage ($V_d$=10 V), a typical behavior for not so well contacted devices. Therefore only transfer characteristics recorded at a higher $V_d$ voltage ($V_d$=40 V) were taken into account. By measuring the transfer before and after illumination of the device at 365 nm it was possible to register an increase in current of 12% in the saturation regime (**Figure 6.26d**) which is, as expected, approximately half of the one registered in a device with AZO SAM on both electrodes. Also in this case, as for the reference, after one hour irradiation with 455 nm wavelength only a slight decrease of the current was observed (**Figure 6.26a**) and unfortunately no decay in current was observed even after 16 h in dark, measuring the device the day after without disconnecting the contacts from the electrodes (**Figure 6.26d**). Since we knew that the azobenzene was blocked in the *cis* configuration we tried to switch the diarylethene on the same device. We first irradiated the device with 365 nm light to be sure to bring completely back the AZO to the *cis* form and then we irradiated with 312 nm light (**Figure 6.26 b**). An increase in current of 27% was registered which was comparable to the one measured for the previous asymmetric device (**Figure 6.26d**). Moreover no recover of the transfer characteristics to their original value were observed after irradiating with 530 nm light (**Figure 6.26c**).

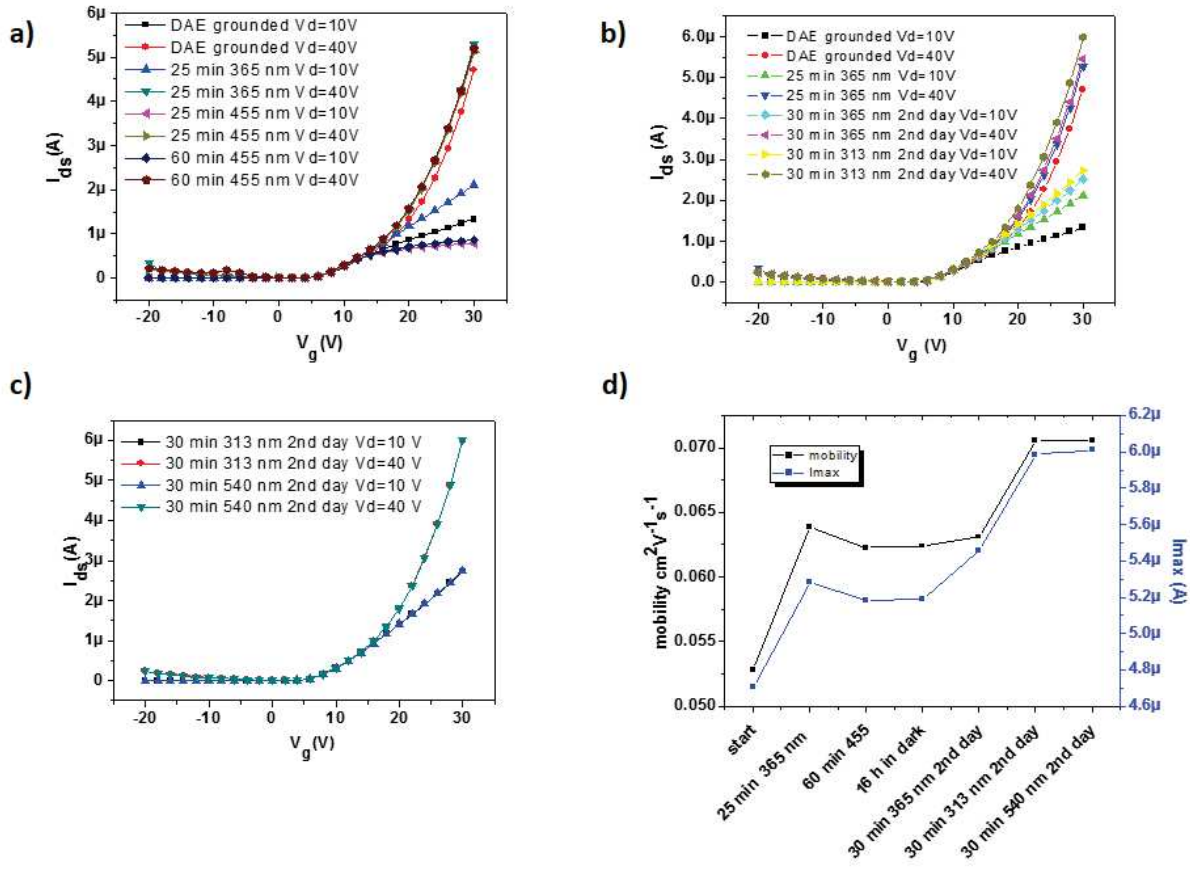


**Figure 6.26 :** Electrical characterization of a device with asymmetric electrodes of channel length 120 μm. a) transfer characteristics in linear ($V_d$=10 V) and saturation regime (Vd=40 V) grounding alternatively one of the two electrodes; b) transfer characteristics in linear and saturation regime for the irradiation cycles performed the day after compared to the day before(The tips remained in contact overnight); c) transfer characteristics recorded after irradiation at 313 nm and 540 nm showing that the diarylethene doesn't switch back; d) mobility and maximum drain –source current in saturation regime for all the experiments performed on the device.

### 6.3.5.4. Blank experiments

To discard any possibility of change in electrical properties of OFETs not correlated with the switching of the SAM we performed two blank experiments. First we tested a transistor without any functionalization of gold electrodes, irradiating with the switching wavelengths of the two molecules. No change occurred upon irradiation (**Figure 6.27a** and **b**), implying that the change in transfer characteristics observed for the previous samples was not correlated with changes in other constituents of the OFETs, such as the organic semiconductor, metals or dielectric.

Moreover also OFETs with electrodes functionalized by monophenylthiols were tested. Also in this case no change in the transfer characteristics was observed after illumination at any of the switching wavelengths (**Figure 6.27 c** and **d**). Thanks to this experiment we excluded also any possible modification induced by the chemisorption of molecules containing aromatic moieties on gold.

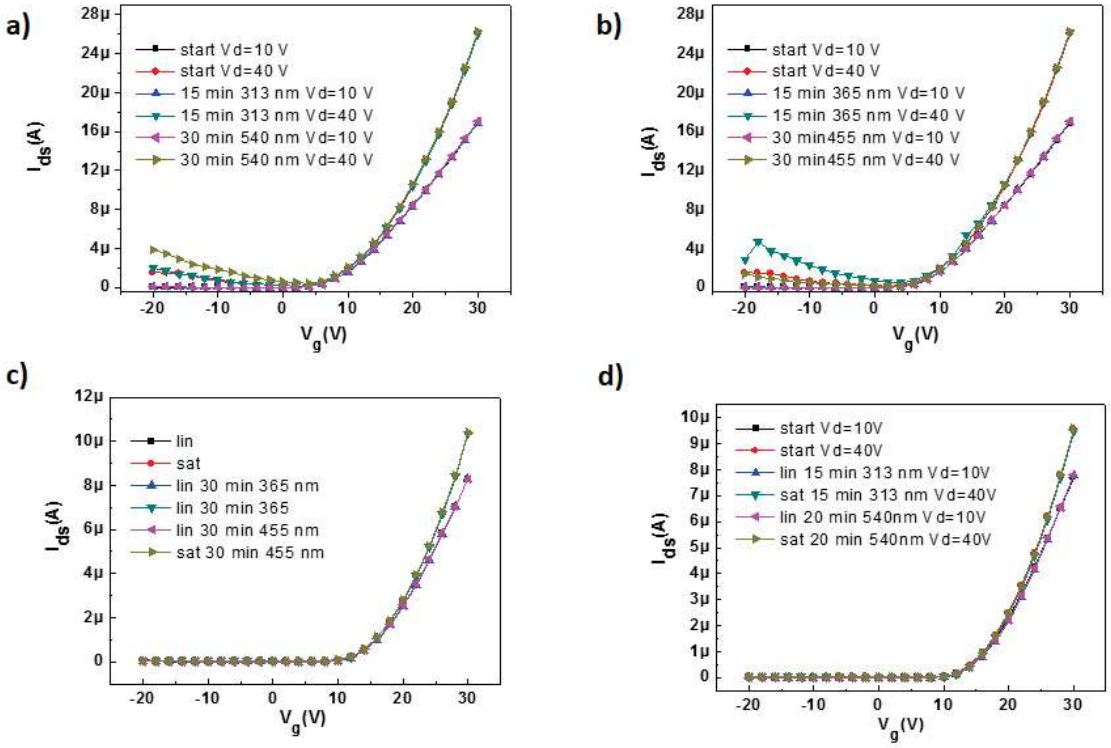


**Figure 6.27 :** Transfer characteristics in linear ($V_d$=10 V) and saturation regime ($V_d$=40 V) for an OFET without any functionalization on the source and drain electrodes before and after irradiation at a) switching wavelengths of diarylethene and b) switching wavelengths of azobenzene; transfer characteristics in linear ($V_d$=10 V) and saturation regime ($V_d$=40 V) for an OFET source and drain electrodes functionalized with a monophenyl thiol SAM before and after irradiation at c) switching wavelengths of azobenzene, and d) switching wavelengths of diarylethene.

## 6.4. Conclusions

In this chapter we have demonstrated that it is possible to functionalize two fully interdigitated electrodes with two different photochromic self-assembled monolayers, thus creating asymmetric electrodes which can respond to different light stimuli. First attempts have been done in order to integrate the asymmetric electrodes in OFETs with bottom contact top gate geometry. The independent switching of the two electrodes has been proven on reference samples bearing the same type of SAM (i.e. AZO or p-t DAE) on both electrodes. When applied in a device, the AZO SAM is blocked in the *cis* form after switching from the *trans* to the *cis* form. We attribute this behavior to the rearrangement of the organic polymer. The p-tDAE SAM switching behavior is ideal in OFETs with both electrodes functionalized with such a molecule forming SAM, while in devices with asymmetric electrodes the p-tDAE SAM becomes blocked in the closed form after the first switching from *open* to *close*. The only difference between the two devices could be a different reorganization of gold after electrochemical desorption which could cause a different packing of the SAM. We believe that though a careful design of the photoswitching molecules it will be possible to overcome these problems and the implementation of this technique will generate new functionalities in devices.

## 6.5. References

1. Yuan, Y.; Giri, G.; Ayzner, A. L.; Zoombelt, A. P.; Mannsfeld, S. C. B.; Chen, J.; Nordlund, D.; Toney, M. F.; Huang, J.; Bao, Z., Ultra-high mobility transparent organic thin film transistors grown by an off-centre spin-coating method. *Nat Commun* **2014,** *5*.
2. Liu, C.; Xu, Y.; Noh, Y.-Y., Contact engineering in organic field-effect transistors. *Mater. Today* **2015,** *18* (2), 79-96.
3. (a) de Boer, B.; Hadipour, A.; Mandoc, M. M.; van Woudenbergh, T.; Blom, P. W. M., Tuning of Metal Work Functions with Self-Assembled Monolayers. *Adv. Mater.* **2005,** *17* (5), 621-625; (b) Campbell, I. H.; Kress, J. D.; Martin, R. L.; Smith, D. L.; Barashkov, N. N.; Ferraris, J. P., Controlling charge injection in organic electronic devices using self-assembled monolayers. *Appl. Phys. Lett.* **1997,** *71* (24), 3528-3530.
4. Di, C.-a.; Zhang, F.; Zhu, D., Multi-Functional Integration of Organic Field-Effect Transistors (OFETs): Advances and Perspectives. *Adv. Mater.* **2013,** *25* (3), 313-330.
5. Orgiu, E.; Samorì, P., 25th Anniversary Article: Organic Electronics Marries Photochromism: Generation of Multifunctional Interfaces, Materials, and Devices. *Adv. Mater.* **2014,** *26* (12), 1827-1845.
6. Irie, M., Photochromism: Memories and SwitchesIntroduction. *Chem. Rev.* **2000,** *100* (5), 1683-1684.
7. (a) Borjesson, K.; Herder, M.; Grubert, L.; Duong, D. T.; Salleo, A.; Hecht, S.; Orgiu, E.; Samori, P., Optically switchable transistors comprising a hybrid photochromic molecule/n-type organic active layer. *J. Mater. Chem. C* **2015**; (b) Gemayel, M. E.; Börjesson, K.; Herder, M.; Duong, D. T.; Hutchison, J. A.; Ruzié, C.; Schweicher, G.; Salleo, A.; Geerts, Y.; Hecht, S.; Orgiu, E.; Samorì, P., Optically switchable transistors by simple incorporation of photochromic systems into small-molecule semiconducting matrices. *Nat Commun* **2015,** *6*; (c) Orgiu, E.; Crivillers, N.; Herder, M.; Grubert, L.; Pätzel, M.; Frisch, J.; Pavlica, E.; Duong, D. T.; Bratina, G.; Salleo, A.; Koch, N.; Hecht, S.; Samorì, P.,

Optically switchable transistor via energy-level phototuning in a bicomponent organic semiconductor. *Nat Chem* **2012,** *4* (8), 675-679.
8. Crivillers, N.; Orgiu, E.; Reinders, F.; Mayor, M.; Samori, P., Optical Modulation of the Charge Injection in an Organic Field-Effect Transistor Based on Photochromic Self-Assembled-Monolayer-Functionalized Electrodes. *Adv. Mater.* **2011,** *23* (12), 1447-1452.
9. Kronemeijer, A. J.; Akkerman, H. B.; Kudernac, T.; van Wees, B. J.; Feringa, B. L.; Blom, P. W. M.; de Boer, B., Reversible Conductance Switching in Molecular Devices. *Adv. Mater.* **2008,** *20* (8), 1467-1473.
10. Liscio, A.; Orgiu, E.; Mativetsky, J. M.; Palermo, V.; Samorì, P., Bottom-Up Fabricated Asymmetric Electrodes for Organic Electronics. *Adv. Mater.* **2010,** *22* (44), 5018-5023.
11. Elbing, M.; Błaszczyk, A.; von Hänisch, C.; Mayor, M.; Ferri, V.; Grave, C.; Rampi, M. A.; Pace, G.; Samorì, P.; Shaporenko, A.; Zharnikov, M., Single Component Self-Assembled Monolayers of Aromatic Azo-Biphenyl: Influence of the Packing Tightness on the SAM Structure and Light-Induced Molecular Movements. *Adv. Funct. Mater.* **2008,** *18* (19), 2972-2983.
12. (a) Bonacchi, S.; El Garah, M.; Ciesielski, A.; Herder, M.; Conti, S.; Cecchini, M.; Hecht, S.; Samorì, P., Surface-Induced Selection During In Situ Photoswitching at the Solid/Liquid Interface. *Angew. Chem. Int. Ed.* **2015**, n/a-n/a; (b) Irie, M.; Lifka, T.; Uchida, K.; Kobatake, S.; Shindo, Y., Fatigue resistant properties of photochromic dithienylethenes: by-product formation. *Chem. Commun.* **1999,** (8), 747-750.
13. Pace, G.; Ferri, V.; Grave, C.; Elbing, M.; von Hanisch, C.; Zharnikov, M.; Mayor, M.; Rampi, M. A.; Samori, P., Cooperative light-induced molecular movements of highly ordered azobenzene self-assembled monolayers. *Proc. Natl. Acad. Sci. U. S. A.* **2007,** *104* (24), 9937-9942.
14. (a) Yang, G.; Liu, G.-y., New Insights for Self-Assembled Monolayers of Organothiols on Au(111) Revealed by Scanning Tunneling Microscopy. *J. Phys. Chem. B* **2003,** *107* (34), 8746-8759; (b) Poirier, G. E., Mechanism of Formation of Au Vacancy Islands in Alkanethiol Monolayers on Au(111). *Langmuir* **1997,** *13* (7), 2019-2026.
15. (a) Ishida, T.; Mizutani, W.; Azehara, H.; Sato, F.; Choi, N.; Akiba, U.; Fujihira, M.; Tokumoto, H., Adsorption Processes of Self-Assembled Monolayers Made from Terphenyl Thiols. *Langmuir* **2001,** *17* (24), 7459-7463; (b) Love, J. C.; Estroff, L. A.; Kriebel, J. K.; Nuzzo, R. G.; Whitesides, G. M., Self-assembled monolayers of thiolates on metals as a form of nanotechnology. *Chem Rev* **2005,** *105* (4), 1103-69.
16. Vericat, C.; Vela, M. E.; Benitez, G.; Carro, P.; Salvarezza, R. C., Self-assembled monolayers of thiols and dithiols on gold: new challenges for a well-known system. *Chem. Soc. Rev.* **2010,** *39* (5), 1805-1834.
17. Crivillers, N.; Liscio, A.; Di Stasio, F.; Van Dyck, C.; Osella, S.; Cornil, D.; Mian, S.; Lazzerini, G. M.; Fenwick, O.; Orgiu, E.; Reinders, F.; Braun, S.; Fahlman, M.; Mayor, M.; Cornil, J.; Palermo, V.; Cacialli, F.; Samori, P., Photoinduced work function changes by isomerization of a densely packed azobenzene-based SAM on Au: a joint experimental and theoretical study. *Phys. Chem. Chem. Phys.* **2011,** *13* (32), 14302-14310.
18. (a) Zhuang, M.; Ernzerhof, M., Reversibility and transport properties of dithienylethene photoswitches. *J. Chem. Phys.* **2009,** *130* (11), 114704; (b) Dulić, D.; van der Molen, S. J.; Kudernac, T.; Jonkman, H. T.; de Jong, J. J. D.; Bowden, T. N.; van Esch, J.; Feringa, B. L.; van Wees, B. J., One-Way Optoelectronic Switching of Photochromic Molecules on Gold. *Phys. Rev. Lett.* **2003,** *91* (20), 207402.
19. Noh, J.; Jeong, Y.; Ito, E.; Hara, M., Formation and Domain Structure of Self-Assembled Monolayers by Adsorption of Tetrahydrothiophene on Au(111). *J. Phys. Chem. C* **2007,** *111* (6), 2691-2695.
20. (a) Ishida, T.; Hara, M.; Kojima, I.; Tsuneda, S.; Nishida, N.; Sasabe, H.; Knoll, W., High resolution x-ray photoelectron spectroscopy measurements of octadecanethiol self-assembled monolayers on Au(111). *Langmuir* **1998,** *14* (8), 2092-2096; (b) Ishida, T.; Choi, N.; Mizutani, W.; Tokumoto, H.; Kojima, I.; Azehara, H.; Hokari, H.; Akiba, U.; Fujihira, M., High-Resolution X-ray Photoelectron Spectra of Organosulfur Monolayers on Au(111): S(2p) Spectral Dependence on Molecular Species. *Langmuir* **1999,** *15* (20), 6799-6806.
21. Mamun, A. H. A.; Hahn, J. R., Effects of Solvent on the Formation of Octanethiol Self-Assembled Monolayers on Au(111) at High Temperatures in a Closed Vessel: A Scanning Tunneling Microscopy and X-ray Photoelectron Spectroscopy Study. *J. Phys. Chem. C* **2012,** *116* (42), 22441-22448.
22. Sun, K.; Jiang, B.; Jiang, X., Electrochemical desorption of self-assembled monolayers and its applications in surface chemistry and cell biology. *J. Electroanal. Chem.* **2011,** *656* (1–2), 223-230.
23. (a) Yang, D. F.; Al-Maznai, H.; Morin, M., Vibrational Study of the Fast Reductive and the Slow Oxidative Desorptions of a Nonanethiol Self-Assembled Monolayer from a Au(111) Single Crystal Electrode. *J. Phys. Chem. B* **1997,** *101* (7), 1158-1166; (b) Sheridan, A. K.; Ngamukot, P.; Bartlett, P. N.; Wilkinson, J. S., Waveguide surface plasmon resonance sensing: Electrochemical desorption of alkane thiol monolayers. *Sens. Actuator B-Chem.* **2006,** *117* (1), 253-260.
24. Carvalhal, R. F.; Sanches Freire, R.; Kubota, L. T., Polycrystalline Gold Electrodes: A Comparative Study of Pretreatment Procedures Used for Cleaning and Thiol Self-Assembly Monolayer Formation. *Electroanalysis* **2005,** *17* (14), 1251-1259.

25. Yan, H.; Chen, Z. H.; Zheng, Y.; Newman, C.; Quinn, J. R.; Dotz, F.; Kastler, M.; Facchetti, A., A high-mobility electron-transporting polymer for printed transistors. *Nature* **2009,** *457* (7230), 679-U1.
26. Luzio, A.; Criante, L.; D'Innocenzo, V.; Caironi, M., Control of charge transport in a semiconducting copolymer by solvent-induced long-range order. *Sci. Rep.* **2013,** *3*.
27. Noriega, R.; Rivnay, J.; Vandewal, K.; Koch, F. P.; Stingelin, N.; Smith, P.; Toney, M. F.; Salleo, A., A general relationship between disorder, aggregation and charge transport in conjugated polymers. *Nat. Mater.* **2013,** *12* (11), 1038-44.

# 7. Conclusion and perspectives

In this thesis we investigated supramolecular interactions with the objective of exploring them as a *tool* towards the development of functional supramolecular architectures useful in nanotechnology.
In the first part of the thesis we studied a well-known host-guest system, the complexation of potassium ions ($K^+$) by cryptand [2.2.2], using an analytical tool explored only recently by supramolecular chemists, the isothermal titration calorimetry (ITC). We demonstrated that by means of ITC it is possible to follow with *in-situ* experiments the reversible complexation / decomplexation of the system cryptand-$K^+$ by subsequent *in-situ* titrations adding after the formation of the cryptate, first a strong acid and then a strong base. In each titration it was possible to determine the thermodynamic parameters relative to the process of complexation of potassium ions by cryptand [2.2.2].The choice of water as a medium can lead to some complications in the analysis of equilibria involving the binding of acidic or basic substrates because in water a significant fraction of cryptand [2.2.2] is present in the monoprotonated form. We showed that optimum condition for the determination of the thermodynamic parameters is a concentration at least of 1 mM.
We believe that ITC is a very useful analytical tool to be still fully explored in supramolecular chemistry, given that with one experiment it is possible to gain knowledge of the entropic and enthalpic contributions of a binding event.

In the second part, we showed that it is possible to exploit supramolecular interactions in order to improve the quality of graphene produced by liquid-phase exfoliation (LPE). In particular, we compared the dispersions produced in presence of two stabilizing agents, a simple coronene molecule and a perchlorinated coronene. Theoretical calculations predicted that chlorine can atoms increase the polarizability of the molecule therefore improving the interaction with graphene. This result was confirmed by thermal desorption spectroscopy where the activation energy for desorption of perchlorocoronene from graphite was found to be higher than the one of simple coronene. In general, the use of these two stabilizing agents during exfoliation in *o*-DCB solvent resulted in an improvement in the quality of the graphene produced. The higher interaction of chlorinated coronene however produced a higher number of monolayers in the final dispersion compared to

coronene. This study showed that supramolecular interactions are useful in order to produce good quality LPE graphene and the more suitable exfoliators/stabilizing agents can be predicted using a simple theoretical model. This model still needs to be improved in order to take into account different liquid media. Successful exfoliations are strictly dependent on the solvent choice with appropriate surface tension, which dictates solvent-molecules and solvent–graphene interactions. The exploitation of *ad-hoc* molecules and the choice of the correct solvent to promote the exfoliation of graphite in liquid media through non-covalent interactions can lead to upscalable production of graphene, which can be used in composites or in organic electronics.

We finally demonstrated that it is possible to prepare asymmetric interdigitated electrodes bearing self-assembled monolayers of two different photochromic switches families on each electrode, i.e. azobenzene and diarylethene. The formation of asymmetric electrodes was proved by XPS and the retained switching properties of the molecules once immobilized on the surface were proved by UV-Vis spectroscopy. First attempts of implementation of these electrodes in organic field-effect transistors were performed in order to show that self-assembled monolayer can be used as active material in a device, to increase the number of functionalities of the device itself. In fact through an appropriate irradiation at different wavelengths it could be possible to modulate the charge injection of each electrode independently thus increasing the number of independent stimuli to which the device can respond. However in our case the switching in the asymmetric device was irreversible for both diarylethene and azobenzene SAMs, showing that in a device structure there can be complex interplays between the different components. An effort in research of suitable device geometries and in the molecular design has to be made in order to overcome these problems.

In summary this thesis shows how supramolecular interactions can be exploited to tune the properties of multicomponent thus multifunctional materials of special interest for fundamental studies in materials and nanosciences towards technological applications in nanotechnology.
Regarding the first section, analytical tools such as ITC are the basis for further developments of supramolecular chemistry. As Cram explained in his Nobel lecture, “evolution has produced chemical compounds exquisitely organized to accomplish the most complicated and delicate of tasks. Many organic chemists viewing crystal structures of enzyme systems or nucleic acids and knowing the marvels of specificity of the immune systems must dream of designing and synthesizing simpler organic compounds that imitate working features of these naturally occurring

compounds." Therefore, bio-inspired supramolecular approaches leading to functional architectures with features similar to the one observed in nature are since ever the goal of synthetic chemists. However, tailoring synthetic receptors to a target analyte requires the perfect understanding of the molecular interactions governing the recognition processes. In this context, ITC is an extremely powerful tool for elucidating the interactions involved in supramolecular recognition and assembly events, thus being an important aid in the design of new receptors. Once designed, these receptors can be employed in nanotechnology in real devices for sensing application.

We have shown that the exploitation of different non-covalent interactions can boost the production of liquid phase exfoliated graphene, and in general of 2-D materials. The intrinsic complexity of all interactions at work in an exfoliation procedure still needs a higher knowledge of fundamental parameters. Adsorption energy and interactions of the surfactant molecules with graphene in presence of the solvent are key parameters for the future design of new efficient stabilizing agents. Thermal desorption spectroscopy and simple theoretical calculations, however, do not take into account the role of the solvent. Therefore ITC is an ideal technique to understand and measure the interaction of potential stabilizing agents with graphene in a specific solvent, therefore being a complementary driving tool in design, choice and exploitation on exfoliating agents beside theoretical calculations.

Graphene and in general 2-D materials hold the future of nanotechnology with their exceptional properties. It is predictable that the applicability of this material will span in every field of nanotechnology, from composites to organic electronics to biomedical applications. However, the current and future market for graphene applications is strictly connected to the production strategies for these materials. The first application available in the market will probability be the one involving graphene inks, since it is at present one of the few kind of graphene potentially producible on a large scale. However, the not highest grade of this graphene will limit its application to flexible electronic devices, such as solar cells and supercapacitors. An effort in improving the quality of produced graphene will lead to further applications of this material in other nanotechnology fields such as biosensors. In this contest supramolecular chemistry can also play an important role. For many biological and analytical applications, graphene surface needs to be functionalized with biomolecules or receptors. Covalent strategies are detrimental for graphene electronic properties since they notch the so desired conductance properties. On this regard, supramolecular chemistry

can have a fundamental role in designing receptors which contain moieties interacting with graphene through non-covalent interactions.

Concerning the last part of this work, the application of photoswitchable self-assembled monolayers in real devices has been shown to be promising for the realization of multi-responsive organic field-effect transistors. More in general, smart surfaces, made of functional molecular units arranged in ordered architectures which are able to respond to a certain stimulus (pH, light, heat, electric or magnetic field) can be integrated in electronic devices, since they are able to change their structure and therefore switching their molecular properties. The application of these functional structures can involve different areas of organic electronics such as chemical sensors, data storage devices, transistors. The demonstration carried out in this thesis is of great importance since transistors are basic components in integrated circuits. Therefore the application of multi-responsive fashion to OFETs is an important step towards integration in market-ready devices.

# 8. Acknowledgements

The journey towards the thesis completion has not always been smooth and easy and, without the help of many people who deserve my gratitude, I would never have reached the final goal.
First of all, I want to thank Prof. Paolo Samorì for giving me the opportunity to perform the PhD in the Nanochemistry Lab. I want to thank him for his advices, his patience and support and for giving me the opportunity to work in the framework of a European project, GENIUS, therefore having the chance to collaborate with scientist from all over Europe in a multidisciplinary environment. Grazie Paolo!

I express all my gratitude to Prof. Jack Harrowfield for his precious help and for the stimulating scientific discussions, which introduced me in the supramolecular chemistry world. I really appreciated the time he spent with me, giving me useful tips and advices, believing that the ITC project could be completed despite all the obstacles. Grazie mille Jack per il tuo prezioso aiuto!

In the framework of the graphene project I want to thank Prof. Klaus Mullen and Prof. Xinliang Feng (Max-Planck Institute for Polymer research, Mainz) for providing me with the chlorinated and hydrogenated aromatic compounds, Dr. Marco Cecchini and Simone Conti (ISIS-Strabourg) for the theoretical calculations and for the useful explanations, Prof. Ovidiu Ersen and Georgian Melinte (IPCMS-Strasbourg) for the TEM analysis, Dr. Cinzia Casiraghi and Yuyoung Shin (University of Manchester) for the Raman characterization and Prof. Manfred Kappes and Dr. Böttcher (KIT-Karlsruhe) for the TPD measurements.

I acknowledge Prof. Marcel Mayor and Dr Federica Reinders (University of Basel) for the synthesis of the biphenyl azobenzene thioacetate and Prof. Stefan Hecht and Dr. Martin Herder (Humboldt University- Berlin) for diarylethenes thioacetate synthesis, Dr. Fanny Richard for the XPS measurements.

I am really grateful to my colleagues which helped me and supported me. From each one of them I learned something not only from the scientific point of you but also most importantly from the human point of you.

I wish to thank Dr. Artur Ciesielski and Dr. Oliver Fenwick for supervising me during these four years of PhD giving me useful advices and tips. I thank Dr. Emanuele Orgiu and Dr. Sara Bonacchi for the useful scientific discussions and help. Thanks to Dr. Alexander Klekachev, Dr. Marco Gobbi, Dr. Lei Zhang, Dr. Fanny Richard, Dr. Corinna Raimondo, Dr. Andrea Cadeddu, Dr. Silvia Colella, Dr. Markus Döbellin, Dr. Jorn-Oliver Vogel, Dr. Appan Merari Masillamani, Dr. Mohamed El Garah, Dr. Karl Börjesson, Dr. Matthias Treier, Dr. Songlin Li, Dr. Xiaoyan Zhang, Dr. Lili Hou, Dr. Anna Llanes-Pallas, Dr. Gareth Nealon, Dr. Nicolas Weibel.

All my gratitude to my PhD colleagues Dr. Laura Ferlauto, Dr. Lucia Gramigna, Marco Squillaci, Tim Leydecker, Wassima Rekab, Sébastien Haar, Tindara Verduci, Dr. Gabriella Zappalà, Agostino Galanti, Matilde Eredia, Serena Morselli and Karima Bouras. I acknowledge in particular Marc-Antoine Stoeckel for the help with the French resumée. I also acknowledge Alessandro Aliprandi for his advices concerning photochemistry. Without your help, the support and the funny moments spent inside and outside the lab these four years would not have been the same. Grazie mille ragazzi!

There are two special girls with whom I started this PhD adventure, Chiara Musumeci and Mirella El Gemayel. Thank you Chiara and Mirella for being always by my side and encouraging me every day, for the laughing and the beautiful days spent together.

I thank Corinne Cledger, Marie-Claude Jouaiti and Axel Duthey for all the administrative help and ISIS staff, in particular Fabien, Muriel, Fabienne, Thierry and Philippe.

In these four years, I met many friends in Strasbourg, which made my stay here constellated of beautiful moments and souvenirs: Gaëlle, Claudio, José, Mihai, Giangi, Enrica, Greta, Dario, Nadia, Petr, Kaca, Federica, Elena, Beatrice, Irene, Alessandro, Pierre, Gareth, Ylenia, Jennie, Lars,… Thank you Gaëlle and Claudio for supporting me and for the funny moments spent together. Giangi you were the best guide ever in the first year of PhD and you encouraged me not to give up soon…grazie mille. Nadia, we shared the “love and hate” parts of a PhD, we gave each other support, and finally we made it! Enrica thanks for the nice promenades together discussing about life, the time spent with you was precious. I thank you all guys!

The most important acknowledgment goes to my family: my parents, my sister Teresa, my grandparents, my uncles Carmela and Vincenzo, my cousins Annamaria and Roberto and my best friend Katiana that always supported me and believed in me.

Words cannot express how grateful I am to Thomas. You were always there by my side, helping me inside and outside the lab, telling me that I could make it despite all the difficulties, always being able to dry my tears and transform them into a smile. You are a great person and a great scientist and you deserve all the best! I do not know how to thank you for all these beautiful two years of love and happiness. Meeting you is the best gift that Strasbourg could give me. We will leave this beautiful city but TOGETHER towards a new chapter of our life.

Maria G. DEL ROSSO

# EXPLORING SUPRAMOLECULAR INTERACTIONS IN HYBRID MATERIALS


## Résumé

Ce travail visait à explorer les interactions supramoléculaires comme un outil dans les domaines de la chimie hôte-invité, les nanomatériaux et les nanotechnologies en général, afin de parvenir à des objectifs différents. D'abord, une interaction classique hôte-invité a été étudiée, au moyen d'une technique innovante telle que l'ITC, puis nous avons exploité les interactions supramoléculaires afin de maitriser la production de graphène exfolié en phase liquide, en mettant un accent particulier sur l'amélioration de la qualité et la quantité du matériau produit. Enfin, nous avons étendu l'utilisation de la chimie supramoléculaire à un dispositif réel par la fonctionnalisation des électrodes d'or avec des molécules photochromiques, ouvrant alors la voie à des dispositifs organiques multifonctionnels, pouvant être contrôlés par la lumière.


Mots-clés: chimie supramoléculaire, ITC, graphène, monocouches auto-assemblées, molécules photochromiques, électronique organique.


## Résumé en anglais

This work was aimed at exploring supramolecular interactions as a *tool* in the fields of host-guest chemistry, nanomaterials and in general nanotechnology, in order to achieve different goals. First, a classical host-guest interaction was studied by means of the ITC technique, then we exploited supramolecular interactions in order to harness the production of liquid-phase exfoliated graphene, with a particular focus on improving the quality and quantity of material produced. Finally, we extended the use of supramolecular chemistry to a real device by functionalization of gold electrodes with photochromic molecules, hence paving the way towards multifunctional organic devices and in prospective to graphene based light-controlled multifunctional devices.


Keywords: Supramolecular chemistry, ITC, graphene, self-assembled monolayers, photochromic molecules, organic electronics